

**UNIVERSITÉ DU QUÉBEC**

THÈSE PRÉSENTÉE À  
L'UNIVERSITÉ DU QUÉBEC À CHICOUTIMI  
COMME EXIGENCE PARTIELLE  
DU DOCTORAT EN INGÉNIERIE

PAR  
**MOJTABA ESKANDARIAN**

**Ice shedding from overhead electrical lines by mechanical breaking**

A ductile model for viscoplastic behaviour of atmospheric ice

**Délestage de glace des câbles électriques par bris mécaniques**

Un modèle du comportement ductile viscoplastique de la glace atmosphérique poreuse

**SEPTEMBRE 2005**



### *Mise en garde/Advice*

Afin de rendre accessible au plus grand nombre le résultat des travaux de recherche menés par ses étudiants gradués et dans l'esprit des règles qui régissent le dépôt et la diffusion des mémoires et thèses produits dans cette Institution, **l'Université du Québec à Chicoutimi (UQAC)** est fière de rendre accessible une version complète et gratuite de cette œuvre.

Motivated by a desire to make the results of its graduate students' research accessible to all, and in accordance with the rules governing the acceptance and diffusion of dissertations and theses in this Institution, the **Université du Québec à Chicoutimi (UQAC)** is proud to make a complete version of this work available at no cost to the reader.

L'auteur conserve néanmoins la propriété du droit d'auteur qui protège ce mémoire ou cette thèse. Ni le mémoire ou la thèse ni des extraits substantiels de ceux-ci ne peuvent être imprimés ou autrement reproduits sans son autorisation.

The author retains ownership of the copyright of this dissertation or thesis. Neither the dissertation or thesis, nor substantial extracts from it, may be printed or otherwise reproduced without the author's permission.



To my spouse, Marjan,

whose patience, encouragement, and moral support were an  
inspiration to me throughout this endeavour.

## RÉSUMÉ

Le givrage atmosphérique des lignes de transport d'énergie électrique peut causer de sérieux problèmes aux réseaux de transport et de distribution en raison de la forte adhésion de la glace aux substrats. Afin d'éviter des pannes majeures d'électricité causées par de sérieuses tempêtes de verglas, l'amélioration des caractéristiques mécaniques des composantes des lignes de transport ainsi que les techniques anti-givre et de dégivrage doivent être considérées. Le développement de ces techniques exige, à son tour, des connaissances approfondies sur les forces d'adhésion et les caractéristiques de résistance volumiques de la glace atmosphérique.

L'*objectif principal* de cette recherche, dans le cadre de la problématique générale du délestage de glace, est de présenter un modèle du comportement ductile viscoplastique de la glace atmosphérique poreuse. Les effets des activités de fissuration devraient être ajoutés au modèle afin de prédire le comportement du matériau en transition et dans des régions fragiles. Cela peut se faire en modifiant, tant les formulations des paramètres élastique, viscoélastique et plastique des matériaux pour mieux tenir compte de l'activité de fissuration, que les surfaces d'écoulement pour refléter l'effet des taux élevés de déformation.

Un *survol de la littérature* a démontré que certains modèles ont été développés, depuis environ deux décennies, afin de prédire le comportement mécanique de l'eau douce glacée. Toutefois, pratiquement tous les modèles prédisent le comportement mécanique de l'eau douce glacée uniforme. Ainsi, l'effet de la pression sur le comportement du matériau, induit par la présence de bulles d'air, n'a pas été considéré dans ces modèles. Cependant, la porosité de la glace atmosphérique varie en fonction du régime d'accumulation, parfois jusqu'à 35 %, ce qui correspond à des densités de glace allant de  $917 \text{ kg/m}^3$  à  $600 \text{ kg/m}^3$ . Les résultats d'essais en laboratoire effectués sur de la glace poreuse ont démontré l'influence significative de la porosité sur le module élastique et la résistance de la glace.

Les essais de matériaux effectués sur différents types de glace polycristalline montrent que la glace présente un comportement de type fluage à des températures au dessus de  $-40^\circ\text{C}$ . Cela veut dire que le comportement mécanique de la glace est sensible à la vitesse de déformation et à la température, et qu'un minimum de trois composantes de déformations macroscopiques, notamment les déformations élastiques (instantanées) et inélastiques, soit de type viscoélastique à retardement et de type viscoplastique (irréversible), décrivent la réponse du matériau. La nature complexe de cette question est due au fluage non linéaire, à la transition de la glace de son état ductile à son état fragile en fonction des taux de déformation, de même qu'à plusieurs paramètres du matériau, à la complexité dans la propagation des fissures, et aux difficultés associées à sa transposition dans des équations constitutives.

La *méthodologie* utilisée pour résoudre le système d'équations non linéaires est basée sur le principe des travaux virtuels qui conduit à une formulation intégrale adaptée à

l'application de la méthode des éléments finis. Le comportement du matériau est exprimée sous forme incrémentale, ce qui requiert un schéma pour l'intégration de la loi d'évolution du comportement en utilisant par exemple un algorithme basé sur la méthode trapézoïdale généralisée (schéma d'Euler implicite / explicite). Le schéma implicite est inconditionnellement stable, alors que la stabilité du schéma explicite est fonction du pas de temps choisi. De plus, une méthode de linéarisation incrémentale suffit pour résoudre ce système d'équations non linéaires. Dans la présente recherche toutefois, le logiciel de calcul des structures ABAQUS est utilisé et le comportement du matériau est décrit à l'aide d'un sous-programme d'intégration numérique d'une loi de comportement spécifique à l'utilisateur (UMAT). La méthodologie de la présente recherche est ensuite adaptée à la formulation des lois de comportements élastiques, viscoélastiques et plastiques pour différents types de glace atmosphérique naturelle accumulée sur des câbles électriques et à leur implémentation dans le logiciel ABAQUS.

Afin de déterminer le domaine d'application de chaque modèle mathématique pour la glace atmosphérique, la texture (morphologie) et la structure des dépôts de glace sur les câbles doivent être connues. Pour ce faire, une étude détaillée de la microstructure et du contenu en bulles d'air de la glace atmosphérique a été conduite par Laforte *et al.* (1983). La structure du grain et des bulles d'air a été étudiée dans diverses conditions atmosphériques, mais la direction des « c-axis » demeurait inconnue. Dans la présente étude, une série d'observations complémentaires de la microstructure ont été conduites et ont démontré que la structure des dépôts de verglas était similaire à celle de la glace en colonne de type S2 (eau douce glacée), alors que la glace en colonne de type S1 est généralement observée dans les régions de transition et initiales du régime d'accrétion de glace dans des conditions sèches (givre lourd). Par contre, la structure granulaire s'observe dans un régime d'accrétion dans des conditions très sèches (givre léger). Dans ce travail, nous utilisons la méthodologie générale suivante pour décrire le comportement ductile de la glace atmosphérique poreuse :

1) Déformations élastiques instantanées : La loi de Hooke établit une relation entre le champ de déformations élastiques et le champ de contraintes associé. Les modules élastiques de la glace polycristalline uniforme sont déterminés à partir des valeurs du monocristal obtenues par une technique d'étalement de Hill (1952). Les constantes élastiques du monocristal, mesurées par Gammon *et al.* (1983), ont été utilisées afin de déterminer les modules élastiques de la glace uniforme. Les limites supérieures et inférieures de chaque module élastique du polycristal sont déterminées à l'aide des techniques de calcul des moyennes de Voigt (1910) et de Reuss (1929), et la valeur moyenne obtenue est considérée comme étant le module élastique de la glace polycristalline.

La modification pour la glace poreuse est rendue possible en définissant la contrainte effective d'un matériau poreux qui consiste en une contrainte induite dans le matériau solide et en une pression des pores. Deux situations extrêmes, c'est-à-dire les modèles avec drainage et sans drainage, sont pris en considération et dans chaque cas, les hypothèses de Voigt (1910) et de Reuss (1929) sont utilisées pour calculer la pression des pores, la force

et la contrainte effective, de même que la variation du contenu liquide. Le modèle avec drainage est alors appliqué aux questions poro-élastiques pour les dépôts de verglas et le modèle sans drainage est mieux adapté pour les dépôts de givre.

2) Déformation viscoélastique à retardement : La rhéologie à court terme proposée par Sinha (1978) est utilisée pour formuler la contrainte viscoélastique à retardement induite par glissement à la frontière du grain en fonction de la déformation élastique. L'effet de la température sur le comportement viscoélastique est introduit à l'aide d'une fonction de décalage dans le modèle. L'effet de la porosité, pour sa part, est intégré dans les formulations en remplaçant la déformation élastique par l'intensité de la contrainte effective correspondante d'un matériau poreux. Finalement, une fonction de changement structurel est définie afin de considérer l'influence de la déformation plastique sur la contrainte viscoélastique. Les paramètres du matériau induits dans la formulation pour la contrainte viscoélastique ont été choisis à partir des calculs de Derradji-Aouat (2000).

3) Déformation plastique permanente : La formulation pour la déformation plastique est développée à partir de la théorie du modèle « cap-plasticity » et en considérant une série de variables internes, les déformations plastiques et leur taux de variation. Le modèle de plasticité pour la glace poreuse inclut la limite élastique, les différences entre le comportement en traction et en compression, de même que les effets de la porosité et de la température. La surface de charge ou fonction d'écoulement, dans ce cas-ci, inclut trois segments importants : un segment parabolique d'écoulement en cisaillement de type Drucker-Prager modifiée, un segment « cap » elliptique qui intersecte l'axe de contraintes hydrostatique et un segment définissant la limite en tension. La critère d'écoulement en cisaillement décrit l'effet de la pression sur la résistance de la glace à l'aide de trois paramètres : la cohésion du matériau, l'angle de friction et la pression hydrostatique correspondant à la contrainte de cisaillement maximale. L'état actuel du «segment cap» est déterminé par deux variables internes : la pression à la contrainte de cisaillement maximum et la pression de fusion de la glace poreuse. La pression à la limite de résistance en tension dans la région ductile est le seul paramètre du matériau en relation avec les limitations en tension. Les données d'analyses de Jones (1982), Nadreau et Michel (1984), et Rist et Murrell (1997) sont utilisées afin de déterminer, en fonction de la surface d'écoulement en cisaillement pour la glace uniforme, les paramètres du matériau qui sont affectés par la structure de la glace, sa température et son taux de déformation, mais qui ne sont pas affectés par la dimension du grain. Une loi d'écoulement associée et un paramètre d'écrouissage du segment cap sont utilisés dans ce travail. L'effet de la porosité est considéré dans le modèle à l'aide d'une définition de la contrainte effective.

Enfin, la catégorisation des contributions scientifiques majeures de cette recherche peut se faire en considérant les objectifs initialement définis et en suivant la méthodologie générale comme suit : (a) en classifiant la structure de la glace atmosphérique accumulée sur les câbles électriques en fonction de la forme des grains (texture) et de l'orientation du «c-axis» (structure) ; (b) en introduisant trois programmes développés dans le progiciel *Maple Mathematical Program* afin de déterminer les modules élastiques pour différents types d'eau douce glacée (glace granulaire et en colonne S1, S2 et S3) ; (c) en introduisant

un modèle poroélastique afin de modifier les modules élastiques de la glace atmosphérique poreuse ; (d) en introduisant un modèle de plasticité de type « cap-model » pour différents types de glace atmosphérique poreuse ; (e) en présentant une nouvelle fonction d'écoulement dans la région ductile d'eau douce gelée, qui est en meilleur accord avec les données d'analyses disponibles, et ensuite en les généralisant pour inclure la porosité à l'aide d'un « cap » elliptique mobile; et (f) en développant un sous-programme d'une loi de comportement viscoplastique spécifique à l'utilisateur (UMAT) pour la glace atmosphérique dans la région ductile, incluant les domaines poroélastique, viscoélastique, et « cap-model » de plasticité.

## ABSTRACT

Atmospheric icing of overhead power lines creates many serious electrical and mechanical problems in the transmission network due to the high adherence of ice to substrates. To avoid major breakdowns in the power network during severe ice storms, the improvement in mechanical characteristics of the line components, as well as anti-icing and de-icing techniques should be taken into consideration. The successful development of those techniques, in turn, requires good knowledge of the adherence and bulk strength characteristics of atmospheric ice.

The *main objective* of this research, as a part of the general ice shedding problem, is to present a model for viscoplastic behaviour of porous atmospheric ice in the ductile region. The effects of cracking activities should be added to the model to predict the material behaviour in transition and brittle regions. This can be done by modifying the formulations of elastic, viscoelastic and plastic material parameters for cracking activities, as well as the yield envelopes in higher ranges of strain rates.

A *literature survey* revealed that some models have been developed to predict the mechanical behaviour of ice over the past two decades. However, almost all the models predict the mechanical behaviour of bubble-free freshwater ice. Thus, the pressure dependency in material constitution, induced by the presence of air bubbles, has not been considered in those models. The porosity of atmospheric ice varies depending on the accretion regime, sometimes by as much as 35%, corresponding to ice densities from 917 down to 600 kg/m<sup>3</sup>. The results of some laboratory tests carried out on porous sea ice shows the significant influence of porosity on the elastic moduli and strength of ice.

The material tests carried out on various types of polycrystalline ice show that ice normally exhibits creep behaviour at an ambient temperatures higher than -40°C. This means that the mechanical behaviour of ice is rate sensitive and temperature dependent, and a minimum of three macroscopically observed strain components, namely instantaneous elastic, delayed viscoelastic, and inelastic strains, describe the material constitution. The complex nature of this problem originates from nonlinear creep deformation, ductile to brittle behaviour of ice that depends highly to strain rates, numerous material parameters, complexity of the mechanism of crack propagation, and the difficulties due to its consideration into the constitutive equations.

The *methodology* for solving the resulting system of non-linear governing equations is based on the principles of virtual work leading to the weak integral form of the governing differential equations suitable for applying the finite-elements method. The material constitutive equations are in rate form, hence the generalized trapezoidal time-integration technique (Explicit Forward / Implicit Backward Euler Scheme) is applied. The latter scheme provides unconditional stability for integration, while the stability of the former scheme depends on the size of time steps. In addition, the incremental linearization method is sufficient for solving this system of non-linear equations. In this work, however, the

ABAQUS FE mechanical analysis program is used and the material evolution is described by means of a user material subroutine (UMAT) appropriate for numerical computations. The methodology of this work is then reduced to the manner of formulating the elastic, viscoelastic, and plastic deformation mechanisms for various types of atmospheric ice deposits naturally accreted on power lines and of implementing those constitutive equations into the ABAQUS program.

To find the applicability domain of each mathematical model for the case of atmospheric ice, the texture (morphology) and fabric of ice deposits on power lines should be known. To this end, a detailed microstructure and bubble-content observation of atmospheric ice deposits was reported by Laforte *et al.* (1983). The grain and bubble structures were studied at various meteorological conditions; however, the c-axis direction still was undetermined. In this work, hence, a series of complementary microstructure observations were performed, which identified that the glaze deposits have a structure similar to that of S2 columnar ice (freshwater ice), while S1 columnar ice is mostly observed in the transition and beginning regions of dry-regime ice accretions (hard rime). On the other hand, the granular structure is observed at a very dry regime of ice accretion (soft rime). The general methodologies below are followed in this research for describing the ductile behaviour of porous atmospheric ice:

1) Instantaneous elastic strain: Hooke's law relates the elastic strain field to the corresponding applied stress. The elastic moduli of freshwater polycrystalline ice are determined from the monocrystal (single crystal) data by using Hill's (1952) averaging technique. The monocrystal elastic constants measured by Gammon *et al.* (1983) were used to determine the temperature-dependent elastic moduli of polycrystalline bubble-free ice. The upper and lower bounds for each elastic modulus of polycrystal are determined using Voigt (1910) and Reuss (1929) averaging techniques, and then the averaged value is considered as the elastic moduli of polycrystalline freshwater ice.

The modification for porous ice is possible by defining the effective stress in porous material that consists of the stress induced in solid material and the pore pressure. Two extreme situations, namely drained and undrained models, are considered, in each case the Voigt (1910) and Reuss (1929) hypothesis were used to calculate the pore pressure, the effective stress and strain, and the variation in fluid content. The drained model is then applied to the poroelastic problems for glaze deposits, while the undrained model is more suitable for rime deposits.

2) Delayed viscoelastic strain: The short-term rheology proposed by Sinha (1978) is used to formulate the delayed viscoelastic strain induced by grain boundary sliding as a function of elastic strain. The temperature dependency of viscoelastic behaviour is considered in the model by means of a shift function. The effect of porosity, on the other hand, is entered into the formulations by replacing the elastic strain with the corresponding magnitude of effective strain in porous material. Finally, a structural change function is also defined for considering the influence of plastic deformation onto this viscoelastic strain. The material parameters induced into the formulation of viscoelastic strain are selected from the measurements of Derradji-Aouat (2000).

3) Permanent plastic strain: The formulation of plastic deformation is developed based on the cap-model plasticity theory and by considering a set of internal / state variables, in this case, the plastic strains and strain rates. This quasi rate-independent plasticity model for porous ice includes pressure-sensitive yielding, difference in tensile and compressive strengths, porosity dependency, as well as rate and temperature dependency of material parameters. The yield surface, in this case, includes three main segments: a parabolic modified Drucker-Prager shear-yield surface, an elliptical moving cap that intersects the pressure stress axis, and a tensile cutoff. The shear-yield criterion describes the pressure dependency of ice strength by means of three parameters: the material cohesion, the friction angle, and the hydrostatic pressure at maximum shear strength. The current state of the cap is determined by two internal variables: the pressure at maximum shear strength of porous ice, and the melting pressure. The pressure at tensile strength is the only material parameter in relation with the tension cutoff. The test data of Jones (1982), Rist and Murrell (1997), and Nadreau and Michel (1984) are used to determine the material parameters of shear-yield envelope for bubble-free ice, which is affected by ice structure, temperature, and strain rate, but unaffected by grain size. An associated flow rule and one hardening parameter for cap yielding are used in this work. The effect of porosity is considered into the model by means of the effective stress definition.

Finally, the major scientific contributions of this study can be categorized by considering the pre-defined objectives and by pursuing the described general methodology as: (a) classification of atmospheric ice structure on power lines on the basis of its grain shape (texture) and c-axis orientation (fabric); (b) presenting three computer codes in *Maple Mathematical Program* for determining the elastic moduli of various types of freshwater ice (granular, columnar S1, S2, S3); (c) presenting a poroelastic model for modifying the elastic moduli of porous atmospheric ice; (d) presenting a cap-model plasticity for various types of porous atmospheric ice; (e) presenting the new freshwater ice yield envelopes in ductile region, which has a better agreement with the available test data, and then generalizing them to take the porosity into consideration by means of an elliptical moving cap; and (f) developing a user-defined material subroutine (UMAT) for viscoplastic behaviour of atmospheric ice in ductile region including the poroelastic, viscoelastic, and cap-model plasticity.

## **ACKNOWLEDGMENTS**

This research has been carried out within the framework of the NSERC/Hydro-Quebec Industrial Chair on Atmospheric Icing of Power Network Equipment (CIGELE) and the Canada Research Chair on Atmospheric Icing Engineering of Power Network (INGIVRE) at the University of Quebec at Chicoutimi (UQAC) in collaboration with Mechanical Engineering Department of Laval University, Quebec, Canada. I am thankful to the sponsors of those industrial chairs for their financial support.

I would like to express my deepest sense of gratitude to my supervisor Prof. Masoud Farzaneh for his support, confidence, and encouragement during my Ph.D. studies. It has been a pleasure to study ice mechanics encouraged by his great experience. I would like also to convey my great appreciation to my thesis co-director Prof. Augustin Gakwaya for his valuable guidance, support, and encouragement.

I am grateful to the reviewers of my thesis, Dr. Robert Gagnon and Dr. Hamid Reza Shakeri for their comments and for accepting to be the members of my thesis committee, and Prof. Marcel Paquet for supporting me as one of the graduate students of UQAC. I am also thankful of all the CIGELE / INGIVRE researchers and staff for their moral support during my studies, especially Mr. Jean Talbot for his gentle comments in the English text.

And finally, most respectfully, I would like to especially thank my wife, Marjan, for her patience, confidence, and moral support during my studies. I also remember our parents who were always our greatest source of inspiration.

# TABLE OF CONTENTS

RÉSUMÉ .....	i
ABSTRACT.....	v
ACKNOWLEDGMENTS .....	viii
TABLE OF CONTENTS.....	ix
LIST OF FIGURES .....	xiii
LIST OF TABLES.....	xix
GLOSSARY OF NOTATIONS .....	xx
CHAPTER 1 .....	1
1. INTRODUCTION.....	1
1.1 General.....	1
1.2 Statement of the problem.....	2
1.3 General objectives.....	7
1.4 General methodology.....	9
1.5 Statements of original contributions .....	11
1.6 Structure of the thesis .....	14
1.7 Conclusions.....	17
CHAPTER 2 .....	18
2. LITERATURE REVIEW.....	18
2.1 Introduction.....	18
2.2 Ice microstructure and texture observations .....	18
2.3 Laboratory measurements of mechanical properties of ice .....	21
2.4 Mathematical modeling of ice constitution.....	29
2.4.1 Determining the elastic moduli of polycrystalline ice.....	30
2.4.2 Formulation of delayed viscoelastic strain .....	33
2.4.3 General modeling of ice behaviour .....	36
2.4.4 Deficiencies of existing viscoplastic models and the areas of improvement: .....	37
2.5 Field measurements and experimental techniques.....	37
2.6 Other related research works .....	38
2.7 Conclusions.....	39

CHAPTER 3 .....	41
3. THEORETICAL BACKGROUND .....	41
3.1 Introduction.....	41
3.2 Stress and strain invariants .....	45
3.3 Elastic moduli of anisotropic polycrystalline material .....	46
3.3.1 Elastic constants of hexagonal monocrystals in an arbitrary direction.....	47
3.3.2 Upper and lower bounds of polycrystal elastic constants.....	49
3.3.3 Hill's averaging technique and polycrystal elastic moduli.....	52
3.4 Viscoelastic model for atmospheric ice .....	54
3.5 Plasticity model for porous materials .....	55
3.5.1 Yield function.....	55
3.5.2 Flow rule.....	56
3.5.3 Hardening rule.....	57
3.5.4 Cap-model plasticity for porous materials.....	58
3.6 Conclusions.....	61
CHAPTER 4 .....	62
4. POROELASTICITY OF ATMOSPHERIC ICE .....	62
4.1 Introduction.....	62
4.2 Elastic moduli of bubble-free polycrystalline ice .....	63
4.2.1 Elastic moduli of ice monocrystal .....	64
4.2.2 Practical elastic formulation for granular ice .....	65
4.2.3 Practical elastic formulation for columnar ice.....	67
4.2.4 Elastic anisotropy of columnar ice .....	71
4.3 Poroelasticity model for atmospheric ice.....	78
4.3.1 Application of Reuss analogy to porous material modeling.....	79
4.3.2 Application of Voigt analogy to porous material modeling.....	83
4.3.3 Porous material modeling for atmospheric ice .....	84
4.4 Conclusions.....	86
CHAPTER 5 .....	88
5. CAP-MODEL PLASTICITY FOR ATMOSPHERIC ICE .....	88
5.1 Introduction.....	88
5.2 Yield envelope for atmospheric ice .....	89
5.2.1 Fixed shear-yield envelope.....	94
5.2.2 Cap-yield envelope.....	105

5.2.3	Tension cut-off .....	107
5.2.4	Factors affecting the yield surface of atmospheric ice .....	108
5.3	Plastic flow and hardening rules in atmospheric ice.....	109
5.3.1	Plastic flow for the fixed shear yield.....	112
5.3.2	Plastic flow and hardening rules for cap yield .....	116
5.3.3	Plastic flow and hardening rules for the tension cut-off.....	120
5.4	Conclusions.....	123
CHAPTER 6 .....		127
6.	LABORATORY TEXTURE AND GRAIN SIZE OBSERVATIONS .....	127
6.1	Introduction.....	127
6.2	In-cloud riming simulation in Refrigerated Wind Tunnel .....	129
6.3	Freezing rain simulation in the icing precipitation simulation laboratory.....	132
6.4	Atmospheric ice texture and fabric .....	135
6.4.1	Ice sample preparation.....	136
6.4.2	Classification of atmospheric ice texture.....	138
6.4.3	Air bubbles in atmospheric ice .....	141
6.5	Conclusions.....	142
CHAPTER 7 .....		144
7.	MODEL ELABORATION AND NUMERICAL RESULTS.....	144
7.1	Introduction.....	144
7.2	Numerical implementations .....	145
7.2.1	Time-integration and incremental procedure .....	146
7.2.2	Poroelastic model implementation .....	149
7.2.3	Delayed-viscoelastic model implementation.....	152
7.2.4	Cap-model plasticity algorithm .....	154
7.3	UMAT Subroutine in ABAQUS Program .....	158
7.4	Numerical results and model evaluation.....	162
7.4.1	Strain-rate dependency of ice yield envelope.....	162
7.4.2	Temperature dependency of ice yield envelope .....	163
7.4.3	Porosity dependency of ice yield envelope .....	165
7.4.4	Ice yield envelope evaluation .....	166
7.5	Case studies for natural loading conditions .....	169
7.5.1	Anisotropic behaviour of atmospheric ice deposit .....	172
7.5.2	Temperature dependency of ice behaviour.....	184

7.6	Conclusions.....	185
	CHAPTER 8 .....	187
8.	GENERAL CONCLUSIONS AND RECOMMENDATIONS.....	187
8.1	General conclusions.....	187
8.2	Recommendations for future work .....	191
9.	REFERENCES.....	194
10.	APPENDIX 1 .....	199
11.	MAPLE CODE FOR ICE ELASTIC MODULI.....	199
12.	APPENDIX 2 .....	217
13.	USER-DEFINED ABAQUS UMAT SUBROUTINE.....	217

## LIST OF FIGURES

<b>Fig. 1.1:</b>	The schematic representation of general ice shedding phenomenon from overhead transmission line, (a) Heat exchange between a piece of accreted ice on electrical line, the electrical conductor, and the environment, (b) Mechanical force components. ....	3
<b>Fig. 1.2:</b>	Schematic representation of some ice shedding sub-problems.....	4
<b>Fig. 1.3:</b>	Elements of the general problem of ice shedding by mechanical breaking.....	6
<b>Fig. 2.1:</b>	The geometric configuration of the hexagonal ice lattice and crystal $I_h$ , (a) Major lattice axes and planes, (b) Monocrystal structure and atoms arrangement.....	19
<b>Fig. 2.2:</b>	Morphology (texture) and crystallographic orientations (fabric) of granular and columnar ice.....	20
<b>Fig. 2.3:</b>	Rate-dependency of ice strength for freshwater ice at $-10^\circ\text{C}$ , grain size 5mm, adopted from the results of material tests performed by S.S. Sunder, Ref. [49]. ....	23
<b>Fig. 2.4:</b>	Stress-strain curves for ice specimens tested at $-5^\circ\text{C}$ , presented by Cole (1987), (a) Low strain-rate tests, ductile behaviour, (b) High strain-rate tests, brittle behaviour. ....	23
<b>Fig. 2.5:</b>	Temperature dependency of ice strength at strain rate of $4 \times 10^{-5} \text{ s}^{-1}$ , reported by Arakawa <i>et al.</i> (1997). ....	25
<b>Fig. 2.6:</b>	Two typical pressure-dependent yield surfaces for S2 columnar ice, reported by (a) Fish <i>et al.</i> (1997), (b) Jones (1982).....	26
<b>Fig. 2.7:</b>	The typical pressure-dependent yield surfaces for granular ice at $-20\text{C}$ (left) and $-40\text{C}$ (right), reported by Derradji (2000) on the basis of the test data of Rist and Murrell (1994).....	27
<b>Fig. 2.8:</b>	Variation of Young's modulus and Poisson's ratio with porosity ( $\phi$ ) in ice shield samples, Ref. [4]. ....	28
<b>Fig. 3.1:</b>	A typical strain history creep curve for ice in uniaxial constant loading.....	42
<b>Fig. 3.2:</b>	Monocrystal principal and rotated coordinate systems.....	47
<b>Fig. 3.3:</b>	Spherical and cylindrical coordinates for averaging integrals formulations for granular and columnar ice types, respectively.....	50
<b>Fig. 3.4:</b>	Shear- and cap-yield surfaces and tension cutoff in the cap-model plasticity.....	58

<b>Fig. 4.1:</b>	Temperature dependence of the Young's and shear moduli of ice monocrystal $I_h$ in various directions and planes. ....	<b>64</b>
<b>Fig. 4.2:</b>	Temperature dependence of Young's and shear moduli for isotropic (granular) ice. ....	<b>66</b>
<b>Fig. 4.3:</b>	Temperature dependence of Young's and shear moduli for S1 columnar ice in various directions and planes. ....	<b>67</b>
<b>Fig. 4.4:</b>	Temperature dependence of Young's and shear moduli for S2 columnar ice in various directions and planes. ....	<b>68</b>
<b>Fig. 4.5:</b>	Variation of Young's and shear moduli with scatter angle for S3 columnar ice, where the mean c-axis is in the $x_1$ -direction. ....	<b>70</b>
<b>Fig. 4.6:</b>	Variation of Poisson's ratio with scatter angle for S3 columnar ice, where the mean c-axis is in the $x_1$ -direction. ....	<b>70</b>
<b>Fig. 4.7:</b>	Variation of Young's and shear moduli with mean c-axis angle for S3 ice, scatter angle $\Delta\theta_0 = 30^\circ$ . ....	<b>71</b>
<b>Fig. 4.8:</b>	Variation of Poisson's ratio with mean c-axis angle for S3 columnar ice, scatter angle $\Delta\theta_0 = 30^\circ$ . ....	<b>72</b>
<b>Fig. 4.9:</b>	Variation of Young's and shear moduli, and Poisson's ratio with mean c-axis angle for S3 columnar ice at $-10^\circ\text{C}$ , where the scatter angle varies in the range 0 to 180 degrees. ....	<b>73</b>
<b>Fig. 4.10:</b>	Variation of Young's and shear moduli, and Poisson's ratio with rotation angle around the $x_2$ -axis for various types of columnar ice at $-10^\circ\text{C}$ . ....	<b>76</b>
<b>Fig. 5.1:</b>	Typical shear- and cap-yield surfaces in the cap plasticity model for atmospheric ice at a certain temperature, strain rate, and porosity. ....	<b>91</b>
<b>Fig. 5.2:</b>	Typical temperature dependency in ice yield envelopes. ....	<b>91</b>
<b>Fig. 5.3:</b>	Typical strain-rate dependency in ice yield envelopes. ....	<b>92</b>
<b>Fig. 5.4:</b>	The effects of porosity changes in the cap-yield surface and tension cutoff of atmospheric ice at a certain temperature, strain rate, and initial porosity. ....	<b>93</b>
<b>Fig. 5.5:</b>	Phase diagram for ice at natural range of temperature. ....	<b>93</b>
<b>Fig. 5.6:</b>	Mohr-Coulomb and the modified Drucker-Prager yield surfaces in (a) Principal stress space, (b) Deviatoric plane. ....	<b>94</b>
<b>Fig. 5.7:</b>	Typical temperature dependence of ice cohesion for granular (left) and columnar S2 (right) ice types, curves are fitted to the data of Refs. [21], [25], and [50]. ....	<b>97</b>
<b>Fig. 5.8:</b>	Typical temperature dependence of the ice friction parameter $b$ for granular (left) and columnar S2 (right) ice types, curves are fitted to the data of Refs. [21], [25], and [50]. ....	<b>99</b>

- Fig. 5.9:** Strain-rate dependence of ice friction angle  $\beta$  for granular (left) and columnar S2 ice (right), curves fitted to the data of Jones (1982) at  $-11.8^{\circ}\text{C}$ . ..... 100
- Fig. 5.10:** Strain-rate dependence of ice friction parameter  $b$  for granular (left) and columnar S2 ice (right), curves fitted to the data of Jones (1982) at  $-11.8^{\circ}\text{C}$ . ..... 100
- Fig. 5.11:** Typical temperature dependence of the pressure at maximum shear strength  $p_{ai}^{\max}(T)$  for bubble-free granular (left) and columnar S2 (right) ice types, curves are fitted to the data of Refs. [21], [25], and [50]. ..... 102
- Fig. 5.12:** Strain-rate dependence of  $p_a^{\max}$  for granular (left) and columnar S2 ice (right), curves fitted to the data of Jones (1982) at  $-11.8^{\circ}\text{C}$ . ..... 104
- Fig. 5.13:** Movement of cap-yield envelope by changes in porosity upon loading for atmospheric ice with initial porosity  $\phi_0$  (dashed curve). ..... 105
- Fig. 5.14:** The volumetric and deviatoric components of yield function gradients for shear- and cap-yield envelopes, and tension cutoff. .... 110
- Fig. 6.1:** Aluminum cylinder placed in test section, and water spraying system of refrigerated wind tunnel. .... 129
- Fig. 6.2:** Specially-designed shutting device and the glass slides for obtaining the droplet size spectrum. .... 130
- Fig. 6.3:** a) Droplet spectrum produced by a typical Spray System Nozzle at water pressure 50 psi, b) Liquid water content produced by the same nozzle at an air speed of 10 m/s. .... 131
- Fig. 6.4:** Ice accretion in a very wet regime with large droplets in the refrigerated wind tunnel. .... 132
- Fig. 6.5:** Collector aluminum surface and insulating foam installed in icing simulation room. .... 133
- Fig. 6.6:** Shutting device for obtaining the water droplet size spectrum and the precipitation rate measuring device in icing simulation laboratory. .... 134
- Fig. 6.7:** Water flat-spray airless nozzle (model H1/4VV-2501) and the delay system installed in icing simulation laboratory for drizzle and freezing rain simulation. .... 134
- Fig. 6.8:** Precipitation rate versus nozzle water pressure and interrupt time for flat-spray airless nozzle (model H1/4VV-2501) at room temperature. .... 135
- Fig. 6.9:** Thick section preparation using a band saw and Sledge-type microtome for thin section preparation. .... 136
- Fig. 6.10:** Stereographic representation (Wulff net) of crystal c-axis orientation. .... 138
- Fig. 6.11:** Texture, fabric and Wulff net of columnar atmospheric ice (glaze), (a) Very wet accretion,  $T_a \approx -5^{\circ}\text{C}$  and Precipitation rate = 2.5 mm/h (S2 ice), (b) Transition from wet to dry accretion,  $T_a \approx -7^{\circ}\text{C}$  and Precipitation rate = 1.3 mm/h (S1 ice). .... 139

<b>Fig. 6.12:</b> Texture, fabric and Wulff net of feathery atmospheric ice, accreted at $T_a = -10^\circ\text{C}$ , $LWC = 1.0 \text{ g/m}^3$ , and air speed = 10 m/s.....	<b>140</b>
<b>Fig. 6.13:</b> Texture, fabric and Wulff net of feathery atmospheric ice, accreted at $T_a = -20^\circ\text{C}$ , $LWC = 0.5 \text{ g/m}^3$ , and air speed = 5 m/s.....	<b>141</b>
<b>Fig. 6.14:</b> Air bubble content at two different deposit temperatures, (a) Transition condition, deposit surface temperature slightly below $0^\circ\text{C}$ , (b) Wet growth regime, deposit surface temperature $0^\circ\text{C}$ .....	<b>142</b>
<b>Fig. 7.1:</b> Flowchart of the incremental solution procedure of ice viscoplastic model.....	<b>148</b>
<b>Fig. 7.2:</b> Flowchart of the undrained poroelastic model implementation. ....	<b>151</b>
<b>Fig. 7.3:</b> Loading scenario and time steps (left), and incremental stress within each time step (right). ....	<b>153</b>
<b>Fig. 7.4:</b> The modes of cap-model: (1) pure tension yield, (2) tension-shear yields, (3) pure shear yield, (4) shear-cap yields, (5) pure cap yield, and (6) pure viscoelastic deformation.....	<b>154</b>
<b>Fig. 7.5:</b> Flowchart of the incremental cap-model numerical implementation. ....	<b>157</b>
<b>Fig. 7.6:</b> Strain-rate dependency of granular ice yield envelope, the tests data are adopted from Jones (1982) at $-11.8^\circ\text{C}$ .....	<b>163</b>
<b>Fig. 7.7:</b> Strain-rate dependency of columnar S2 ice yield envelope, the tests data are adopted from Jones (1982) at $-11.8^\circ\text{C}$ .....	<b>163</b>
<b>Fig. 7.8:</b> Temperature dependency of granular ice yield envelope, the tests data are adopted from Jones (1982) at $-11.8^\circ\text{C}$ for strain rate $1.4 \times 10^{-3} \text{ s}^{-1}$ , and Rist and Murrell (1994) at $-20^\circ\text{C}$ and $-40^\circ\text{C}$ for strain rate $1.0 \times 10^{-3} \text{ s}^{-1}$ . ....	<b>164</b>
<b>Fig. 7.9:</b> Temperature dependency of columnar S2 ice yield envelope, the tests data are adopted from Jones (1982) at $-11.8^\circ\text{C}$ for strain rate $4.7 \times 10^{-3} \text{ s}^{-1}$ , and Gagnon and Gammon (1995) at $-1.0^\circ\text{C}$ and $-16.0^\circ\text{C}$ for strain rates $5.4 \times 10^{-3} \text{ s}^{-1}$ and $4.3 \times 10^{-3} \text{ s}^{-1}$ , respectively. ....	<b>164</b>
<b>Fig. 7.10:</b> Porosity dependence of granular atmospheric ice yield envelope, the tests data of freshwater ice are adopted from Jones (1982) at $-11.8^\circ\text{C}$ for strain rate of $5.4 \times 10^{-3} \text{ s}^{-1}$ .....	<b>165</b>
<b>Fig. 7.11:</b> Porosity dependence of columnar atmospheric ice yield envelope, the tests data of freshwater ice are adopted from Jones (1982) at $-11.8^\circ\text{C}$ for strain rate of $5.4 \times 10^{-3} \text{ s}^{-1}$ .....	<b>165</b>
<b>Fig. 7.12:</b> A comparison between the yield (failure) envelopes of this model and Derradji (2000) for freshwater granular ice, the tests data are adopted from Jones (1982) at $-11.8^\circ\text{C}$ . ....	<b>166</b>
<b>Fig. 7.13:</b> A comparison between the yield (failure) envelopes of this model and Derradji (2000) for freshwater granular ice, the tests data are adopted from Rist and Murrell (1994) at $-40^\circ\text{C}$ .....	<b>167</b>

<b>Fig. 7.14:</b> A comparison between the yield (failure) envelopes of this model and Fish <i>et al.</i> (1997) for columnar S2 ice, the tests data are adopted from Jones (1982) at -11.8°C. ....	<b>168</b>
<b>Fig. 7.15:</b> A comparison between the yield (failure) envelopes of this model and Fish <i>et al.</i> (1997) for columnar S2 ice, the tests data are adopted from Gagnon and Gammon (1995) at -16°C.....	<b>168</b>
<b>Fig. 7.16:</b> External forces and the force balance diagram for ice deposits on electrical power lines.....	<b>170</b>
<b>Fig. 7.17:</b> Selected case studies for model elaboration at static load condition, (a) Radial compression (wind load), (b) Axial compression (ice confinement), (c) Torsion (cable twist), (d) Bending moments (gradual ice accretion or galloping) .....	<b>172</b>
<b>Fig. 7.18:</b> Selected case study for determining the ice anisotropy due to static wind pressure, (a) Case-G, (b) Case G-S2 and G-S1.....	<b>174</b>
<b>Fig. 7.19:</b> Displacement contours in $x_1$ -direction (U1) and $x_2$ -directions (U2) and the corresponding legends for wind pressure $0.5 \times 10^6$ Pa (Case-G), U1 and U2 are given in meter. ....	<b>174</b>
<b>Fig. 7.20:</b> The comparison between the von-Mises stress contours in Pa for ice structures of cases GS1, GS2, and G at static wind pressure $0.5 \times 10^6$ Pa. ....	<b>175</b>
<b>Fig. 7.21:</b> The comparison of the von-Mises stress variations along the cylinder surface and along the $x_1$ -axis at wind pressure 0.5MPa in the cases G, GS1, and GS2.....	<b>176</b>
<b>Fig. 7.22:</b> The comparison of the hydrostatic pressure variations along the cylinder surface and along the $x_1$ -axis at wind pressure 0.5MPa in the cases G, GS1, and GS2.....	<b>177</b>
<b>Fig. 7.23:</b> The comparison of the hydrostatic pressure in Pa contours and the corresponding legends for ice structures of the cases GS1, GS2, and G at wind pressure $0.5 \times 10^6$ Pa. ....	<b>178</b>
<b>Fig. 7.24:</b> The effects of mesh size and element type on the accuracy of displacement, von-Mises stress and hydrostatic pressure in case G at wind pressure 0.5MPa.....	<b>179</b>
<b>Fig. 7.25:</b> Selected case study for determining the ice anisotropy due to torsion traction of 0.5 MPa applied to the outer surface of ice deposit, in the cases GS1 (left) and GS2 (right). ....	<b>180</b>
<b>Fig. 7.26:</b> The comparison of von-Mises stress in Pa (left) and displacement contours in meter (right) at torsion traction of 0.5 MPa in the case GS1. ....	<b>181</b>
<b>Fig. 7.27:</b> The variation of von-Mises stress and displacement magnitude with $x_1$ -coordinate at torsion traction of 0.5 MPa in the cases GS1 and GS2.....	<b>181</b>
<b>Fig. 7.28:</b> Selected case study for determining the ice anisotropy due to confinement of 0.5 MPa applied to the ice deposit in the cases GS1 and GS2.....	<b>182</b>
<b>Fig. 7.29:</b> The comparison of the von-Mises stress contours in Pa and the corresponding legends for the ice structures of cases GS1 and GS3-0-10 at confining pressure of $0.5 \times 10^6$ Pa. ....	<b>183</b>

- Fig. 7.30:** The comparison of the hydrostatic pressure contours in Pa and the corresponding legends for the ice structures of the cases GS1 and GS3-0-10 at confining pressure of  $0.5 \times 10^6$  Pa ..... **183**
- Fig. 7.31:** The comparison of the contours of displacement (in meter) in x1-direction (U1) and the corresponding legends for the ice structures of the cases GS1 and GS3-0-10 at confining pressure of  $0.5 \times 10^6$  Pa. .... **184**

## LIST OF TABLES

<b>Table 2.1:</b>	Adiabatic measurements of ice monocrystal elastic constants at $-16^{\circ}\text{C}$ , Gammon <i>et al.</i> (1983).....	<b>32</b>
<b>Table 2.2:</b>	Material parameters in viscoelastic formulation of freshwater ice at $-10^{\circ}\text{C}$ , Ref. [14] and [58]. .....	<b>35</b>
<b>Table 5.1:</b>	Material constants involved in the formulation of ice cohesion for granular and columnar S2 ice types. ....	<b>97</b>
<b>Table 5.2:</b>	Material constants involved in the formulation of ice friction parameter for granular and columnar S2 ice types. ....	<b>99</b>
<b>Table 5.3:</b>	Variation of ice friction parameter $b$ versus strain rate for granular and columnar ice types at $-11.8^{\circ}\text{C}$ calculated from the data of Jones (1982).....	<b>101</b>
<b>Table 5.4:</b>	Material constants involved in the formulation of ice pressure at maximum shear strength for granular and columnar ice types.....	<b>103</b>
<b>Table 5.5:</b>	Variation of ice pressure at maximum shear strength versus strain rate for granular and columnar ice types at $-11.8^{\circ}\text{C}$ calculated from the data of Jones (1982). .....	<b>103</b>
<b>Table 7.1:</b>	Material constants (PROPS) defined in UMAT subroutine.....	<b>160</b>
<b>Table 7.2:</b>	State variables (STATEV) defined in UMAT subroutine. ....	<b>161</b>

## GLOSSARY OF NOTATIONS

$\alpha, \alpha_{ij}$	Thermal expansion tensor and its components
$\alpha$	The parameter in time-integration scheme
$\alpha$	The material parameter in the formulation of ice cohesion
$\beta, \beta_0$	Friction angle and its value at freezing point
$\beta_1$	The strain-dependent function in the formulation of ice friction angle
$\beta_{ij}$	Biot effective elastic stress coefficient tensor for porous material
$\lambda$	Material constant in the formulation of ice parameter $p_a^{\max}$
$\delta_{ij}$	Kronecker delta
$\Delta\lambda^{ve}$	Viscoelastic structural change function due to plastic deformation
$\Delta t$	Time increment
$\varepsilon_{ij}, \varepsilon_i$	The tensorial and engineering components of strain tensor in reference Cartesian coordinates
$\hat{\varepsilon}_{ij}, \hat{\varepsilon}_i$	The tensorial and engineering components of strain tensor in monocystal principal coordinates
$\varepsilon'_{ij}, \varepsilon'_i$	The tensorial and engineering components of strain tensor in monocystal rotated coordinates
$\varepsilon_{ij}^e$	The elastic strain components
$\bar{\varepsilon}_{ij}^e$	The effective elastic strain components in porous material
$\varepsilon^{ve}$	Uniaxial viscoelastic strain
$\varepsilon_{ij}^{ve}$	The viscoelastic or delayed elastic strain components
$\varepsilon_{ij}^p$	The steady-state or plastic strain components
$\varepsilon_{ij}^c$	The crack-activity strain components
$\dot{\varepsilon}^e$	The elastic contribution in the total strain rate of creep deformation
$\dot{\varepsilon}^{ie}$	The inelastic contribution in the total strain rate of creep deformation
$\dot{\varepsilon}^{ve}$	The transition flow or viscoelastic contribution in the total strain rate of creep deformation

$\dot{\epsilon}^p$	The steady-state flow or plastic contribution in the total strain rate of creep deformation
$\dot{\epsilon}^c$	The crack activity contribution in the total strain rate of creep deformation
$\epsilon_{ij}^{de}, \epsilon_{ij}^{pe}$	Effective drained and pore elastic strain of porous material
$\epsilon_{ij}^{me}$	Induced elastic strain in the matrix of porous material
$\epsilon_{vol}$	Volumetric strain, $\epsilon_{kk}$
$\epsilon_{dev}$	von-Mises equivalent deviatoric strain
$\dot{\epsilon}_0, \dot{\epsilon}_1$	Reference strain-rates
$\dot{\epsilon}_N$	Nominal strain rate
$\phi, \phi_0$	Current and initial ice porosity, the ratio of voids to the total volume
$\gamma$	Material constant in the definition of ice friction parameter
$\hat{\gamma}_{ij}, \gamma'_{ij}, \gamma_{ij}$	The engineering components of shear strain in monocystal, rotated, and reference coordinate systems
$\Gamma_x^{history}$	Plasticity memory function related to yield curve $f_x$
$\eta$	Material constant in the definition of ice parameter $p_a^{max}$
$\kappa_\alpha^k$	A set of internal variables associated with the yield surface $f_k$ in plasticity model
$\lambda$	Material constant in the formulation of ice parameter $p_a^{max}$
$\lambda_x^p$	Plastic consistency parameter (plastic multiplier) associated with the yield surface $f_x$
$\mu$	Material constant in the definition of ice friction parameter
$\nu$	Material constant in the formulation of ice friction parameter
$\nu$	Poisson's ratio for isotropic material
$\nu_{ij}$	Poisson's ratio that characterizes the normal strain in $x_j$ direction resulting from the normal stress applied in $x_i$ direction
$\nu_p$	In-plane Poisson's ratio for transversely isotropic material
$\nu_{pt}, \nu_{tp}$	Transverse Poisson's ratios for transversely isotropic material
$\theta, \varphi$	Rotation angles, spherical coordinate

$\Theta$	Temperature in °C
$\Theta_r$	Reference temperature in °C
$\rho$	Density
$\rho_w, \rho_{w_0}$	Current and initial water density in porous material
$\sigma$	Uniaxial stress
$\sigma_{ij}, \sigma_i$	The tensorial and engineering components of Cauchy stress tensor in reference Cartesian coordinates
$\bar{\sigma}_{ij}$	The effective stress components in porous material
$\hat{\sigma}_{ij}, \hat{\sigma}_i$	The tensorial and engineering components of stress tensor in monocrystal principal coordinates
$\sigma'_{ij}, \sigma'_i$	The tensorial and engineering components of stress tensor in monocrystal rotated coordinates
$\sigma_{ij}^d, \sigma_{ij}^m$	Effective drained and matrix stress of porous material
$\sigma_c$	Compressive strength
$\omega_1$	Material parameter in the definition of material friction angle
$\Omega, d\Omega$	Material volume and its elemental representation
$\Omega_v, \Omega_s$	Void and solid volumes in porous material
$\zeta$	Variation in fluid content of porous material
$a_T$	The temperature-dependant parameter of viscoelastic deformation
$a_{T_0}$	The parameter $a_T$ determined at temperature $T_0$
$A$	Material parameter in the definition of ice melting pressure
$A_\lambda$	Material parameter in structure change function of viscoelastic formulation
$b$	Material constant of viscoelastic deformation
$b, b_0$	Tangent of friction angle and the its value at freezing point
$b_1$	The temperature-dependent function in the formulation of ice friction parameter
$B_\lambda$	Material parameter in structure change function of viscoelastic formulation

$B_{ij}$	Skempton tensor of porous material
$c_k$	A scalar in a non-associated plastic model associated with the yield surface $f_k$
$C_1$	Material constant of viscoelastic deformation
$C_c$	The composite compressibility of porous material
$\hat{C}$ , $\hat{C}_{ij}$	Elastic stiffness constants of monocrystal, the matrix and components
$C'$ , $C'_{ij}$	Rotated elastic stiffness constants of monocrystal, the matrix and components
$\bar{C}$ , $\bar{C}_{ij}$	Averaged elastic stiffness constants of polycrystal, the matrix and components
$C_{ijkl}$	The components of elastic stiffness tensor
$C_{ijkl}^d$ , $C_{ijkl}^u$	The drained and undrained elastic stiffness tensor of porous material
$C_{ijkl}^m$	The matrix elastic stiffness tensor of porous material
$C_p$	Heat capacity at constant stress
$d$ , $d_0$	Material cohesion and its magnitude at freezing point
$d_g$	Grain size
$d_1$	Material constant of viscoelastic deformation
$e$	Void ratio, void to solid volume ratio for porous material
$e_{ij}$	Components of the deviatoric strain tensor
$e_0^p$ , $e^p$	Initial and current plastic deviatoric strains
$e^p$ , $e_{ij}^p$	The plastic deviatoric strain tensor and its components
$E$	Young's modulus of elasticity for isotropic material
$E_{11}$ , $E_{22}$ , $E_{33}$	Young's modulus of elasticity in $x_1$ , $x_2$ , and $x_3$ directions
$E_t$ , $E_p$	Transverse and in-plane Young's modulus for transversely isotropic material
$f_k$	$k^{\text{th}}$ yield function, $f_s$ for shear and $f_c$ for cap-yield envelopes
$F(\theta, \varphi)$ , $F(\theta)$	Probability density function for monocrystal c-axis orientation
$g_k$	Plastic potential function associated with the yield surface $f_k$
$G$	Shear modulus of elasticity for isotropic material
$G_{12}$ , $G_{13}$ , $G_{23}$	Shear modulus of elasticity in $x_1$ - $x_2$ , $x_1$ - $x_3$ , and $x_2$ - $x_3$ planes
$G_t$ , $G_p$	Transverse and in-plane shear modulus for transversely isotropic material

$h_{\alpha}^k$	A set of hardening functions associated with the hardening parameter $H_{\alpha}^k$
$H_{\alpha}^k$	Hardening parameters
$J_1, J_2, J_3$	Invariants of total stress tensor (Cauchy)
$J_{1D}, J_{2D}, J_{3D}$	Invariants of deviatoric stress tensor
$K$	Material parameter in modified Drucker-Prager yield model
$K_c$	The composite bulk modulus of porous material
$K_w$	The bulk modulus of water infiltrated in porous material
$K_{\text{Reff}}^d$	Reuss effective bulk modulus in drained porous material
$K_{\text{Reff}}^m$	Reuss effective bulk modulus in the matrix of porous material
$L_{ij}^d, L_{ij}^m$	The drained and matrix elastic tensor of porous material
$L^{\epsilon}, L_{ij}^{\epsilon}$	Rotation matrix and components for strain tensor in engineering notation
$L^{\sigma}, L_{ij}^{\sigma}$	Rotation matrix and components for stress tensor in engineering notation
$n$	Creep power exponent that is about 3 at the stresses of engineering interest
$p$	Hydrostatic pressure
$p_a^0, p_a$	Initial and current hydrostatic pressures at maximum shear strength for porous ice
$p_a^{\text{max}}$	Hydrostatic pressure at maximum shear strength for bubble free ice
$p_{a0}^{\text{max}}$	Material constant in the formulation of $p_a^{\text{max}}$
$p_{a1}^{\text{max}}$	Temperature-dependent function in the formulation of $p_a^{\text{max}}$
$p_b$	Ice melting pressure
$p_t^0, p_t$	Initial and current pressure strengths of materials in tension
$p_t^{\text{max}}$	Pressure strength of bubble-free ice in tension
$p_v$	Pore pressure in porous material
$P_x^{\text{history}}$	Plasticity memory function related to yield curve $f_x$
$q$	von-Mises equivalent stress
$q_a^0, q_a, q_a^{\text{max}}$	von-Mises equivalent stresses at pressures $p_a^0, p_a, p_a^{\text{max}}$
$Q, Q_{ij}$	Rotation tensor and components

$Q_a$	Creep activation energy, $Q_a = 66.9 \text{ kJ} \cdot \text{mole}^{-1}$ for ice
$r$	Parameter representing the third invariant of deviatoric stress
$r, \theta, \varphi$	Spherical coordinate system
$R$	Universal gas constant $R = 8.314 \text{ J} \cdot \text{mole}^{-1} \cdot \text{°K}^{-1}$
$s$	Material constant of viscoelastic deformation
$s_{ij}$	Components of the deviatoric stress tensor
$S_{1,2}$	Shift function of viscoelastic deformation
$\hat{S}, \hat{S}_{ij}$	Elastic compliance constants of monocrystal, matrix and components
$S', S'_{ij}$	Rotated elastic compliance constants of monocrystal, matrix and components
$\bar{S}, \bar{S}_{ij}$	Averaged elastic compliance constants of polycrystal, the matrix and components
$S_{ijkl}$	The components of elastic compliance tensor
$S_{ijkl}^d, S_{ijkl}^u$	The drained and undrained elastic compliance tensor of porous material
$S_{ijkl}^m$	The matrix elastic compliance tensor of porous material
$t$	Shear stress measure
$t_a, t_{\max}$	Magnitudes of $t$ at pressure $p_a$ and $p_a^{\max}$
$t_0, t_1, t_2$	Time measures
$T$	Absolute temperature in °K
$T_0$	Reference temperature in °K
$T_1, T_2$	Temperature values
$T_m$	Melting temperature in °K
$V$	Temperature-dependant parameter representing the material creep resistance
$V_0$	Material parameter of creep with unit of stress
$W_{\text{vol}}^P, W_{\text{dev}}^P$	Volumetric and deviatoric parts of mechanical dissipation energy
$x_i$	Reference Cartesian coordinates
$x'_i$	Monocrystal rotated coordinates
$\hat{X}_i$	Monocrystal principal coordinates

# CHAPTER 1

## INTRODUCTION

### 1.1 General

The consequences of atmospheric icing of overhead power lines are extremely important in terms of human life security, material damage, and reliability of electrical transmission lines. This often creates many serious electrical and mechanical problems in the transmission network due to the high adherence of ice to substrates and its bulk strength characteristics. The major consequences are overloading the conductors and towers; short-circuits due to wire sag; and galloping of cables in high wind conditions. Galloping and other dynamic loads result in line component fatigue and damage. The impulse loads due to sudden ice shedding are another source of troubles in power networks. The lessons from the January 1998 ice storm reveal the huge impact of this phenomenon. That ice storm was one of the most terrible catastrophic ones because of its tremendous impact on overhead power lines in Quebec, Ontario and neighboring US states. The structural damages to Hydro-Quebec's network alone were more than 1,300 km of lines because of the failure of more than 16,000 line components, Ref. [67]. Although many transmission lines collapsed under vertical loads that were near the theoretical design loads, several towers collapsed due to premature failure and cascade collapse, while the wind at that time was classified as moderate at most.

To avoid major breakdowns in electrical power during severe ice storms, improving the mechanical characteristics of line components, anti-icing and de-icing methods should be taken into consideration. The successful development of anti-icing methods requires good knowledge of adherence properties of ice, while, the bulk characteristics of atmospheric ice is also of interest for developing de-icing techniques as well as for describing the natural mechanisms of ice shedding. A review of the literature shows that while ice accretion on electrical lines is a well-documented phenomenon, very few studies have been made on ice shedding. Naturally, three physical mechanisms are expected to induce ice shedding from electrical lines, melting, sublimation and mechanical ice breaking. In reality, a combination of the above-mentioned mechanisms occurs, which makes ice shedding a complex phenomenon.

## **1.2 Statement of the problem**

The general problem of ice shedding from overhead transmission lines should be investigated based on mechanical and heat transfer considerations. Heat may be transferred from or to the system in the forms of solar radiation; air convection; Joule effect; latent heats of evaporation, sublimation and melting; and thermodynamic heating, as shown in Fig. 1.1a. The mechanical forces applied to the system of power lines and towers comprise the static, dynamic and impulse loads, as shown in Fig. 1.1b. Each ice shedding mechanism (melting, sublimation and mechanical breaking) can be characterized separately by the environmental parameters, mechanical and electrical characteristics of the line, accretion regime, ice micro-structure, ice load variations, etc. Coupled modeling is a very complex task that requires it to be broken down into some individual and less complex problems.

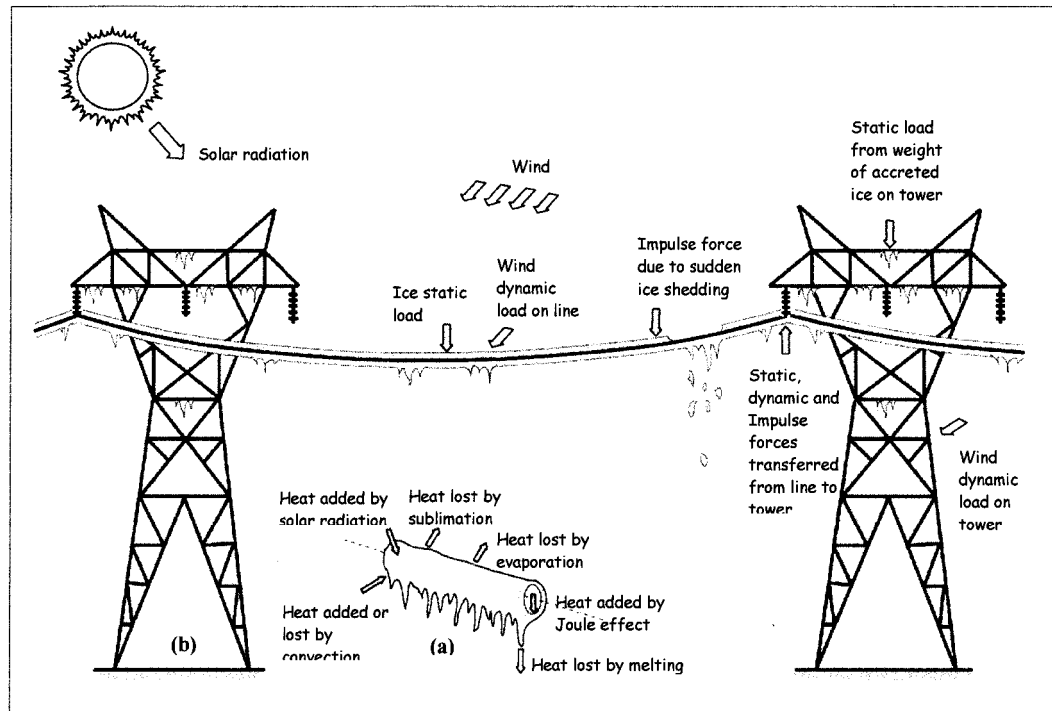


**Fig. 1.1:** The schematic representation of general ice shedding phenomenon from overhead transmission line, **(a)** Heat exchange between a piece of accreted ice on electrical line, the electrical conductor, and the environment, **(b)** Mechanical force components.

A few sub-problems must be solved to be able to gain the general solution of the ice shedding problem. The typical mechanical and heat transfer sub-problems are shown in Fig. 1.2. They are mainly concerned with the response of the system without ice, and the ice shedding characteristics by melting, sublimation, and mechanical breaking. Merging all the formulations and the experimental test results makes it possible to find the response of the whole system of accreted ice, lines and towers to a variety of mechanical loads under different thermal conditions. This work, however, is concerned with the ice shedding from overhead power lines by mechanical breaking. The temperature dependency of the material parameters involved in this phenomenon is taken into account, while the heat transfer, melting and sublimation considerations can be coupled to this work in future studies.

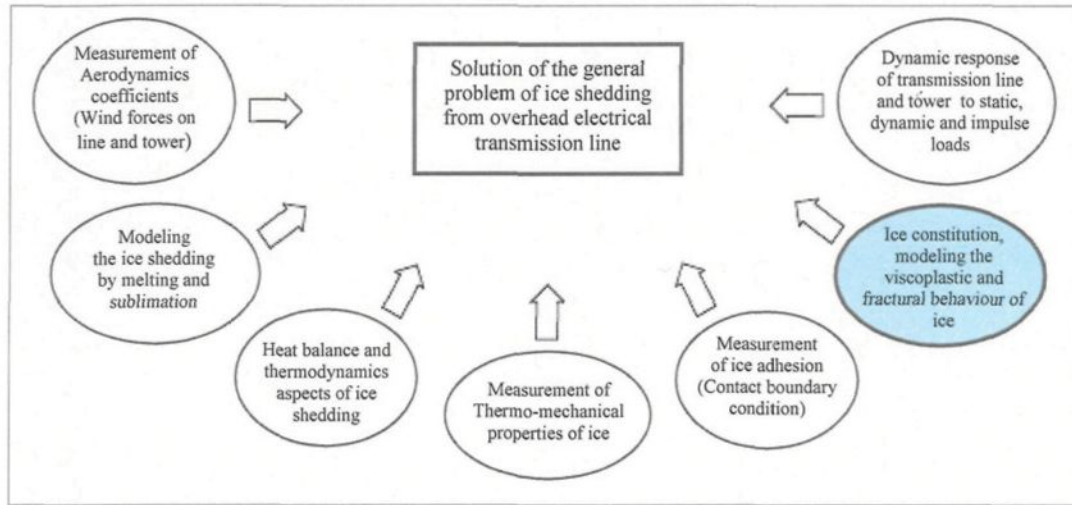


**Fig. 1.2:** Schematic representation of some ice shedding sub-problems.

Like in any other well-posed mechanical problem, four elements should be precisely described in the general problem of ice shedding by mechanical breaking. They are the governing equations, loading scenarios, material constitutive equations, and traction and displacement boundary conditions, Fig. 1.3. As governing equation, here, the balance equation is enough for the isothermal process of this study. The natural forces exerted on a piece of ice deposit can be divided into: (a) static loads due to the weight of accreted ice (ice weight, confinement, bending moments from gradual ice accretion, and torsional loads from cable twist), (b) thermal stresses resulting from temperature gradients in ice deposit resulting from Joule effect and temperature changes, (c) dynamic wind pressure loads, and (d) impulse load from sudden ice shedding, Fig. 1.3. More details of natural loading conditions are given in Section 7.5.

As a contact boundary condition, the adhesive strength at ice-aluminum interface is to be studied, where the influencing factors should also be determined. Conductor galloping,

on the other hand, originates from the wind forces in an ice accretion process with asymmetrical deposit shapes. This can be assumed to be a displacement boundary condition after taking out the rigid body motion from the conductor displacement, Fig. 1.3.

Finally, the ice constitutive equations, the main goal of this study, should be described to relate the stress field within the material to the induced strain field. The available ice models should be reviewed for possible shortcomings for modeling the mechanical behaviour of porous atmospheric ice. Finally, the general objectives and methodology of this study can be specified considering the research requirements, Fig. 1.3.

A literature survey revealed that some models have been developed to predict the mechanical behaviour of freshwater ice over the past two decades. However, almost all the models predict the mechanical behaviour of freshwater or bubble-free ice. The pressure dependency of material constitution, induced by the presence of air-bubbles, should be applied to those models. The reported results of some experimental works are reviewed here to justify the need for a porous material formulation for the case of atmospheric ice. The porosity of atmospheric ice varies depending on the accretion regime, sometimes by as much as 35%, corresponding to ice densities from 917 down to 600 kg/m<sup>3</sup>. Very few laboratory tests have been carried out to show the influence of porosity on the elastic moduli and strength of ice. Rogachko *et al.* (1997) have investigated the influence of ice porosity on the strength of artificial porous ice samples containing macro scale voids, while Bentley *et al.* (1957) focused on the measurement of the elastic moduli of the Greenland porous ice-cap. A reduction of 30% in compressive strength and 35% in Young's modulus were reported when the porosity increased from 2 to 16%.

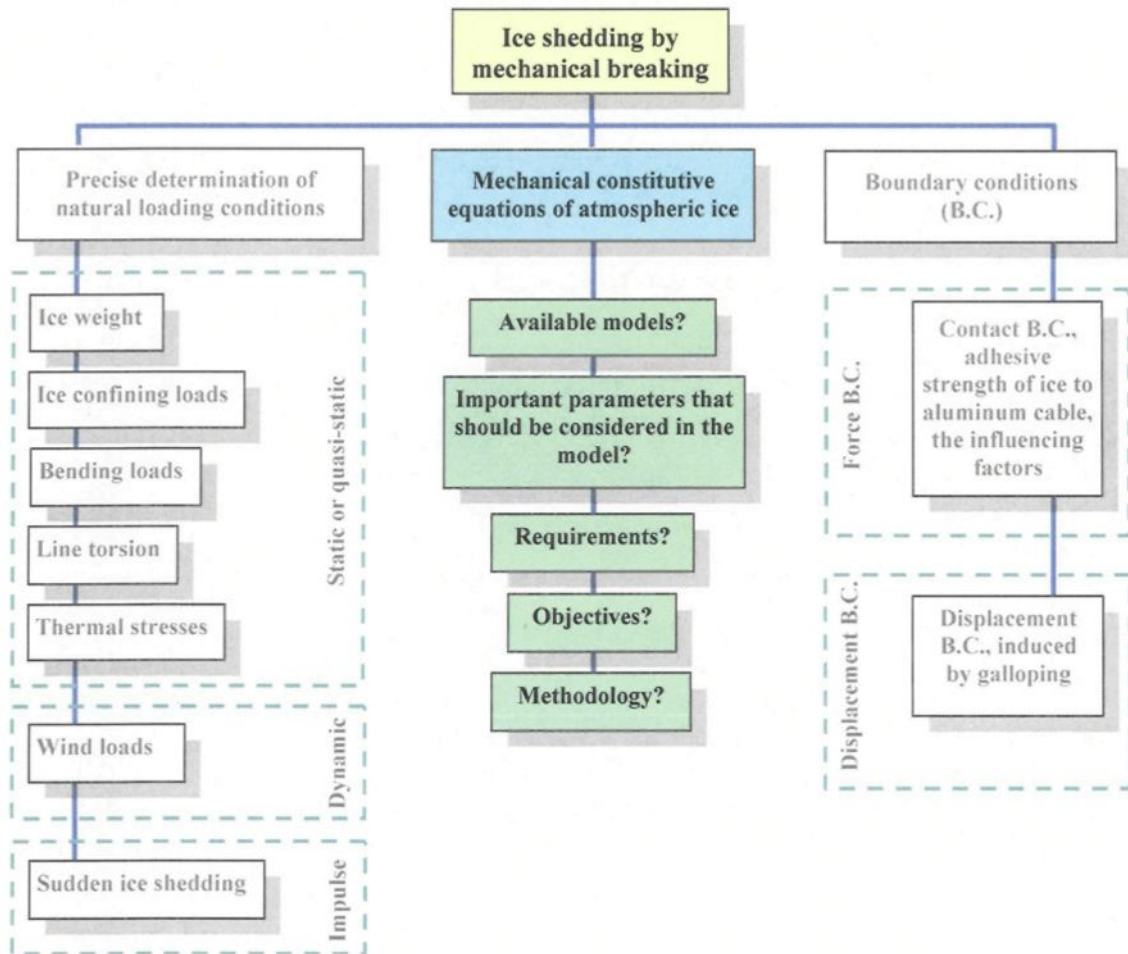


Fig. 1.3: Elements of the general problem of ice shedding by mechanical breaking.

The effect of porosity on tensile behaviour is more critical as the presence of air bubbles increases the stress intensity factor and thus facilitates the mechanisms of crack propagation. This situation is even more critical for sharp-tip air bubbles. Compared to the normal range of porosity for glaze and hard rime, which is about 15%, it is found that the porosity still has a significant influence on mechanical behaviour of ice and cannot be ignored in the constitutive equations of the material.

The main objective of this research work is then selected to be the mathematical modeling of the viscoplastic behaviour of atmospheric ice. In the next section, the general objectives of this study are specified, while the place of this study in the general problem of ice shedding is marked by blue-colored areas in Fig. 1.2 and Fig. 1.3.

### **1.3 General objectives**

The main objective of this research, as a part of the general ice shedding problem, is to present a model for viscoplastic behaviour of atmospheric ice in ductile region. The model formulation takes into consideration the non-linearity in material constitution, the material anisotropy, and the temperature and rate dependency. The term “ductile” refers to the capability of the model to predict the mechanical behaviour of atmospheric ice over a limited range of low strain-rates and higher temperatures. This means that the efforts are made in this work to provide the required fundamentals for further research leading to a model that predicts the mechanical behaviour of atmospheric ice in the full range of deformation and strain rates. The results of the final model will be used to explain the dominant mechanisms of natural ice breaking, and to improve mechanical de-icing techniques. Within the general framework of the present research, the following steps are aimed at in order to achieve the predefined objectives:

- 1) Review of the previous material tests on freshwater ice: Much of the information on the mechanical properties of polycrystalline ice is derived from cyclic or monotonic laboratory tests. On the basis of the results, realistic material modeling can be formulated for ice behaviour. In addition, the material parameters involved in the formulations can be obtained from a series of creep tests over a certain range of temperatures and loading rates.

- 2) Mathematical modeling and development of numerical procedures: The mathematical formulations should be developed for granular and columnar types of atmospheric ice. The granular ice is an isotropic material, while a transversely isotropic model is applicable for the case of columnar ice, see Chapter 6. The non-linear formulation can then be applied to a commercial finite element program for numerical evaluation.
- 3) Evaluation of the model: A comprehensive evaluation of the proposed mathematical model is necessary to justify whether or not the solution is realistic. Normally, efforts can be made to verify the capability of the model through a series of material tests on the ice samples subjected to various loading and thermal conditions.
- 4) Laboratory texture and grain size observation (morphology): The texture and crystallographic orientation strongly influence the mechanical behaviour of atmospheric ice. To find the applicability domain of each mathematical model for the case of atmospheric ice, the texture and fabric of ice deposits on electrical power lines should be known. A series of laboratory texture observations should be carried out on various types of atmospheric ice samples for selecting the proper mechanical model for each regime of ice accretion, see Chapter 6.
- 5) Case studies and model implementation: The proposed model should be implemented in a few less complex case studies at different loading and environmental conditions. The effects of temperature variations, loading rate, and confining pressure on mechanical behaviour of atmospheric ice should be studied.

## 1.4 General methodology

The following methodology will be used in order to achieve the above-defined goals. The results of material tests carried out on various types of polycrystalline ice show that ice normally undergoes a typical deformation process to some other materials at high temperatures. It normally exhibits intergranular creep behaviour at a temperature higher than  $-40^{\circ}\text{C}$ , that is 85% of its melting point. The same situation may occur at a temperature of about 40% of the melting point for metals, Ref. [59]. Because of this high-temperature deformation, the mechanical behaviour of ice is rate-sensitive and temperature dependent. For such viscoplastic deformation, a minimum of four macroscopically observed deformation mechanisms describe the mechanical behaviour of polycrystalline materials. They are (a) the instantaneous elastic deformation, (b) the delayed viscoelastic deformation, (c) the viscous or permanent plastic flow, and (d) the crack-activity deformation. A non-cracking model for this type of viscoplastic behaviour for atmospheric ice is developed here, based on the enhanced theories of orthotropic elasticity, viscoelasticity, and cap-model plasticity. This presented model is thus based on the following assumptions about the strain contributions induced in atmospheric ice by various deformation mechanisms:

- 1) Instantaneous elastic strain: The elastic moduli of polycrystalline bubble-free ice are determined from the corresponding monocrystal (single crystal) values using Hill's (1952) averaging technique. Three computer codes in Maple Mathematical Program are developed to extract the practical formulation of elastic moduli for various types of granular and columnar ice, Appendix 1. The presence of air-bubbles is considered in elastic moduli by using the porous elasticity model, see Chapter 4.

2) Delayed viscoelastic strain: The short-term rheology proposed by Sinha (1978b) is used to formulate the delayed viscoelastic strain induced by grain boundary sliding. The effect of porosity, on the other hand, is entered into the formulations by replacing the strain tensor with the effective strain in porous material.

3) Permanent plastic strain: The formulation of viscous or plastic deformation is developed based on the cap-model plasticity theory. The pressure-dependency of the material and the presence of voids in porous media can be modeled by this theory, which is the most popular plastic model in geological engineering.

The methodology for solving the resulting set of non-linear equations is based on the principle of virtual work that leads to the integral weak form of governing differential equations. These equations are then transformed into a set of matrix equations by applying the finite elements approximation and discretization technology. In addition, an iterative solution scheme should also be implemented. In the present study, however, the ABAQUS FE structural analysis program is used to solve this coupled system of non-linear equations. The material behaviour is provided to ABAQUS by using a user material subroutine (UMAT).

The material parameters describing the viscoplastic formulations are determined by fitting the available stress-strain time history records obtained from a series of uniaxial creep tests on intact ice samples. A comparison of the model predictions with the available data for bubble-free ice is performed to show the effects of air bubbles on the mechanical behaviour of polycrystalline ice.

The existing test data for freshwater ice are also used for model evaluation at low-porosity situations (glaze). The precise model justification is required in higher ranges of porosity by performing some material tests using the Refrigerated Material Testing Machine. The model is also implemented in a few more realistic case studies. These simple problems are chosen based on a series of laboratory texture (morphology) observations on atmospheric ice deposits accreted on an aluminum cylinder placed in the test section of the refrigerated wind tunnel, see Chapter 6.

### **1.5 Statements of original contributions**

In Section 1.2, an effort was made to highlight the common drawbacks of the existing freshwater ice models to predict the mechanical behaviour of atmospheric ice. The need of some adjustments in those models is also justified. The pressure-dependency in material behaviour due to ice porosity is the most important shortcoming of the existing models for predicting the viscoplastic constitution of atmospheric ice. This justification and the original contributions of the present study are outlined in this section, while the corresponding theoretical formulations, experimental results, and numerical elaboration are detailed in Chapters 4, 5, 6, and 7:

1) Improvement of elastic formulations of granular and columnar ice S1, S2 and S3: The formulations of elastic moduli of granular and columnar ice  $I_h$  were developed by Sinha (1989) on the basis of corresponding values of ice monocrystal (single crystal) measured by Dantl (1969). Later in 1994, another elastic formulation is given by Sunder (1994) for columnar ice using the monocrystal data of Gammon *et al.* (1983). In the present work, a complete set of practical formulations for elastic moduli are presented for granular and

columnar ice types S1, S2 and S3 on the basis of Gammon's monocrystal data. A typical Maple code for the most general case (granular ice) is presented in Appendix 1.

2) Development of ice poroelastic model: Porosity is known to significantly influence the compressive and tensile strength, as well as Young's modulus of polycrystalline ice, see Ref. [4] and [51]. The size and density of bubbles in atmospheric ice vary depending on the accretion regime and meteorological conditions causing the ice porosity to be as high as 35% for soft rime. The corresponding ice density variation is from  $917 \text{ kg/m}^3$  for bubble-free ice, down to  $600 \text{ kg/m}^3$  for soft rime. For glaze and hard rime that are of interest here, however, the ice porosity is limited to 15% that still has a significant influence on ice strength and its elastic moduli. An approximate reduction of 35% in Young's modulus of Greenland ice samples with 15% porosity is reported by Bentley (1957), compared to the corresponding modulus of freshwater ice. But no significant change in Poisson's ratio was observed in those series of experiments.

Based on this experimental observation, the necessity of presenting a porous model for the pressure-dependence of atmospheric ice is justified and a poroelastic model is developed here to adjust the predefined elastic moduli of freshwater ice. The effect of wetting liquid is considered by means of the drained and undrained poroelastic models, see Chapter 4.

3) Development of the cap-model plasticity for various types of porous atmospheric ice: Porosity also has significant influence on plastic behaviour and failure envelopes of materials. Rogachko *et al.* (1997) reported a 30% reduction in compressive strength when the porosity varies in the range of 2 to 16% for spherical voids. A reduction of 64% was reported for irregular shapes of voids in the same range of porosity. Even relatively dense

samples of ice contain bubbles with average diameters in the range of 0.06 to 0.12 mm, and average bubble densities of 350 to 6500 bubbles per cubic centimeters, Ref. [4]. Ice porosity in this range, 0.004% to 0.6%, has negligible effect on strength and modulus of the material. Nevertheless, the presence of pores even in relatively dense ice affect the crack nucleation process and thus requires study in the general problem of ice shedding. This situation is even more critical for smaller grain sizes, less than 5mm, which is the normal case for atmospheric ice, see chapter 6 and Ref. [4]. This pressure-dependency was ignored in the presented material constitutive models of freshwater ice so that no volumetric strain was induced by plastic deformation. In our material constitutive model, however, the pressure dependency of volumetric plastic strain is considered through the use of a cap-model plasticity that is the most popular plastic model in geological and geotechnical engineering.

4) Material model implementation in the ABAQUS program: The model is implemented as a user-defined material subroutine UMAT in ABAQUS program for numerical calculation. The subroutine is written in FORTRAN language to define the material Jacobian matrix, to modify the stress tensor, and to update the solution-dependant state variables in each iteration of every time step, see Section 7.3.

5) Texture observation of atmospheric ice deposits (morphology): A series of laboratory works were performed in the refrigerated wind tunnel for preparing the rime samples, and another set of glaze samples were prepared in the accretion simulation laboratory under various icing conditions. The samples, then, were examined to confirm that the texture was similar to the natural structure of atmospheric ice deposits on electrical transmission lines.

On the basis of these laboratory observations, it is found that the texture of the ice deposits is granular for the primary layers of ice accretion. A columnar structure (S1, S2 or S3) is normally observed for the layers far enough from the surface of cable, see Chapter 6 for further details.

6) Model elaboration and some case studies: Atmospheric ice is composed of numerous crystals oriented in different directions. The change in texture and fabric of atmospheric ice deposits on power lines causes a significant variation in mechanical behaviour of ice, ranging from an isotropic material very close to the cable surface to a general orthotropic material for the other locations. A few realistic case studies are selected on the basis of laboratory texture observation to simulate the natural loading scenarios exerted on a section of electrical line and the accreted ice deposit.

## **1.6 Structure of the thesis**

A short history of the typical problems created by atmospheric icing of power lines is given in the previous sections. In addition, the statement of the problem, the necessity of the research and the expected results, the general objectives and the contributions, and the methodology are outlined briefly in those sections. The thesis structure is organized on the basis of the steps followed in order to achieve the predefined objectives. A brief conclusion is given at the end of each chapter, while the general conclusions and recommendations are presented in the last chapter, followed by a reference list and a few appendices. The steps below are followed within the general framework of this research:

- 1) Literature review: A literature survey revealed that some ice mechanics researchers tried to approximate physical observations of the real behaviour of freshwater over a restricted range of temperatures and strain rates. A brief review of the recent developments in ice mechanics modeling is given in Chapter 2. The mathematical developments are classified into “cracking” and “non-cracking” models, the latter with three, and the former with four macroscopically observed strain components. In addition, the results of reported material tests are reviewed for adopting the material parameters of viscoplastic formulation.
- 2) Review of the theoretical background: Having a solid background in the theories of elasticity, viscoelasticity and cap-model plasticity, as well as a good knowledge of finite element method were essential in model development. A brief description of the fundamental theories is given in Chapter 3.
- 3) The practical formulation of ice poroelasticity: The engineering elastic moduli, such as Young’s modulus, shear modulus, and Poisson’s ratio are formulated for porous granular and columnar types of atmospheric ice in Chapter 4. The elastic moduli of freshwater ice are determined from three computer codes in Maple Mathematical Program, Appendix 1. The elastic moduli then are modified by using a drained and undrained poroelasticity models to take into account the effects of air-bubbles in elastic formulations.
- 4) Numerical implementation of viscoelastic formulation: The formulation of delayed-viscoelastic strain presented by Sinha (1978b) is used in this research, see Chapter 2. The incremental implementation of that model is given in Chapter 7.
- 5) The formulation of cap-model plasticity: Plastic strain is normally induced by the intra-crystalline mechanisms of deformation, particularly the movement of dislocations. Here,

the viscous or plastic strain is formulated by using the cap-model plasticity to take into account the pressure-dependency in the material constitutive equations, see Chapter 5.

6) Laboratory texture and grain size observation (morphology): The grain size, grain shape, porosity, and crystallographic orientation strongly influence the viscoplastic deformation and elastic moduli of atmospheric ice. A series of atmospheric ice samples, prepared under various accretion regimes, were examined for texture observation. The brief description of the sample preparation techniques, thick and thin sectioning, the methods of texture observation, as well as the air-bubble and grain size measurements are presented in Chapter 6.

7) Model elaboration and numerical simulation: The material constitutive equations are implemented as a user subroutine UMAT into the ABAQUS finite element program, the printout of the FORTRAN code is presented in Appendix 2. The readers may refer to Section 7.3 for more details. A brief explanation of the model elaboration together with the model evaluation is given in Chapter 7. A few simple case studies are defined on the basis of texture observation of atmospheric ice deposits. Finally, the effects of some influencing factors are studied at the end of this chapter.

## 1.7 Conclusions

The general objective of this research work, as a part of general ice shedding problem, is to model the ductile behaviour of atmospheric ice. The need for this research work comes from the fact that uncontrolled ice shedding creates many serious problems in the power transmission line industry. It provides the fundamentals for modeling the fracture behaviour of atmospheric ice over a wide range of temperatures and loading rates. The model is developed based on the existing models for the mechanical behaviour of freshwater ice. The presence of air-bubbles is considered in elastic formulations using a drained porous elasticity model. The pressure-dependency of the mechanical behaviour is considered in plastic deformation by using the cap-model plasticity. The methodology of the problem is based on the application of both experimental and numerical simulation approaches, as well as the development of a user-defined subroutine UMAT in the ABAQUS structural analysis program. The results are to be used to explain the natural mechanisms of ice breaking and also to improve mechanical de-icing techniques.

## **CHAPTER 2**

### **LITERATURE REVIEW**

#### **2.1 Introduction**

In the last few decades, ice mechanics researchers have focused on the development of models for predicting the mechanical behaviour of ice under various loading and temperature conditions. Efforts have been made in developing models on the basis of ice microstructure parameters. The domain of such work is not limited to North America, but many complementary efforts have been ongoing in the United Kingdom, Germany, Finland, China, Russia and Japan. Almost all the physical models are presented for freshwater ice, while on the other hand, there are also some empirical models resulting from the material tests on sea and lake ice. In this chapter, the recent developments in ice mechanics are classified into five major disciplines described in the next sections.

#### **2.2 Ice microstructure and texture observations**

From a macro-scale point of view, ice is a polycrystalline material for which the texture depends on the growth process and its thermo-mechanical history. At atmospheric pressure and temperatures, the stable phase of ice structure is hexagonal ice,  $I_h$ . An ice monocrystal (single crystal) of this type is a transversely isotropic material having its hexagonal symmetry about its c-axis, see Fig. 2.1. The c-axes of crystals in polycrystalline

ice can exhibit various degrees of alignment, thereby providing a definite crystallographic fabric to the solid.

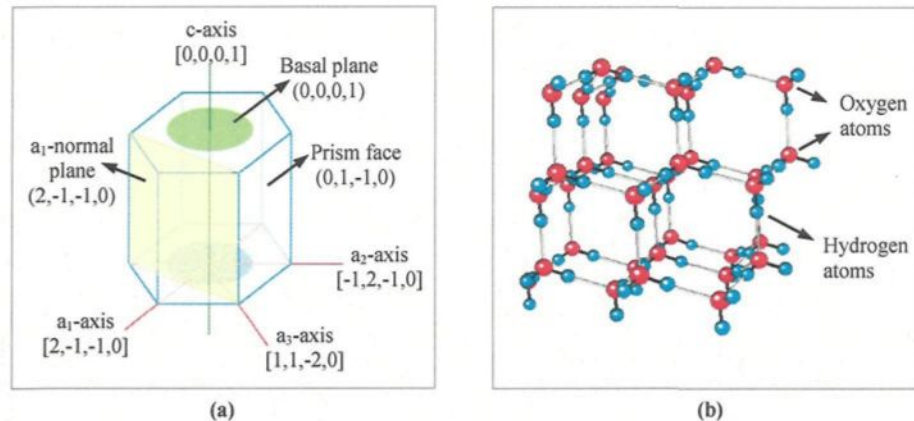


**Fig. 2.1:** The geometric configuration of the hexagonal ice lattice and crystal  $I_h$ ,  
 (a) Major lattice axes and planes, (b) Monocrystal structure and atoms arrangement.

In an ideal lattice of ice  $I_h$ , four oxygen atoms surround each oxygen atom in a tetrahedral arrangement inside the lattice with an angle of  $109^{\circ}28'$  and a distance of about  $2.76 \text{ \AA}$ . Each atom of oxygen is surrounded by two hydrogen atoms much like in a free water molecule with an angle of  $104^{\circ}31'$  and a distance of  $0.985 \text{ \AA}$ . Only one hydrogen atom lies between each pair of oxygen atoms. The hexagonal prism includes two hexagonal "basal" planes and six rectangular "prism" faces.

Michel and Ramseier (1971) established an ice classification on the basis of grain shape and size, and crystallographic orientations. Later, Ramseier (1976) made a detailed analysis of that classification. Two distinct types of *ice textures* were reported, granular and columnar structures, each divided into a few subdivisions. The term "ice texture" is a commonly-used expression in the ice mechanics branches that refers to the morphology or grain structure of polycrystalline ice. The term "ice fabric", on the other hand, denotes the

c-axis orientations within ice crystals. The c-axes in granular ice are randomly oriented, giving rise to an isotropic mechanical behaviour, regardless of anisotropy of ice monocrystal, Fig. 2.2. Three basic types of columnar ice; S1, S2 and S3 are shown, where the formation of S2 type occurs when the water is near the freezing point and its surface is seeded. In this case, the grains grow in columnar shapes in the direction of heat flow and the c-axes are randomly distributed in a plane perpendicular to the columns.

S1 ice is another common type of ice with larger columnar structure that can be found in lakes, reservoirs, and rivers with low flow velocities. The preferred crystallographic orientations of the c-axes are in a columnar direction. In the presence of strong currents, the c-axes still remain on horizontal plane, but with a strong preference of c-axes orientation that is characteristic of S3 ice. This type of ice is usually found at the bottom of thick ice sheets. Within the categories S1 and S2, ice can be considered as a transversely isotropic material, while S3 ice belongs to the family of orthotropic materials.

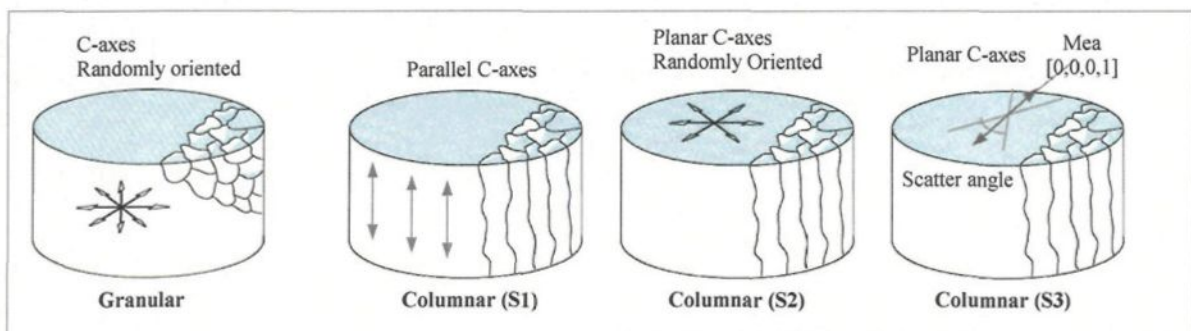


**Fig. 2.2:** Morphology (texture) and crystallographic orientations (fabric) of granular and columnar ice.

A variety of methods are refined for ice microstructure observation. Sinha (1977) proposed a double-microtome technique using cross-polarized light to examine the microstructure of ice. This technique is used in this research as it does not disturb the thermal

state and microscopic structure of the material. A few other techniques using the scattered light, scanning electron microscope, acoustic emission are also proposed by Sinha (1978a, 1984) to investigate the micro-structural changes by temperature, and the dislocation pile-up and damage accumulation during a creep process. A detailed microstructure and bubble-content observations of atmospheric ice deposits on power lines is reported by Laforte *et al.* (1983). The grain and bubble structures were studied at various meteorological conditions; however, the c-axis direction still was undetermined.

In this work, the texture of atmospheric ice deposits on electrical power lines is classified on the basis of a series of texture observations that are detailed in Chapter 6.

### **2.3 Laboratory measurements of mechanical properties of ice**

While empirical models are useful for predicting the material behaviour based on field observations, their extension beyond the specified limits cannot be done with confidence. The physical models should be used as a predictive tool for much wider limits. The successful development of physically-based models depends on our understanding of the mechanical properties of the material. Ice mechanics is concerned with the typical properties, such as compressive, tensile and shear strengths, elastic moduli, creep parameters, fracture toughness, adhesive strengths, density, and material fabric. Many loading and formation parameters have influence on ice properties, amongst which the most important are the temperature, the loading rate, the ice texture and fabric, and even the specimen size. Numerous experimental tests are required to take into account the influence of all these factors in the physical behaviour of ice. The experiments can be carried out as uniaxial tensile or compressive tests, or multiaxial laboratory tests. The basic and major

tests are (a) monotonic creep or constant-stress test, (b) damage test under constant strain rate condition, and (c) cyclic-load test. Over the years, a lot of experimental works have been carried out to measure the tensile or compression strength of ice that is the maximum stress an ice specimen can support. A list of such experimental work is given in references [49] and [64]. The earlier measurements were performed by Gold (1970, 1978) and Michel (1978) for freshwater ice, while the results of more enhanced measurements are presented by Sunder *et al.* (1989, 1990a, 1990b), Kim *et al.* (1997), and Arakawa *et al.* (1997).

At low hydrostatic pressure and common temperatures in nature, the strength values ranging from 0.5 to 10 MPa are reported for polycrystalline ice as a strong function of temperature and strain rates. At low strain rates, ice is generally ductile up to very large viscous strains with no signs of material damage or micro crack formation. At high strain rates, the material exhibits brittle behaviour. A multitude of plane micro cracks with dimensions in the order of the material grain size is initiated at quite small strains, Ref. [32]. A typical curve for this ductile to brittle behaviour of ice is shown Fig. 2.3. It is provided by Sunder (1989) from a series of material tests on freshwater ice samples at a -10°C, see Ref. [49].

The typical stress-strain plots for bubble-free ice at various strain-rate deformations are presented by Cole (1987) as shown in Fig. 2.4. At lower strain rates, nearly the normal elastic-plastic behaviours are observed for the ductile behaviour of ice, while, at higher strain rates, the material exhibits only a slight deviation from linearity that is the characteristics of near-perfect brittle behaviour. The reader is referred to the reference for the minor changes in the curves resulting from the change in grain size.

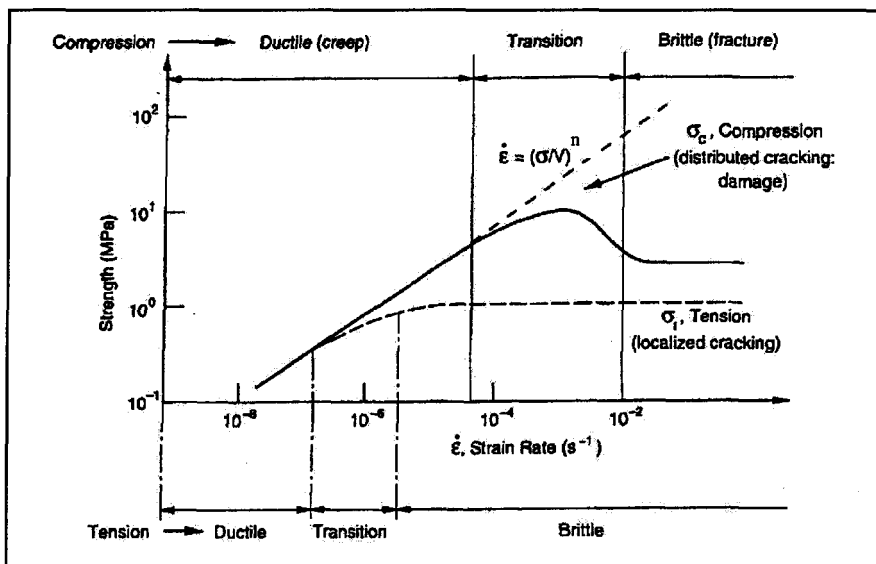


Fig. 2.3: Rate-dependency of ice strength for freshwater ice at  $-10^{\circ}\text{C}$ , grain size 5mm, adopted from the results of material tests performed by S.S. Sunder, Ref. [49].

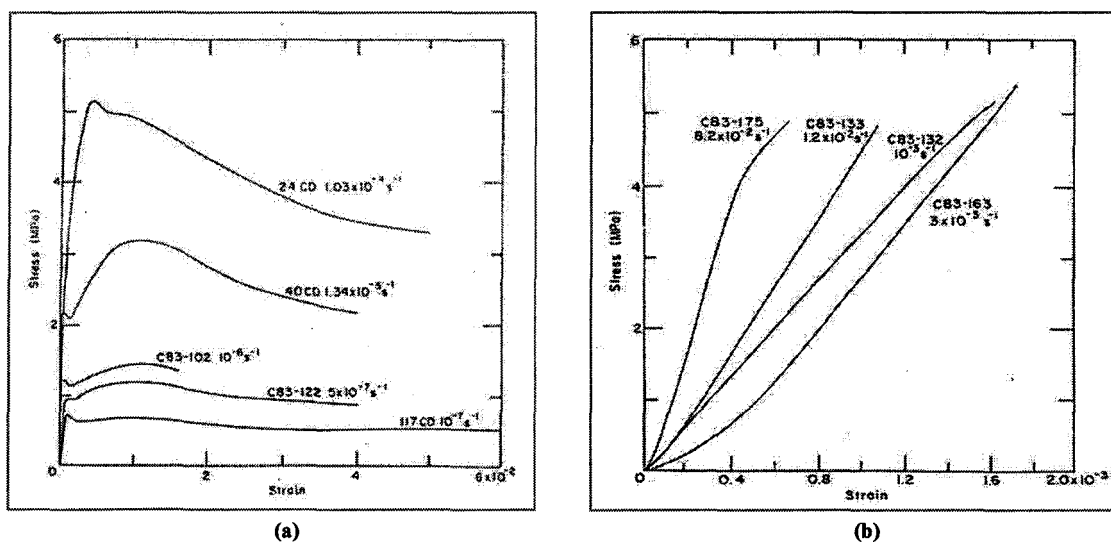


Fig. 2.4: Stress-strain curves for ice specimens tested at  $-5^{\circ}\text{C}$ , presented by Cole (1987),  
 (a) Low strain-rate tests, ductile behaviour, (b) High strain-rate tests, brittle behaviour.

Most of the proposed formulations in the ductile region originate from Glen's power law model that assumes polycrystalline ice to be isotropic and incompressible. The following steady flow model is proposed by Sunder (1990b), after generalizing Glen's model for an orthotropic material.

$$\dot{\epsilon}_N = \dot{\epsilon}_0 \left( \frac{\sigma_c}{V} \right)^n, \quad V = V_0 \exp(Q_a/RT) \quad \text{for } 233^\circ \text{K} \leq T \leq 263^\circ \text{K} \quad (2.1)$$

This equation relates the nominal plastic flow  $\dot{\epsilon}_N$  to the compressive strength  $\sigma_c$  for low strain-rate deformation, where  $n$  is the power law exponent that is approximately 3 for pure flow at stresses of engineering interest,  $\dot{\epsilon}_0$  is a reference strain rate that may be set to unity without loss of generality,  $V$  is a temperature-dependent parameter with the unit of stress representing the creep resistance of the material,  $V_0$  is material constant,  $T$  is the absolute temperature in  $^\circ\text{K}$ , creep activation or the necessary energy to break the atomic bond for ice is  $Q_a = 66.9 \text{ kJ} \cdot \text{mole}^{-1}$ , and  $R = 8.314 \text{ J} \cdot \text{mole}^{-1} \cdot ^\circ\text{K}^{-1}$  is the universal gas constant.

The compressive strength reaches its maximum value in the transition zone at a strain rate of  $10^{-3} \text{ s}^{-1}$ . It is recognized that both creep and brittle failure operate in the transition zone, Ref. [70]. Beyond the transition zone at strain rates higher than  $10^{-2} \text{ s}^{-1}$ , the brittle fracture of ice occurs and the strength remains independent of strain-rate. In this brittle region, Michel proposed the following formulation for the crushing compressive strength,  $\sigma_c$  in Pa, as a function of grain size,  $d_g$  in m, and ice temperature,  $\Theta$  in  $^\circ\text{C}$ .

$$\sigma_c = 9.4 \times 10^4 \cdot (d_g^{-1/2} + |\Theta|^{0.78}) \quad (2.2)$$

The temperature dependence of compressive strength of bubble-free ice at strain-rates as low as  $4 \times 10^{-5} \text{ s}^{-1}$  is shown in Fig. 2.5, adopted from Ref. [3]. Ductile behaviour is observed at ambient temperatures at this rate of deformation. However, the slope of the curve discontinuously changes at two temperatures,  $-63^\circ\text{C}$  and  $-103^\circ\text{C}$ , which corresponds to the transition from ductile to brittle I (transition region in Fig. 2.3) and from brittle I into brittle II regions.

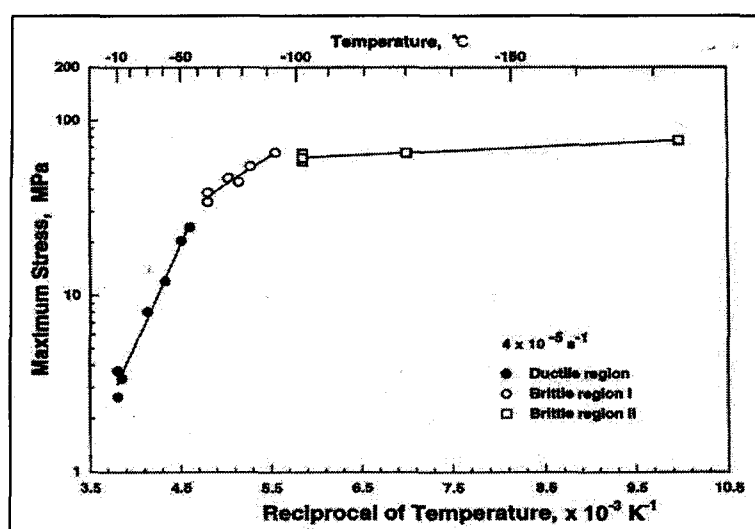
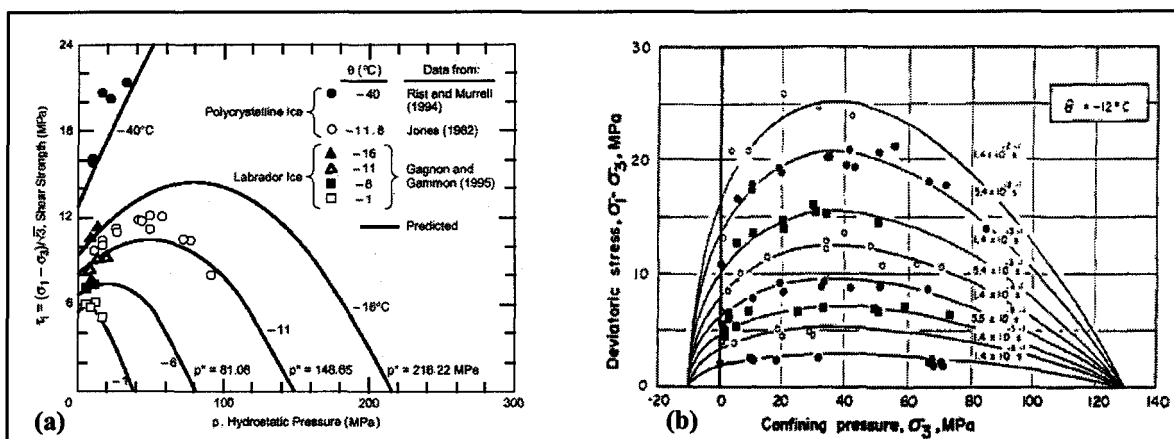


Fig. 2.5: Temperature dependency of ice strength at strain rate of  $4 \times 10^{-5} \text{ s}^{-1}$ , reported by Arakawa *et al.* (1997).

The first studies of the effect of low confining pressure on creep strength of ice under triaxial compression were carried out by Sayles (1974). The studies showed that the ice strength is nonlinear function of the confining pressure. More detailed investigations of the effect of the strain rate and high confining pressures on the ice strength under triaxial compression were performed by Jones (1982). The studies, carried out over a wide range of constant strain rates and confining pressures, lead to results that the ice strength is a power function of the axial strain rate.

Further experimental studies revealed the effects of temperature, salinity, structure, and other factors on the strength of various types of ice. Hausler (1983), Nadreau and Michel (1986), Richter-Menge *et al.* (1986), Timco and Frederking (1984 and 1986), Sinha (1985 and 1986), Nadreau *et al.* (1991), Rist and Murrell (1994), Gagnon and Gammon (1995), Weiss and Schulson (1995), Fish *et al.* (1997) and others reported the results of a series of confined multiaxial compression tests with various ice types and over a range of loading rates, confinements, and temperatures. They deduced that the confined ice strength could be ten times greater than the uniaxial case. Two typical failure envelopes for columnar S2 ice are shown in Fig. 2.6, in which  $J_2$  denotes the second invariant of deviatoric stress,  $T$  the temperature,  $p$  the hydrostatic pressure,  $\phi$  the friction angle,  $c$  the ice cohesion, and  $p^*$  the melting pressure. The temperature dependence of failure envelopes are shown in Fig. 2.6a by Fish *et al.* (1997) on the basis of the test data of Rist and Murrell (1994), Jones (1982), and Gagnon and Gammon (1995). The variations of failure envelopes by strain rate were presented by Jones (1982) in Fig. 2.6b.



**Fig. 2.6:** Two typical pressure-dependent failure surfaces for S2 columnar ice, reported by (a) Fish *et al.* (1997), (b) Jones (1982).

Fish *et al.* (1997) fitted a series of parabolic curves for temperature and strain-rate dependency of failure envelopes by using three material parameters: cohesion, friction angle, and melting pressure. On the other hand, Michel and Nadreau (1986), Jones (1982), and Derradji (2000) proposed the teardrop and elliptical functions for pressure dependency of ice failure envelopes in different ranges of temperature and strain rate, mainly in ductile region, see Fig. 2.6b and Fig. 2.7. Other failure envelopes are presented by Derradji (2000) on the basis of the test data of Rist and Murrell (1994) for granular ice as shown in Fig. 2.7. The convergence of the curves to the point of ice cohesion, i.e. shear strength at zero hydrostatic pressure, can be interpreted as the strain-rate independency of ice cohesion that is the characteristics of materials and independent of loading conditions. The failure envelope of this study is retained on the basis of the Fish *et al.* (1997) model for shear yielding. The formulations of material parameters are modified to achieve better agreement with the existing experimental results. The effects of porosity changes upon loading are added to this model through a cap-yielding mechanism, see Chapter 5.

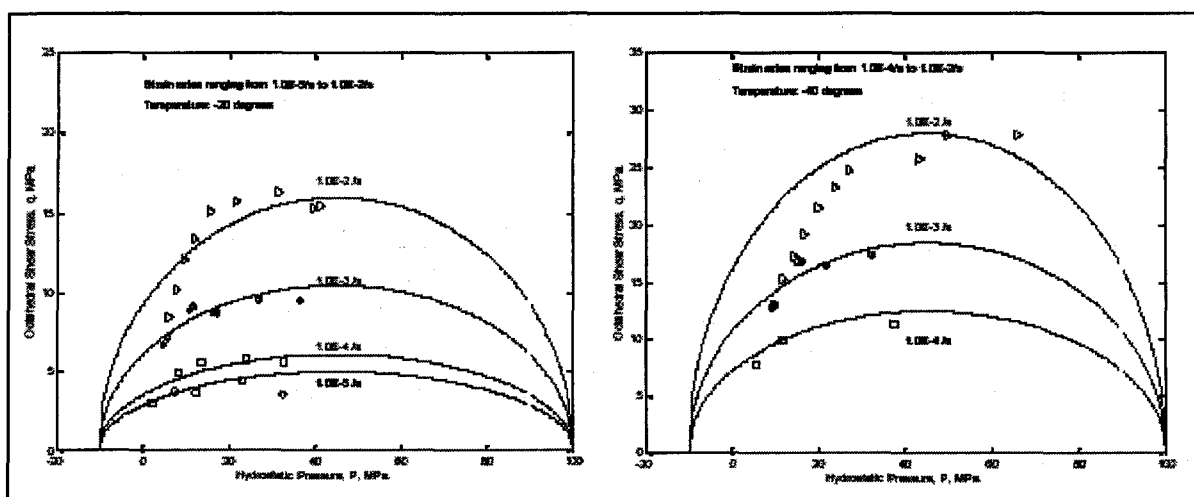


Fig. 2.7: The typical pressure-dependent failure surfaces for granular ice at -20C (left) and -40C (right), reported by Derradji (2000) on the basis of the test data of Rist and Murrell (1994).

The other mechanical properties such as shear and adhesive strengths, fracture toughness, and density were also of interest to some other researchers, see Refs. [49] and [64] for more details. The influence of ice porosity on mechanical properties of ice has interested some other researchers as well. Rogachko *et al.* (1997) presented the results of their laboratory tests, carried out on artificial porous ice samples containing spherical and irregular voids. The tests were conducted at a constant strain rate of  $10^{-3} \text{ s}^{-1}$  at  $-5^\circ\text{C}$ . Thirty percent and 64% reductions in compressive strength were observed when the porosity varies in the range of 2 to 16% for spherical and irregular voids. Bentley *et al.* (1957) measured the elastic moduli and propagation velocities of elastic waves for Greenland porous ice shelf samples. Strong porosity dependence was observed for the Young's modulus of ice ( $E$ ), while no significant change in Poisson's ratio ( $\nu$ ) was reported, Fig. 2.8. Using this figure, more than 70% reduction in Young's modulus is calculated as the porosity increases to 35%. Hence, it can be concluded that the porosity has a significant influence on the mechanical behaviour of atmospheric ice, so the material constitutive equations presented for freshwater ice should be modified for porosity changes.

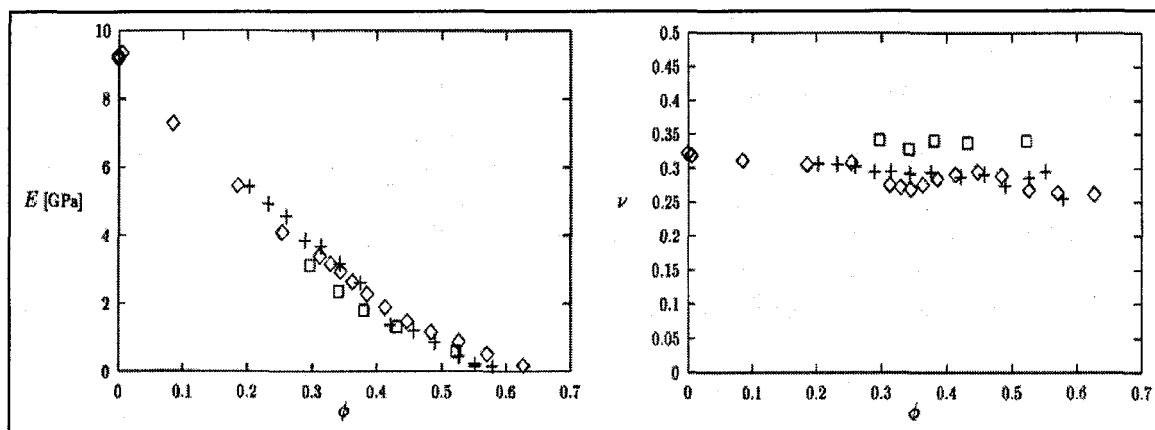


Fig. 2.8: Variation of Young's modulus and Poisson's ratio with porosity ( $\phi$ ) in ice shield samples, Ref. [4].

Further to the experimental works on freshwater or sea ice, there are very few reports on the measurement of mechanical properties of atmospheric ice or snow. The strength measurement of atmospheric ice deposits on electrical power lines reported by Druetz *et al.* (1986) is a good example of those works. A number of laboratory tests have been conducted to measure the adhesive strength of ice. The maximum value of 181 kPa at  $-12^{\circ}\text{C}$  is reported for ice adhesive strength to an aluminum substrate. Itagaki (1984) also measured the shear adhesive strength of atmospheric ice within the range of 30 to 150 kPa, see Ref. [17].

## **2.4 Mathematical modeling of ice constitution**

Upon high-temperature loading, polycrystalline materials, including ice, undergo a creep deformation and grain boundary brittleness. In this case, the strain history shows four distinct stages: an initial stage resulting from the instantaneous elastic deformation, a primary or transient creep, a secondary or steady-state flow, and a tertiary creep stage, Ref. [6]. A reduction in strain rate occurs in the primary stage and continues to its minimum value in the secondary stage. After this stage, the material deformation accelerates and the strain rate increases with time, leading to its maximum value in the tertiary stage of deformation. The nonlinearity tends to result from the fact that the minimum is reached earlier for higher applied stresses. The total strain for such creep deformation comprises the elastic and inelastic parts. Sinha (1978b) showed that the recoverable pure elastic part is associated with lattice deformation, while, the inelastic part is further decomposed into three components, a transient flow, a steady-state part, and a crack activity strain. The transient flow results from structural changes associated with the elastic back-stresses

generated during kinematics hardening and the drag-stresses due to isotropic hardening, Ref. [68]. It represents the recoverable grain boundary sliding, which is normally called delayed-elastic strain. The steady-state part is generated entirely by intra-granular mechanisms of deformation, such as viscous flow and the movement of dislocations, Ref. [77]. The crack-activity strain can also be added to take into account the effects of micro crack nucleation in transient flow and its propagation in steady flow. The damage due to micro and macro crack distribution may be followed by strain softening which particularly affects the elastic properties of the material.

#### **2.4.1 Determining the elastic moduli of polycrystalline ice**

The instantaneous elastic strain has been related to the applied stress by generalized Hooke's law. In general, the elastic moduli of polycrystalline materials can be measured through a series of the standard static compression, tensile and bending tests. However, these static results become inaccurate for ice that undergoes high-temperature deformation. In this range, both viscoelastic and plastic behaviours contribute to the measured stresses and strains that do not correspond to the true instantaneous elastic deformation. The error percentage involved in the measured values of elastic moduli is well demonstrated by Sinha (1978b). As an alternative, Michel (1978) and Sinha (1989) presented their formulations for elastic moduli of granular and columnar ice types as a function of temperature. The elastic moduli for polycrystalline ice have been calculated from those corresponding to monocrystal (single crystal) using Reuss's (1929) averaging method. The prediction of elastic deformation of polycrystalline ice, then, depends on the accuracy of measurements of the monocrystal elastic constants. The elastic compliances measured by Dantl (1969),

who implemented a supersonic pulse-echo method, were the basis of those calculations. Later, a more detailed study was reported by Nanthikesan and Sunder (1994) to determine this temperature dependence of elastic moduli for general anisotropic polycrystalline ice. In this work, the elastic compliances measured by Gammon *et al.* (1983) by Brillouin spectroscopy were the basis of the formulation and two upper and lower limits of elastic moduli were determined using Voigt (1910) and Reuss (1929) averaging methods. The advantages of using Gammon's data have been explained based on lower uncertainty within 1.05% for Gammon's in comparison with 20% for Dantl's measurements. In addition, the results of Dantl (1969) are found to violate the inverse relationship between the moduli and the compliance matrices. Gagnon (1988) used a Brillouin spectroscopy method to determine the pressure-dependence of monocrystal elastic constants to 2.8 kbar. He also determined the average elastic constants of isotropic ice as a function of pressure. In this work, Gammon's measurements are used in conjunction with Hill's (1952) averaging method to calculate the elastic moduli of ice. The temperature dependence of the constants is determined in accordance with Dantl's correction by neglecting the quadratic terms as

$$\hat{X}(\Theta) = \hat{X}(\Theta_r) \frac{1 \pm a \Theta}{1 \pm a \Theta_r} \quad (2.3)$$

where  $\hat{X}$  denotes an arbitrary monocrystal constant, positive sign for elastic compliances  $\hat{S}_{\alpha\beta}$  and negative sign for elastic moduli  $\hat{C}_{\alpha\beta}$ , ( $\alpha, \beta = 1$  to 6);  $\Theta$  denotes the temperature in °C; and  $\Theta_r$  denotes a reference temperature at which the measured value for  $\hat{X}$  exists. The corresponding values for Gammon's measurements are  $\Theta_r = -16^\circ\text{C}$  and  $a = 1.418 \times 10^{-1} \text{ } ^\circ\text{C}^{-1}$ .

The results reported by Gammon *et al.* (1983) are tabulated in Table 2.1 for adiabatic measurements, as a reference for the elastic formulations presented in Chapter 4. It should be noted that the values are reported with respect to a rectangular coordinate system with a 3-axis in the direction of the c-axis, and  $S_{66}$  represents the inverse of shear modulus in monocystal plane of isotropy (plane 12). In situations where the stress is applied gradually, the isothermal values that can be calculated from the following equation are appropriate.

$$\hat{S}_{ijkl}^T = \hat{S}_{ijkl}^S + \alpha_{ij} \alpha_{kl} \frac{T}{\rho \cdot C_p} \quad (2.4)$$

In which  $\hat{S}^T$  and  $\hat{S}^S$  denote the isothermal and adiabatic elastic compliance tensors,  $T$  the absolute temperature,  $\rho$  the density,  $\alpha$  the thermal expansion tensor, and  $C_p$  the heat capacity per unit mass at constant stress. According to the references, the values of density, thermal expansion and heat capacity at  $-16^\circ\text{C}$  are reported as  $\rho = 919.5 \text{ kg} \cdot \text{m}^{-3}$ ,  $\alpha_{ij} = 50.83 \times 10^{-6} \delta_{ij}$ , and  $C_p = 1.9854 \text{ kJ} \cdot \text{kg}^{-1} \cdot ^\circ\text{C}^{-1}$ , where  $\delta_{ij}$  is the Kronecker delta.

**Table 2.1:** Adiabatic measurements of ice monocystal elastic constants at  $-16^\circ\text{C}$ , Gammon *et al.* (1983).

Adiabatic values					
Elastic Compliance	GPa <sup>-1</sup>	Uncertainty (%)	Elastic Module	GPa	Uncertainty (%)
$\hat{S}_{11}$	0.10318	± 0.50	$\hat{C}_{11}$	13.929	± 0.41
$\hat{S}_{12}$	-0.04287	± 1.05	$\hat{C}_{12}$	7.082	± 0.39
$\hat{S}_{13}$	-0.02316	± 0.73	$\hat{C}_{13}$	5.765	± 0.23
$\hat{S}_{33}$	0.08441	± 0.45	$\hat{C}_{33}$	15.010	± 0.46
$\hat{S}_{44} = \hat{S}_{55}$	0.33179	± 0.06	$\hat{C}_{44} = \hat{C}_{55}$	3.014	± 0.11

#### 2.4.2 Formulation of delayed viscoelastic strain

Experimental observations show that ice does not behave as an ideal elastic material, even at relatively high loading rates. Upon loading, the interaction between adjacent grains in polycrystalline ice generates an intergranular recoverable deformation called delayed viscoelastic strain. In this case, the total strain imposed on ice is recoverable for a significant time after initiation of loading. Only a few researchers have been involved in this initial creep transition associated with intra-granular sliding phenomena, Sinha (1978b), Gold (1983), Michel (1978), and recently Schapery (1997). Most of the models presented, including this work, were done on the basis of the short-time rheology proposed by Sinha (1978b) in accordance with Zener's hypothesis (1948). Zener (1948) indicated that this viscoelastic deformation builds up a back stress opposing the movements of grain boundaries stored in the material as elastic energy. The deformation will be stopped when the back stress reaches the magnitude of the imposed stress. Upon unloading, the stored energy reverses the process of sliding and drives back the boundaries towards their initial position. The following relationship is proposed by Sinha (1978b) to relate the short-term viscoelastic deformation  $d\epsilon^{ve}$  to the applied uniaxial stress  $\sigma$ , in which  $d_g$  denotes the grain size,  $dt$ , the time increment,  $E$ , Young's modulus, and the material constants  $C_1$ ,  $d_1$ ,  $s$ , and  $b$  should be obtained from material tests.

$$d\epsilon^{ve} = \frac{C_1 d_1}{d_g} \left(\frac{\sigma}{E}\right)^s \left\{1 - \exp[-(a_T dt)^b]\right\} \quad (2.5)$$

The temperature-dependant parameter  $a_T$  can also be calculated from a reference value  $a_{T_0}$  corresponding to the temperature  $T_0$  using Arrhenius type equation (2.6).

$$a_T = a_{T_0} \exp \left[ \frac{Q_a}{R} \left\{ \frac{1}{T_0} - \frac{1}{T} \right\} \right] \quad (2.6)$$

This Arrhenius relation originates from the fact that ice is a rheological simple and stress-dependant material. Hence, the deformation curves at various temperatures can be reduced to a single master curve by means of a shift function  $S_{1,2}$  given by

$$\ln(t_1/t_2) = \ln S_{1,2} = \frac{Q_a}{R} \left\{ \frac{1}{T_1} - \frac{1}{T_2} \right\} \quad (2.7)$$

in which  $t_1$  and  $t_2$  are the times required to produce a given strain at temperatures  $T_1$  and  $T_2$ . Later, equation (2.5) was extended by Derradji-Aouat *et al.* (2000) for the three-dimensional case by replacing the term containing  $\sigma/E$  by the elastic strain tensor  $e_{ij}^e$ . This ensures that no volume change is induced by grain boundary sliding in freshwater ice. In addition, the intracrystalline plastic deformation drives the vacancies and imperfections towards the boundaries, which weakens the grain boundary. This weakness is considered in the formulation by using a structural change function  $d\lambda^{ve}$ , that results in the short-term representation of delayed-elastic deformation as

$$d\varepsilon_{ij}^{ve} = \frac{(1 + d\lambda^{ve}) C_1 d_1}{d_g} (e_{ij}^e)^s \left\{ 1 - \exp[-(a_T dt)^b] \right\} \quad (2.8)$$

where  $d_g$  is the grain size in mm. The structural change function  $d\lambda^{ve}$  is formulated as a function of initial and current von-Mises deviatoric strains ( $\varepsilon_{0dev}^p$  and  $\varepsilon_{dev}^p$ ) by Derradji-Aouat *et al.* (2000) through a series of standard creep tests for freshwater ice. The plots are obtained for the variation of viscoelastic strain versus the change in plastic deviatoric strain ( $d\varepsilon_{dev}^p$ ) leading to:

$$d\lambda^{ve} = \frac{A_\lambda}{t^{2b}} |d\varepsilon_{dev}^p| + \frac{1}{t^{2b}} \frac{B_\lambda}{\ln(1 + d\varepsilon_{dev}^p / \varepsilon_{0dev}^p)} |d\varepsilon_{dev}^p| \quad (2.9)$$

In which the von-Mises deviatoric strain is defined by

$$d\varepsilon_{dev}^p = \left[ \frac{2}{3} de_{ij}^p de_{ij}^p \right]^{\frac{1}{2}} \quad (2.10)$$

Derradji-Aouat *et al.* (2000) reported the values of material parameters  $A_\lambda$  and  $B_\lambda$  in Ref. [14], while, the other material parameters have already been determined by Sinha (1978b) through a curve fitting of the stress-strain time history record obtained from a series of uniaxial creep tests on intact freshwater ice samples. Both results are summarized below in Table 2.2 as a reference for the formulation of delayed viscoelastic strain in Chapter 7.

**Table 2.2:** Material parameters in viscoelastic formulation of freshwater ice at  $-10^\circ\text{C}$ , Ref. [13] and [57].

Parameter	Symbol	Value
Material Constant (coefficient)	$C_1$	$9 \times 10^{-3}$
Material Constant (coefficient)	$d_1$	1 mm
Material constant (power of elastic strain)	$s$	1
Damping factor in viscoelastic deformation	$b$	0.34
Material parameter measured at $T_0 = -10^\circ\text{C}$ for thermal shift function	$a_{T_0}$	$2.5 \times 10^{-4} \text{ s}^{-1}$
Creep activation energy	$Q_a$	$66.9 \times 10^3 \text{ J.mole}^{-1}$
Universal gas constant	$R$	$8.314 \text{ J}^\circ\text{K}^{-1} \text{ mole}^{-1}$
Material constant in structural change function due to plastic deformation	$A_\lambda$	$7.5 \times 10^5 \text{ s}$
Material constant in structural change function due to plastic deformation	$B_\lambda$	$1.9 \times 10^4 \text{ s}$

### 2.4.3 General modeling of ice behaviour

Over the years, a number of mathematical models have been developed to describe the cracking or non-cracking constitution of ice. Conceptually, in the models including this one, efforts are made to describe the ice constitution in a series of explicit rate equations adequate for numerical calculation. However, the ice constitutive models may also be derived from a Helmholtz free energy based on some thermodynamical state and internal variables. For example, Sjolind (1987), and Sunder *et al.* (1989) have presented their models based on those principles. Some of the models have been developed particularly for damage formulation and crack propagation, e.g. the models presented by Sunder and Wu (1990a), Xiao and Jordaan (1996), and Kim and Sunder (1997), while the rest are developed in a more general manner for describing the various stages of creep, e.g. the models presented by Sinha (1983), Fish (1991), Zhan *et al.* (1994), and Derradji-Aouat *et al.* (2000). A few conclusions extracted from those existing viscoelastic models are reviewed here. The reader is referred to the corresponding references for further details.

- 1) The negligible amount of plastic strain is generated in the direction of columns. This plastic anisotropy and the orthotropic elasticity facilitate the nucleation of cracks.
- 2) The tertiary creep starts mainly because of the effects of micro cracking. However, the microcracks may nucleate even during the transition from primary to tertiary creep.
- 3) The strain softening and creep dilatation induced by cracks in a low-rate deformation should be considered, even in a non-cracking model, by modifying the elastic moduli and viscoelastic characteristics of ice. However, for higher rates of deformation, failure takes place immediately after elastic deformation where the crack activity cannot be ignored.

#### **2.4.4 Deficiencies of existing viscoplastic models and the areas of improvement:**

The following major deficiencies are observed in the constitutive relations proposed for freshwater ice, in predicting the mechanical behaviour of porous atmospheric ice:

- 1) The effects of hydrostatic pressure on the ice-failure envelopes are considered in some existing measurements. Those envelopes are modified in this study to have a better agreement with test data. The hardening due to porosity changes is considered in those envelopes by means of the cap-model plasticity.
- 2) No plastic volume change is considered in the existing cracking or non-cracking models. However, it should be taken into account for porous atmospheric ice by using an appropriate procedure like cap-model plasticity.
- 3) Porosity has a significant influence on the elastic moduli of atmospheric ice, see Section 2.3. This should be added to the elasticity models presented for freshwater ice by using the appropriate poroelasticity model.
- 4) The effects of porosity on the delayed-viscoelastic behaviour of atmospheric ice should also be added to the Sinha's model (1978b).

#### **2.5 Field measurements and experimental techniques**

The results of field measurements are important in terms of operational notes to be considered in theoretical formulation and laboratory experimental works. Cold climate regions, including Canada, have benefited from having the opportunity of monitoring ice behaviour in nature. The static or dynamic ice loads in structures and transmission lines can be measured by using different standard sensors. Additional loads due to ice accretion and dynamic or impulse response of structure may also be measured in the field.

Over the years, Frederking and Timco (1986), Graham *et al.* (1983), and Witney *et al.* (1986) have performed some in-situ tests on sea ice. Some other works performed in the United States and Canada before 1990 are reviewed by Sinha *et al.* (1987) and Richter-Menge (1992) in references [49] and [64].

## **2.6 Other related research works**

Referring to Fig. 1.2, all the other subjects related to this work can be categorized in this section. Most of the related subjects are accomplished within the framework of research activities carried out at the NSERC/Hydro-Quebec Industrial Chair on Atmospheric Icing of Power Network Equipment (CIGELE) and the Canada Research Chair on Atmospheric Icing Engineering of Power Network (INGIVRE) at the Université du Québec à Chicoutimi. As an example, a few related research works are listed below.

- 1) Ice shedding from conductors by melting and sublimation, Ref. [5].
- 2) Numerical modeling of the response of ice shedding on electrical power lines, Ref. [52].
- 3) Study of ice accretion and ice shedding on overhead power lines, Refs. [18] and [19].

## 2.7 Conclusions

A brief review of the recent developments in ice mechanics is given in this chapter to determine whether the existing models are appropriate for this study. If not, what are the shortcomings of those models in predicting of the mechanical behaviour of porous atmospheric ice? In the existing ice models, efforts are made to take into account the anisotropy and creep in describing the mechanical behaviour of ice. The mathematical models can be classified into “cracking” and “non-cracking” categories. A maximum of four macroscopically-observed strain components defines the cracking constitution of ice: the instantaneous elastic part, the delayed viscoelastic deformation, the viscoplastic flow, and the crack-activity strain. The non-cracking models, on the other hand, are not concerned with the cracking activities. The mechanical behaviour of ice, in both cases, is a function of temperature and strain rate. The following conclusions are drawn from the literature review given in this chapter:

- 1) The material parameters and failure envelopes should be obtained from the experimental tests on various types of ice. The existing material data is mainly available in ductile region, thus, can be used for developing a ductile model for mechanical behaviour of atmospheric ice at low strain-rate deformation and in higher ranges of temperature. The formulations of the ice-failure curves may be originated from Fish *et al.* (1997) model and the material parameters can be obtained from the available test data. A series of high strain-rate material tests should be designed to extend the formulations to the transition and brittle regions of ice behaviour. A Refrigerated Material Testing Machine has been ordered upon this need, which can be used in future studies.

- 2) The influence of low-rate cracking activities in elastic and viscoelastic deformations may also be considered in ductile models.
- 3) The elastic moduli can be calculated from the corresponding monocrystal data, in this case from Gammon's measurements. An averaging technique similar to the works of Sinha (1989) and Nanthikesan and Sunder (1994) can be used for determining the elastic moduli of freshwater polycrystalline ice. The results then can be modified for taking the effects of porosity into account by using an appropriate poroelastic model.
- 4) The short-term rheology presented by Sinha (1978b) can be used to describe the delayed-viscoelastic strain after some adjustments for considering the porosity effects.
- 5) The pressure dependence of plastic strain is not considered in the previous works where it should be taken into account for the case of atmospheric ice by using cap-model plasticity.
- 6) To find the applicability domain of the formulations, the microstructure of ice deposits should be examined. A series of microstructure observations should be performed to determine the c-axis direction that is still undetermined for atmospheric ice deposits on power lines. This study may be considered as a follow-up work to the Laforte *et al.* (1983) observations for relating the type of ice to some meteorological factors such as liquid water content (LWC), droplet size, wind velocity, and air temperature.

## CHAPTER 3

### THEORETICAL BACKGROUND

#### 3.1 Introduction

Atmospheric ice can be found in nature in granular or columnar structures. The granular ice, in engineering approaches, is interpreted as an isotropic material, while the various types of columnar ice (S1, S2, and S3) can be considered as transversely isotropic or orthotropic materials, see Chapter 6. The mechanical properties of atmospheric ice depend on several factors, the most important of which are: grain shape and size, crystallographic c-axis orientations, ice porosity, loading rate, and temperature. The deformation, failure curves and ice strength are considerably affected by strain rate. Depending on the loading conditions, the ice can be interpreted either by continuum elastic and ductile deformations or by fracture behaviour characterizing a brittle process in crack formation. In this work, the main efforts focus on the elastic and ductile behaviour of atmospheric ice as it occurs in higher temperatures and lower strain rates.

Upon high-temperature loading (closer to melting point), ice as a polycrystalline material undergoes creep deformation, in which the time-dependent deformation is divided into four creep stages: instantaneous deformation, primary creep (transient), secondary creep deformation (steady-state), and tertiary stage resulting in failure.

The total strain rate can be decomposed into the elastic ( $\dot{\epsilon}^e$ ) and inelastic ( $\dot{\epsilon}^{ie}$ ) parts if the elastic strain is infinitesimal. The recoverable elastic part is associated with lattice deformation, while the inelastic part is further decomposed into a viscoelastic (delayed-elastic) part ( $\dot{\epsilon}^{ve}$ ), a steady-state (plastic) flow ( $\dot{\epsilon}^p$ ), and a crack-activity part ( $\dot{\epsilon}^c$ ), Fig. 3.1.

$$\dot{\epsilon} = \dot{\epsilon}^e + \dot{\epsilon}^{ie} = \dot{\epsilon}^e + \dot{\epsilon}^{ve} + \dot{\epsilon}^p + \dot{\epsilon}^c \quad (3.1)$$

The viscoelastic part results from the structural changes associated with the elastic back-stress and drag-stress generated during kinematic and isotropic hardening, while the plastic part is generated by intra-granular mechanisms of plastic deformation, Ref. [67]. The material constitutive equations relate the state of stress to the strain field within the material. Thus, each contribution to equation (3.1) should be related to the state of stress using the principles of viscoelasticity and rate-dependent plasticity. The resulting equations can be substituted into equilibrium equations to determine the unknowns of the problem.

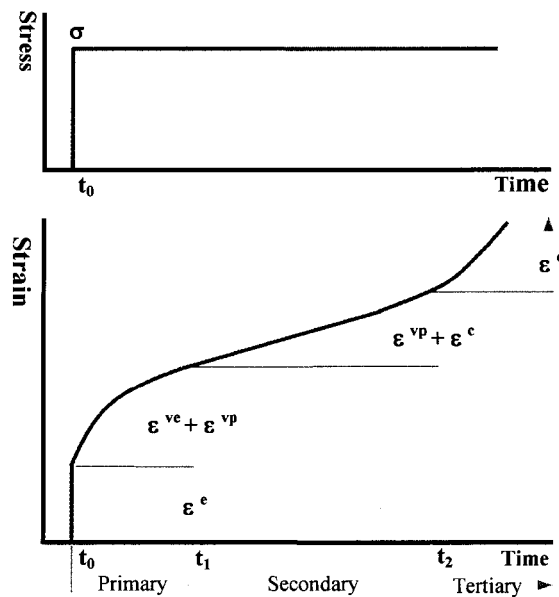


**Fig. 3.1:** A typical strain history creep curve for ice in uniaxial constant loading.

The balances of mass and momentum, equations (3.2) and (3.3) and the boundary conditions (3.4) in general form can be written as

$$\dot{\rho} + \rho \dot{u}_{j,j} = 0 \quad (3.2)$$

$$\sigma_{ij,j} + \rho b_i = \rho \ddot{u}_i \quad (3.3)$$

$$u_i = u_i^0 \quad \text{on } \partial\Omega_u, \quad \sigma_{ij} n_j = \sigma_i^0 \quad \text{on } \partial\Omega_\sigma \quad (3.4)$$

where  $\rho$  denotes the material density;  $u_j$ ,  $\dot{u}_j$ , and  $\ddot{u}_j$  the vectors of displacement, velocity, and acceleration, respectively;  $b_i$  the components of body force per unit of mass,  $\sigma_{ij}$  the Cauchy stress tensor,  $u_i^0$  the prescribed displacement vector on part  $\partial\Omega_u$  of the boundary  $\partial\Omega$ ,  $\sigma_i^0$  the components of traction vector on stress boundary  $\partial\Omega_\sigma$  with unit normal vector  $n_j$ .

For linear small strain problems, the strain tensor is related to the displacement field by:

$$\varepsilon_{ij} = \frac{1}{2} \left( \frac{\partial u_i}{\partial x_j} + \frac{\partial u_j}{\partial x_i} \right) \quad (3.5)$$

For the rate and temperature-dependent materials, the yet unknown constitutive equations corresponding to the assumed deformation mechanisms in equation (3.1), can be assumed to be a function of temperature, strain, strain rate, and a set of internal state variables ( $\kappa_\alpha$ ) as:

$$\sigma_{ij} = \Sigma_{ij}(\varepsilon_{ij}, \dot{\varepsilon}_{ij}, T, \kappa_\alpha) \quad (3.6)$$

Equations (3.2), (3.3), (3.5) and (3.6) provide altogether sixteen relations for finding the sixteen unknowns  $\rho$ ,  $u_j$ ,  $\sigma_{ij}$ , and  $\varepsilon_{ij}$ .

The resulting non-linear partial differential equations should be solved by a numerical procedure, the finite element method (FEM), in this case. The methodology for solving this type of solid-mechanics problems by FEM is based on the principle of virtual works. This leads to the integral weak form of the governing differential equations over the material domain,  $\Omega$ , which can be written as:

$$\int_{\Omega} (\sigma_{ij} \delta \dot{\epsilon}_{ij} - \rho b_k \delta \dot{u}_k + \rho \ddot{u}_k \delta \dot{u}_k) d\Omega - \int_{\partial\Omega_o} \sigma_k^o \delta \dot{u}_k d\partial\Omega = 0 \quad (3.7)$$

where  $\delta \dot{\epsilon}_{ij}$  and  $\delta \dot{u}_i$  are the virtual strain and virtual displacement rates. The viscoplastic constitutive equations are in rate form, and thus should be integrated with time, see Section 7.2.1.

In this chapter, the required theoretical fundamentals for describing the stress-strain relation for viscoplastic behaviour of materials are outlined. The detailed formulations for atmospheric ice are then given in Chapters 4, 5 and 7, where the material microstructure fundamentals are given only for hexagonal crystals, which is the case of ice monocrystal.

### 3.2 Stress and strain invariants

For porous materials, the constitutive laws are commonly presented by dividing the stress  $\sigma_{ij}$  and the strain  $\varepsilon_{ij}$  tensors into deviatoric and dilatation parts, equations (3.8) and (3.9), where hydrostatic pressure  $p$ , deviatoric stress  $s_{ij}$ , deviatoric strain  $e_{ij}$ , volumetric (dilatation) strain, and the von-Mises deviatoric strain are defined by

$$\sigma_{ij} = s_{ij} - p \delta_{ij}, \quad p = -\frac{1}{3} \sigma_{kk} \quad s_{ij} = \sigma_{ij} - \frac{1}{3} \sigma_{kk} \delta_{ij} \quad (3.8)$$

$$\varepsilon_{ij} = e_{ij} + \frac{1}{3} \varepsilon_{vol} \delta_{ij}, \quad \varepsilon_{vol} = \varepsilon_{kk} \quad e_{ij} = \varepsilon_{ij} - \frac{1}{3} \varepsilon_{kk} \delta_{ij} \quad (3.9)$$

Many of the constitutive models are commonly formulated in terms of stress invariants, in particular in terms of the first invariant ( $J_1$ ) of total stress, and the second ( $J_{2D}$ ) and third ( $J_{3D}$ ) invariants of deviatoric stress. The first invariant of stress tensor ( $J_1$ ) is sometimes represented by von-Mises equivalent stress “ $q$ ”, while the third invariant of deviatoric stress ( $J_{3D}$ ) is identified by “ $r$ ” in some other references, e.g. Ref. [1].

$$J_1 = \sigma_{kk} = -3p \quad (3.10)$$

$$J_{2D} = \frac{1}{2} s_{ij} s_{ij} \quad \text{or} \quad q = \left[ \frac{3}{2} s_{ij} s_{ij} \right]^{\frac{1}{2}} \quad (3.11)$$

$$J_{3D} = \det |s_{ij}| = \frac{1}{3} s_{ij} s_{jk} s_{ki} \quad \text{or} \quad r = \left[ \frac{9}{2} s_{ij} s_{jk} s_{ki} \right]^{\frac{1}{3}} \quad (3.12)$$

### 3.3 Elastic moduli of anisotropic polycrystalline material

Generally, a polycrystalline material consists of a number of grains, each with a different orientation. Each individual grain exhibits macroscopically anisotropic elastic behaviour that depends on the c-axis orientation within the hexagonal crystal. The effective macroscopic behaviour, however, depends on the fabric and the number of grains within the aggregate.

The constitutive properties are characterized by the effective Young's and shear moduli, as well as the effective Poisson's ratio for a sufficient large number of grains where the c-axes are randomly distributed in the material. In high-temperature deformation, the effective moduli of the polycrystalline aggregate are normally determined from the corresponding monocrystal (single crystal) values using an averaging technique, or by applying a self-consistent method. The ice elastic moduli within the former method can be determined from the corresponding monocrystal values using an averaging technique. First, the elastic constants of monocrystal in any arbitrary direction should be determined in a spherical coordinate system. The upper and lower bounds are then calculated by using the Voigt (1910) and Reuss (1929) assumptions. Finally, the averaged values can be determined from the implementation of Hill's (1952) averaging technique.

Hooke's law of elasticity relates the strain field to the corresponding stress applied to the monocrystal. The matrix equation (3.13) or (3.14) represents this law in the principal coordinates of hexagonal monocrystal in engineering format, where the c-axis coincides with the 3-axis of principal coordinates. The superscript e refers to "elastic", while the hat symbol (^) denotes the "principal" monocrystal values, respectively.

$$\{\hat{\varepsilon}^e\} = [\hat{S}] \{\hat{\sigma}\} \quad \text{or} \quad \{\hat{\sigma}\} = [\hat{C}] \{\hat{\varepsilon}^e\} \quad (3.13)$$

$$\begin{bmatrix} \hat{\varepsilon}_{11}^e \\ \hat{\varepsilon}_{22}^e \\ \hat{\varepsilon}_{33}^e \\ \hat{\gamma}_{23}^e \\ \hat{\gamma}_{13}^e \\ \hat{\gamma}_{12}^e \end{bmatrix} = \begin{bmatrix} \hat{S}_{11} & \hat{S}_{12} & \hat{S}_{13} & 0 & 0 & 0 \\ \hat{S}_{12} & \hat{S}_{11} & \hat{S}_{13} & 0 & 0 & 0 \\ \hat{S}_{13} & \hat{S}_{13} & \hat{S}_{33} & 0 & 0 & 0 \\ 0 & 0 & 0 & \hat{S}_{44} & 0 & 0 \\ 0 & 0 & 0 & 0 & \hat{S}_{44} & 0 \\ 0 & 0 & 0 & 0 & 0 & 2(\hat{S}_{11} - \hat{S}_{12}) \end{bmatrix} \begin{bmatrix} \hat{\sigma}_{11} \\ \hat{\sigma}_{22} \\ \hat{\sigma}_{33} \\ \hat{\sigma}_{23} \\ \hat{\sigma}_{13} \\ \hat{\sigma}_{12} \end{bmatrix} \quad (3.14)$$

where  $\hat{S}_{ij}$  are the principal elastic compliance components of a monocrystal of material.

### 3.3.1 Elastic constants of hexagonal monocrystals in an arbitrary direction

The monocrystal elastic constants at a given orientation  $(\theta, \varphi)$  can be determined by two consecutive transformations of the respective stiffness  $[\hat{C}]$  and compliance matrices  $[\hat{S}]$  in the principal directions of the crystal, Fig. 3.2.

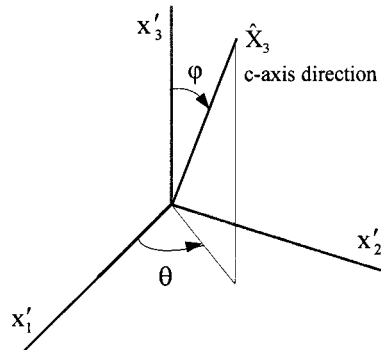


Fig. 3.2: Monocrystal principal and rotated coordinate systems.

The state of stress and strain in the rotated coordinates  $(x')$  can be determined from the corresponding values of monocrystal principal coordinates  $(\hat{x})$  by

$$\sigma'_{ij} = Q_{ki} Q_{lj} \hat{\sigma}_{kl} \quad \Rightarrow \text{in Engineering notation} \Rightarrow \quad \{\sigma'\} = [L^\sigma]^T \{\hat{\sigma}\} \quad (3.15)$$

$$\varepsilon'_{ij} = Q_{ki} Q_{lj} \hat{\varepsilon}_{kl}^e \quad \Rightarrow \text{in Engineering notation} \Rightarrow \quad \{\varepsilon'\} = [L^\varepsilon]^T \{\hat{\varepsilon}^e\} \quad (3.16)$$

where the rotation matrix  $[Q]$ , the engineering stress and strain vectors  $\{\sigma'\}$  and  $\{\varepsilon'^e\}$ , and the transformation matrices  $[L^\sigma]$  and  $[L^\varepsilon]$  are given by the following definitions, see Appendix 1,

$$\{\sigma'\}^T = \{\sigma'_{11} \quad \sigma'_{22} \quad \sigma'_{33} \quad \sigma'_{23} \quad \sigma'_{13} \quad \sigma'_{12}\} \quad (3.17)$$

$$\{\varepsilon'^e\}^T = \{\varepsilon'^e_{11} \quad \varepsilon'^e_{22} \quad \varepsilon'^e_{33} \quad \gamma'^e_{23} \quad \gamma'^e_{13} \quad \gamma'^e_{12}\} \quad (3.18)$$

$$[Q] = \begin{bmatrix} \cos \varphi & 0 & -\sin \varphi \\ 0 & 1 & 0 \\ \sin \varphi & 0 & \cos \varphi \end{bmatrix} \begin{bmatrix} \cos \theta & \sin \theta & 0 \\ -\sin \theta & \cos \theta & 0 \\ 0 & 0 & 1 \end{bmatrix} = \begin{bmatrix} \cos \varphi \cos \theta & \cos \varphi \sin \theta & -\sin \varphi \\ -\sin \theta & \cos \theta & 0 \\ \sin \varphi \cos \theta & \sin \varphi \sin \theta & \cos \varphi \end{bmatrix} \quad (3.19)$$

$$[L^\sigma] = \begin{bmatrix} l_\varphi^2 \cdot l_\theta^2 & l_\varphi^2 \cdot (1-l_\theta^2) & 1-l_\varphi^2 & -\frac{1}{2} \sin 2\varphi \cdot \sin \theta & -\frac{1}{2} l_\theta \cdot \sin 2\varphi & \frac{1}{2} l_\varphi^2 \cdot \sin 2\theta \\ 1-l_\theta^2 & l_\theta^2 & 0 & 0 & 0 & -\frac{1}{2} \sin 2\theta \\ (1-l_\varphi^2) \cdot l_\theta^2 & (1-l_\varphi^2) \cdot (1-l_\theta^2) & l_\varphi^2 & \frac{1}{2} \sin 2\varphi \cdot \sin \theta & \frac{1}{2} l_\theta \cdot \sin 2\varphi & \frac{1}{2} \sin^2 \varphi \cdot \sin 2\theta \\ -\sin \varphi \cdot \sin 2\theta & \sin \varphi \cdot \sin 2\theta & 0 & l_\varphi \cdot l_\theta & -l_\varphi \cdot \sin \theta & \sin \varphi \cdot (2l_\theta^2 - 1) \\ \sin 2\varphi \cdot l_\theta^2 & \sin 2\varphi \cdot (1-l_\theta^2) & -\sin 2\varphi & \sin \theta \cdot (2l_\varphi^2 - 1) & l_\theta \cdot (2l_\varphi^2 - 1) & \frac{1}{2} \sin 2\varphi \cdot \sin 2\theta \\ -l_\varphi \cdot \sin 2\theta & l_\varphi \cdot \sin 2\theta & 0 & -l_\theta \cdot \sin \varphi & \sin \varphi \cdot \sin \theta & l_\varphi \cdot (2l_\theta^2 - 1) \end{bmatrix}$$

$$[L^\varepsilon] = \begin{bmatrix} l_\varphi^2 \cdot l_\theta^2 & l_\varphi^2 \cdot (1-l_\theta^2) & 1-l_\varphi^2 & -\sin 2\varphi \cdot \sin \theta & -l_\theta \cdot \sin 2\varphi & l_\varphi^2 \cdot \sin 2\theta \\ 1-l_\theta^2 & l_\theta^2 & 0 & 0 & 0 & -\sin 2\theta \\ (1-l_\varphi^2) \cdot l_\theta^2 & (1-l_\varphi^2) \cdot (1-l_\theta^2) & l_\varphi^2 & \sin 2\varphi \cdot \sin \theta & l_\theta \cdot \sin 2\varphi & \sin^2 \varphi \cdot \sin 2\theta \\ -\frac{1}{2} \sin \varphi \cdot \sin 2\theta & \frac{1}{2} \sin \varphi \cdot \sin 2\theta & 0 & l_\varphi \cdot l_\theta & -l_\varphi \cdot \sin \theta & \sin \varphi \cdot (2l_\theta^2 - 1) \\ \frac{1}{2} \sin 2\varphi \cdot l_\theta^2 & \frac{1}{2} \sin 2\varphi \cdot (1-l_\theta^2) & -\frac{1}{2} \sin 2\varphi & \sin \theta \cdot (2l_\varphi^2 - 1) & l_\theta \cdot (2l_\varphi^2 - 1) & \frac{1}{2} \sin 2\varphi \cdot \sin 2\theta \\ -\frac{1}{2} l_\varphi \cdot \sin 2\theta & \frac{1}{2} l_\varphi \cdot \sin 2\theta & 0 & -l_\theta \cdot \sin \varphi & \sin \varphi \cdot \sin \theta & l_\varphi \cdot (2l_\theta^2 - 1) \end{bmatrix}$$

in which  $l_\varphi = \cos \varphi$  and  $l_\theta = \cos \theta$  are the direction cosines. (3.20)

The elastic constants in the rotated coordinates  $[C']$  can be related to the corresponding values of the monocrystal principal constants  $[\hat{C}]$  by substituting Hooke's law of elasticity (3.13) into equations (3.15) and (3.16):

$$\{\sigma'\} = [L^\sigma]^T \{\hat{\sigma}\} = [L^\sigma]^T [\hat{C}] \{\hat{\varepsilon}^e\} = [L^\sigma]^T [\hat{C}] [L^\varepsilon]^{-T} \{\varepsilon'^e\} \quad (3.21)$$

$$\{\varepsilon'\} = [L^\varepsilon]^T \{\hat{\varepsilon}^e\} = [L^\varepsilon]^T [\hat{S}] \{\hat{\sigma}\} = [L^\varepsilon]^T [\hat{S}] [L^\sigma]^{-T} \{\sigma'\} \quad (3.22)$$

Thus, the matrix relations for elastic constants in rotated coordinates can be obtained as

$$[C'] = [L^\sigma]^T [\hat{C}] [L^\varepsilon]^{-T} \quad \text{and} \quad [S'] = [L^\varepsilon]^T [\hat{S}] [L^\sigma]^{-T} \quad (3.23)$$

### 3.3.2 Upper and lower bounds of polycrystal elastic constants

The polycrystalline material, then, can be considered as a homogeneous body with the average values of elastic constants. These effective constants of aggregate are normally determined by taking a spatial average of the corresponding value of all the crystals using a uniform probability density function  $F(\theta, \varphi)$ , Ref. [43]. This continuous and smooth function can be determined depending on the distributions of c-axis orientation within material that satisfies the normality condition  $\int_{\Omega} F(\theta, \varphi) d\Omega = 1$ .

An upper limit for elastic constants can be obtained by assuming that all the grains undergo the same uniform strain, (Voigt (1910) assumption):

$$\bar{C} = \int_{\Omega} C'(\theta, \varphi) \cdot F(\theta, \varphi) d\Omega \quad (3.24)$$

while the lower limit of elastic constants can be determined by assuming the uniform stress field for all the grains, (Reuss (1929) assumption):

$$\bar{S} = \int_{\Omega} S'(\theta, \varphi) \cdot F(\theta, \varphi) d\Omega \quad (3.25)$$

where the spatial integral is taken over the whole material volume ( $\Omega$ ) for all possible c-axis orientations and where the rotated elastic constants  $C'$  and  $S'$  can be taken from equations (3.23). The density function  $F(\theta, \varphi) = F$  corresponds to a uniform distribution of c-axes and can be obtained for an isotropic material from the normality condition as

$$\int_{\Omega} F(\theta, \varphi) d\Omega = 1 \quad \Rightarrow \quad \int_0^1 \int_0^{2\pi} \int_0^{\pi} F \cdot r^2 \sin \varphi \, d\varphi \, d\theta \, dr = 1 \quad \Rightarrow \quad F = \frac{3}{4\pi} \quad (3.26)$$

where the spherical coordinate system of this integration is shown in Fig. 3.3a, and the function is normalized with respect to the  $r$ -dimension without lack of generality.

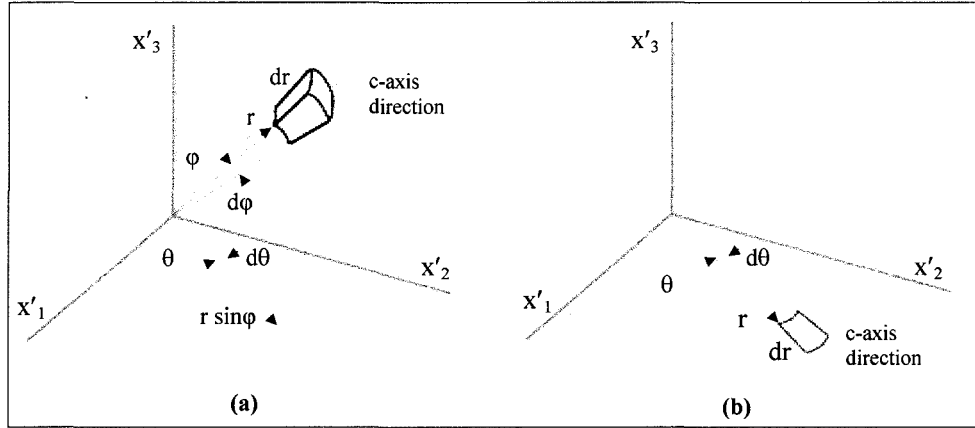


**Fig. 3.3:** Spherical and cylindrical coordinates for averaging integrals formulations for granular and columnar ice types, respectively.

In Appendix 1, two bounds of elastic constants are calculated for isotropic (granular) ice using equations (3.23) to (3.26). The results of those calculations are given by following relations, in which the subscripts “V” and “R” denote the Voigt (1910) and Reuss (1929) assumptions.

$$C_{11}^V = C_{22}^V = C_{33}^V = \frac{1}{15}(8\hat{C}_{11} + 4\hat{C}_{13} + 3\hat{C}_{33} + 8\hat{C}_{44})$$

$$C_{12}^V = C_{13}^V = C_{23}^V = \frac{1}{15}(\hat{C}_{11} + 5\hat{C}_{12} + 8\hat{C}_{13} + \hat{C}_{33} - 4\hat{C}_{44})$$

$$C_{44}^V = C_{55}^V = C_{66}^V = \frac{1}{30}(7\hat{C}_{11} - 5\hat{C}_{12} - 4\hat{C}_{13} + 2\hat{C}_{33} + 12\hat{C}_{44})$$

$$C_{14}^V = C_{15}^V = C_{16}^V = C_{24}^V = C_{25}^V = C_{26}^V = C_{34}^V = C_{35}^V = C_{36}^V = C_{45}^V = C_{46}^V = C_{56}^V = 0 \quad (3.27)$$

$$\begin{aligned}
S_{11}^R = S_{22}^R = S_{33}^R &= \frac{1}{15} (8\hat{S}_{11} + 4\hat{S}_{13} + 3\hat{S}_{33} + 2\hat{S}_{44}) \\
S_{12}^R = S_{13}^R = S_{23}^R &= \frac{1}{15} (\hat{S}_{11} + 5\hat{S}_{12} + 8\hat{S}_{13} + \hat{S}_{33} - \hat{S}_{44}) \\
S_{44}^R = S_{55}^R = S_{66}^R &= \frac{2}{15} (7\hat{S}_{11} - 5\hat{S}_{12} - 4\hat{S}_{13} + 2\hat{S}_{33} + 3\hat{S}_{44}) \\
S_{14}^R = S_{15}^R = S_{16}^R = S_{24}^R = S_{25}^R = S_{26}^R = S_{34}^R = S_{35}^R = S_{36}^R = S_{45}^R = S_{46}^R = S_{56}^R &= 0
\end{aligned} \tag{3.28}$$

For a transversely isotropic material, on the other hand, the density function corresponding to a uniform horizontal distribution of c-axis orientation can be obtained for a cylindrical sample of material with the unit length and radius, see Fig. 3.3b, as

$$\int_{\Omega} F(\theta) d\Omega = 1 \quad \Rightarrow \quad \int_0^1 \int_0^{2\pi} F \cdot r d\theta dr = 1 \quad \Rightarrow \quad F = \frac{1}{\pi} \tag{3.29}$$

The elastic constants of a monocrystal in arbitrary direction, for a transversely isotropic polycrystal, are determined from (3.19) to (3.23) with  $\varphi = 0$ , where c-axes are in the vertical direction (similar to S1 ice), and with  $\varphi = \pi/2$  for the horizontal c-axis orientation (similar to S2 and S3 ice). The upper and lower elastic constants are, then, calculated from equations (3.23) to (3.25) and (3.29), using another Maple code that is a particular case of the program presented in Appendix 1, which leads to equations (3.30) and (3.31) for uniform horizontal c-axis distribution (S2 ice). The relations for S3 ice are functions of the mean c-axis and scatter angle, which are omitted here, see Ref. [43].

The density function yields the equation (3.32) for the general orthotropic material (S3 ice), in which the c-axes are randomly oriented horizontally around  $\theta_0$  within the angle  $\Delta\theta_0$ . The bounds of elastic constants are given in Ref. [43] for this type of material.

$$\begin{aligned}
C_{11}^V = C_{22}^V &= \frac{1}{8}(3\hat{C}_{11} + 2\hat{C}_{13} + 3\hat{C}_{33} + 4\hat{C}_{44}) & C_{33}^V &= \hat{C}_{11} \\
C_{12}^V &= \frac{1}{8}(\hat{C}_{11} + 6\hat{C}_{13} + \hat{C}_{33} - 4\hat{C}_{44}) & C_{13}^V = C_{23}^V &= \frac{1}{2}(\hat{C}_{12} + \hat{C}_{13}) \\
C_{44}^V = C_{55}^V &= \frac{1}{2}(\hat{C}_{44} + \hat{C}_{66}) & C_{66}^V &= \frac{1}{8}(\hat{C}_{11} - 2\hat{C}_{13} + \hat{C}_{33} + 4\hat{C}_{44}) \\
C_{14}^V = C_{15}^V = C_{16}^V = C_{24}^V = C_{25}^V = C_{26}^V = C_{34}^V = C_{35}^V = C_{36}^V = C_{45}^V = C_{46}^V = C_{56}^V &= 0 & & (3.30)
\end{aligned}$$

$$\begin{aligned}
S_{11}^R = S_{22}^R &= \frac{1}{8}(3\hat{S}_{11} + 2\hat{S}_{13} + 3\hat{S}_{33} + \hat{S}_{44}) & S_{33}^R &= \hat{S}_{11} \\
S_{12}^R &= \frac{1}{8}(\hat{S}_{11} + 6\hat{S}_{13} + \hat{S}_{33} - \hat{S}_{44}) & S_{13}^R = S_{23}^R &= \frac{1}{2}(\hat{S}_{12} + \hat{S}_{13}) \\
S_{44}^R = S_{55}^R &= \frac{1}{2}(\hat{S}_{44} + \hat{S}_{66}) & S_{66}^R &= \frac{1}{2}(\hat{S}_{11} - 2\hat{S}_{13} + \hat{S}_{33} + \hat{S}_{44}) \\
S_{14}^R = S_{15}^R = S_{16}^R = S_{24}^R = S_{25}^R = S_{26}^R = S_{34}^R = S_{35}^R = S_{36}^R = S_{45}^R = S_{46}^R = S_{56}^R &= 0 & & (3.31)
\end{aligned}$$

$$\int_0^1 \int_{\theta_0 - \Delta\theta_0/2}^{\theta_0 + \Delta\theta_0/2} \mathbf{F} \cdot \mathbf{r} \, d\theta \, dr = 1 \quad \Rightarrow \quad \mathbf{F} = \frac{2}{\Delta\theta_0} \quad (3.32)$$

### 3.3.3 Hill's averaging technique and polycrystal elastic moduli

Hill (1952) proposed to take an algebraic average of the values of the Voigt (1910) and Reuss (1929) assumptions to obtain the elastic constants of polycrystalline material. The effective Young's and shears moduli, and Poisson's ratio in principal directions, then, can be calculated from the averaged elastic constants using relations (3.33) and (3.34), in which the averaged elastic compliance and stiffness constants can be taken from equations (3.28) and the inverse of the matrix given by equations (3.27) for isotropic polycrystals. For transversely isotropic polycrystals, on the other hand, the equations (3.30) and (3.31) can be used, respectively.

- Isotropic material, Ref. [2]:

$$E = \frac{1}{\bar{S}_{11}} = \frac{1}{\bar{S}_{22}} = \frac{1}{\bar{S}_{33}} \quad G = \frac{1}{\bar{S}_{44}} = \frac{1}{\bar{S}_{55}} = \frac{1}{\bar{S}_{66}} \quad \nu = \frac{E}{2G} - 1 \quad (3.33)$$

- Transversely isotropic material, Ref. [2]:

$$\begin{aligned} E_t &= \frac{1}{\bar{S}_{33}} & E_p &= \frac{1}{\bar{S}_{11}} \\ G_t &= \frac{1}{\bar{S}_{44}} & G_p &= \frac{1}{2(\bar{S}_{11} - \bar{S}_{12})} \\ \nu_p &= -\frac{\bar{S}_{12}}{\bar{S}_{11}} & \nu_{\varphi} &= -\frac{\bar{S}_{13}}{\bar{S}_{33}} & \nu_{pt} &= -\frac{\bar{S}_{13}}{\bar{S}_{11}} \end{aligned} \quad (3.34)$$

In equations (3.34), the subscripts “t” and “p” stand for “transverse” and “in-plane” values, respectively. Thus,  $E_t$  denotes the transverse Young’s modulus, and  $E_p$ , the corresponding value to the other coordinates lying in the plane of isotropy. In addition,  $\nu_p$  denotes Poisson’s ratio in isotropic plane, while  $\nu_{\varphi}$  has the physical interpretation of Poisson’s ratio and characterizes the strain in the plane of isotropy that results from the transverse stress normal to it. Similar formulations can also be derived for the general orthotropic materials like S3 ice as follows, Ref. [2].

$$\begin{aligned} E_{11} &= \frac{1}{\bar{S}_{11}} & E_{22} &= \frac{1}{\bar{S}_{22}} & E_{33} &= \frac{1}{\bar{S}_{33}} \\ G_{23} &= \frac{1}{\bar{S}_{44}} & G_{13} &= \frac{1}{\bar{S}_{55}} & G_{12} &= \frac{1}{\bar{S}_{66}} \\ \nu_{23} &= -\frac{\bar{S}_{23}}{\bar{S}_{22}} & \nu_{13} &= -\frac{\bar{S}_{13}}{\bar{S}_{11}} & \nu_{12} &= -\frac{\bar{S}_{12}}{\bar{S}_{11}} \\ \nu_{32} &= -\frac{\bar{S}_{23}}{\bar{S}_{33}} & \nu_{31} &= -\frac{\bar{S}_{13}}{\bar{S}_{33}} & \nu_{21} &= -\frac{\bar{S}_{12}}{\bar{S}_{22}} \end{aligned} \quad (3.35)$$

### 3.4 Viscoelastic model for atmospheric ice

An expression for short-term viscoelastic (delayed elastic) strain  $d\epsilon^{ve}$  under constant stress was proposed by Sinha (1978b) for freshwater ice; see Section 2.4.2 for more details. The model ensures that no volume change is induced by grain boundary sliding for freshwater ice. For the case of porous ice, however, the model can be adjusted to consider the effects of volume change and porosity in the formulations by replacing the deviatoric elastic strain by the effective poroelastic strain  $\epsilon_{ij}^e$ , see Section 4.3, that results in

$$d\epsilon_{ij}^{ve} = \frac{(1 + d\lambda^{ve}) C_1}{d_g} \left\{ 1 - \exp[-(a_T dt)^b] \right\} (\epsilon_{ij}^e) \quad (3.36)$$

The structural-change function due to plastic deformation is defined and formulated in Section 2.4.2. The material parameters are determined through a series of uniaxial creep tests at  $-10^\circ\text{C}$ , and the temperature dependence of viscoelastic deformation, on the other hand, is considered into the model by means of the shift function. The tabulated material parameters and the definition of shift function are given in Section 2.4.2.

In plasticity calculation, on the other hand, it is required to define a viscoelastic stiffness matrix. For such viscoelastic deformation at natural hydrostatic pressures, the stress tensor can be related to the elastic strain tensor by using the following formulation, which is obtained after substituting equation (3.36) in Hooke's law.

$$d\sigma_{ij} = C_{ijkl} d\epsilon_{kl}^e = C_{ijkl}^{ve} d\epsilon_{kl} = C_{ijkl}^{ve} (d\epsilon_{kl}^e + d\epsilon_{kl}^{ve}) \quad (3.37)$$

in which the viscoelastic stiffness matrix can be determined by

$$C_{ijkl}^{ve} = \frac{C_{ijkl}}{1 + \frac{(1 + d\lambda^{ve}) C_1}{d_g} \left\{ 1 - \exp[-(a_T dt)^b] \right\}} \quad (3.38)$$

### 3.5 Plasticity model for porous materials

The basic assumption of elastic-plastic models is that the deformation can be divided into elastic and inelastic parts. When the strains are considered infinitesimal, a consistent approximation is commonly used by additive strain-rate decomposition. In the common plasticity models, three ingredients determine the state of a plastic deformation. They are: (a) a yield function  $f$  that defines the limit to the region of purely elastic response, (b) a flow rule that defines the plastic strain, and finally (c) a set of evolution equations (or hardening laws) for the hardening parameters.

#### 3.5.1 Yield function

The yield function is an equation that sets a limit on the stress that can be supported by the material while it deforms elastically. Once the yield condition is reached the material can respond in an inelastic manner under further deformation. In many cases, the yield condition can be described as a surface in a “stress space”, whose coordinate axes represent components of stress; in stress space each point corresponds to a possible state of stress at a physical point in the material. Such a graphical representation of a yield condition is called a yield surface. In porous materials, the yield behaviour is commonly modeled with several independent plastic yield systems  $f_x$ , which can be written in a general form by, Ref. [7],

$$f_x(\boldsymbol{\sigma}, T, \kappa_\alpha^x) = 0 \quad (3.39)$$

in which  $T$  denotes the temperature, and  $\kappa_\alpha^x$ ,  $\alpha = 1, 2, \dots, n$  denotes a set of internal-state variables for each yield system. The subscripts “ $\alpha$ ” indicates that there may be several internal variables describing the inelastic response of the real materials. For the perfect plasticity model, the yield surface acts as the failure surface with no hardening parameters.

The yield function defines the purely elastic limit by  $f_x < 0$  in the  $x^{\text{th}}$  plastic system. The state of stress causes the yield function to have a positive value ( $f_x > 0$ ) for the rate-dependent plasticity models, while it is constrained to its zero value ( $f_x = 0$ ) during a rate-independent inelastic flow. For ice, like any other porous materials, the plastic response is neither necessarily rate-independent nor incompressible. Hence, the plastic volumetric strain and then the yield functions depend on the pressure stress. In this work, however, a quasi rate-independent plasticity model is presented for atmospheric ice in such a way that the yield functions are considered to be constrained to their zero value ( $f_x = 0$ ) during the inelastic flow, while the rate-dependency of material parameters are considered in the plasticity model.

The proposed cap-model plasticity of this work has three yield surfaces, a fixed-shear envelope, together with a movable cap, and a tension cutoff. The material on the shear-yield surfaces is assumed to follow the perfect plasticity model. But, one hardening parameter is considered for the cap-yield mode and tension cutoff, see Chapter 5.

### 3.5.2 Flow rule

The flow rule is the relation between the plastic strain increment and the applied stress that is often written in a potential form as in equation (3.40). In this equation,  $g_x$  denotes the potential function,  $\lambda_x^p$ , the plastic consistency parameter of the yield surface  $f_x$ , and  $N$ , the total number of plastic flow systems, Ref. [7].

$$d\varepsilon_{ij}^p = \sum_{x=1}^N d\lambda_x^p \frac{\partial g_x}{\partial \sigma_{ij}} \quad (3.40)$$

For some of the plasticity models, the direction of flow is the same as the direction of the outward normal to the yield surface. These models are called associated flow plasticity models, for which the potential function  $g_x$  can be replaced by yield function  $f_x$  from equation (3.41). In this equation,  $c_x$  is a scalar determined for each yield surface  $f_x$ , where the repeated index “x” on the right-hand side of the equation does not have a summation meaning, Ref. [7].

$$\frac{\partial g_x}{\partial \sigma_{ij}} = c_x \frac{\partial f_x}{\partial \sigma_{ij}} \quad (3.41)$$

### 3.5.3 Hardening rule

The final ingredient in plasticity models is a set of evolution equations through which the evolution of the hardening parameters takes place. These equations are normally written in rate form as, Ref. [7],

$$dH_{x,\alpha} = d\lambda_x^p h_\alpha^x(\boldsymbol{\sigma}, T, \kappa_\beta^x) \quad (3.42)$$

where  $H_\alpha^x$  and  $h_\alpha^x$  are the hardening parameters and the hardening functions for the  $x^{\text{th}}$  plastic system (related to the yield surface  $f_x$ ) that should be written in rate form. Equations (3.40) to (3.42) define the general structure of the plasticity models, which are written in rate form and must be integrated, see Chapter 5.

### 3.5.4 Cap-model plasticity for porous materials

The plasticity of porous materials is quite complex, involving pressure-sensitive yielding, difference in tensile and compressive strengths, the Bauschinger effect, and porosity dependency. To capture these behaviours, the use of the non-linear plasticity approach embodied in the cap-model is proposed in this work. This plasticity approach was first introduced by Drucker and Prager (1952) based on the theory of plasticity and has been used primarily for geological materials such as soils, rocks and concrete, Ref. [15]. However, it is also capable of representing many other types of materials such as composite materials or in this particular case the porous atmospheric ice.

The yield surface in the cap-model has a moving elliptical cap to include the pressure-dependent yield by allowing the control of dilatancy by means of a hardening cap, Fig. 3.4. As shown in the figure, the yield surface of this model is composed of a fixed shear-yield curve ( $f_s = 0$ ) together with a movable cap ( $f_c = 0$ ) that intersects the hydrostatic loading line, whose position is a function of plastic volumetric strain. The cap intersects the shear-yield curve in a non-smooth manner. The tension failure surface ( $f_t = 0$ ) represents the limit stress state beyond which the fracture takes place, Ref. [7].

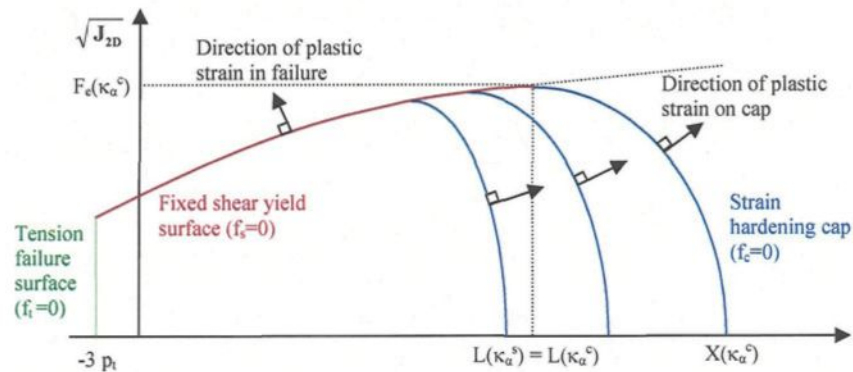


Fig. 3.4: Shear- and cap-yield surfaces and tension cutoff in the cap-model plasticity.

The coordinates in the yield surface of the cap-model, Fig. 3.4, represent the two invariants of the stress tensor at any material point. The abscissa is the first invariant of the stress tensor ( $J_1$ ), which is three times the hydrostatic pressure  $p$ . The ordinate, on the other hand, is the “shear stress” or more precisely the second invariant of the deviatoric stress tensor, which is related to von-Mises equivalent stress ( $q$ ) by  $\sqrt{J_{2D}} = q/\sqrt{3}$ .

In Fig. 3.4, the stress is represented by a point, which can never lie outside the shear-yield surface when the material undergoes an ideal plastic deformation. In this case, three different types of behaviour are possible. The *elastic deformation* arises when the stress point lies within the yield surface. The *shear failure* occurs when the stress point lies on the fixed-shear envelope or tension cutoff, which can be generalized to introduce isotropic and kinematic hardening into the model when the need arises. Finally, *cap mode of behaviour* happens when the stress point lies on the moving caps and pushes it outward.

The cap does not move during purely elastic deformation. However, the behaviour of the cap depends on the resulting plastic volumetric strain when the stress point lies on the failure envelope. In this case, the cap can move toward the stress point and must stop when the cap reaches the point. The fixed-yield surface ( $f_s = 0$ ) is defined by an exponential function as in equation (3.43). In reality, it is derived from two different Drucker–Prager yield surfaces, Ref. [7], as

$$f_s = \sqrt{J_{2D}} - F_e(J_1) = 0 \quad \text{for} \quad -3p_t \leq -J_1 \leq L(\kappa_\alpha^s) \quad (3.43)$$

where

$$F_e(J_1) = -\theta J_1 - \gamma e^{\beta J_1} + \alpha \quad (3.44)$$

in which  $\alpha$ ,  $\beta$ ,  $\gamma$  and  $\theta$  are the parameters of the fixed-yield surface  $f_s$ , which control the deviatoric stress limit. In equation (3.43),  $\kappa_\alpha^s$  represents a number of internal variables for the shear yielding mechanism.

The cap-yield surface ( $f_c = 0$ ) is an elliptical function, equation (3.45), in which  $R$  denotes the ratio of two elliptical cap's diameters. While, the function ( $f_t = 0$ ) indicates the tension cutoff zone, with  $-p_t$  denoting the material's tension limit, equation (3.46). It is assumed that the material has no significant plastic deformation in tension and goes directly from the elastic deformation to failure.

$$f_c = J_{2D}^2 - \frac{1}{R^2} [J_1 + L(\kappa_\alpha^c)]^2 - [F_c(\kappa_\alpha^c)]^2 = 0 \quad \text{for} \quad L(\kappa_\alpha^c) \leq -J_1 \leq X(\kappa_\alpha^c) \quad (3.45)$$

$$f_t = -3p_t + J_1 = 0 \quad (\text{Tension cutoff}) \quad (3.46)$$

In an associated flow rule, equation (3.47), the components of plastic strain rate form a "vector" normal to the yield surfaces in stress space. The use of the associated flow rule has often been questioned on the basis of experimental data, for which the use of a more complicated non-associative flow rule should be justified, Ref. [7].

$$\dot{\epsilon}_{ij}^p = \sum_{x=s,c,t} \dot{\lambda}_x^p \frac{\partial f_x(\boldsymbol{\sigma}, \kappa_\alpha^x)}{\partial \sigma_{ij}} \quad (3.47)$$

In this equation,  $\lambda_x^p$  denotes the plastic consistency parameter associated with the yield surface  $f_x$ . For this type of associated flow rule, the plastic strain is directed upward and leftward when the stress point lies on the failure envelope. In this case, therefore, the plastic strain can be decomposed into an irreversible deviatoric component together with a volumetric component during failure. The movement of the cap is related to the plastic

volumetric strain through the use of a hardening rule, equation (3.48). This is modeled through the evolution of the hardening parameters, which relates  $X(\kappa_\alpha^c)$  to the internal variables  $\kappa_\alpha^c$  by, Ref. [7],

$$X(\kappa_\alpha^c) = \frac{-1}{D} \ln \left( 1 - \frac{\varepsilon_{vol}^p}{W} \right) + X_0 \quad (3.48)$$

where  $D$  and  $W$  denotes the material parameters, and  $X_0$  the initial cap position. Both plastic hardening and softening modulus are zero for tension and shear envelopes  $f_t$  and  $f_s$ .

### 3.6 Conclusions

At natural temperatures, atmospheric ice undergoes a typical deformation like some other materials at high temperatures, in which the creep behaviour is dominant. In this case, the total strain rate induced in the material can be decomposed into four distinct components, a recoverable elastic part, a viscoelastic part, a plastic flow part, and a crack activity strain rate. The required theoretical backgrounds for describing the stress-strain relation for a non-cracking model were outlined in this chapter. This includes the anisotropy in elastic moduli of hexagonal monocrystals, the upper and lower bounds for elastic moduli of granular and columnar hexagonal polycrystalline materials, a brief review of Sinha's (1978b) viscoelastic model, and finally, the fundamentals of cap-model plasticity for porous materials. Those are the general requirements for the detailed formulations presented in Chapters 4, 5 and 7.

## CHAPTER 4

### POROELASTICITY OF ATMOSPHERIC ICE

#### 4.1 Introduction

The elastic compliance and stiffness constants of ice monocrystal were determined by Dantl (1969) and Gammon *et al.* (1983) as outlined in Section 2.4.1. Those data were used by Sinha (1989) to present some practical formulations for temperature dependency of different types of granular and columnar freshwater bubble-free polycrystalline ice. There were, however, some discrepancies in Sinha's formulations, particularly in the formulations for Poisson's ratio. A few years later, Nanthikesan *et al.* (1994) presented their elastic formulations to overcome this discrepancy. Following that work, a complete set of practical elastic formulations for granular and various types of bubble-free columnar ice (S1, S2, and S3) are developed in this study by using three computer codes in Maple Mathematical Program. This can be assumed as one of the contributions of this chapter, while the effects of temperature, ice types, and rotation angle are also investigated. The monocrystal (single crystal) data measured by Gammon *et al.* (1983) are used and the Hill's (1952) averaging technique is applied.

The influence of ice porosity is considered in the elastic formulations of freshwater ice by considering two extreme situations, namely the drained and undrained cases adopted

from geological poroelasticity models. This is another contribution of this chapter to the ice mechanics field. Those models are developed to be more consistent with atmospheric ice poroelastic behaviour, in which the liquid phase is considered but the interactions of solid and liquid phases are ignored. The upper and lower bounds for poroelastic behaviours are obtained using procedures similar to the Voigt (1910) and the Reuss (1929) averaging techniques, respectively. The new terms “Voigt analogy” and “Reuss analogy” are adopted for those poroelastic procedures to show the similarities with Voigt (1910) and Reuss (1929) averaging techniques, which were used for determining the upper and lower limits of polycrystalline freshwater ice elastic moduli. The applicability of the poroelasticity models, drained or undrained, granular or columnar, can be determined from the microstructure observations of atmospheric ice deposits on power lines, see Chapter 6.

#### **4.2 Elastic moduli of bubble-free polycrystalline ice**

The elastic moduli of bubble-free polycrystalline ice are determined here from the monocrystal data of Gammon *et al.* (1983), see section 2.4.1. The upper and lower limits of elastic moduli are calculated using Voigt (1910) and Reuss (1929) averaging techniques. Finally, the Hill’s (1952) averaging technique is implemented to extract the practical formulation of elastic moduli for polycrystalline bubble-free ice, see Section 3.3.3.

Three computer codes are developed in Maple mathematical language to formulate the temperature dependence of elastic moduli for the various types of granular and columnar ice, see Appendix 1. The resulting practical formulations are presented in this section for two major types of polycrystalline ice. They are the granular (isotropic) ice, and columnar fabrics (transversely isotropic) that can be found in nature as S1, S2, and S3 ice.

#### 4.2.1 Elastic moduli of ice monocrystal

The principal values of ice monocrystal elastic moduli are determined by replacing the principal monocrystal constants in equations (3.34). The temperature dependency of elastic moduli resulting from the monocrystal data of Gammon *et al.* (1983) and Dantl (1969) is compared in Fig. 4.1, where in this case, the subscripts “p” and “c” denote the elastic moduli in basal plane and c-axis directions, respectively, see Section 2.4.1 and Section 3.3.3 for more details.

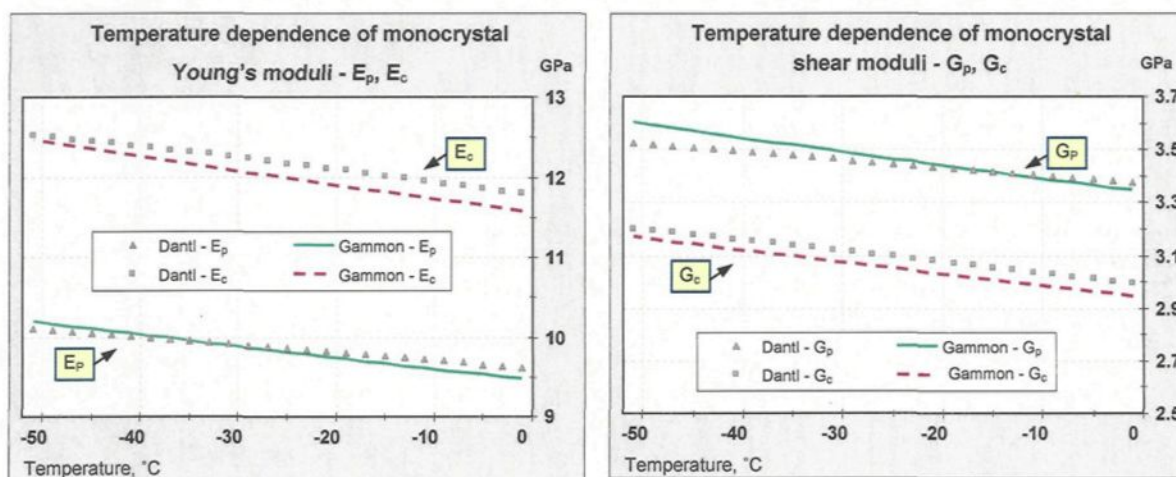


Fig. 4.1: Temperature dependence of the Young's and shear moduli of ice monocrystal  $I_h$  in various directions and planes.

The maximum discrepancy of 19.1% is calculated for the elastic moduli of ice monocrystals by using these two models. This maximum value is related to the transverse Poisson's ratio  $\hat{\nu}_{cp}$ , which characterizes the induced strain in basal plane resulting from the applied stress in the c-axis direction. Almost everywhere in those curves, Gammon's measurement predicts lower elastic moduli, but higher rates of variation for the Young and shear moduli. The ice monocrystal is significantly stiffer in the c-axis direction, but it has

lower resistance to transverse shear deformation in that direction as well. The Gammon's data predicts a maximum variation of 7.4% for the Young's and shear moduli as the temperature decreases from 0 to  $-50^{\circ}\text{C}$ , but temperature-independent formulations for Poisson's ratios. The value of in-plane Poisson's ratio is  $\hat{\nu}_p = 0.415$ , which characterizes the monocrystal to be nearly incompressible in the basal plane. The transverse Poisson's ratios are calculated to be  $\hat{\nu}_{cp} = 0.274$  and  $\hat{\nu}_{pc} = 0.225$ .

#### 4.2.2 Practical elastic formulation for granular ice

The macroscopic effective elastic moduli of granular ice are calculated from Hill's averaged elastic compliances using equation (3.33). The upper and lower bounds of elastic constants were formulated using Voigt (1910) and Reuss (1929) assumptions in Section 3.2, equations (3.27) and (3.28), after taking the inverse of the Voigt elastic stiffness matrix. The temperature dependence of these elastic bounds for granular ice is determined by substituting the monocrystal values of Gammon *et al.* (1983) into those equations. This yields to equations (4.1) and (4.2), in which the non-zero components of elastic stiffness and compliance matrices are presented.

$$\begin{aligned}
 C_{11}^V &= C_{22}^V = C_{33}^V = 13.274 - 1.882 \times 10^{-2} \Theta \\
 C_{12}^V &= C_{13}^V = C_{23}^V = 6.415 - 9.097 \times 10^{-3} \Theta \\
 C_{44}^V &= C_{55}^V = C_{66}^V = 3.430 - 4.863 \times 10^{-3} \Theta
 \end{aligned} \tag{4.1}$$

$$\begin{aligned}
 S_{11}^R &= S_{22}^R = S_{33}^R = 1.126 \times 10^{-1} + 1.593 \times 10^{-4} \Theta \\
 S_{12}^R &= S_{13}^R = S_{23}^R = -3.712 \times 10^{-2} - 5.263 \times 10^{-5} \Theta \\
 S_{44}^R &= S_{55}^R = S_{66}^R = 2.993 \times 10^{-1} + 4.243 \times 10^{-4} \Theta
 \end{aligned} \tag{4.2}$$

The elastic moduli of granular ice, then, are obtained by inserting the monocrystal data (4.2) and the inverse of (4.1) into equations (3.33). The linear trends of temperature dependence of Young's and shear moduli, and Poisson's ratio for isotropic ice (granular) can be approximated by the following relations, where  $\Theta$  is the temperature in  $^{\circ}\text{C}$ .

$$\begin{aligned} E^{\text{iso}} &= 8.990 (1 - 1.471 \times 10^{-3} \Theta) \\ G^{\text{iso}} &= 3.386 (1 - 1.471 \times 10^{-3} \Theta) \\ \nu^{\text{iso}} &= 0.328 \end{aligned} \quad (4.3)$$

The results of these calculations are sketched in Fig. 4.2, where a comparison is also presented with respect to the Sinha model (1989). These results are in a good agreement with the data presented by Sunder (1994). Young's modulus increases by 7.4%, from 8.990 to 9.650 GPa, with a decrease in temperature in the range 0 to  $-50^{\circ}\text{C}$ . The shear modulus also increases by the same percentage, from 3.386 to 3.634 GPa, within the same range of temperature variation. There is a little temperature dependency in Poisson's ratio, as determined by Sinha (1989). However, Gammon's data indicates that Poisson's ratio is independent of temperature and equal to 0.328.

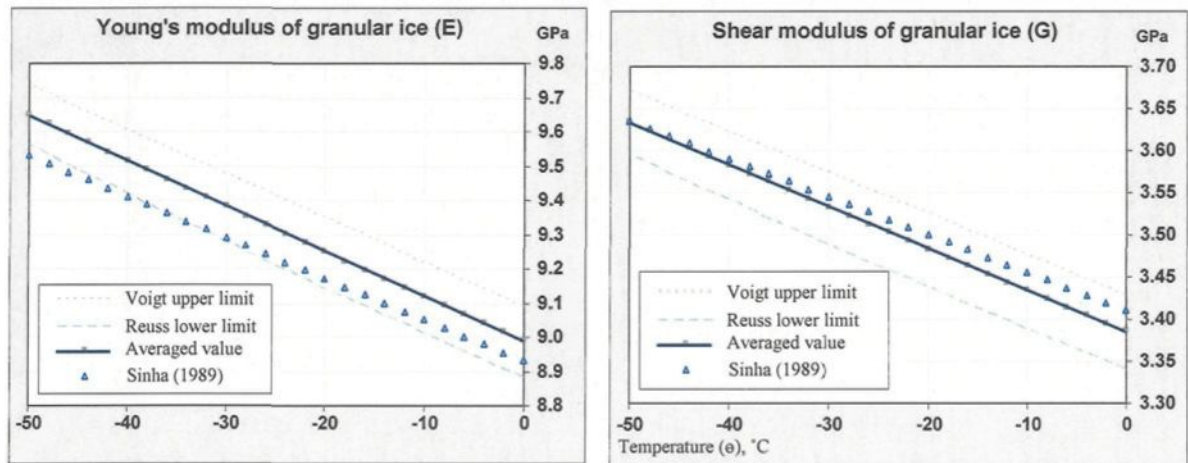


Fig. 4.2: Temperature dependence of Young's and shear moduli for isotropic (granular) ice.

### 4.2.3 Practical elastic formulation for columnar ice

The elastic moduli of columnar ice are determined following a similar procedure as for granular ice. In the microstructure of columnar ice S1, the preferred c-axis orientation is in the columnar direction, providing that this ice exhibits the elastic behaviour similar to that of ice monocrystal. The elastic moduli of this type of ice can be calculated by substituting the monocrystal data, section 2.4.1, into equation (3.34), which yields

$$\begin{aligned}
 E_p^{S1} &= 9.470 (1 - 1.471 \times 10^{-3} \Theta) & E_t^{S1} &= 11.578 (1 - 1.471 \times 10^{-3} \Theta) \\
 G_p^{S1} &= 3.346 (1 - 1.471 \times 10^{-3} \Theta) & G_t^{S1} &= 2.946 (1 - 1.471 \times 10^{-3} \Theta) \\
 \nu_p^{S1} &= 0.415 & \nu_{tp}^{S1} &= 0.274 & \nu_{pt}^{S1} &= 0.224
 \end{aligned} \tag{4.4}$$

where  $\Theta$  denotes the temperature in  $^{\circ}\text{C}$ , and subscripts “t” and “p” stands for “transverse”, or in column direction, and “in-plane” of isotropy, respectively. This type of ice is nearly incompressible in the plane of isotropy, however, the Sinha (1989) model predicts overestimated incompressibility for the material (0.51). Young’s and shear moduli increase by 7.4% as the temperature decreases in the range of 0 to  $-50^{\circ}\text{C}$ , see Fig. 4.3.

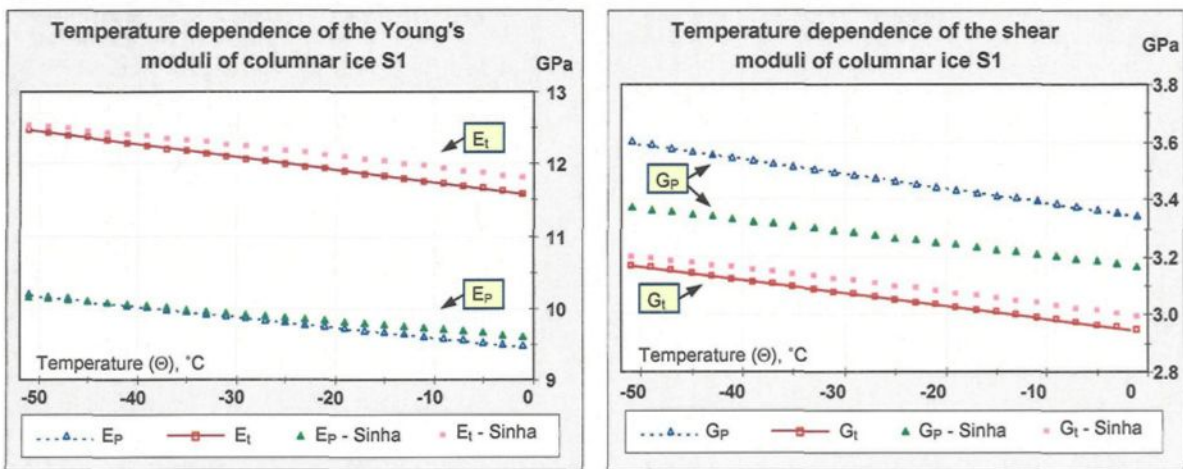
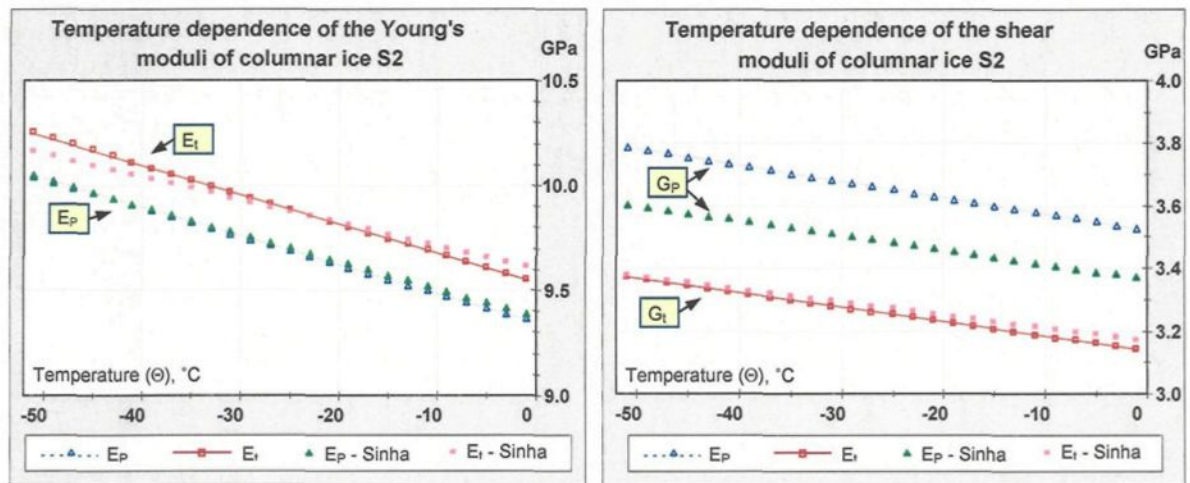


Fig. 4.3: Temperature dependence of Young’s and shear moduli for S1 columnar ice in various directions and planes.

The preferred c-axes orientation in S2 ice, however, is oriented randomly in the plane perpendicular to the columns. The upper and lower bounds of elastic constants for this type of material were formulated in Section 3.3.2, equations (3.30) and (3.31), after taking the inverse of the Voigt elastic stiffness matrix. The temperature dependence of these elastic bounds is substituted from Gammon's monocrystal values, which yields

$$\begin{aligned}
 E_p^{S2} &= 9.363 (1 - 1.471 \times 10^{-3} \Theta) & E_t^{S2} &= 9.551 (1 - 1.471 \times 10^{-3} \Theta) \\
 G_p^{S2} &= 3.528 (1 - 1.471 \times 10^{-3} \Theta) & G_t^{S2} &= 3.140 (1 - 1.471 \times 10^{-3} \Theta) \\
 \nu_p^{S2} &= 0.327 & \nu_{tp}^{S2} &= 0.319 & \nu_{pt}^{S2} &= 0.312
 \end{aligned} \tag{4.5}$$

where  $\Theta$  denotes the temperature in  $^{\circ}\text{C}$ , and subscripts "t" and "p" stand for "transverse", or in column direction, and "in-plane" of isotropy, respectively. The Young's and shear moduli increase by 7.4% as the temperature decreases in the range 0 to  $-50^{\circ}\text{C}$ , see Fig. 4.4. But, there is again negligible temperature dependence for Poisson's ratios.



**Fig. 4.4:** Temperature dependence of Young's and shear moduli for S2 columnar ice in various directions and planes.

The c-axes orientation in S3 ice is oriented randomly within a scatter angle around the mean c-axis direction in the plane perpendicular to the columns. The upper and lower bounds of constants, as well as the elastic moduli of this type of material, then, depend on both the mean ( $\theta_0$ ) and scatter angle ( $\Delta\theta_0$ ) that can be obtained using equations (3.24) and (3.25) together with (3.32), which yields

$$\bar{C} = \frac{1}{\Delta\theta_0} \int_{\theta_0 - \Delta\theta_0/2}^{\theta_0 + \Delta\theta_0/2} C'(\theta, \varphi) \cdot r \, d\theta \, dr \quad (4.6)$$

$$\bar{S} = \frac{1}{\Delta\theta_0} \int_{\theta_0 - \Delta\theta_0/2}^{\theta_0 + \Delta\theta_0/2} S'(\theta, \varphi) \cdot r \, d\theta \, dr \quad (4.7)$$

The elastic constants  $C'(\theta, \varphi)$  and  $S'(\theta, \varphi)$  can be replaced from equations (3.23) and the temperature dependence of Gammon's monocrystal values. Another Maple code is developed for calculating the elastic moduli of S3 ice using equations (3.35). Fig. 4.5 shows the variation of elastic moduli versus the scatter angle when the mean c-axes are oriented in the  $x_1$ -direction. The curves corresponding to the other magnitudes of mean c-axis direction lie somewhere in between these two limiting cases, see next section. The magnitude of in-plane Young's modulus ( $E_{11}$ ) of S3 ice decreases by 19.2% with scatter angles varying from the largest value for the parallel c-axes ( $\Delta\theta_0 = 0^\circ$ ) to its least value equal to the corresponding value for S2 ice ( $\Delta\theta_0 = 180^\circ$ ), while the other in-plane modulus,  $E_{22}$  decreases by 7.5% to its minimum value around a scatter angle of 120 degrees. There is no significant variation for transverse Young's modulus  $E_{33}$ , which varies from 9.513 to 10.216 GPa as temperature decreases from 0 to  $-50^\circ\text{C}$ . The shear moduli  $G_{23}$  and  $G_{13}$ , on the other hand, vary in the narrower bands reversely by 6.3%, while shear modulus  $G_{12}$  reaches its maximum value at the scatter angle of 120 degrees (24.2%).

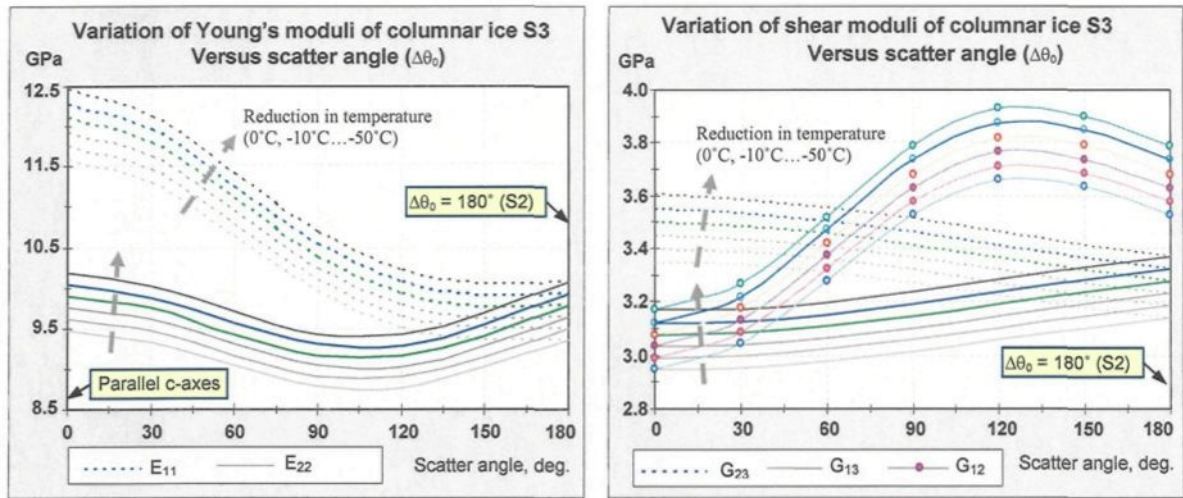


Fig. 4.5: Variation of Young's and shear moduli with scatter angle for S3 columnar ice, where the mean c-axis is in the  $x_1$ -direction.

It is evident that the normal rigidity of S3 ice varies between a maximum for parallel c-axes orientation to its minimum for S2 ice, while the maximum shear rigidity corresponds to S3 ice with a scatter angle of 120 degrees. The elastic moduli for S3 ice vary by 7.4% with the temperature in the range 0 to  $-50^\circ\text{C}$ , but there is no significant temperature dependence for Poisson's ratio that varies with scatter angle, as shown in Fig. 4.6.

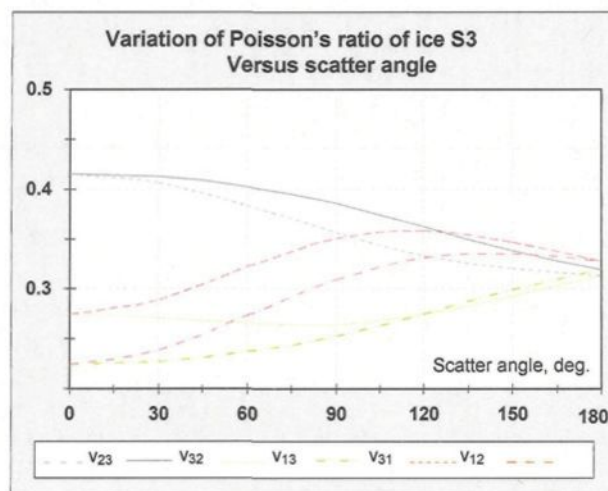


Fig. 4.6: Variation of Poisson's ratio with scatter angle for S3 columnar ice, where the mean c-axis is in the  $x_1$ -direction.

These ratios converge to a narrower band as the scatter angle increases to the final value equal to that of S2 ice. The maximum variation of 48.9% belongs to  $\nu_{21}$  as scatter angle varies from 0 to  $180^\circ$ , while the other variations were 24.8%, 23.3%, 3.7%, 42.0%, and 30.5% for  $\nu_{23}$ ,  $\nu_{32}$ ,  $\nu_{13}$ ,  $\nu_{31}$ , and  $\nu_{12}$ , respectively.

#### 4.2.4 Elastic anisotropy of columnar ice

The magnitude of anisotropy of elastic moduli for various types of columnar ice is discussed in this section. First, the influence of mean c-axes direction on elastic moduli of S3 ice is investigated, see Fig. 4.7.

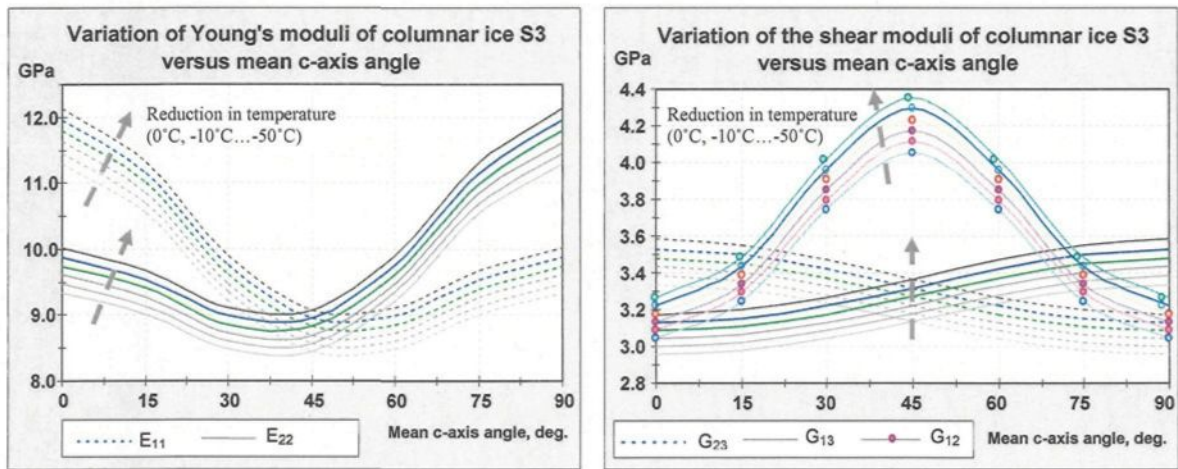
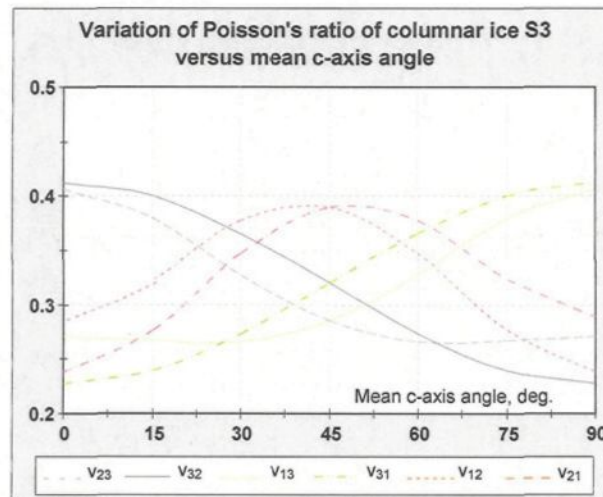


Fig. 4.7: Variation of Young's and shear moduli with mean c-axis angle for S3 ice, scatter angle  $\Delta\theta_0 = 30^\circ$ .

The magnitude of in-plane Young's modulus ( $E_{11}$ ) decreases by 25.2% to a minimum corresponding to the mean c-axis angle of  $45^\circ$  and then increases to an amount less than its initial value, while the other in-plane modulus,  $E_{22}$ , varies inversely. There is no significant variation for transverse Young's modulus  $E_{33}$ , which varies from 9.478 to 10.176 GPa as temperature decreases from 0 to  $-50^\circ\text{C}$ . The shears moduli  $G_{23}$  and  $G_{13}$ , on the other hand,

vary inversely in a narrower band by 11.5%, while shear modulus  $G_{12}$  reaches its maximum at the mean angle of  $45^\circ$  by a variation of 33.2%. Again, a temperature dependence of 7.4% is obtained for the moduli.

The variation of Poisson's ratio with mean c-axis angle is shown in Fig. 4.8. There is no significant temperature dependence for Poisson's ratio. The maximum variation of 63.1% was calculated for  $\nu_{12}$  and  $\nu_{21}$  as the mean c-axis angle varies from 0 to 90 degrees, while the other variations were 34.5% for  $\nu_{23}$  and  $\nu_{13}$ , and 44.8% for  $\nu_{32}$  and  $\nu_{31}$ .



**Fig. 4.8:** Variation of Poisson's ratio with mean c-axis angle for S3 columnar ice, scatter angle  $\Delta\theta_0 = 30^\circ$ .

Another comparison is made for elastic moduli of S3 ice, as a function of the mean c-axis direction when the scatter angle varies in the range 0 to 180 degrees. The results are compared at  $-10^\circ\text{C}$ , as shown in Fig. 4.9.

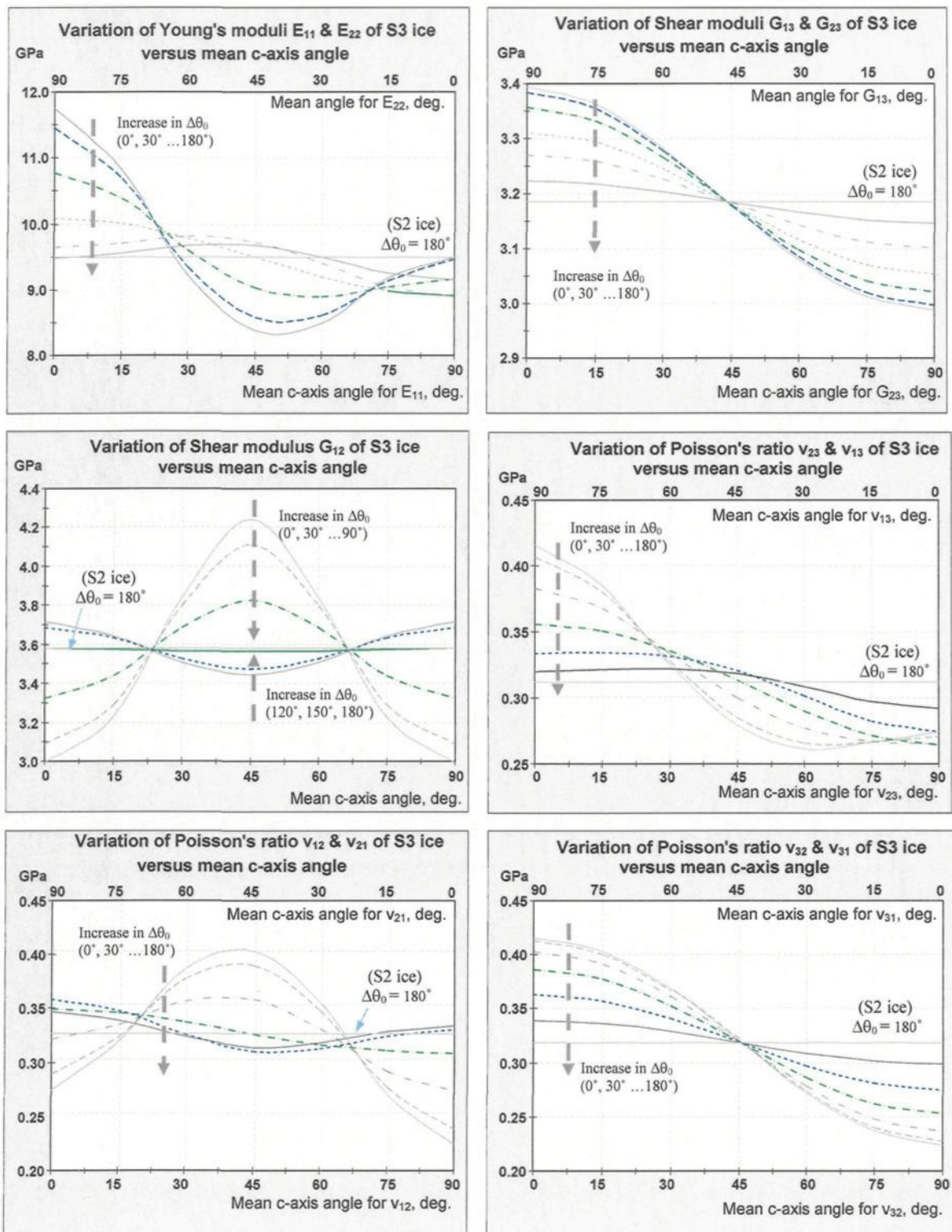


Fig. 4.9: Variation of Young's and shear moduli, and Poisson's ratio with mean c-axis angle for S3 columnar ice at  $-10^\circ\text{C}$ , where the scatter angle varies in the range 0 to 180 degrees.

For the parallel c-axes, the magnitude of in-plane Young's modulus ( $E_{11}$ ) shows a decrease of 28.6% with mean c-axis angle and then increases to the corresponding value for S2 ice; the mean c-axis angle at minimum point is varying from 45 to 90 degrees, while the scatter angle varies from zero to about 60°. For higher scatter angles, the trend of variation is different when the maximum points on the curves vary from zero to 45°. The other in-plane modulus,  $E_{22}$ , varies inversely, as shown in the same graph by reversing the horizontal axis, (see the axis for  $E_{22}$ ). There is no significant variation for the transverse Young's modulus  $E_{33}$ , which has an average value of 9.649 GPa. The maximum magnitude of in-plane anisotropy in Young's moduli ( $E_{11}-E_{22}$ ) is 18.2% for S3 ice with parallel c-axis direction (zero scatter-angle); however, it depends on the mean angle as well. The dependence to scatter angle is minimum for the mean angles of about 20° and 70°.

Shears moduli  $G_{23}$  and  $G_{13}$ , on the other hand, vary inversely with the mean c-axis direction from a maximum of about 3.390 GPa to 2.990 GPa (12.0% of variation), while shear modulus  $G_{12}$  reaches its maximum or minimum at the mean angle of 45°, with a maximum variation of 41.8%. The dependence of elastic moduli to mean c-axis orientation diminishes from these maximum values as the scatter angle increases, so that there is no such dependence for S2 ice. On the other hand, the shear moduli are independent from scatter angle when the mean c-axis direction is 45° for  $G_{23}$  and  $G_{13}$ , and about 20° and 70° for  $G_{12}$ .

Again, a similar shift of about 7.4% exists in the curves of elastic moduli when the temperature varies in the range of zero to -50°C, while Poisson's ratios vary in the mean c-axis direction and scatter angle almost independently of temperature. The maximum

variation of 79.4% was calculated for  $\nu_{12}$  and  $\nu_{21}$  as the mean c-axis angle varies from 0 to 90 degrees, while the other variations were 37.1% for  $\nu_{23}$  and  $\nu_{13}$ , and 46.0% for  $\nu_{32}$  and  $\nu_{31}$ . The Poisson's ratios are almost independent from the variation of scatter angle when the mean c-axis angle is about 30° for  $\nu_{23}$  and  $\nu_{13}$ , 20° and 70° for  $\nu_{12}$  and  $\nu_{21}$ , and 45° for  $\nu_{32}$  and  $\nu_{31}$ .

The magnitude of anisotropy of elastic moduli for various types of columnar ice is compared in a rotation around  $x_2$ -axis, normal to the columnar direction, Fig. 4.10. The curves are obtained at -10°C, however, the same 7.4% shift in elastic moduli can be assumed when the temperature varies in the range of 0°C down to -50°C. For nearly all the rotation angles, there are two extreme curves for the variation of elastic moduli. These are the curves obtained for S1 and S2 ice; all the other curves are laid down in between.

The maximum anisotropy of elastic moduli corresponds to S1 ice when the rotation angle varies in the full range from zero to 90 degrees. The maximum variations in elastic moduli are 29.2% for the  $E_{33}$  modulus of S1 ice ( $E_{11}$  modulus of S3 ice with parallel c-axes in  $x_1$ -direction), 12.0% for  $G_{12}$  and  $G_{23}$ , 41.8% for  $G_{13}$ , 46.0% for  $\nu_{21}$  and  $\nu_{23}$ , 37.1% for  $\nu_{32}$  and  $\nu_{12}$ , and 80.2% for  $\nu_{13}$  and  $\nu_{31}$ . The elastic moduli of S3 ice with parallel c-axes are conjugated with the corresponding moduli of S1 ice, e.g.  $E_{11}$  with  $E_{33}$ ,  $G_{12}$  with  $G_{23}$ , and so on. These conjugated moduli are denoted on Fig. 4.10 as "other moduli of S1 ice". The minimum anisotropy, on the other hand, corresponds to S2 ice with 9.6%, 12.4%, 14.5%, 4.6%, 9.8%, and 20.0% of variation in  $E_{11}$ ,  $G_{23}$  and  $G_{12}$ ,  $G_{13}$ ,  $\nu_{21}$  and  $\nu_{23}$ ,  $\nu_{32}$  and  $\nu_{12}$ , and  $\nu_{13}$  and  $\nu_{31}$ , respectively.

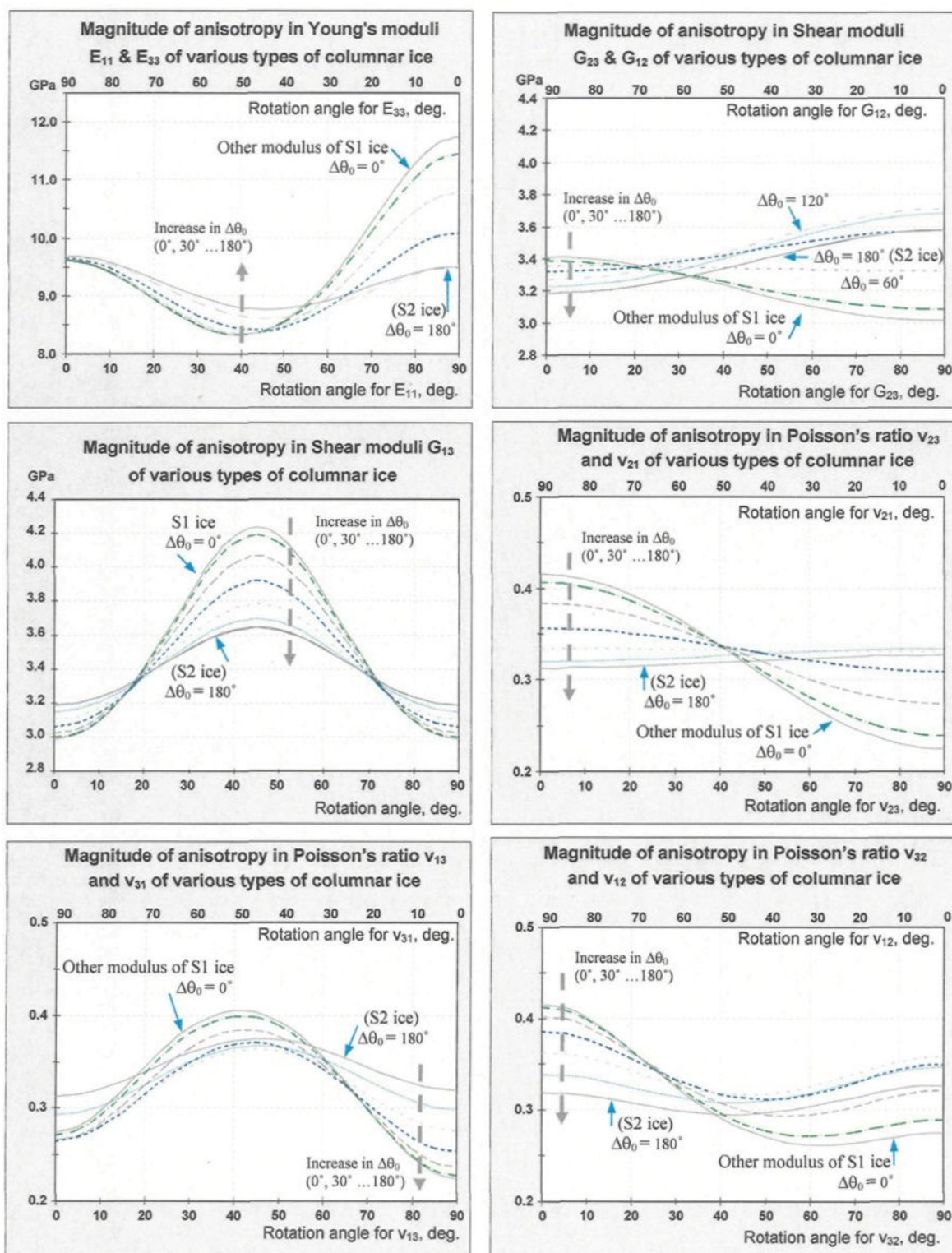


Fig. 4.10: Variation of Young's and shear moduli, and Poisson's ratio with rotation angle around the  $x_2$ -axis for various types of columnar ice at  $-10^\circ\text{C}$ .

The maximum magnitude of difference in shear moduli ( $G_{12}$ – $G_{13}$ ) occurs for the parallel c-axes orientations with the mean angle of  $45^\circ$  (33.4%), while 46.0% difference in Poisson's ratios occurs for the parallel c-axes orientated in the direction of mean c-axis. It is interesting to note that the dependence of elastic moduli of S3 ice to scatter angle are maximum in the direction of the mean c-axes (or normal to it) for most of the moduli except for  $G_{13}$ , which is maximum at rotation angle of  $45^\circ$ . This dependence is minimum or null in rotation angles of about  $45^\circ$ ;  $20^\circ$  and  $70^\circ$ ;  $30^\circ$ ; and  $60^\circ$  for Young's moduli,  $\nu_{21}$  and  $\nu_{23}$ , and  $\nu_{32}$  and  $\nu_{12}$ ;  $G_{13}$ ,  $\nu_{13}$  and  $\nu_{31}$ ;  $G_{23}$ ; and  $G_{12}$ , respectively.

### 4.3 Poroelasticity model for atmospheric ice

Atmospheric ice can be considered as a multiphase material comprised of a wetting liquid, voids (air-bubbles), and pure ice. Two extreme situations associated with the effects of fluid pressure in a poroelastic medium are considered, the drained and undrained cases. In the drained situation, negligible fluid pressure may cause the wetting fluid to move out from the volume element. In the undrained situation, on the other hand, the volume element is assumed to be sealed. In this case, pressure will build-up in the specimen under loading, but it cannot cause the fluid movement in the representative volume element. In both cases, it is assumed that the material is saturated by wetting fluid, the pores are connected, and the size of the representative volume element is large enough compared to the size of the largest pores, so that the porous material may be considered as homogeneous. The porosity ( $\phi$ ) is defined as the ratio of voids volume ( $\Omega_v$ ) to the total representative volume ( $\Omega$ ), while the void ratio ( $e$ ) can also be defined as the ratio of voids to solid volume ( $\Omega_s$ ), Ref. [1]:

$$\phi = \frac{d\Omega_v}{d\Omega}, \quad e = \frac{d\Omega_v}{d\Omega_s} \quad \text{where} \quad e = \frac{\phi}{1-\phi} \quad \text{or} \quad \phi = \frac{e}{1+e} \quad (4.8)$$

The drained, undrained and matrix elastic compliance tensors are denoted by  $S_{ijkl}^d$ ,  $S_{ijkl}^u$ , and  $S_{ijkl}^m$ . The effective compliance (or stiffness) tensor of poroelastic material can be related to its matrix values, using the similar Reuss (or Voigt) analogy. The averaged values are then calculated for the atmospheric ice poroelastic model in this work, using the results of these two assumptions. The drained situation nearly simulates the wet regime of ice accretion (glaze), while the undrained situation is closer to riming or dry conditions. In the transition region, the averaged values are applicable.

### 4.3.1 Application of Reuss analogy to porous material modeling

The porous medium modeling in this analogy uses a similar analogy with Reuss averaging assumption, where the total stress is decomposed into an effective stress in drained solid  $\sigma_{ij}^d$ , and the average pore pressure stress  $\sigma_{ij}^{pe}$  in the voids as

$$\sigma_{ij} = \sigma_{ij}^d + \phi \sigma_{ij}^{pe} \quad (4.9)$$

where the drained stress can be related to the matrix stress by  $\sigma_{ij}^d = (1 - \phi) \sigma_{ij}^m$ , and then the drained compliance tensor by  $S_{ijkl}^m = (1 - \phi) S_{ijkl}^d$ . For this case, the elastic constants of Reuss assumption are used in the formulations. Consequently, the effective elastic strain induced in porous material can be decomposed into a part related to the stress tensor in solid material (matrix) and the pore pressure part ( $p_v$ ), Ref. [11]. It should be noted that the pore pressure is a positive quantity.

$$\epsilon_{ij}^e = S_{ijkl}^d \sigma_{kl} + \frac{1}{K_{Rc}} B_{ij} p_v \quad (4.10)$$

$$\zeta = \frac{1}{K_{Rc}} (p_v + B_{ij} \sigma_{ij}) \quad (4.11)$$

In equations (4.10) and (4.11),  $\zeta$  denotes the variation in fluid content and  $B_{ij}$  is the modified Skempton tensor defined by equation (4.12), Ref. [11].

$$B_{ij} = K_{Rc} (S_{ijkk}^d - S_{ijkk}^m) = K_{Rc} (L_{ij}^d - L_{ij}^m) \quad (4.12)$$

$$\zeta = \frac{\rho_w}{\rho_{w_0}} \phi - \phi_0 \quad (4.13)$$

In the above equations,  $\phi$ ,  $\phi_0$ ,  $\rho_w$ , and  $\rho_{w_0}$  are the current and initial porosity and water density. The Reuss composite bulk modulus  $K_{Rc}$  that appears in equations (4.11) and (4.12) can also be calculated by (4.14), in which  $K_w$  is the water bulk modulus, Ref. [11].

$$\frac{1}{K_{\text{Re}}} = \frac{1}{K_{\text{Reff}}^{\text{d}}} - \frac{1}{K_{\text{Reff}}^{\text{m}}} + \phi \left[ \frac{1}{K_{\text{w}}} - \frac{1}{K_{\text{Reff}}^{\text{m}}} \right], \quad K = -\frac{dp}{d\Omega/\Omega} = -\frac{dp}{d\varepsilon_{\text{vol}}} \quad (4.14)$$

In equation (4.14), the Reuss effective bulk modulus  $K_{\text{Reff}}^{\text{x}}$  is the equivalent isotropic value of an anisotropic material that can be defined by equation (4.15). The superscript “x” in that equation refers to “d” or “m” for drained or matrix materials, while the superscript “R”, denoting the Reuss effective compliance, is omitted for notation simplicity. The tensors  $L_{ij}^{\text{x}}$  and  $K_{\text{Reff}}^{\text{x}}$  are related to the elastic moduli for various types of materials by equations (4.16) to (4.21), where the other components of  $L_{ij}^{\text{x}}$  are zero.

Anisotropic materials:

$$\frac{1}{K_{\text{Reff}}^{\text{x}}} = S_{\text{ijij}}^{\text{x}} = \text{tr}(L_{ij}^{\text{x}}) = S_{11}^{\text{x}} + S_{22}^{\text{x}} + S_{33}^{\text{x}} + 2S_{23}^{\text{x}} + 2S_{13}^{\text{x}} + 2S_{12}^{\text{x}} \quad (4.15)$$

Orthotropic materials:

$$\frac{1}{K_{\text{Reff}}^{\text{x}}} = \frac{1}{E_1^{\text{x}}} + \frac{1}{E_2^{\text{x}}} + \frac{1}{E_3^{\text{x}}} - \frac{2\nu_{23}^{\text{x}}}{E_2^{\text{x}}} - \frac{2\nu_{31}^{\text{x}}}{E_3^{\text{x}}} - \frac{2\nu_{12}^{\text{x}}}{E_1^{\text{x}}} \quad (4.16)$$

$$L_{ij}^{\text{x}} = \begin{bmatrix} (1-\nu_{12}^{\text{x}}-\nu_{13}^{\text{x}})/E_1^{\text{x}} & 0 & 0 \\ 0 & (1-\nu_{21}^{\text{x}}-\nu_{23}^{\text{x}})/E_2^{\text{x}} & 0 \\ 0 & 0 & (1-\nu_{31}^{\text{x}}-\nu_{32}^{\text{x}})/E_3^{\text{x}} \end{bmatrix} \quad (4.17)$$

Transversely isotropic materials:

$$\frac{1}{K_{\text{Reff}}^{\text{x}}} = \frac{2}{E_{\text{p}}^{\text{x}}} + \frac{1}{E_{\text{t}}^{\text{x}}} - \frac{4\nu_{\text{tp}}^{\text{x}}}{E_{\text{t}}^{\text{x}}} - \frac{2\nu_{\text{p}}^{\text{x}}}{E_{\text{p}}^{\text{x}}} \quad (4.18)$$

$$L_{ij}^{\text{x}} = \begin{bmatrix} (1-\nu_{\text{p}}^{\text{x}}-\nu_{\text{pt}}^{\text{x}})/E_{\text{p}}^{\text{x}} & 0 & 0 \\ 0 & (1-\nu_{\text{p}}^{\text{x}}-\nu_{\text{pt}}^{\text{x}})/E_{\text{p}}^{\text{x}} & 0 \\ 0 & 0 & (1-2\nu_{\text{tp}}^{\text{x}})/E_{\text{t}}^{\text{x}} \end{bmatrix} \quad (4.19)$$

Isotropic materials:

$$\frac{1}{K_{\text{Reff}}^x} = \frac{3(1-2\nu^x)}{E^x} \quad (4.20)$$

$$L_{ij}^x = \frac{1}{3K_{\text{Reff}}^x} \delta_{ij} \quad (4.21)$$

In the drained situation, where the increase in pore pressure can be ignored ( $p_v \approx 0$ ), the constitutive relations, for non-confining conditions, are reduced to

$$\varepsilon_{ij}^e = S_{ijkl}^d \sigma_{kl} = \frac{1}{1-\phi} S_{ijkl}^m \sigma_{kl} \quad (\text{Drained}) \quad (4.22)$$

$$\zeta = \frac{1}{K_{\text{Rc}}} B_{ij} \sigma_{ij} = (L_{ij}^d - L_{ij}^m) \sigma_{ij} = \frac{\phi}{1-\phi} L_{ij}^m \sigma_{ij} \quad (\text{Drained}) \quad (4.23)$$

$$\phi_0 = \phi - \zeta = \phi - (L_{ij}^d - L_{ij}^m) \sigma_{ij} = \phi \left[ 1 - \frac{L_{ij}^m \sigma_{ij}}{1-\phi} \right] \quad (\text{Drained}) \quad (4.24)$$

For the undrained situation, however, the variation of fluid content can be ignored ( $\zeta = 0$ ).

The constitutive relations of this type can be determined by ignoring the initial pore pressure as follows:

$$\varepsilon_{ij}^e = \left[ S_{ijkl}^d - \frac{1}{K_{\text{Rc}}} B_{ij} B_{kl} \right] \sigma_{kl} = \frac{1}{1-\phi} \left[ S_{ijkl}^m - \frac{\phi^2 K_{\text{Rc}}}{1-\phi} L_{ij}^m L_{kl}^m \right] \sigma_{kl} = S_{ijkl}^u \sigma_{kl} \quad (4.25)$$

$$p_v = -B_{ij} \sigma_{ij} = -\frac{\phi K_{\text{Rc}}}{1-\phi} L_{ij}^m \sigma_{ij} \quad (\text{Undrained}) \quad (4.26)$$

$$\phi = \frac{\rho_{w_0}}{\rho_w} \phi_0 \quad (\text{Undrained}) \quad (4.27)$$

where the existing data for temperature dependence of super-cooled water density in  $\text{kg/m}^3$  can be fitted by the Glenn (1974) adiabatic equation of state (4.28), in which the absolute temperature  $T$  is measured in  $^\circ\text{K}$ , and water pressure, in Pa, Ref. [10].

$$\frac{\rho_w}{\rho_{w_0}} = \left[ 1 + \frac{p_v}{\alpha K_w} \right]^\alpha \quad (4.28)$$

$$\rho_{w_0} = -6.5315 \times 10^{-7} T^4 + 8.313 \times 10^{-4} T^3 - 3.9951 \times 10^{-1} T^2 + 8.5505 \times 10^1 T - 5.8538 \times 10^3 \quad (4.29)$$

Where the average values for material constant  $\alpha$  and water bulk modulus  $K_w$  are given by  $\alpha \approx 0.13986$  and  $K_w \approx 2.196$  GPa .

It should be noted that the shear stress components do not have any contribution to the term  $L_{ij}^m \sigma_{ij}$  in equations (4.23) and (4.26), as  $L_{ij}^m$  is a diagonal matrix. In addition, the elastic compliance tensor of ice is a function of current state of porosity, and so depends on the volumetric part of total strain. That ensures that the pore pressure and variation in liquid content, equations (4.23) and (4.26), are produced entirely by normal stress and strain components.

### 4.3.2 Application of Voigt analogy to porous material modeling

In this analogy, the Voigt averaging assumption is considered in porous medium modeling, where the total strain is decomposed into an effective strain in drained solid  $\varepsilon_{ij}^{de}$ , and the average pore part in the voids  $\varepsilon_{ij}^{pe}$  as

$$\varepsilon_{ij}^e = \varepsilon_{ij}^{de} + \phi \varepsilon_{ij}^{pe} \quad (4.30)$$

where the drained strain can be related to the matrix strain by  $\varepsilon_{ij}^{me} = (1 - \phi) \varepsilon_{ij}^{de}$ , and then the drained compliance tensor by  $C_{ijkl}^d = (1 - \phi) C_{ijkl}^m$ . For this case, the elastic constant of Voigt assumption is used in the formulations below. By pursuing a procedure similar to that followed for the Reuss analogy, the following stress-strain relations relate the effective stress of porous material to the solid strain and the pore pressure by

$$\sigma_{ij} = C_{ijkl}^d \varepsilon_{kl}^e - \beta_{ij} p_v \quad (4.31)$$

$$p_v = K_{Vc} (\zeta - \beta_{ij} \varepsilon_{ij}^e) \quad (4.32)$$

where  $\beta_{ij}$  denotes the Biot effective stress coefficient that is related to Skempton tensor by

$$\beta_{ij} = \frac{1}{K_{Vc}} C_{ijkl}^d B_{kl} \quad \text{or} \quad B_{ij} = K_{Rc} S_{ijkl}^d \beta_{kl} \quad (4.33)$$

The Voigt composite bulk modulus  $K_{Vc}$ , in this case, is defined by equation (4.34), in which the Voigt effective bulk modulus  $K_{Veff}^x$  is defined by equation (4.35), Ref. [11].

$$\frac{1}{K_{Vc}} = \frac{1}{K_{Veff}^d} - \frac{1}{K_{Veff}^m} + \phi \left[ \frac{1}{K_w} - \frac{1}{K_{Veff}^m} \right] \quad (4.34)$$

$$9 K_{Veff}^x = C_{11}^x + C_{22}^x + C_{33}^x + 2C_{23}^x + 2C_{13}^x + 2C_{12}^x \quad (4.35)$$

In the drained situation, the constitutive relations of porous materials are reduced to equations (4.36) to (4.38) for the non-confining condition ( $p_v \approx 0$ ).

$$\sigma_{ij} = C_{ijkl}^d \varepsilon_{kl}^e = (1 - \phi) C_{ijkl}^m \varepsilon_{kl}^e \quad (\text{Drained}) \quad (4.36)$$

$$\zeta = \beta_{ij} \varepsilon_{ij}^e = \phi C_{ijkl}^m L_{kl}^m \varepsilon_{ij}^e \quad (\text{Drained}) \quad (4.37)$$

$$\phi_0 = \phi - \zeta = \phi - \beta_{ij} \varepsilon_{ij}^e = \phi \left( 1 - C_{ijkl}^m L_{kl}^m \varepsilon_{ij}^e \right) \quad (\text{Drained}) \quad (4.38)$$

For the undrained situation, on the other hand, the variation of fluid content can be ignored ( $\zeta = 0$ ) and the constitutive relations of this type are reduced to

$$\sigma_{ij} = \left( C_{ijkl}^d + K_{vc} \beta_{ij} \beta_{kl} \right) \varepsilon_{kl}^e = C_{ijkl}^u \varepsilon_{kl}^e \quad (\text{Undrained}) \quad (4.39)$$

$$p_v = -K_{vc} \beta_{ij} \varepsilon_{ij}^e \quad (\text{Undrained}) \quad (4.40)$$

$$\phi = \frac{\rho_{w_0}}{\rho_w} \phi_0 \quad (\text{Undrained}) \quad (4.41)$$

The formulation of parameters  $K_w$ ,  $\rho_w$ , and  $\rho_{w_0}$  were given in the previous section. In this case, the Voigt stiffness tensor should be used in formulations to calculate the elastic moduli of porous material.

In equations (4.37), (4.38) and (4.40), the term  $\beta_{ij} \varepsilon_{ij}^e$  is related to the equivalent pressure stress, so the pore pressure is produced by normal stresses only. In those equations, the elastic stiffness tensor of porous material is a function of current state of porosity, and so depends on the equivalent pressure stress.

### 4.3.3 Porous material modeling for atmospheric ice

In this research, the atmospheric ice is assumed to follow more or less the drained porous model within the wet regime of ice accretion (*glaze*). The increase in pore pressure is ignored for this case, and the constitutive relations of this type are reduced to the averaged Reuss and Voigt equations (4.22) to (4.24) and (4.36) to (4.38) for the non-

confining conditions ( $p_v \approx 0$ ). For this drained model, the current state of porosity can be determined from a second-order algebraic equation, so no iteration procedure is required. Ice porosity is normally not greater than 5% in this type of ice accretion, and then has a less significant influence on ice poroelasticity.

For the dry regimes of ice accretion close to the transition boundary (*hard rime*), however, the material is assumed to follow the undrained porous model, in which the variation of fluid content is negligible ( $\zeta = 0$ ). In this case, the constitutive relations are reduced to the averaged Reuss and Voigt equations (4.25) to (4.27) and (4.39) to (4.41). The system of nonlinear equations in this undrained model is solved by iteration for determining the unknowns  $\phi$  and  $p_v$ . The initial porosity is considered as initial guess of this iteration procedure. The poroelastic parameters of Reuss and Voigt models are then calculated. After convergence, the material Jacobian matrix is also updated, see Section 7.2.2. The atmospheric ice deposits that are produced under dry regimes of ice accretion contain more air-bubbles. In this case, the magnitude of ice porosity is higher, sometimes as much as 15%, thus, it has a significant influence on the elastic behaviour of atmospheric ice.

In a very dry regime of ice accretion (*soft rime*), on the other hand, the liquid phase does not exist any more, so the formulations similar to those of drained situations can be used. In this case, ice porosity has the highest degree of influence on ice elastic behaviour, sometimes even more than 35%, and then cannot be ignored. For the transition situation from wet to dry regimes of ice accretion (*SI structure*), the averaged elastic behaviour of drained and undrained models is used in the poroelasticity model of this work.

#### 4.4 Conclusions

The practical elastic formulations for granular and various types of columnar ice were presented in this chapter. The poroelastic moduli of ice are determined by considering two extreme situations: the drained and undrained models. The following conclusions were drawn on the basis of the analysis of this chapter:

- 1) The discrepancy of the calculated elastic moduli of ice monocrystal varies in the range of 1.5% to 19.1% for the measurements of Gammon *et al.* (1983) and Dantl (1969). In this work, Gammon's data were used because of the lower degree of measurement uncertainties, as well as the violation in inverse relationship of monocrystal compliance and stiffness matrices in Dantl's data.
- 2) The temperature dependency of elastic moduli of ice mono or polycrystal is almost 7.4%, causing a shift in elastic characteristics of various types of ice. This means that all the conclusions obtained at a certain temperature,  $-10^{\circ}\text{C}$  here, may be extended to other temperatures considering a shift in elastic behaviours.
- 3) The elastic behaviour of ice depends on its texture and the c-axis orientation, which exhibits a significant anisotropy in material behaviour. The maximum anisotropy belongs to Poisson's ratio  $\nu_{13}$  or  $\nu_{31}$  of S1 ice (or for S3 ice with parallel c-axes) that varies 80.2% with rotation angle, where the other 29.2% and 41.8% were observed for Young's and shear moduli.
- 4) The two extreme situations exist in the elastic behaviour of columnar ice; the upper bound corresponds to S1 ice and the lower, to S2 ice. The elastic characteristics of S3 ice lie somewhere in between.

- 5) Minimum normal elastic rigidity corresponds to S3 ice at a scatter angle of  $120^\circ$  in the direction normal to the mean c-axis ( $E_{22} = 8.770$  GPa at  $0^\circ\text{C}$  or  $8.895$  GPa at  $-10^\circ\text{C}$ ).
- 6) Maximum normal elastic rigidity belongs to S1 ice in columnar direction ( $E_{33} = 12.462$  GPa at  $-50^\circ\text{C}$  or  $11.744$  GPa at  $-10^\circ\text{C}$ ), similar to S3 ice with parallel c-axes in the direction of the mean angle. This type of structure is normally observed for atmospheric ice deposits that are formed under the transition condition from the wet to dry regimes of ice accretion.
- 7) Maximum shear rigidity occurred for S1 ice (or S3 ice with parallel c-axes) at a rotation angle (or mean angle for S3 ice) of  $45^\circ$  ( $G_{13} = 4.486$  GPa at  $-50^\circ\text{C}$  or  $4.238$  GPa at  $-10^\circ\text{C}$ ), while the minimum magnitude is calculated in the same shear modulus of  $2.946$  GPa or  $2.988$  GPa, at  $0^\circ\text{C}$  or  $-10^\circ\text{C}$  respectively, for the same ice types.
- 8) Poisson's ratios vary in the range of  $0.416$  to  $0.224$  for various types of ice.
- 9) The total stress (strain) in porous ice is decomposed into drained and pore parts by using the analogy similar to Reuss (Voigt) averaging techniques.
- 10) The pore pressure is generated entirely by volumetric strain, so that the poroelastic behaviour of ice is under the influence of loading conditions.
- 11) The elastic compliance and stiffness tensors of porous ice depend on porosity, which is affected, in turn, by volumetric strain and equivalent elastic pressure.
- 12) The original contributions of this chapter are: (a) presenting the practical formulations and developing three computer codes in Maple Mathematical Program for calculating the elastic moduli of granular and different types of columnar freshwater ice (S1, S2, and S3), (b) development of ice poroelasticity model considering the wetting liquid by means of Voigt and Reuss analogies as well as the drained and undrained assumptions.

## CHAPTER 5

### CAP-MODEL PLASTICITY FOR ATMOSPHERIC ICE

#### 5.1 Introduction

The cap-model plasticity is adopted and used to simulate the plastic behaviour of porous atmospheric ice due to similarities in the plastic response of ice and the geological materials such as soils, rocks and concrete. The plasticity model for porous materials, including atmospheric ice, is quite complex, involving pressure-sensitive yielding, differences in tensile and compressive strengths, porosity dependency, rate and temperature dependency, and Bauschinger effect.

The theoretical principles of the cap-model plasticity were outlined in Chapter 3. In Section 2.3, on the other hand, a few available failure envelopes of freshwater ice were reviewed. The fixed parabolic or teardrop curves were proposed by Nadreau and Michel (1986), Jones (1982), Fish *et al.* (1997), and Derradji (2000) as the failure envelope of ice at some ranges of temperature and strain rates. Fish *et al.* (1997) presented their parabolic model on the basis of the formulations of ice parameters like cohesion, friction angle and melting pressure. Those formulations are improved, in this study, to achieve better agreement with the test results of Jones (1982), Rist and Murrell (1994), and Gagnon and Gammon (1995) and used in the fixed shear segment of ice yield envelope. The yield

envelope of porous ice is then considered to consist of three segments, a fixed parabolic shear envelope, an elliptical moving cap, and a tension cutoff. The other material parameters are formulated by using the existing test data. The yield envelopes of this study are compared with the above-mentioned ones in Section 7.4. This is the first contribution of this chapter. An associated flow rule is developed together with the corresponding hardening rules, which are the next contributions of this chapter. Finally, the implementation of the cap-model plasticity as a subroutine of UMAT is the last contribution of this chapter.

## 5.2 Yield envelope for atmospheric ice

The yield functions of Tresca, von-Mises and Mohr-Coulomb have been used commonly to describe the yield behaviour of materials. Unlike the latter case, the yield criteria of Tresca and von-Mises are independent of hydrostatic pressure. Tresca's criterion assumes that failure is controlled by the maximum shear stress, which has been identified by Nadreau and Michel (1986) to be relevant to various ice types at very small strain rates and relatively small confining pressures. For higher strain rates and confining pressures, they proposed the use of the Mohr-Coulomb yield criterion. In the model proposed by Fish *et al.* (1997), a parabolic yield function extended from the Drucker-Prager yield criterion is used. This yield criterion describes the pressure-dependency of ice strength by means of three parameters: ice cohesion  $d$ , ice friction angle  $\beta$ , and the hydrostatic pressure at maximum shear strength  $p_a$  (the parameters are identified in Fig. 5.1, which are identical to  $c$ ,  $\phi$ , and  $\sigma_{\max}$  in Fish's model, Fig. 2.6, respectively). The ice cohesion  $d$  defines the ice strength at zero hydrostatic pressure, which is a characteristic of the material and so a

function of temperature. A little strain-rate dependency, however, is observed for this parameter in the existing test data, which can be applied to the model in future works. The friction angle, on the other hand, depends on the viscosity of the liquid phase at grain boundaries (lubricants), hence, is affected by temperature and loading rate. Fish's model, however, cannot model the material dilatation or strain softening due to volumetric strain (pressure dependency of the yield surface resulting mainly from ice porosity). In this work, the cap-model yield criterion is used, which includes three main segments: a modified parabolic Drucker-Prager shear-yield surface providing dominantly shearing flow (similar to that of Fish's model), an elliptical moving cap that intersects the pressure stress axis, and a tensile cutoff, see Fig. 5.1. The abscissa, in this figure, represents the hydrostatic pressure  $p$ , while the ordinate  $t$  is a deviatoric stress measure that is related to von-Mises equivalent stress  $q$  by the following equation, Ref. [1].

$$t = \frac{q}{2} \left[ 1 + \frac{1}{K} - \left( 1 - \frac{1}{K} \right) \left( \frac{r}{q} \right)^3 \right] \quad (5.1)$$

in which  $r$  denotes the third invariant of the deviatoric stress and  $K$  is a material parameter. In uniaxial tension,  $(r/q)^3 = 1$  so that  $t = q/K$ , while in uniaxial compression  $(r/q)^3 = -1$  and then  $t = q$ . When  $K=1$ , the dependence on the third deviatoric stress invariant is removed, thus, the von-Mises circle is recovered in the deviatoric plane, hence  $t = q$ .

In Fig. 5.1,  $p_a$  denotes the pressure at maximum shear strength  $t_a$  ( $q_a$ ), and  $p_t$  the ice tensile strength, both at the current state of porosity, temperature and loading rate. The melting pressure is also denoted by  $p_b$  at which the ice strength is zero.

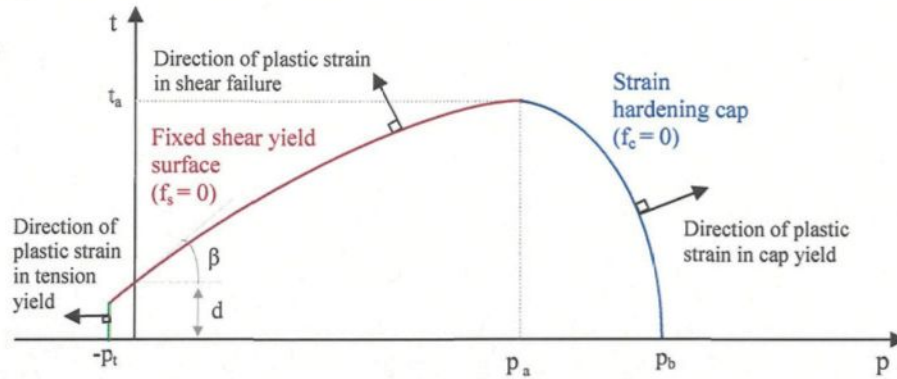


**Fig. 5.1:** Typical shear- and cap-yield surfaces in the cap plasticity model for atmospheric ice at a certain temperature, strain rate, and porosity.

On the basis of the results reported by Jones (1982), Rist and Murrell (1994), Fish *et al.* (1997), Sunder (1989) and Arakawa (1997), the temperature and strain-rate dependency of ice yield curves are schematically shown in Fig. 5.2 and Fig. 5.3, respectively.

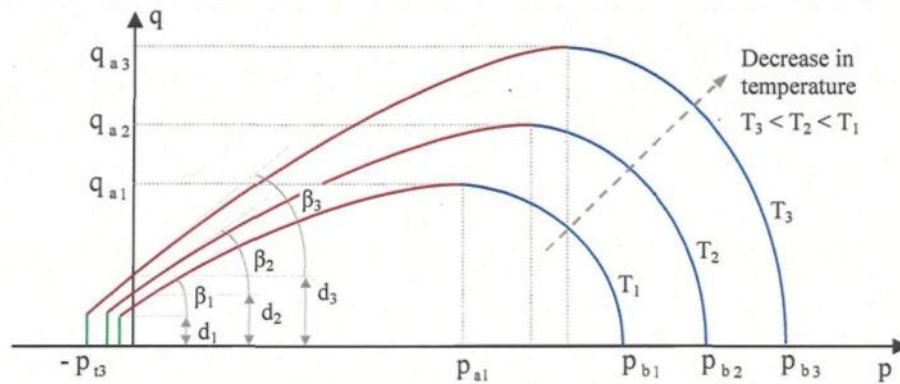


**Fig. 5.2:** Typical temperature dependency in ice yield envelopes.

As shown in Fig. 5.2, the extent of elastic region is assumed to increase continuously by reduction in ice temperature. This assumption is made on the basis of the test results reported by Arakawa (1997), see Fig. 2.5. For a certain temperature, however, the ice melting pressure  $p_b$  and cohesion  $d$  are assumed to be unaffected by loading rate, hence, the

strain-rate dependency of yield envelopes is similar to Fig. 5.3 in the ductile region. In the transient region, however, the maximum strength of ice decreases by an increase in strain rate, see Fig. 2.3 and Ref. [49]. Therefore, the elastic region reduces by increasing the strain rate, in a contrary manner to Fig. 5.3. The yield envelopes, in the brittle region, can be assumed to be unaffected by strain-rate in agreement with the test results of Sunder (1989).

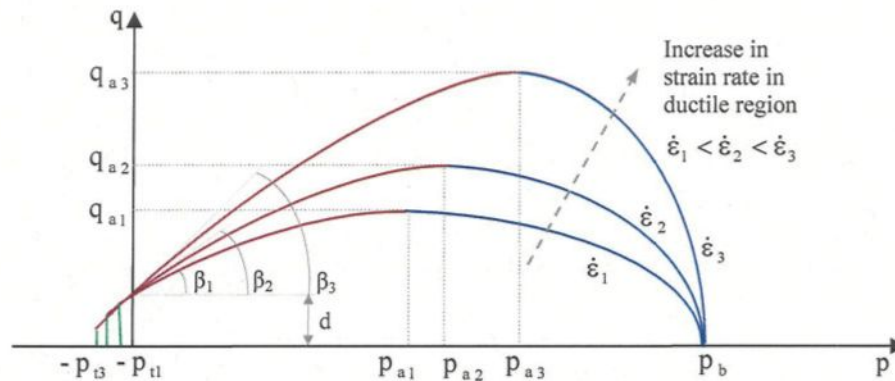


Fig. 5.3: Typical strain-rate dependency in ice yield envelopes.

It seems also that all three yield envelopes are affected by porosity as well as porosity changes upon loading. The major effects, however, occur for the cap-yield curve, where the hydrostatic pressure and then the porosity changes are higher. In this work, hence, it is assumed that the shear envelope is unaffected by porosity, while the effects of porosity and its variation upon loading are considered in the cap-yield envelope and tension cutoff. A schematic representation of the effects of porosity on yield envelopes is shown in Fig. 5.4, in which the initial and current states of porous ice envelopes are compared with the similar envelopes for bubble-free ice. The parameters at the initial state of porosity are denoted by superscript “0”, while the corresponding parameters to bubble-free ice are identified by the superscript “max”.

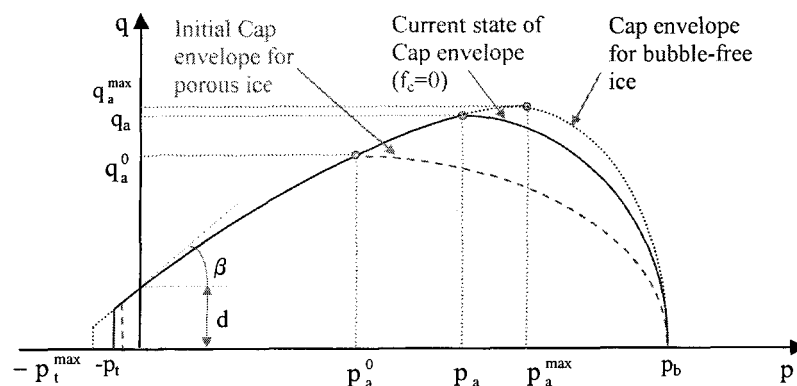


Fig. 5.4: The effects of porosity changes in the cap-yield surface and tension cutoff of atmospheric ice at a certain temperature, strain rate, and initial porosity.

In describing the yield envelope of ice, it should be considered that ice is known to change phases according to the phase diagram shown in Fig. 5.5. Ice  $I_h$  changes the phase to ice III when subjected to pressures higher than 200 MPa. Based on this feature of ice, Nadreau and Michel (1986) proposed a teardrop shape, while Fish *et al.* (1997) used a parabolic function for the yield envelope of ice. In this work, however, a parabolic function and an elliptical shape are used for fixed-shear and cap envelopes, respectively.

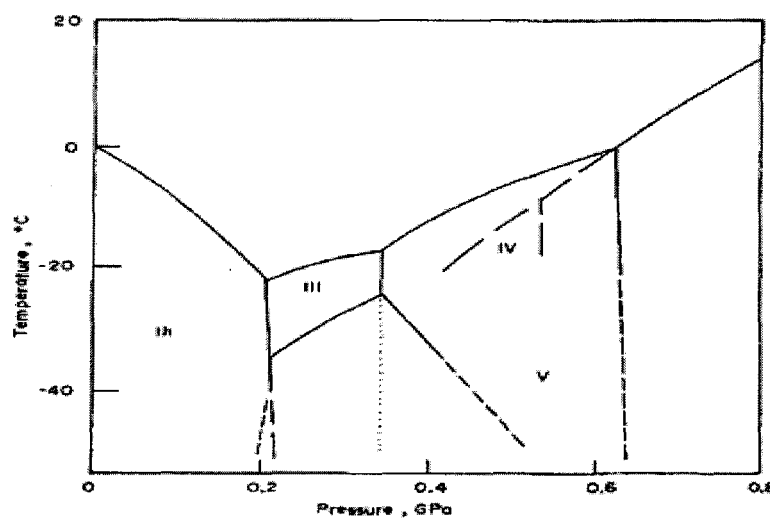
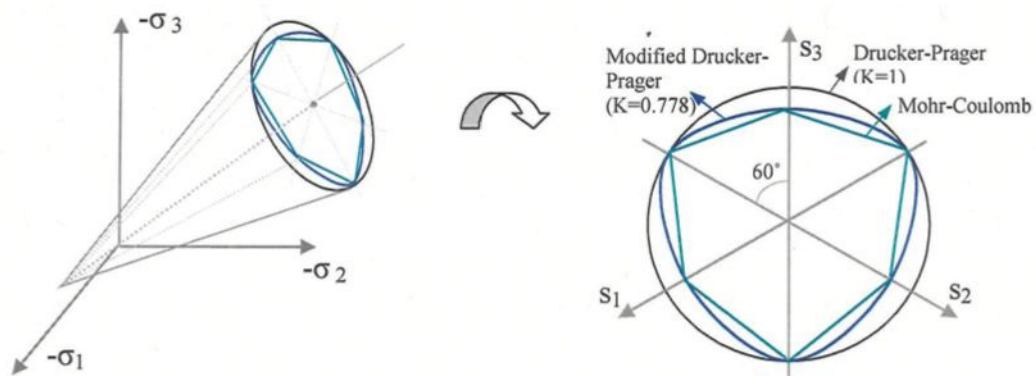


Fig. 5.5: Phase diagram for ice at natural range of temperature.

In the next sub-sections, the typical shear and cap functions for atmospheric ice are developed on the basis of the test results reported for freshwater ice or icebergs. The temperature and strain-rate dependence of the material parameters and the influences of ice texture and grain size on its yield envelope and on ice plastic behaviour are described for granular ice and columnar S2 ice in the normal direction to ice columns. It is still required to perform some complementary material tests on freshwater and porous columnar S2 ice in the columnar direction, as well as a complete set of strength tests for columnar S1 ice. Unlike the cap envelope, the shear-yield surface is fixed and unaffected by porosity changes. The effect of ice porosity on cap movement is explained in the subsequent sub-sections.

### 5.2.1 Fixed shear-yield envelope

The Mohr-Coulomb yield model assumes that the failure is independent of the value of the intermediate principal stress. Because of this and the existing corners in the Mohr-Coulomb model (singularities in yield surface), the modified parabolic Drucker-Prager yield model is used in this work to model the fixed shear-yield envelope, Fig. 5.6.



**Fig. 5.6:** Mohr-Coulomb and the modified Drucker-Prager yield surfaces in (a) Principal stress space, (b) Deviatoric plane.

In this model, the material parameter  $K(T)$  varies in the range of 0.778 to 1.0 to ensure the convexity of the yield surface, Ref. [1]. This parameter should be determined by performing a set of material tests at various temperatures, which is assumed to be one in this work. In this case the stress measure  $t$  is equal to the von-Mises equivalent stress  $q$ .

Following the procedure of Fish *et al.* (1997), a parabolic function is used here to simulate the fixed-shear envelope of ice, see Fig. 5.4. In this case, the ice shear strength can be described by three material parameters (internal variables): ice cohesion ( $d$ ), ice friction angle ( $\beta$ ), and the hydrostatic pressure at maximum shear strength of bubble-free ice ( $p_a^{\max}$ ) that can be related to ice melting pressure ( $p_b$ ), see Section 5.2.1.3. The following relation is proposed by Fish *et al.* (1997) for the pressure-dependency of ice shear strength:

$$f_s(\sigma_{ij}, p_a^{\max}, d, b) = q - d - bp + \frac{b}{2p_a^{\max}} p^2 = 0 \quad \text{for } -p_t \leq p \leq p_a \quad (5.2)$$

All three material parameters in equation (5.2) have a definite physical meaning and should be determined from the test data at various temperatures and strain rates. It is interesting to note that, at low stress levels ( $p \ll p_a^{\max}$ ), the shear-yield envelope reduces to the linear Drucker-Prager yield criterion  $f_s = q - d - bp = 0$ .

### 5.2.1.1 Ice cohesion

The ice cohesion  $d$  defines the ice strength when the hydrostatic pressure is equal to zero ( $p = 0$ ). During ice formation, a number of intermolecular bonds in the unit volume of ice are formed during freezing of water at  $0^\circ\text{C}$ , while the formation of other new bonds is continued by further temperature decrease. Thus, it is concluded that the ice cohesion is a function of temperature and consists of two components: the first cohesion components  $d_0$  related to the time of ice formation at  $0^\circ\text{C}$ , and the second temperature-dependent part  $d_1(T)$  for freezing below  $0^\circ\text{C}$ . In the domain of low temperatures (less than  $-20^\circ\text{C}$ ), a linear relationship is proposed by Fish *et al.* (1977) for the temperature dependence of ice cohesion on the basis of test data. For higher temperatures, however, the relationship becomes non-linear and is described by following exponential function.

$$d(T) = d_0 \exp\left(\alpha \left[1 - \frac{T}{T_m}\right]\right) \quad (5.3)$$

in which,  $\alpha$  denotes the material constant, and  $T$  the temperature in  $^\circ\text{K}$ . The maximum value of ice cohesion occurs at  $0^\circ\text{K}$ ,  $d(-273.16^\circ\text{C}) = d_0 \exp(\alpha)$ , while  $d_0$  is its value at freezing point. The typical temperature dependence of ice cohesion is shown in Fig. 5.7. The curve, in the left part of the figure, is fitted to the test results of Gagnon and Gammon (1995), and Jones (1982) for columnar ice at relatively low pressure and at strain rate of  $5 \times 10^{-3} \text{ s}^{-1}$ . For the case of granular (isotropic) ice, a similar trend is fitted to the data reported by Jones (1982), and Rist and Murrell (1994) at low pressures and a strain rate of  $1.4 \times 10^{-4} \text{ s}^{-1}$ , see the right figure. The values of ice cohesion at the freezing point and material constant  $\alpha$  for both granular and columnar ice types are tabulated in Table 5.1.

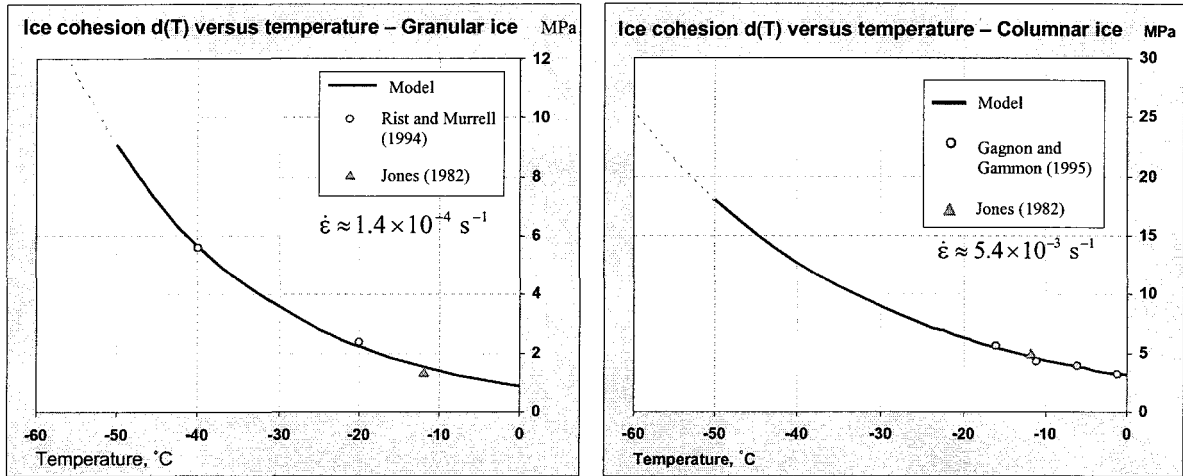


**Fig. 5.7:** Typical temperature dependence of ice cohesion for granular (left) and columnar S2 (right) ice types, curves are fitted to the data of Refs. [21], [25], and [50].

It is also important to examine the relationship of ice cohesion with other physical characteristics, e.g. ice grain size. On the basis of the available experimental measurements on polycrystalline ice, it can be stated that the ice cohesion may not be sensitive to variations of grain size and strain rate, but is strongly dependent of the texture of ice. Thus, equation (5.3) can be used here for the temperature dependency of ice cohesion in a full range of strain rates and temperature for columnar (glaze and hard rime) and granular (soft rime) atmospheric ice types. However, the accuracy of the formulation should be validated by performing some laboratory tests on atmospheric ice samples at various ranges of liquid water content (LWC), droplet size and air temperature. A little strain-rate dependency is also observed for this parameter, which can be considered in the future works.

**Table 5.1:** Material constants involved in the formulation of ice cohesion for granular and columnar S2 ice types.

Constant	Symbol	Granular	Columnar	Unit
Ice cohesion at freezing point	$d_0$	0.875	3.10	MPa
Material constant	$\alpha$	12.78	9.61	---

### 5.2.1.2 Ice friction angle

The friction angle  $\beta$  may also be assumed to consist of two components. It can be represented by a simple linear function of temperature as

$$\beta(T, \dot{\epsilon}) = \beta_1(\dot{\epsilon}) + \omega_1(\dot{\epsilon})(T_m - T) \quad (5.4)$$

in which, the material parameters  $\beta_1(\dot{\epsilon})$  and  $\omega_1(\dot{\epsilon})$  are assumed to be functions of strain rate only, determined by Fish *et al.* (1997) to be  $2^\circ 50'$  and  $16.4' \text{ } ^\circ\text{C}^{-1}$  at a strain rate of  $1.4 \times 10^{-3} \text{ s}^{-1}$ . An alternative form of equation (5.4) could be written in terms of the ice friction parameter,  $b(T, \dot{\epsilon})$ , which is defined as the tangent of ice friction angle  $\beta$  as

$$b(T, \dot{\epsilon}) = \tan \beta(T, \dot{\epsilon}) \quad (5.5)$$

Considering the available test results, the following relation (5.6) is in a good agreement with the variation of friction parameters in the ductile region for different types of granular and columnar ice. In the transition region, the trend is different so it should be obtained by performing material tests at higher strain rates. The friction parameter in the brittle region, however, can be assumed to be unaffected by strain-rate variations.

$$b(T, \dot{\epsilon}) = b_1(T) \left( \frac{\dot{\epsilon}}{\dot{\epsilon}_1} \right)^{\frac{1}{\mu}} \quad (5.6)$$

In this equation, the temperature dependency of friction parameter,  $b_1(T)$ , is assumed to be known at a certain strain rate  $\dot{\epsilon}_1$ . The parameter  $b_1(T)$  depends on ice texture, but still is unaffected by grain size. In this research, the data of Jones (1982), Rist and Murrell (1994), and Gagnon and Gammon (1995) are used to formulate this friction parameter for various ice types in the ductile region. Two curves are fitted to the data above for granular and columnar ice types at strain rates  $1.4 \times 10^{-4} \text{ s}^{-1}$  and  $5.4 \times 10^{-3} \text{ s}^{-1}$ , respectively, see Fig. 5.8.

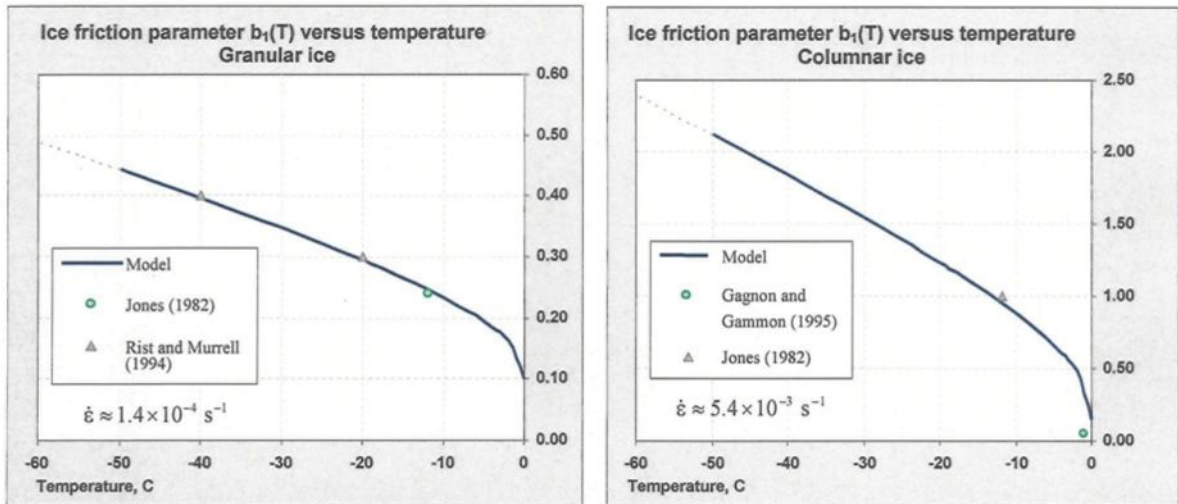


**Fig. 5.8:** Typical temperature dependence of the ice friction parameter  $b$  for granular (left) and columnar S2 (right) ice types, curves are fitted to the data of Refs. [21], [25], and [50].

The following trend, equation (5.7), can be fitted to the variation of  $b_1(T)$  versus temperature, as shown in Fig. 5.8. In this equation, the material constants  $b_0$ ,  $\gamma$ , and  $\nu$  are determined from the available failure envelopes of granular and columnar ice types at different temperatures, which are tabulated in Table 5.2.

$$b_1(T) = b_0 \exp\left(\gamma \left[1 - \frac{T}{T_m}\right]^\nu\right) \quad (5.7)$$

**Table 5.2:** Material constants involved in the formulation of ice friction parameter for granular and columnar S2 ice types.

Constant	Symbol	Granular	Columnar	Unit
Ice friction parameter at freezing point in equation (5.7)	$b_0$	0.10	0.15	MPa
Reference strain rate in equation (5.6)	$\dot{\epsilon}_1$	$1.4 \times 10^{-4}$	$5.4 \times 10^{-3}$	$\text{s}^{-1}$
Material constant in equation (5.7)	$\gamma$	2.70	4.05	---
Material constant in equation (5.7)	$\nu$	0.35	0.25	---
Material constant in equation (5.6)	$\mu$	4.20	5.20	---

The material parameter  $\mu$ , in equation (5.6) and Table 5.2, is determined from the available data of Jones (1982) at  $-11.8^\circ\text{C}$  for different strain rates. First, the variation of friction angle with strain rate is determined by using the data measured at low hydrostatic pressure, as shown in Fig. 5.9. The numerical results are then tabulated in Table 5.3, on which a curve is fitted for strain-rate dependency of friction parameter for granular and columnar ice types, see Fig. 5.14.

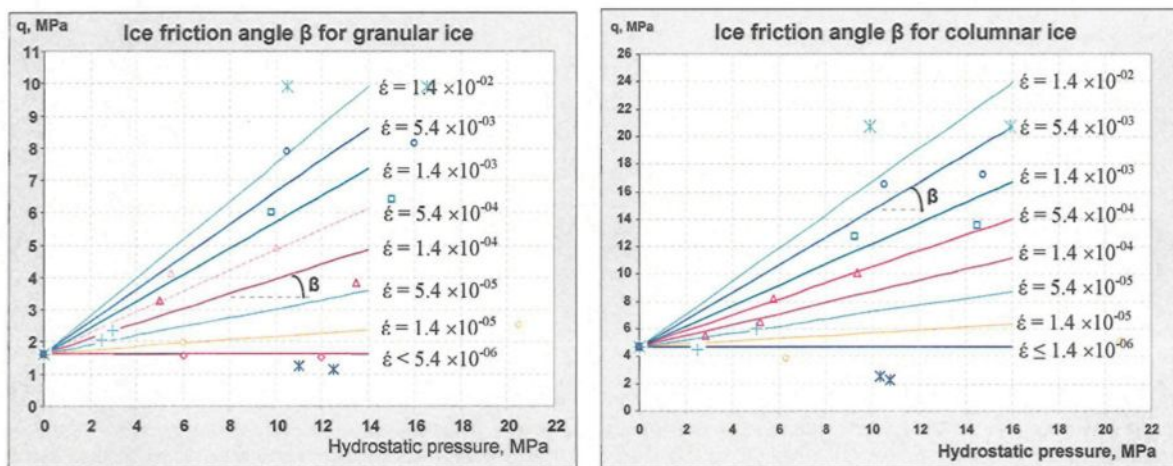


Fig. 5.9: Strain-rate dependence of ice friction angle  $\beta$  for granular (left) and columnar S2 ice (right), curves fitted to the data of Jones (1982) at  $-11.8^\circ\text{C}$ .

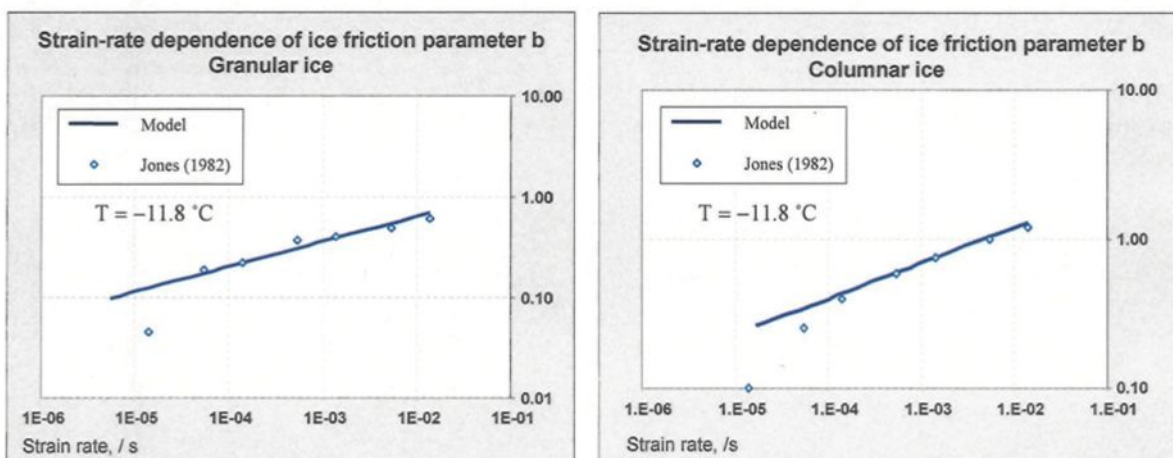


Fig. 5.10: Strain-rate dependence of ice friction parameter  $b$  for granular (left) and columnar S2 ice (right), curves fitted to the data of Jones (1982) at  $-11.8^\circ\text{C}$ .

**Table 5.3:** Variation of ice friction parameter  $b$  versus strain rate for granular and columnar ice types at  $-11.8^\circ\text{C}$  calculated from the data of Jones (1982).

↓ Ice type	Strain rate ( $\dot{\epsilon}$ )	$1.4 \times 10^{-06}$	$5.4 \times 10^{-06}$	$1.4 \times 10^{-05}$	$5.4 \times 10^{-05}$	$1.4 \times 10^{-04}$	$5.4 \times 10^{-04}$	$1.4 \times 10^{-03}$	$5.4 \times 10^{-03}$	$1.4 \times 10^{-02}$
	→									
Granular	Test results	0.00	0.01	0.05	0.19	0.22	0.35	0.40	0.51	0.71
	Model	0.082	0.113	0.142	0.196	0.246	0.339	0.425	0.586	0.736
Columnar	Test results	0.00	---	0.02	0.10	0.30	0.58	0.75	1.00	1.20
	Model	0.194	---	0.302	0.392	0.471	0.610	0.733	0.951	1.142

In equations (5.4) and (5.6), the strain rate dependence function  $\omega_1(\dot{\epsilon})$  and the temperature-dependence function  $b_1(T)$  can be extracted, one from the other, when either a series of failure curves versus temperature or strain rate are available. At a certain temperature  $T_0$  and strain rate  $\dot{\epsilon}_0$ , this relationship can be determined by

$$\omega_1(\dot{\epsilon}_0) = \frac{1}{T_m - T_0} \left\{ \tan^{-1} \left( b_1(T_0) \left[ \frac{\dot{\epsilon}_0}{\dot{\epsilon}_1} \right]^{\frac{1}{\mu}} \right) - \beta_1(\dot{\epsilon}_0) \right\} \quad (5.8)$$

For example, the parameter  $\omega_1(\dot{\epsilon})$  can be determined from  $b_1(T)$  using the existing data of Jones (1982) for columnar S2 ice at  $T_m - T_0 = 11.8^\circ\text{C}$  and  $\dot{\epsilon}_0 = 1.4 \times 10^{-3} \text{ s}^{-1}$  by

$$\omega_1(1.4 \times 10^{-3}) = \frac{1}{11.8} \left\{ \tan^{-1} \left( 1.0 \left[ \frac{1.4 \times 10^{-3}}{5.4 \times 10^{-3}} \right]^{\frac{1}{5.2}} \right) - 2.8333 \right\} = 2^\circ 57' \quad ^\circ\text{C}^{-1}$$

### 5.2.1.3 Hydrostatic pressure at maximum shear strength of bubble free ice

The hydrostatic pressure at maximum shear strength of bubble free ice ( $p_a^{\max}$ ) is assumed to be a function of temperature and strain rate. Following a similar procedure as for ice friction parameter, the trend of equation (5.9) is found to be in good agreement with the variation of  $p_a^{\max}$  in the ductile region and for temperatures below  $-3^\circ\text{C}$ .

$$p_a^{\max}(T, \dot{\epsilon}) = p_{a1}^{\max}(T) \left\{ 1 - \exp\left(-\frac{\dot{\epsilon}}{\dot{\epsilon}_1}\right) \right\}^{\eta} \quad (5.9)$$

In this equation, the temperature dependency of this parameter,  $p_{a1}^{\max}(T)$ , is assumed to be known at a certain strain rate  $\dot{\epsilon}_1$ . The parameter  $p_{a1}^{\max}(T)$  depends on ice texture, but still is assumed to be unaffected by grain size. In this research, the data of Jones (1982), Rist and Murrell (1994), and Gagnon and Gammon (1995) are used to determine the material constants that appear in the formulations of  $p_a^{\max}$  in the ductile region. Two curves are fitted to the data above for granular and columnar ice at strain rates  $1.4 \times 10^{-4} \text{ s}^{-1}$  and  $5.4 \times 10^{-3} \text{ s}^{-1}$ , respectively, see Fig. 5.11.

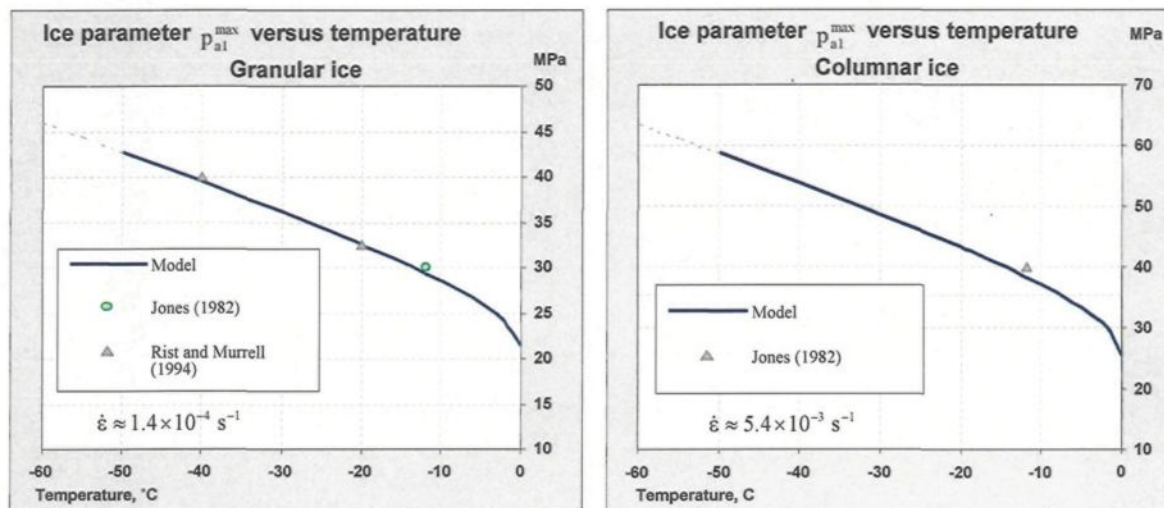


**Fig. 5.11:** Typical temperature dependence of the pressure at maximum shear strength  $p_{a1}^{\max}(T)$  for bubble-free granular (left) and columnar S2 (right) ice types, curves are fitted to the data of Refs. [21], [25], and [50].

The following trend, equation (5.10), can be fitted to the variation of  $p_{a1}^{\max}(T)$  versus temperature as shown in Fig. 5.11. In this equation, the material constants  $p_{a0}^{\max}$ ,  $\lambda$ , and  $\delta$  are

determined from the available failure envelopes of granular and columnar ice types at different temperatures, which are tabulated in Table 5.4.

$$p_{a1}^{\max}(T) = p_{a0}^{\max} \exp\left(\lambda \left[1 - \frac{T}{T_m}\right]^{\delta}\right) \quad (5.10)$$

**Table 5.4:** Material constants involved in the formulation of ice pressure at maximum shear strength for granular and columnar ice types.

Constant	Symbol	Granular	Columnar	Unit
Ice pressure at maximum shear strength at freezing point in equation (5.10)	$p_{a0}^{\max}$	21.50	25.50	MPa
Reference strain rate in equation (5.9)	$\dot{\epsilon}_1$	$1.4 \times 10^{-4}$	$5.4 \times 10^{-3}$	$s^{-1}$
Material constant in equation (5.10)	$\lambda$	1.75	1.95	---
Material constant in equation (5.10)	$\delta$	0.55	0.50	---
Material constant in equation (5.9)	$\eta$	0.40	0.25	---

The material parameter  $\eta$ , in equation (5.9) and Table 5.4, is determined from the available data of Jones (1982) at  $-11.8^\circ\text{C}$  for different strain rates. First, the variation of pressure at maximum shear strength  $p_a^{\max}$  with strain rate is determined. The numerical results are then tabulated in Table 5.5, on which a curve is fitted for strain-rate dependency of  $p_a^{\max}$  for granular and columnar ice types, see Fig. 5.12.

**Table 5.5:** Variation of ice pressure at maximum shear strength versus strain rate for granular and columnar ice types at  $-11.8^\circ\text{C}$  calculated from the data of Jones (1982).

↓ Ice type	Strain rate ( $\dot{\epsilon}$ )	$1.4 \times 10^{-06}$	$5.4 \times 10^{-06}$	$1.4 \times 10^{-05}$	$5.4 \times 10^{-05}$	$1.4 \times 10^{-04}$	$5.4 \times 10^{-04}$	$1.4 \times 10^{-03}$	$5.4 \times 10^{-03}$	$1.4 \times 10^{-02}$
	→									
Granular	Test results	2.0	6.5	13.0	21.0	25.5	28.7	29.5	30.0	28.0
	Model	4.641	7.918	11.450	18.600	24.421	29.089	29.338	29.338	29.338
Columnar	Test results	4.0	---	7.5	15.0	17.0	24.0	30.0	33.0	35.0
	Model	4.853	---	8.627	12.079	15.296	21.241	26.437	34.100	37.507

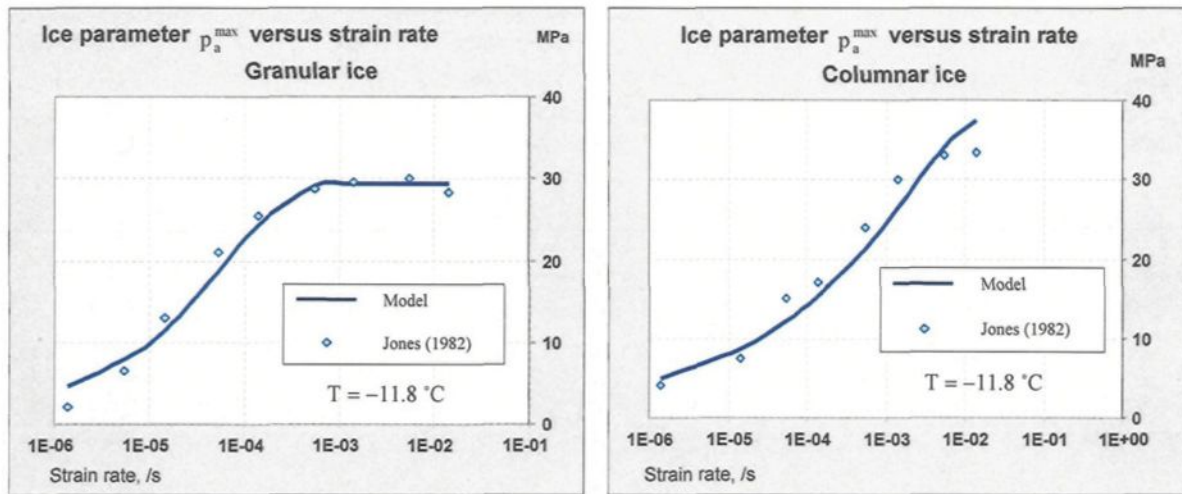


Fig. 5.12: Strain-rate dependence of  $p_a^{\max}$  for granular (left) and columnar S2 ice (right), curves fitted to the data of Jones (1982) at  $-11.8^\circ\text{C}$ .

Equations (5.3), (5.6), and (5.9) can be used to determine the cohesion, friction parameter, pressure at maximum shear strength of granular (soft rime) and columnar (glaze and hard rime) atmospheric ice types regardless of the grain size. However, the independency of those parameters to ice porosity should be validated by performing a series of material tests on various types of atmospheric ice, and to justify the applicability of the material parameters for columnar S1 (hard rime) and S3 ice types. One can also establish a relationship between those ice parameters and meteorological factors such as liquid water content (LWC), wind velocity, air temperature, and droplet size by performing the material tests on the ice samples produced in a refrigerated wind tunnel or icing simulation laboratories, see Chapter 6. In addition, the little strain-rate dependency of ice cohesion can also be considered in future works.

### 5.2.2 Cap-yield envelope

The cap envelope bounds the yield surface in hydrostatic compression, Fig. 5.13. In this figure, the initial state of cap is denoted by superscript “0”, which refers to the material cap-yield surface before loading. Upon loading, the stress point moves toward this cap envelope and pushes it forward, and thus provides an inelastic hardening mechanism to represent plastic compaction. The moving cap also controls the volume dilatancy due to softening created as the material yields on the shear failure surface.

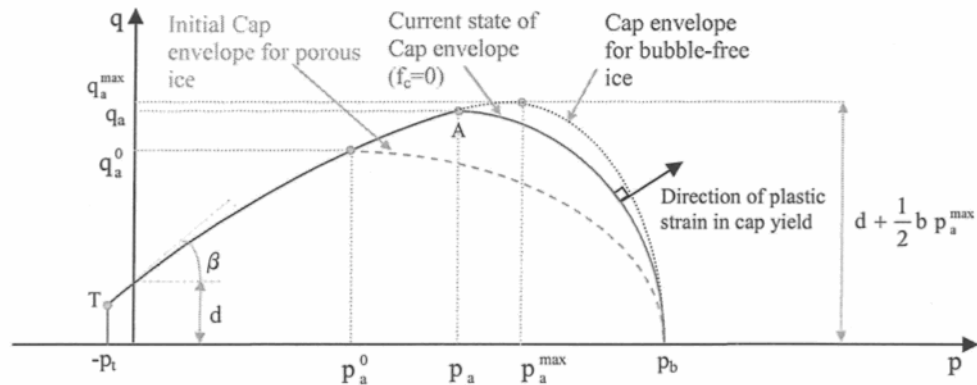


Fig. 5.13: Movement of cap-yield envelope by changes in porosity upon loading for atmospheric ice with initial porosity  $\phi_0$  (dashed curve).

In Fig. 5.13, point A refers to the intersection of the fixed-shear envelope and the cap, which is the current point of maximum shear strength. The hydrostatic pressure and stress measure at this point are denoted by  $p_a$  and  $q_a$ . At this point, as well as the transition point from the tension-yield envelope, point T, there is a discontinuity in the slope of yield envelope, and thus requires a special calculating procedure, see Section 7.2. The other pressure notations  $p_t$ ,  $p_b$ , and  $p_a^0$  refer to the equivalent pressure of tension strength, the melting pressure, and the initial hydrostatic pressure at maximum shear strengths  $q_a^0$ , respectively.

A moving elliptical cap is used in the plasticity model of this work, which is fixed at the intersection point with the axis of hydrostatic pressure. This point refers to the pressure melting point ( $p_b$ ), which is a characteristic of the material and is affected by temperature only, see equation (5.14). Hence, the material parameters  $p_a$  and  $p_b$  determine the current state of the cap by the following equation, as shown in Fig. 5.13.

$$f_c(\sigma_{ij}, p_a, p_b) = q - \frac{q_a}{p_b - p_a} \sqrt{(p_b - p_a)^2 - (p - p_a)^2} = 0 \quad \text{for} \quad p_a \leq p \leq p_b \quad (5.11)$$

In this case,  $\sigma_{ij}$  denotes the effective stress in porous ice, which is, in turn, a function of volumetric strain ( $\varepsilon_{vol}$ ), see Section 4.3. This yield surface intersects the shear-failure envelope at the transition point A, for which the maximum shear strength  $q_a$  can be determined by

$$q_a = d + b p_a - \frac{b}{2p_a^{\max}} p_a^2 \quad (5.12)$$

#### 5.2.2.1 Pressure at maximum shear strength of porous ice ( $p_a$ )

The volumetric plastic compaction (when yielding on the cap) causes hardening, while volumetric plastic dilation (when yielding on the shear failure surface) causes softening of the cap-yield envelope. In this case, the cap behaviour depends on the resultant plastic volumetric strain. The principles of effective stress in porous materials are applied to the formulations to take into account the hardening rules of ice cap yield. In this case, the pressure at maximum shear strength  $p_a$  can be related to  $p_a^{\max}$  using equation (4.31) as

$$p_a = (1 - \phi) p_a^{\max} + 3 \beta_{kk} p_v, \quad p_a^0 = (1 - \phi_0) p_a^{\max} \quad (5.13)$$

### 5.2.2.2 Ice melting pressure ( $p_b$ )

The ice melting pressure  $p_b$  refers to the hydrostatic pressure at which ice starts melting. At this pressure, hence, it has no shear strength even at very small levels of loading. Like other materials, the ice melting pressure  $p_b$  can be determined from the Clapeyron equation, which results in a linear relationship between the small temperature changes from the melting point to the small changes in hydrostatic pressure, Ref. [21].

$$dT_m = -A dp \quad \Rightarrow \quad p_b = \frac{T_m - T}{A} \quad (5.14)$$

In this equation,  $p_b$  is in MPa, and the parameter  $A$  has been calculated by using the data of Jones (1982) to be  $A = 0.0908 \text{ } ^\circ\text{K MPa}^{-1}$ . As an example, the melting pressure at  $-11.8^\circ\text{C}$  can be obtained from equation (5.14) results in  $p_b = 129.96 \text{ MPa}$ . It should be noted that the ice melting pressure  $p_b$  is the characteristic of material so independent of loading condition but a function of temperature only.

### 5.2.3 Tension cut-off

The tension cut-off intersects the shear envelope at point T by equation (5.15), see Fig. 5.13, in which  $p_t$  is related to the tensile strength of bubble-free ice  $p_t^{\max}$  by (5.16).

$$f_t = -p_t - p = 0 \quad (5.15)$$

$$p_t = (1 - \phi) p_t^{\max} \quad (5.16)$$

The tensile strength of bubble-free ice  $p_t^{\max}$  shows no significant variations with strain rate or temperature in the ranges of  $-5^\circ\text{C}$  to  $-20^\circ\text{C}$ , and strain rates greater than  $10^{-5} \text{ s}^{-1}$ , Ref. [12]. It is assumed to be 1.0 MPa in the ductile region and the range of temperatures of this work, see Ref. [12], Refs. [49], and Fig. 2.3.

#### 5.2.4 Factors affecting the yield surface of atmospheric ice

The pressure-dependency of ice yield envelopes; equations (5.2), (5.11) and (5.15); was described by four material parameters (internal variables): ice cohesion  $d$ , ice friction angle  $\beta$  or friction parameter  $b$ , the hydrostatic pressure at maximum shear strength  $p_a^{\max}$ , and ice melting pressure  $p_b$ . These parameters are the principal strength parameters of ice, hence, it is important to examine their relationship with the other physical characteristics of ice, such as structure, grain size, porosity, temperature, and strain rate.

In the previous sections, it was concluded that all of these material parameters are strongly affected by ice structure, texture and its fabric (ice type), while the grain size does not have a significant influence on those parameters. The ice cohesion and melting pressure are assumed to be the characteristics of materials and so are affected by temperature only. The other two parameters, ice friction angle and hydrostatic pressure at maximum shear strength of bubble-free ice, on the other hand, are functions of strain rate and temperature. Upon loading, the main influence of porosity on the mechanical behaviour of ice returns to the volumetric characteristic of the material. Thus, the shear envelope is assumed to be unaffected by porosity changes, while the location and shape of the cap depends on the current state of porosity. The definitions of effective stress and strain are used here to take into account the effects of porosity on the cap-yield surface, see Section 4.3.

In most of the plasticity models, the yield surface is also affected by creep, where the existence of two independent creep mechanisms is normally considered: the cohesion and consolidation mechanisms. For the case of ice at natural temperatures, the creep is started at the earliest stage of loading, and thus should be normally considered from the beginning.

### 5.3 Plastic flow and hardening rules in atmospheric ice

Plastic deformation occurs only when the yield condition ( $f = 0$ ) is met. The plastic strain rate ( $\dot{\varepsilon}_{ij}^p$ ) is often specified in terms of a plastic flow potential ( $g$ ), which is equal to the yield function  $f$  for an associated flow rule ( $g = f$ ). Here, like many other plasticity models, an associated flow rule is used for both shear and cap plastic flows. In this case, the flow direction in each plastic mechanism is normal to the yield surface, see Fig. 5.1, which can be given by

$$d\varepsilon_{ij}^p = \begin{cases} \sum_{x=s,c,t} d\lambda_x^p \frac{\partial f_x}{\partial \sigma_{ij}} & \text{if } f_x = 0 \text{ and } \frac{\partial f_x}{\partial \sigma_{ij}} d\sigma_{ij} > 0 \\ 0 & \text{if } f_x < 0, \text{ or } f_x = 0 \text{ and } \frac{\partial f_x}{\partial \sigma_{ij}} d\sigma_{ij} \leq 0 \end{cases} \quad (5.17)$$

in which,  $\lambda_x^p$  is the plastic multiplier related to yield surface  $f_x$ , where the subscript “x” may be replaced by “s”, “c”, or “t” for the shear-, cap-, or tension-yield surface, respectively. In classical plasticity models, the rate of mechanical dissipation work ( $W^p$ ) can be decomposed into volumetric ( $W_{vol}^p$ ) and deviatoric ( $W_{dev}^p$ ) parts by

$$dW^p = \sigma_{ij} d\varepsilon_{ij}^p = dW_{vol}^p + dW_{dev}^p = -p d\varepsilon_{vol}^p + s_{ij} de_{ij}^p \quad (5.18)$$

in which  $e_{ij}^p$  denotes the deviatoric part of plastic strain. Based on this energy decomposition, a measure for deviatoric strain ( $\varepsilon_{dev}^p$ ) can be defined to be conjugate to the equivalent von-Mises stress  $q$ , so that  $dW_{dev}^p = s_{ij} de_{ij}^p = q d\varepsilon_{dev}^p$ . Thus, equation (5.18) can be rewritten as

$$dW^p = -p d\varepsilon_{vol}^p + q d\varepsilon_{dev}^p \quad (5.19)$$

in which the equivalent deviatoric plastic strain  $\varepsilon_{\text{dev}}^p$  and its increment  $d\varepsilon_{\text{dev}}^p$  are related to the total deviatoric plastic strain  $e_{ij}^p$  by

$$\varepsilon_{\text{dev}}^p = \left[ \frac{2}{3} de_{ij}^p de_{ij}^p \right]^{\frac{1}{2}} \quad (5.20)$$

$$d\varepsilon_{\text{dev}}^p = \left[ \frac{2}{3} de_{ij}^p de_{ij}^p \right]^{\frac{1}{2}} \quad (5.21)$$

In this case, the plastic flow rule (5.17) can be written as two equivalent equations as

$$d\varepsilon_{\text{vol}}^p = - \sum_{x=s,c,t} d\lambda_x^p \frac{\partial f_x}{\partial p}, \quad d\varepsilon_{\text{dev}}^p = \sum_{x=s,c,t} d\lambda_x^p \frac{\partial f_x}{\partial q} \quad (5.22)$$

in which the volumetric part represents the horizontal component of the gradient of the yield surface in the meridian (p-q) plane, while the deviatoric part is the vertical component, see Fig. 5.14.

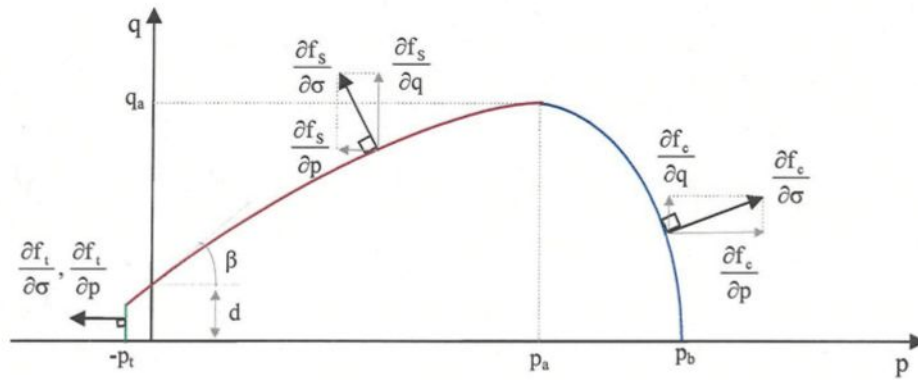


**Fig. 5.14:** The volumetric and deviatoric components of yield function gradients for shear- and cap-yield envelopes, and tension cutoff.

The plastic multiplier  $\lambda_x^p$  can be determined by considering the Kuhn-Tucker complementary conditions for rate-independent plasticity models, which requires

$$\lambda_x^p \geq 0, \quad f_x(\sigma_{ij}, \kappa_\alpha^x) \leq 0, \quad \text{and} \quad \lambda_x^p f_x(\sigma_{ij}, \kappa_\alpha^x) = 0 \quad (5.23)$$

in which the internal variables  $\kappa_\alpha^x$ , in this case, are functions of the volumetric and deviatoric plastic strains ( $\varepsilon_{vol}^p, \varepsilon_{dev}^p$ ) and the total strain rate ( $\dot{\varepsilon}_{vol}, \dot{\varepsilon}_{dev}$ ). The last condition in equation (5.23) enables us to determine the actual value of  $\lambda_x^p$  at any given time by

$$\lambda_x^p \dot{f}_x(\sigma_{ij}, \kappa_\alpha^k) = 0 \quad (\text{Persistency or consistency condition}) \quad (5.24)$$

For ice, however, the viscous deformation is in a scale much lower than the elastic and viscoelastic contributions, and can even be ignored beyond the ductile region. Hence, a quasi rate-independent plasticity flow rule is proposed for atmospheric ice in such a way that the yield functions are considered to be constrained ( $df_x = 0$ ) during each time increment of the inelastic flow, while the rate-dependency of material parameters are considered in the plasticity model. The flow and hardening rules of this plasticity model are described below, while the strain-rate dependency of material parameters were formulated in Sections 5.2.1 and 5.2.2.

### 5.3.1 Plastic flow for the fixed shear yield

In Section 5.2.1, a shear-yield function was presented for ice as a function of three material parameters. The perfect plasticity model is considered for this yield envelope. After time differentiating, the consistency condition, in this case, reduces to

$$df_s(\sigma_{ij}, d, b, p_a^{\max}) = \frac{\partial f_s}{\partial \sigma_{ij}} d\sigma_{ij} + \frac{\partial f_s}{\partial d} dd + \frac{\partial f_s}{\partial b} db + \frac{\partial f_s}{\partial p_a^{\max}} dp_a^{\max} = 0 \quad (5.25)$$

in which  $\sigma_{ij}$  denotes the effective stress, which can be related to the induced stress in matrix material using equation (4.31) by

$$\sigma_{ij} = (1 - \phi) \sigma_{ij}^m - \beta_{ij} p_v \quad (5.26)$$

The gradients of shear-yield function  $f_s$  can be derived from equation (5.2) by considering Fig. 5.14 as

$$\left| \frac{\partial f_s}{\partial \sigma_{ij}} \mathbf{n}_j \right| = \left[ \left( \frac{\partial f_s}{\partial p} \right)^2 + \left( \frac{\partial f_s}{\partial q} \right)^2 \right]^{\frac{1}{2}} \quad \text{where} \quad \frac{\partial f_s}{\partial p} = -b \left[ 1 - \frac{p}{p_a^{\max}} \right] \quad \text{and} \quad \frac{\partial f_s}{\partial q} = 1 \quad (5.27)$$

$$\frac{\partial f_s}{\partial p_a^{\max}} = -\frac{b}{2} \left[ \frac{p}{p_a^{\max}} \right]^2 \quad (5.28)$$

$$\frac{\partial f_s}{\partial b} = p \left[ \frac{p}{2p_a^{\max}} - 1 \right] \quad (5.29)$$

$$\frac{\partial f_s}{\partial d} = -1 \quad (5.30)$$

The term  $\partial f_s / \partial \sigma_{ij}$  in equation (5.25) represents the direction normal to the shear-yield curve having the unit normal  $\mathbf{n}_j$  in the meridian plane, which can be determined by

$$\frac{\partial f_s}{\partial \sigma_{ij}} = \frac{\partial f_s}{\partial p} \frac{\partial p}{\partial \sigma_{ij}} + \frac{\partial f_s}{\partial q} \frac{\partial q}{\partial \sigma_{ij}} \quad (5.31)$$

in which, the following terms can be determined using equations (3.8) and (3.11) by

$$\frac{\partial p}{\partial \sigma_{ij}} = -\frac{1}{3} \delta_{ij} \quad (5.32)$$

$$\frac{\partial q}{\partial \sigma_{ij}} = \frac{3}{2q} \left( s_{ij} - \frac{1}{3} s_{kk} \delta_{ij} \right) \quad (5.33)$$

In the first term of equation (5.25), the stress increment can be determined by using Hooke's law for porous material, in which  $C_{ijkl}^{ve}$  denotes the viscoelastic stiffness tensor, equation (3.38).

$$d\sigma_{ij} = C_{ijkl}^{ve} (d\varepsilon_{kl}^e + d\varepsilon_{kl}^{ve}) = C_{ijkl}^{ve} (d\varepsilon_{kl} - d\varepsilon_{kl}^p) \quad (5.34)$$

The effective elastic strain, in this case, can be related to the matrix elastic strain tensor by

$$d\varepsilon_{kl}^e = d\varepsilon_{kl} - d\varepsilon_{kl}^{ve} - d\varepsilon_{kl}^p = \frac{1}{1-\phi} (d\varepsilon_{kl} - d\varepsilon_{kl}^{ve} - d\varepsilon_{kl}^p)^m + \frac{1}{K_{Rc}} B_{ij} p_v \quad (5.35)$$

The incremental viscoelastic strain is related to elastic deformation by equation (3.36), and the effect of porosity in shear failure is ignored. Shear hardening due to plastic deformation can be applied to the model in future works. After substituting from equation (5.17), the stress rate for a purely shear-yielding mechanism can be given by

$$d\sigma_{ij} = C_{ijkl}^{ve} \left( d\varepsilon_{kl} - d\lambda_s^p \frac{\partial f_s}{\partial \sigma_{kl}} \right) \quad (5.36)$$

where  $d\lambda_s^p$  denotes the plastic multiplier relevant to the shear-yield envelope  $f_s$ . The second term in equation (5.25) vanishes in an isothermal deformation as the ice cohesion parameter  $d$  is only a function of temperature. The evolution equation for friction parameter  $b$ , in the third term of equation (5.25), can be written for an isothermal deformation as

$$db(T, \dot{\varepsilon}_{ij}^p) = \frac{\partial b}{\partial \dot{\varepsilon}_{ij}^p} d\dot{\varepsilon}_{ij}^p = \frac{\partial b}{\partial \dot{\varepsilon}_{vol}^p} d\dot{\varepsilon}_{vol}^p + \frac{\partial b}{\partial \dot{\varepsilon}_{dev}^p} d\dot{\varepsilon}_{dev}^p \quad (5.37)$$

in which the derivatives of  $b$  can be determined by using equations (5.6) and (3.9) as

$$\frac{\partial b}{\partial \dot{\epsilon}_{\text{vol}}^p} = \frac{1}{3} \frac{\partial}{\partial \dot{\epsilon}} \left[ b_1(T) \left( \frac{\dot{\epsilon}}{\dot{\epsilon}_1} \right)^{\frac{1}{\mu}} \right] = \frac{1}{3 \mu \dot{\epsilon}_1} b_1(T) \left( \frac{\dot{\epsilon}}{\dot{\epsilon}_1} \right)^{\frac{1-\mu}{\mu}} \quad (5.38)$$

$$\frac{\partial b}{\partial \dot{\epsilon}_{\text{dev}}^p} = \frac{\partial b}{\partial \dot{\epsilon}_{ij}^p} \frac{\partial \dot{\epsilon}_{ij}^p}{\partial \dot{\epsilon}_{kl}^p} \frac{\partial \dot{\epsilon}_{kl}^p}{\partial \dot{\epsilon}_{\text{dev}}^p} = \sqrt{\frac{3}{2}} \frac{\partial b}{\partial \dot{\epsilon}_{\text{vol}}^p} \quad (5.39)$$

The friction parameter  $b$  can be considered as a tensor for anisotropic materials. For such materials, the uniaxial strain rate  $\dot{\epsilon}$  should be replaced by the total strain-rate tensor  $\dot{\epsilon}_{ij}$ .

In this work, however, the ice friction parameter  $b$  is assumed to be a scalar that is determined from the results of material tests in the direction normal to ice columns. This parameter is then considered to be the same for all the other directions within the material.

Additional tests are required to determine the ice friction tensor in the columnar direction of a columnar ice sample. The material constant  $\mu$  and the reference strain rate  $\dot{\epsilon}_1$  are given in Table 5.2, while the temperature-dependent parameter  $b_1(T)$  can be determined from equation (5.7), Section 5.2.1.2.

The evolution equations for  $p_a^{\text{max}}$ , in the fourth term of equation (5.25), can be written for an isothermal deformation as

$$d p_a^{\text{max}}(T, \dot{\epsilon}_{ij}^p) = \frac{\partial p_a^{\text{max}}}{\partial \dot{\epsilon}_{ij}^p} d \dot{\epsilon}_{ij}^p = \frac{\partial p_a^{\text{max}}}{\partial \dot{\epsilon}_{\text{vol}}^p} d \dot{\epsilon}_{\text{vol}}^p + \frac{\partial p_a^{\text{max}}}{\partial \dot{\epsilon}_{\text{dev}}^p} d \dot{\epsilon}_{\text{dev}}^p \quad (5.40)$$

in which the derivatives of  $b$  can be determined by using equations (5.9) and (3.9) as

$$\frac{\partial p_a^{\text{max}}}{\partial \dot{\epsilon}_{\text{vol}}^p} = \frac{1}{3 \dot{\epsilon}_1} \eta p_a^{\text{max}}(T) \exp\left(-\frac{\dot{\epsilon}}{\dot{\epsilon}_1}\right) \left[ 1 - \exp\left(-\frac{\dot{\epsilon}}{\dot{\epsilon}_1}\right) \right]^{\eta-1} \quad (5.41)$$

$$\frac{\partial p_a^{\text{max}}}{\partial \dot{\epsilon}_{\text{dev}}^p} = \sqrt{\frac{3}{2}} \frac{\partial p_a^{\text{max}}}{\partial \dot{\epsilon}_{\text{vol}}^p} \quad (5.42)$$

Similar to the friction parameter, the parameter  $p_a^{\max}$  is also a tensorial variable. Additional material tests are required to determine this parameter in the columnar direction of a columnar ice sample. The material constant  $\eta$  and the reference strain rate  $\dot{\epsilon}_1$  are given in Table 5.4, while the temperature-dependent parameter  $p_{a1}^{\max}(T)$  can be determined from equation (5.10), Section 5.2.1.3.

Finally, a non-linear differential equation of first order can be obtained in terms of the plastic multiplier  $d\lambda_s^p$  after substitution of equations (5.28) to (5.30), (5.36), (5.37) and (5.40) into (5.25), and by using equations (5.22) as

$$d\lambda_s^p + P_s(t) d\lambda_s^p = Q_s(t) \quad (5.43)$$

where the time-dependent coefficients  $P_s(t)$  and  $Q_s(t)$  can be determined by

$$P_s(t) = \frac{\frac{\partial f_s}{\partial \sigma_{ij}} C_{ijkl}^{ve} \frac{\partial f_s}{\partial \sigma_{kl}}}{\left[ \frac{\partial f_s}{\partial b} \frac{\partial b}{\partial \dot{\epsilon}_{vol}^p} + \frac{\partial f_s}{\partial p_a^{\max}} \frac{\partial p_a^{\max}}{\partial \dot{\epsilon}_{vol}^p} \right] \frac{\partial f_s}{\partial p} - \left[ \frac{\partial f_s}{\partial b} \frac{\partial b}{\partial \dot{\epsilon}_{dev}^p} + \frac{\partial f_s}{\partial p_a^{\max}} \frac{\partial p_a^{\max}}{\partial \dot{\epsilon}_{dev}^p} \right] \frac{\partial f_s}{\partial q}} \quad (5.44)$$

$$Q_s(t) = \frac{\frac{\partial f_s}{\partial \sigma_{ij}} C_{ijkl}^{ve} d\epsilon_{kl}}{\left[ \frac{\partial f_s}{\partial b} \frac{\partial b}{\partial \dot{\epsilon}_{vol}^p} + \frac{\partial f_s}{\partial p_a^{\max}} \frac{\partial p_a^{\max}}{\partial \dot{\epsilon}_{vol}^p} \right] \frac{\partial f_s}{\partial p} - \left[ \frac{\partial f_s}{\partial b} \frac{\partial b}{\partial \dot{\epsilon}_{dev}^p} + \frac{\partial f_s}{\partial p_a^{\max}} \frac{\partial p_a^{\max}}{\partial \dot{\epsilon}_{dev}^p} \right] \frac{\partial f_s}{\partial q}} \quad (5.45)$$

This non-linear equation can be converted to an ordinary differential equation by substituting the last-time-increment magnitudes of the strain-rate tensor into equations (5.38), (5.39), (5.41), and (5.42). The solution of the resulting ordinary differential equation can be obtained using the following integrating factors as

$$d\lambda_s^p = \frac{1}{\mu_s(t)} \int_0^t \mu_s(\tau) Q_s(\tau) d\tau, \quad \mu_s(t) = \text{EXP} \left[ \int_0^t P_s(\tau) d\tau \right] \quad (5.46)$$

### 5.3.2 Plastic flow and hardening rules for cap yield

In Section 5.2.2, an elliptical yield function was presented for ice as a function of two material parameters (internal variables). The principles of effective stress in porous materials and a similar perfect plasticity model are considered. After time differentiating, the consistency condition, in this case, reduces to

$$df_c(\sigma_{ij}, p_a, p_b) = \frac{\partial f_c}{\partial \sigma_{ij}} d\sigma_{ij} + \frac{\partial f_c}{\partial p_a} dp_a + \frac{\partial f_c}{\partial p_b} dp_b = 0 \quad (5.47)$$

in which  $\sigma_{ij}$  denotes the effective stress in porous material, which can be related to the state of stress in solid material by using equation (4.31) for porous material as

$$\sigma_{ij} = (1 - \phi) \sigma_{ij}^m - \beta_{ij} p_v \quad (5.48)$$

where the porosity  $\phi$  and pore pressure  $p_v$  are functions of effective volumetric strain, see Section 4.3 for more details. The gradients of cap-yield function, then, can be determined from equation (5.11) by considering Fig. 5.14 as

$$\left| \frac{\partial f_c}{\partial \sigma_{ij}} n_j \right| = \left[ \left( \frac{\partial f_c}{\partial p} \right)^2 + \left( \frac{\partial f_c}{\partial q} \right)^2 \right]^{\frac{1}{2}} \quad \text{where} \quad \frac{\partial f_c}{\partial p} = \frac{p - p_a}{p_b - p_a} \frac{q_a}{\sqrt{(p_b - p_a)^2 - (p - p_a)^2}}, \quad \frac{\partial f_c}{\partial q} = 1 \quad (5.49)$$

$$\frac{\partial f_c}{\partial p_a} = \frac{q_a}{(p_b - p_a)^2} \frac{(p - p_a)(p - p_b)}{\sqrt{(p_b - p_a)^2 - (p - p_a)^2}} - \frac{\partial q_a}{\partial p_a} \sqrt{1 - \left( \frac{p - p_a}{p_b - p_a} \right)^2} \quad (5.50)$$

$$\frac{\partial f_c}{\partial p_b} = \frac{q_a}{(p_b - p_a)^2} \frac{(p - p_a)^2}{\sqrt{(p_b - p_a)^2 - (p - p_a)^2}} \quad (5.51)$$

in which

$$\frac{\partial q_a}{\partial p_a} = b \left( 1 - \frac{p_a}{p_a^{\max}} \right) \quad (5.52)$$

The term  $\partial f_c / \partial \sigma_{ij}$  in equation (5.47) represents the direction normal to the cap-yield curve having the normal unit-vector  $n_j$  in the meridian plane, which can be determined by

$$\frac{\partial f_c}{\partial \sigma_{ij}} = \frac{\partial f_c}{\partial p} \frac{\partial p}{\partial \sigma_{ij}} + \frac{\partial f_c}{\partial q} \frac{\partial q}{\partial \sigma_{ij}} \quad (5.53)$$

in which, the terms  $\partial p / \partial \sigma_{ij}$  and  $\partial q / \partial \sigma_{ij}$  are given by equations (5.32) and (5.33).

In the first term of equation (5.47), the stress increment can be determined by using Hooke's elastic law for a purely cap-yielding mechanism as

$$d\sigma_{ij} = C_{ijkl}^{ve} (d\varepsilon_{kl}^e + d\varepsilon_{kl}^{ve}) = C_{ijkl}^{ve} (d\varepsilon_{kl} - d\lambda_c^p \frac{\partial f_c}{\partial \sigma_{kl}}) \quad (5.54)$$

in which  $d\lambda_c^p$  denotes the plastic multiplier relevant to the cap-yield envelope  $f_c$ , and the incremental viscoelastic strain is related to elastic deformation by equation (3.36). Here, the time increment is considered to be small enough for the time changes of porosity to be ignored. Hence, the time increment of pore pressure  $dp_v$  in undrained situation can be determined using equation (4.40) as

$$dp_v = -K_{vc} \beta_{ij} d\varepsilon_{ij} \quad (5.55)$$

then

$$\frac{\partial p_v}{\partial \varepsilon_{vol}^p} = -K_{vc} \beta_{kk} \quad (5.56)$$

The third term in equation (5.47) vanishes in an isothermal deformation as the ice melting pressure  $p_b$  is a function of temperature only. The evolution equation for the pressure at maximum shear strength  $p_a$ , in the second term of equation (5.47), can be determined using equation (5.13) as

$$d\mathbf{p}_a(T, \varepsilon_{ij}^p, \dot{\varepsilon}_{ij}^p) = \frac{\partial \mathbf{p}_a}{\partial \varepsilon_{vol}^p} d\varepsilon_{vol}^p + \frac{\partial \mathbf{p}_a}{\partial \dot{\varepsilon}_{vol}^p} d\dot{\varepsilon}_{vol}^p + \frac{\partial \mathbf{p}_a}{\partial \dot{\varepsilon}_{dev}^p} d\dot{\varepsilon}_{dev}^p \quad (5.57)$$

in which the derivative terms can be determined from the similar derivatives of pore pressure and parameter  $p_a^{\max}$ , equations (5.55), (5.41) and (5.42), as

$$\frac{\partial \mathbf{p}_a}{\partial \varepsilon_{vol}^p} = 3 \beta_{kk} \frac{\partial p_v}{\partial \varepsilon_{vol}^p} = -3 K_{Vc} \beta_{kk}^2 \quad (\text{Undrained}), \quad \frac{\partial \mathbf{p}_a}{\partial \varepsilon_{vol}^p} = 0 \quad (\text{Drained}) \quad (5.58)$$

$$\frac{\partial \mathbf{p}_a}{\partial \dot{\varepsilon}_{vol}^p} = (1 - \phi) \frac{\partial p_a^{\max}}{\partial \dot{\varepsilon}_{vol}^p} \quad (5.59)$$

$$\frac{\partial \mathbf{p}_a}{\partial \dot{\varepsilon}_{dev}^p} = (1 - \phi) \frac{\partial p_a^{\max}}{\partial \dot{\varepsilon}_{dev}^p} \quad (5.60)$$

The terms  $d\varepsilon_{vol}^p$ ,  $d\dot{\varepsilon}_{vol}^p$ , and  $d\dot{\varepsilon}_{dev}^p$  can also be determined from equations (5.22) for constrained yield envelope  $f_c$ .

Finally, a non-linear differential equation of first order can be obtained in terms of the plastic multiplier  $d\lambda_c^p$  after substitution of equations (5.50), (5.51), (5.53), (5.54) and (5.57) into (5.47), and by using equation (5.22) as

$$d\lambda_c^p + P_c(t) d\lambda_c^p = Q_c(t) \quad (5.61)$$

where the time-dependent coefficients  $P_c(t)$  and  $Q_c(t)$  can be determined by

$$P_c(t) = \frac{\frac{\partial f_c}{\partial \sigma_{ij}} C_{ijkl}^{ve} \frac{\partial f_c}{\partial \sigma_{kl}} + \frac{\partial f_c}{\partial p_a} \frac{\partial p_a}{\partial \varepsilon_{vol}^p} \frac{\partial f_c}{\partial p}}{\frac{\partial f_c}{\partial p_a} \frac{\partial p_a}{\partial \dot{\varepsilon}_{vol}^p} \frac{\partial f_c}{\partial p} - \frac{\partial f_c}{\partial p_a} \frac{\partial p_a}{\partial \dot{\varepsilon}_{dev}^p} \frac{\partial f_c}{\partial q}} \quad (5.62)$$

$$Q_c(t) = \frac{\frac{\partial f_c}{\partial \sigma_{ij}} C_{ijkl}^{ve} d\varepsilon_{kl}}{\frac{\partial f_c}{\partial p_a} \frac{\partial p_a}{\partial \dot{\varepsilon}_{vol}^p} \frac{\partial f_c}{\partial p} - \frac{\partial f_c}{\partial p_a} \frac{\partial p_a}{\partial \dot{\varepsilon}_{dev}^p} \frac{\partial f_c}{\partial q}} \quad (5.63)$$

This non-linear equation can be converted to an ordinary differential equation by substituting the last-time-increment magnitudes of the strain-rate tensor into equations (5.59) and (5.60). The solution of the resulting equation can be obtained using the following integrating factors as

$$d\lambda_c^p = \frac{1}{\mu_c(t)} \int_0^t \mu_c(\tau) Q_c(\tau) d\tau, \quad \mu_c(t) = \text{EXP} \left[ \int_0^t P_c(\tau) d\tau \right] \quad (5.64)$$

In this type of formulation, the hardening law can be written in general form as

$$dH_\alpha^x = d\lambda_c^p h_\alpha^x \quad (5.65)$$

in which  $H_\alpha^x$  and  $h_\alpha^x$  denote a set of hardening parameters and hardening functions for  $x^{\text{th}}$  plastic flow system, respectively. In the case of cap yielding,  $p_a$  is the unique hardening parameter, which is a function of  $\epsilon_{\text{vol}}^p$ ,  $\dot{\epsilon}_{\text{vol}}^p$ , and  $\dot{\epsilon}_{\text{dev}}^p$ . The hardening function can be written from equations (5.57) to (5.60), and (5.22) as

$$dp_a = 3 d\lambda_c^p K_{vc} \beta_{kk}^2 \frac{\partial f_c}{\partial p} + (1-\phi) d\lambda_c^p \left[ -\frac{\partial p_a^{\text{max}}}{\partial \dot{\epsilon}_{\text{vol}}^p} \frac{\partial f_c}{\partial p} + \frac{\partial p_a^{\text{max}}}{\partial \dot{\epsilon}_{\text{dev}}^p} \frac{\partial f_c}{\partial q} \right] \quad (5.66)$$

which reduces to the following equation for small time increments  $\Delta t$ .

$$dp_a \approx d\lambda_c^p \left\{ \left[ 3 K_{vc} \beta_{kk}^2 - \frac{1-\phi}{\Delta t} \frac{\partial p_a^{\text{max}}}{\partial \dot{\epsilon}_{\text{vol}}^p} \right] \frac{\partial f_c}{\partial p} + \left[ \frac{1-\phi}{\Delta t} \frac{\partial p_a^{\text{max}}}{\partial \dot{\epsilon}_{\text{dev}}^p} \right] \frac{\partial f_c}{\partial q} \right\} \quad (5.67)$$

### 5.3.3 Plastic flow and hardening rules for the tension cut-off

In Section 5.2.3, the tension cut-off function was presented as a function of pressure at tensile strength  $p_t$ . After time differentiating, the consistency condition, in this case, reduces to

$$df_t(\sigma_{ij}, p_t) = \frac{\partial f_t}{\partial \sigma_{ij}} d\sigma_{ij} + \frac{\partial f_t}{\partial p_t} dp_t = 0 \quad (5.68)$$

Again,  $\sigma_{ij}$  denotes the effective stress in porous material, which can be related to the state of stress in solid material by using equation (4.31) or (5.48). The gradients of tension cut-off function can be determined from equation (5.15) by considering Fig. 5.14 as

$$\frac{\partial f_t}{\partial p} = -1, \quad \frac{\partial f_t}{\partial q} = 0 \quad (5.69)$$

$$\frac{\partial f_t}{\partial p_t} = -1 \quad (5.70)$$

The term  $\partial f_t / \partial \sigma_{ij}$  in equation (5.68) represents the direction normal to the tension cut-off having the unit normal  $n_j$  in meridian plane, which can be determined by

$$\frac{\partial f_t}{\partial \sigma_{ij}} = \frac{\partial f_t}{\partial p} \frac{\partial p}{\partial \sigma_{ij}} = -\frac{\partial p}{\partial \sigma_{ij}} \quad (5.71)$$

in which, the term  $\partial p / \partial \sigma_{ij}$  is given by equation (5.32). In the first term of equation (5.68), the stress increment can be determined by using Hooke's elastic law for a purely tensile-yielding mechanism as

$$d\sigma_{ij} = C_{ijkl}^{ve} (d\varepsilon_{kl}^e + d\varepsilon_{kl}^{ve}) = C_{ijkl}^{ve} (d\varepsilon_{kl} - d\lambda_t^p \frac{\partial f_t}{\partial \sigma_{kl}}) = C_{ijkl}^{vp} d\varepsilon_{kl} \quad (5.72)$$

in which  $d\lambda_t^p$  denotes the plastic multiplier relevant to the tension cut-off  $f_t$ ,  $C_{ijkl}^{vp}$  the viscoplastic tangent tensor, and the viscoelastic terms are given in Section 3.4.

The evolution equation for the pressure at tensile strength  $p_t$ , in the second term of equation (5.68), can be determined for an isothermal process as

$$dp_t(T, \dot{\epsilon}_{ij}^p) = \frac{\partial p_t}{\partial \dot{\epsilon}_{dev}^p} d\dot{\epsilon}_{dev}^p \quad (5.73)$$

in which the term  $d\dot{\epsilon}_{dev}^p$  can be determined from equations (5.22) for the constrained yield envelope  $f_t$ , and the derivative term can be related to the pressure at tensile strength of freshwater ice  $p_t^{\max}$  by using equation (5.16) as

$$\frac{\partial p_t}{\partial \dot{\epsilon}_{dev}^p} = (1 - \phi) \frac{\partial p_t^{\max}}{\partial \dot{\epsilon}_{dev}^p} \quad (5.74)$$

The tensile strength of bubble-free ice  $p_t^{\max}$  reported to show no significant variations with strain rate or temperature in the ranges of  $-5^\circ\text{C}$  to  $-20^\circ\text{C}$  and strain rates greater than  $10^{-5} \text{ s}^{-1}$ , Ref. [12]. This assumption is in a good agreement with the ice failure envelopes of Fig. 5.2 and Fig. 5.3. The little strain-rate dependency of this parameter at  $-10^\circ\text{C}$ , however, can be determined by using the test data of Sunder (1989) and by using equation (5.2), see Fig. 2.3, from

$$(p_t^{\max})^2 + 2 p_a^{\max} p_t^{\max} + 2 \frac{P_a^{\max}}{b} (d - q_t) = 0 \quad (5.75)$$

in which, the term  $q_t$  refers to ice shear strength at the tensile pressure  $-p_t$ . This parameter can be formulated as a function of strain rate in ductile region by using the test data of Sunder (1989) given at  $-10^\circ\text{C}$ . In transition and brittle regions, however, no rate-dependency is reported for this parameter. The formulations can also be extended for other temperatures by performing some more tensile tests, thus, may be considered in future.

Finally, a non-linear differential equation of first order can be obtained in terms of the plastic multiplier  $d\lambda_t^p$  after substitution of equations (5.72) and (5.73) into (5.68), and by using equation (5.22) as

$$d\lambda_t^p + P_t(t) d\lambda_t^p = Q_t(t) \quad (5.76)$$

where the time-dependent coefficients  $P_t(t)$  and  $Q_t(t)$  can be determined by

$$P_t(t) = - \frac{\frac{\partial f_t}{\partial \sigma_{ij}} C_{ijkl}^{ve} \frac{\partial f_t}{\partial \sigma_{kl}}}{\frac{\partial f_t}{\partial p_t} \frac{\partial p_t}{\partial \dot{\epsilon}_{dev}^p} \frac{\partial f_t}{\partial q}}, \quad Q_t(t) = - \frac{\frac{\partial f_t}{\partial \sigma_{ij}} C_{ijkl}^{ve} d\epsilon_{kl}}{\frac{\partial f_t}{\partial p_t} \frac{\partial p_t}{\partial \dot{\epsilon}_{dev}^p} \frac{\partial f_t}{\partial q}} \quad (5.77)$$

This non-linear equation can be converted to an ordinary differential equation by substituting the last-time-increment magnitudes of the strain-rate tensor into equation (5.74). The solution of the resulting equation can be obtained by using the integrating factors below

$$d\lambda_t^p = \frac{1}{\mu_t(t)} \int_0^t \mu_t(\tau) Q_t(\tau) d\tau, \quad \mu_t(t) = \text{EXP} \left[ \int_0^t P_t(\tau) d\tau \right] \quad (5.78)$$

For this tension yielding,  $p_t$  is the unique hardening parameter, which is a function of  $\dot{\epsilon}_{dev}^p$ . The hardening function can be written from equations (5.73), (5.74), and (5.22) as

$$dp_t = d\lambda_t^p \left\{ (1 - \phi) \frac{\partial p_t^{\max}}{\partial \dot{\epsilon}_{dev}^p} \frac{\partial f_t}{\partial q} \right\} \quad (5.79)$$

The linear differential equation can also be converted to an algebraic relation for  $d\lambda_t^p$  if the hardening in tension yielding mechanism is ignored, i.e. no rate dependency for  $p_t^{\max}$ .

$$d\lambda_t^p = \frac{\frac{\partial f_t}{\partial \sigma_{mn}} C_{mnpq}^{ve} d\epsilon_{pq}}{\frac{\partial f_t}{\partial \sigma_{rs}} C_{rstu}^{ve} \frac{\partial f_t}{\partial \sigma_{tu}}} \Rightarrow C_{ijkl}^{vp} = C_{ijkl}^{ve} - \frac{C_{ijmn}^{ve} \frac{\partial f_t}{\partial \sigma_{mn}} \frac{\partial f_t}{\partial \sigma_{pq}} C_{pqkl}^{ve}}{\frac{\partial f_t}{\partial \sigma_{rs}} C_{rstu}^{ve} \frac{\partial f_t}{\partial \sigma_{tu}}} \quad (5.80)$$

The constitutive equations (5.36), (5.54), and (5.72) are written for shear, cap, and tension modes of plastic deformation. In these formulations, however, it is not easy to find a straight formulation like equation (5.80) for elastoplastic stiffness matrix at time  $t$  because of the integral equations (5.46), (5.64), and (5.78). However, the tangent moduli can be obtained for each time increment by transforming the integral formulation to a summation and considering the appropriate history functions, see Section 7.2.

#### **5.4 Conclusions**

The plastic behaviour of atmospheric ice is assumed to be somehow modeled by the cap-model plasticity, which is commonly used for geological materials. The plasticity model for this type of porous material is quite complex, involving pressure-sensitive yielding, difference in tensile and compressive strengths, porosity dependency, strain rate and temperature dependency, and the Bauschinger effect. The yield surface, in this multi-surface plasticity model of atmospheric ice, consists of a shear-yield curve, a moving cap, and a tension cutoff segment. The temperature and strain-rate dependencies of the material parameters of those curves are formulated. An associated flow rule is considered for the yield models including one hardening parameter for the cap yield surface and another one for the tension yielding mechanism. The following conclusions are drawn from the analysis of this chapter:

- 1) The shear-yield envelope is considered to be unaffected by porosity and its changes, while the influence of this parameter is considered in plastic deformation through the cap- and the tension-yielding mechanisms.

- 2) A parabolic fixed-shear envelope is used for ice, in which the pressure dependency is described by means of three material parameters: ice cohesion ( $d$ ), ice friction angle ( $\beta$ ), and the hydrostatic pressure at maximum shear strength for bubble-free ice ( $p_a^{\max}$ ). The test results of Jones (1982), Rist and Murrell (1994), and Gagnon and Gammon (1995) are used to formulate those parameters as the functions of temperature and strain rate.
- 3) Ice cohesion is a characteristic of materials, so it is assumed to be a function of temperature only. It is modeled by an exponential function of temperature given by Fish *et al.* (1997) by modifying the coefficients to have a better agreement with the tests data. A small strain-rate dependency, however, is observed for this parameter in the existing test data, which can be applied to the model in future works. The other two material parameters, on the other hand, are further functions of plastic strain rate, which are determined by using the linear and exponential functions of temperature and strain-rate, respectively.
- 4) An elliptical parabolic function, fixed at one end, is used here to simulate the cap-yield envelope of ice, where the pressure dependency of this yield surface can be described by means of two material parameters: the hydrostatic pressure at maximum shear strength ( $p_a$ ), and ice melting pressure ( $p_b$ ).
- 5) Ice-melting pressure is characteristic of the material and a function of temperature only, which is modeled by a linear function of temperature resulting from the Clapeyron equation presented by Fish *et al.* (1997). The hydrostatic pressure at maximum shear strength ( $p_a$ ), on the other hand, is further function of ice porosity ( $\phi$ ), pore pressure( $p_v$ ), and pressure at maximum shear strength of bubble-free ice ( $p_a^{\max}$ ), which are determined by using the principles of effective stress in porous materials.

- 6) The tension cutoff function is described by means of one material parameter: the tensile strength of bubble-free ice ( $p_t^{\max}$ ). This parameter shows no significant variations with strain rate or temperature, especially beyond the ductile region. The strain-rate dependency of this parameter is considered in the cap-model formulation, but not in UMAT subroutine. The strain-rate dependency of this parameter, however, can be considered in future works on the basis of some material tensile tests.
- 7) Ice yield surface is strongly affected by ice structure, while the size of ice grains has no significant influence. Thus, it is required to perform a series of material tests on columnar S1 and S3 ice samples to determine the corresponding material parameters. The effects of porosity, temperature, strain rate, and creep are considered in the presented model for granular and columnar S2 ice.
- 8) The associated flow rules are considered for both plasticity models relevant to fixed-shear and cap-yield surfaces, in which the direction of plastic flow is normal to the yield surface.
- 9) Perfect plastic behaviour is assumed for shear yielding (no hardening parameter), in which the stress is considered to be constant during plastic deformation. For the cap and tension yielding, on the other hand, two hardening rules are proposed for the hardening parameters: the hydrostatic pressure at maximum shear strength ( $p_a$ ) and the tensile strength ( $p_t$ ) of porous ice.

The original contributions of this chapter can then be summarized as:

- 1) Presentation of a new yield envelope for atmospheric ice, taking porosity into account. This envelope consists of three segments: a fixed parabolic shear envelope, an elliptical moving cap, and a tension cutoff.
- 2) Modification of the material constants involved in the formulations of cohesion, friction angle, and melting pressure of bubble-free ice presented by Fish *et al.* (1997) to achieve better agreement with test results. Those parameters are used in the formulation of the fixed-yield envelope of atmospheric ice.
- 3) Description of the material parameters involved in the cap- and tension-yielding mechanisms of atmospheric ice as functions of temperature and strain-rate.
- 4) Presentation of the associated flow rules together with the corresponding hardening rules for each plasticity mechanism.
- 5) Implementation of the developed cap-model plasticity as a user-defined subroutine using the UMAT facilities of ABAQUS Structural Analysis Program.

## CHAPTER 6

### LABORATORY TEXTURE AND GRAIN SIZE OBSERVATIONS

#### 6.1 Introduction

To find the applicability domain of each mathematical model presented in Chapters 3, 4, and 5 for the case of atmospheric ice, the texture and fabric of ice deposits on power lines should be known. A detailed microstructure and air bubble observations were reported by Laforte *et al.* (1983) for the atmospheric ice deposits on electrical power lines. The grain and bubble structures were studied at various meteorological conditions; however, the c-axis orientations still were undetermined in those works. Hence, a series of complementary works were required. Two series of texture observations were performed in this study to determine the preferences of the c-axis orientation in atmospheric ice deposits for a certain meteorological conditions. The atmospheric ice textures are classified in granular and columnar S1, S2, and S3 categories, which is the main contribution of this chapter. This type of classification is proposed by Michel and Ramseier (1971) for sea ice that is used here without losing the generality and by ignoring their terminology.

In one set of the experimental tests, in-cloud riming events were simulated in the horizontal refrigerated wind tunnel, while the freezing rain simulations were performed at

the icing precipitation simulation laboratory, both at CIGELE<sup>1</sup>. Two sets of thin-slice ice samples were prepared in each test, one set in radial cross section and the other in the transverse direction, both with an approximate thickness of 0.5 mm. The texture and air-bubble content of the two sets of ice samples were qualitatively studied using a low magnification microscope equipped with transmitted light and polarized filters.

The term “ice texture” is a commonly-used expression in the ice mechanics branches that refers to the morphology or grain structure of polycrystalline ice, while the term “ice fabric” denotes the c-axis orientations within the single crystals of ice.

Atmospheric ice deposits are naturally formed by the accretion of super cooled water droplets on cold substrates. The most frequent types of atmospheric ice deposits on electrical transmission lines are glaze and hard and soft rime, each having a different texture, and growth conditions. Glaze is the transparent deposit with a density very close to that of pure ice ( $0.917 \text{ g/cm}^3$ ). It can be accreted during a freezing rain event where the bigger droplets, normally between 0.5 and 5mm, have enough time to cover a surface area prior to freezing (wet regime type of ice accretion). Hard rime is less transparent with a density between  $0.700$  to  $0.900 \text{ g/cm}^3$ , while soft rime is white and opaque with a density as low as  $0.600 \text{ g/cm}^3$ . Rime deposits are naturally produced during an in-cloud riming event where the smaller droplets up to maximum size of  $100 \text{ }\mu\text{m}$  freeze on a cold substrate (dry regime type of ice accretion), Ref. [36].

---

<sup>1</sup> La Chaire industrielle sur le givrage atmosphérique des équipements des réseaux électriques (CIGELE)

## 6.2 In-cloud riming simulation in Refrigerated Wind Tunnel

For the purpose of this simulation, a rime deposit was accreted on an aluminum cylinder similar to a Bersimis conductor, 35.1 mm in diameter and 400 mm in length, placed in the middle of the test section of the refrigerated horizontal wind tunnel. The cylinder was insulated on both ends by two pieces of Teflon, each approximately 300mm in length. The assembly was cleaned with alcohol and set in place for two hours while the system was cooling down. The tunnel test section, aluminum cylinder, cylinder rotating equipment and water spray nozzles are shown in Fig. 6.1.

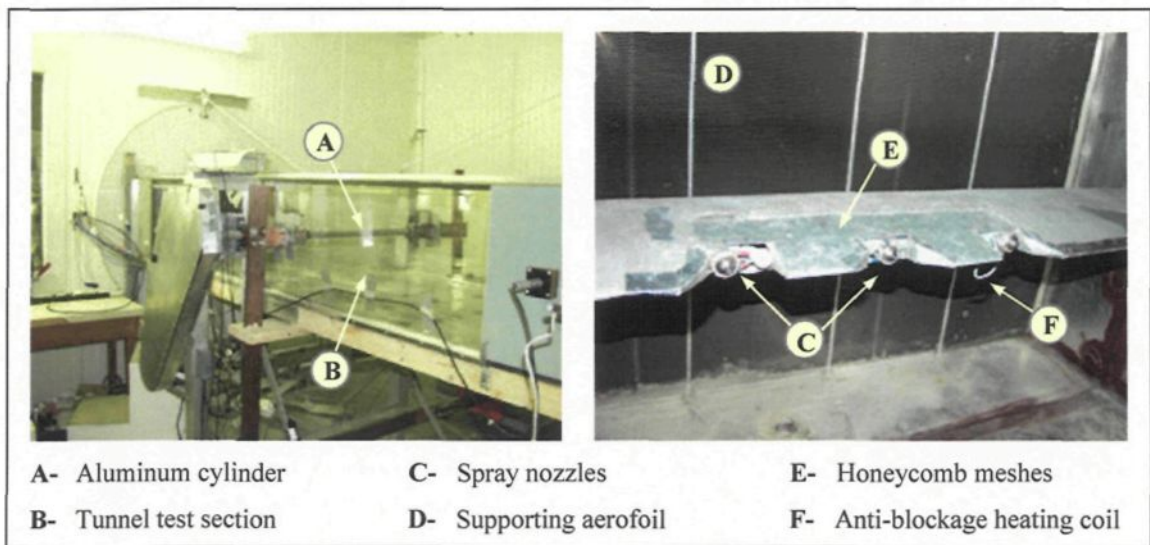


**Fig. 6.1:** Aluminum cylinder placed in test section, and water spraying system of refrigerated wind tunnel.

The controlling factors for simulating the meteorological conditions in the wind tunnel were: (a) air speed ranging from 5 to 20 m/s; (b) conductor rotating speed, from 1 to 5Hz; (c) air temperature, -3 to -9°C; (d) Spray System Co. nozzle type, fluid cap 2050, air cap 67147; and (e) water to air pressure ratio, typically around 55/40. For each combination of the affecting factors, both the liquid water content (LWC) and the water droplet

spectrum were measured. The median volume diameter (MVD) of droplets was calculated from the water droplet spectrum. The droplet size distribution was measured by exposing a glass slide covered by a film of silver colloid at the centre of the test section for a short period of time. The droplets were then counted and measured as to their size under microscope to provide the data for the droplet spectrum. MVD was calculated from the spectrum, which covers the natural range of in-cloud and drizzle icing, up to  $100\ \mu\text{m}$ . The specially designed shutting device and the prepared glass slides are shown in Fig. 6.2.

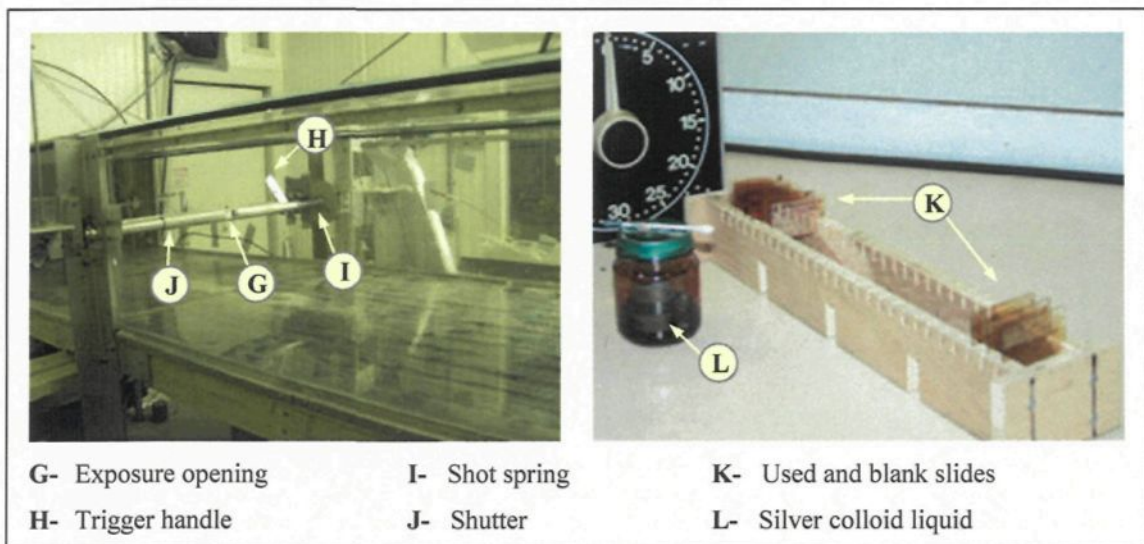


**Fig. 6.2:** Specially-designed shutting device and the glass slides for obtaining the droplet size spectrum.

Liquid water content (LWC) was measured before each ice accumulation using the single rotating cylinder method, and could be varied up to a maximum of  $12\ \text{g}/\text{m}^3$ . The range of  $0.4$  to  $2.0\ \text{g}/\text{m}^3$  was of more interest for simulating the conditions closer to the natural in-cloud riming, where  $P_{\text{mm/hr}} = 3.6 V_{\text{m/s}} \cdot \text{LWC}_{\text{g}_w/\text{m}^3}$  in wind tunnel tests.

The droplet spectrum for the above-mentioned Spray system nozzle at a water pressure of 50 psi for three different air pressures is shown in Fig. 6.3a. The calculated median volume diameter (MVD) is also noted for each spectrum in the figure. In Fig. 6.3b, on the other hand, the variation of liquid water content (LWC) as the function of nozzle pressure difference ( $p_w - p_a$ ) is shown for three different nozzle air pressures ( $p_a$ ), obtained on the basis of the available data from the previous research work carried out at CIGELE at an air speed of 10 m/s.

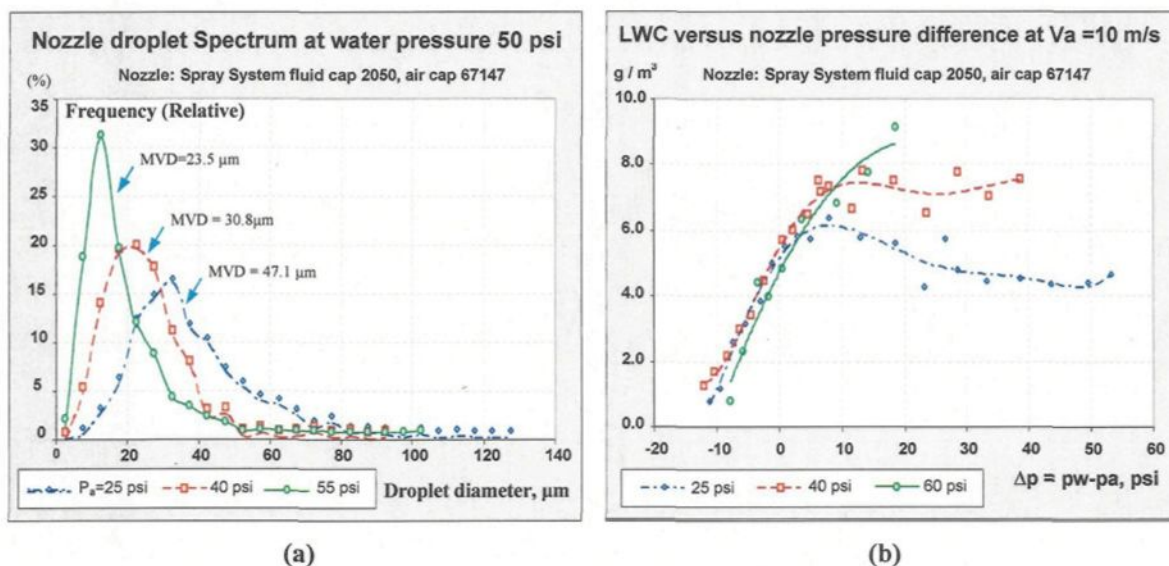


**Fig. 6.3:** a) Droplet spectrum produced by a typical Spray System Nozzle at water pressure 50 psi, b) Liquid water content produced by the same nozzle at an air speed of 10 m/s.

### 6.3 Freezing rain simulation in the icing precipitation simulation laboratory

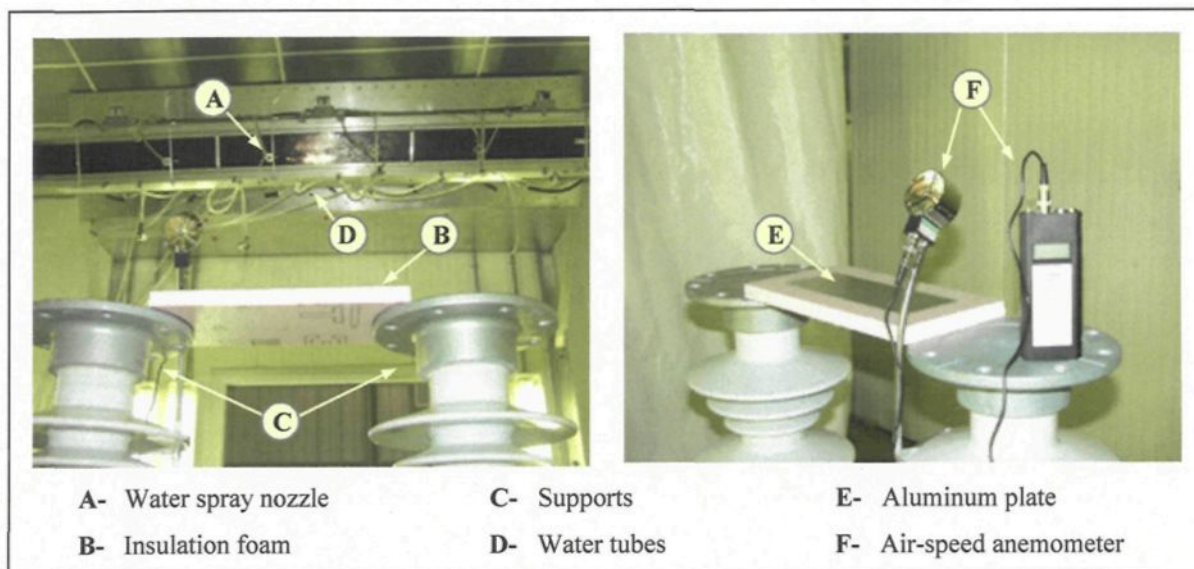
Wind tunnel icing simulation under very wet conditions (higher LWC and air speeds, and bigger droplets) produces icicles and causes the larger droplets to fall down prior to reaching the conductor, mainly due to gravity, Fig. 6.4. In order to obtain more uniform and thicker ice deposits for the freezing-rain simulations, the ice deposits were accumulated on an aluminum plate (3/8"- 110×400 mm<sup>2</sup>) with the same volume per length as a conductor, as shown in Fig. 6.5. The plate was insulated from underneath to simulate the symmetrical boundary conditions existing at the center of the conductor. It should be noted that an aluminum plate was used to try simulating the thermal conditions of an aluminum cylinder as closely as possible. However, a genuine simulation for the cylinder would be much more complex, if not impossible.



Fig. 6.4: Ice accretion in a very wet regime with large droplets in the refrigerated wind tunnel.

Larger water droplets, up to 1mm, were produced and sprayed using a single flat-spray airless nozzle (model H1/4VV-2501). A time-delay system was designed to interrupt the nozzle movement, causing the precipitation rate to vary independently from water droplet size. In addition to nozzle type, the air speed was also kept constant for the tests, so the

controlling factors were (a) air temperature,  $-3$  to  $-9^{\circ}\text{C}$ ; (b) water pressure, 20 to 85 psi (138 to 586 kPa); and (c) time-delay between each nozzle cycle, 1 to 30 seconds.



**Fig. 6.5:** Collector aluminum surface and insulating foam installed in icing simulation room.

The main reason for using the interrupting system is that it makes it possible to simulate precipitation rates close to the normal range of a natural freezing rain event by varying the spraying time interval. As an example, the vertical component of the natural precipitation rate in a freezing rain event normally varies in the range of 0 to 5 mm/hr. The controlling parameters had an influence on the droplet size distribution in addition to the precipitation rate. The droplet size distribution was obtained using the same techniques as those of the riming simulation, as shown in the left-hand side picture of Fig. 6.6.

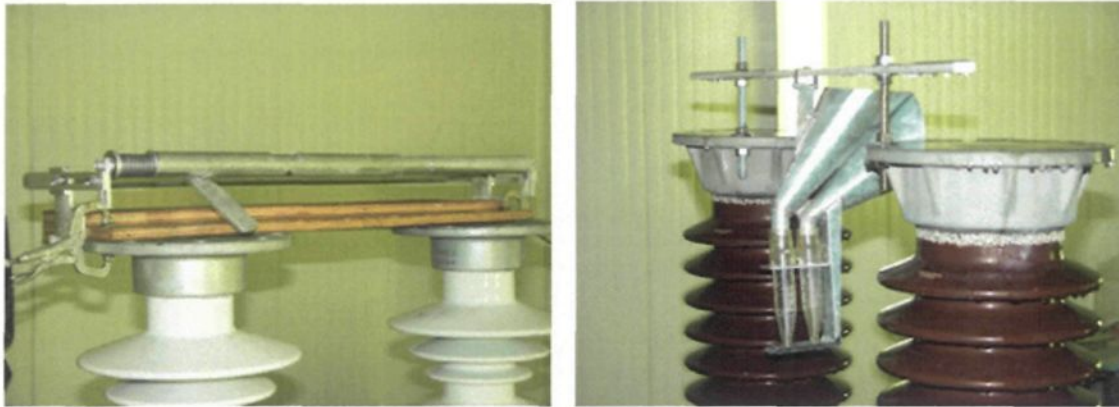


**Fig. 6.6:** Shutting device for obtaining the water droplet size spectrum and the precipitation rate measuring device in icing simulation laboratory.

The precipitation rate was measured by using the standard precipitation measurement device as shown in Fig. 6.6. The spray nozzle system and corresponding delay mechanism are shown in Fig. 6.7, while the resulting charts for the variation of the precipitation rate versus the nozzle water pressure and interrupt time are shown in Fig. 6.8.

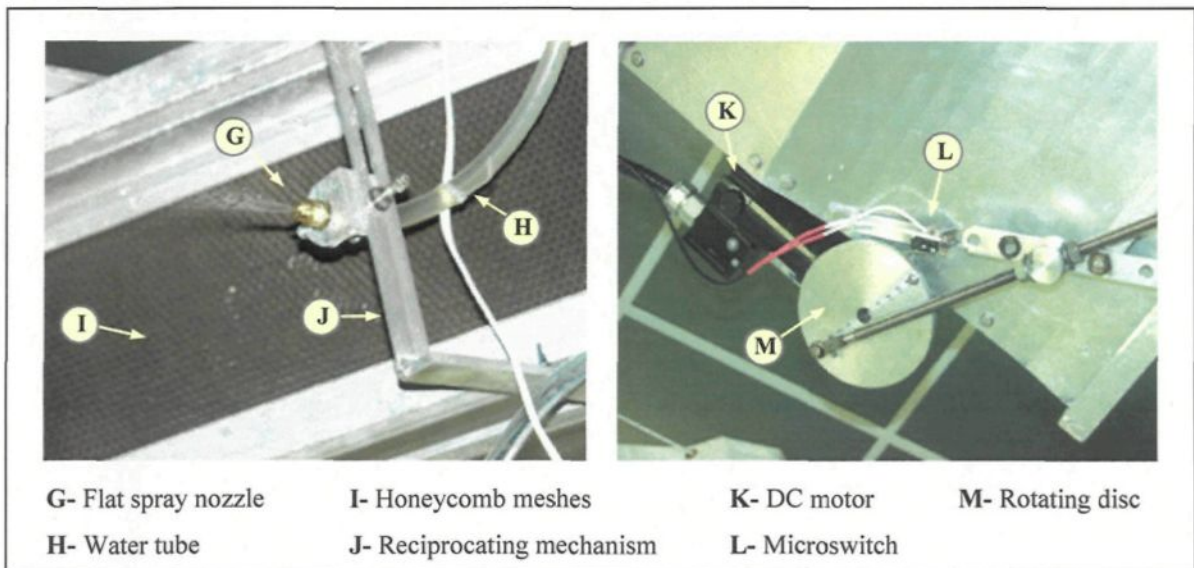


**Fig. 6.7:** Water flat-spray airless nozzle (model H1/4VV-2501) and the delay system installed in icing simulation laboratory for drizzle and freezing rain simulation.

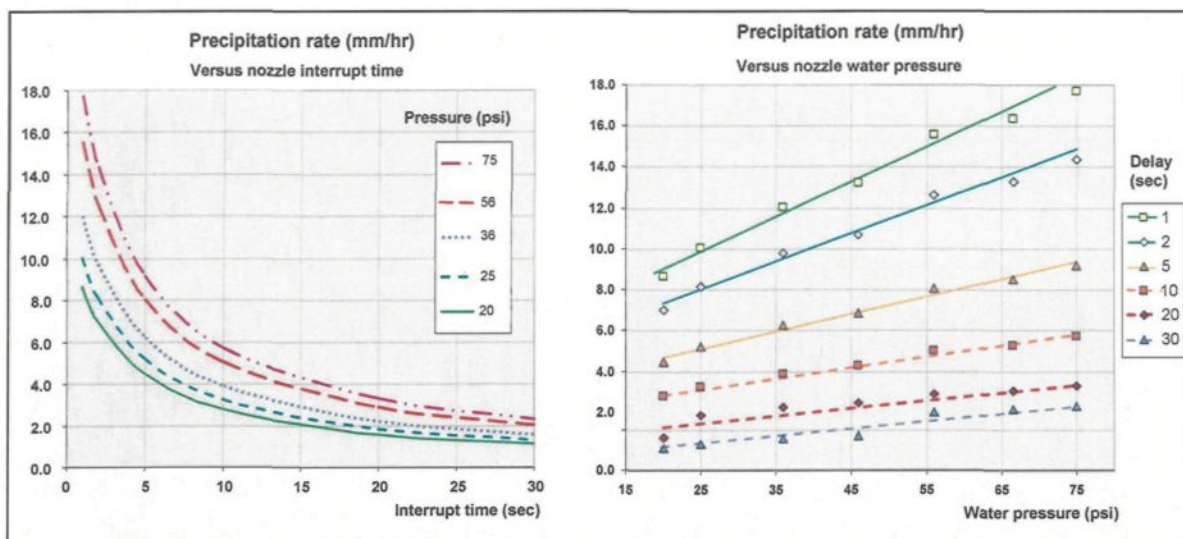


**Fig. 6.8:** Precipitation rate versus nozzle water pressure and interrupt time for flat-spray airless nozzle (model H1/4VV-2501) at room temperature.

#### 6.4 Atmospheric ice texture and fabric

Atmospheric ice is composed of numerous crystals (grains) the c-axis of each being oriented in a certain direction. An individual grain in atmospheric ice may be granular, columnar, feathery, or of a less common form. The size of grains has been usually limited to a range between fine to medium sizes, normally less than 5mm. External factors such as degree of super-cooling, air temperature, precipitation rate, and impurities affect the growth of ice crystals. The mechanical behaviour of atmospheric ice depends highly on its texture, fabric, and bubble structure, which are affected consequently by meteorological conditions. For example, a decrease of only a few degrees in deposit temperature forms rime rather than glaze, or soft rime rather than hard rime, each having very different mechanical properties.

In the next sections, the sample preparation procedure for ice texture and bubble content observations are reviewed first, and then, the atmospheric ice textures are classified on the basis of the observed grain shape and c-axis orientation within ice crystals.

#### 6.4.1 Ice sample preparation

The grain size and air-bubble content for both the radial (vertical) and the transverse (horizontal) directions were qualitatively analyzed for both series of experiments. First, the rough ice sections were cut along the cylinder using a band saw, as shown in Fig. 6.9. From these, two 15-mm thick sections were prepared, one in the radial and the other one in the transverse direction. Then, the thick sections were cut into sizes adequate for the microtome stage plate. The band saw and microtome were placed in a cold chamber for a few hours before they were used to cut the samples.

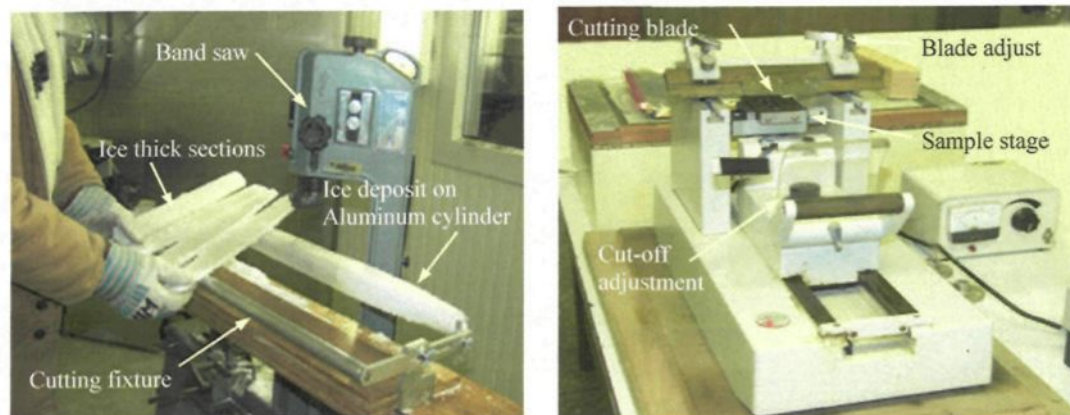


**Fig. 6.9:** Thick section preparation using a band saw and Sledge-type microtome for thin section preparation.

The bottom surface of each resized thick section was processed through a Sledge-type microtome to remove the cutting marks from the band saw, see Fig. 6.9. First, a 4 mm surface layer was cut by microtoming a number of 10- $\mu$ m-thick layers. Then, a 0.6 mm

surface layer, followed by another of 0.4 mm, for a total of 5 mm, were likewise cut by microtoming 5  $\mu\text{m}$ , and 2 to 1  $\mu\text{m}$  layers, respectively. Before cutting each layer, the microtome blade was wiped clean with a soft tissue paper. The thick section was then mounted on a clear glass plate using freezing drops of water at its edges. A slight pressure was then applied to the ice sample to ensure that no water remained on the contact surface. At that point, it became possible to start using the microtome on the top surface of the thick section by removing successive 10  $\mu\text{m}$  layers until a thickness of about 2 mm was finally reached. This was followed by shaving off another cut, first removing 5  $\mu\text{m}$  layers, and then 2 to 1  $\mu\text{m}$  ones, to a final thickness of 0.5 mm. This procedure provided a smooth, clean, and reflective surface. The thin section was then placed on the rotating-stage of a normal microscope equipped with a color camera for texture and bubble-size observations. With ordinary light, the bubble-size distribution of the thin section was obtained using the AVM software, which was calibrated prior to each measurement. The texture and crystallographic orientation of the ice sample were also examined by placing the thin section between crossed Polaroid filters under white light. Depending on the ice type, each crystal of the thin section had a different color and brightness. The c-axis orientation of the black-colored crystals was assumed to be (a) parallel to either one of the Polarized filters, or (b) in the vertical direction. In the former case, the color of the crystal changes as the ice sample turns, while the polarized light passes through the crystal as the ice sample turns without changing its color in the latter case.

### 6.4.2 Classification of atmospheric ice texture

The crystallographic orientation of a polycrystalline material is normally represented by a stereographic projection, also called a Wulff net, Fig. 6.10. In this representation, the SP line originates from South Pole in the c-axis orientation, where point “p” is the projection of this orientation onto the equator plane.

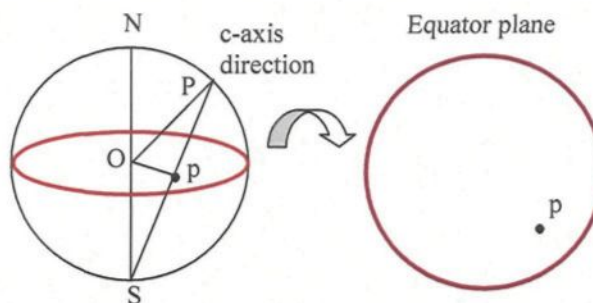


Fig. 6.10: Stereographic representation (Wulff net) of crystal c-axis orientation.

Following the rules set by Michel and Ramseier (1971), the texture of atmospheric ice deposits on power lines is classified into four major categories, described according to deposit temperatures from high to low.

#### 6.4.2.1 Columnar atmospheric ice

This texture is common under a wet growth regime when the deposit temperature is zero at or very close to the melting point (glaze). In this case, the droplets have enough time to spread into a thin water film before freezing. The small air bubbles escape from the water film, thus producing a very clear ice deposit containing a relatively limited number of large bubbles and causing the density to be very close to the corresponding value of pure ice, usually higher than  $0.9 \text{ g/cm}^3$ . Under very wet growth regimes, ice is clear and may contain some large spherical bubbles. The c-axes are randomly oriented in a transverse

plane giving rise to the transverse isotropic behaviour of the material, Fig. 6.11a. This type of ice has almost the same structure as S2 ice with medium to large grains, normally less than 5 mm in diameter. The air temperature ( $T_a$ ) and deposit surface temperature ( $T_s$ ) are higher than  $-6^\circ\text{C}$  and  $0^\circ\text{C}$  for this type of ice accretion, respectively.

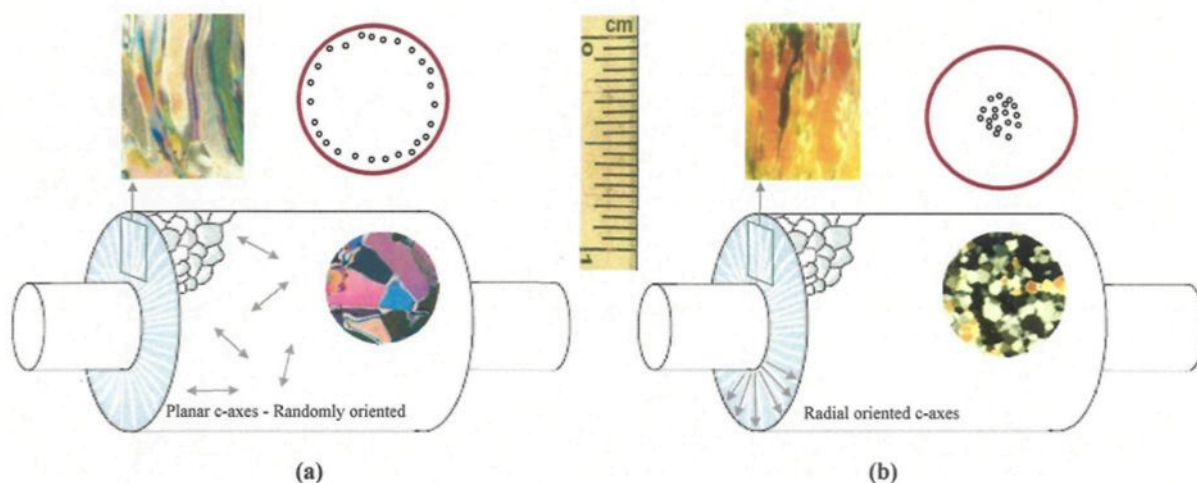


**Fig. 6.11:** Texture, fabric and Wulff net of columnar atmospheric ice (glaze),

(a) Very wet accretion,  $T_a \approx -5^\circ\text{C}$  and Precipitation rate = 2.5 mm/h (S2 ice),

(b) Transition from wet to dry accretion,  $T_a \approx -7^\circ\text{C}$  and Precipitation rate = 1.3 mm/h (S1 ice).

The transition from wet to dry regime occurs as the air temperature, droplet size, or precipitation rate decrease, so that the droplets do not have enough time to spread out. In this case, the c-axes turn to be aligned in the columnar direction, giving rise to the stiffest transverse isotropic behaviour in the material, Fig. 6.11b. This type of ice has almost the same structure as S1 ice with fine to medium grains. The bubbles are smaller but the ice deposit contains more air bubbles than the previous case, where the density varies in a range between 0.9 to a minimum value of  $0.8 \text{ g/cm}^3$ . The deposit surface temperature ( $T_s$ ) is slightly lower than  $0^\circ\text{C}$  for this type of ice accretion.

#### 6.4.2.2 Feathery atmospheric ice

The crystal structure becomes finer and more complex with a columnar feathery appearance at the starting stages of a dry growth regime (hard rime), Fig. 6.12. In this case, the droplets freeze immediately after reaching the surface, and small air bubbles are trapped inside the ice deposit. The resulting ice is opaque and contains a large number of small bubbles causing the density to vary between  $0.7$  and  $0.9 \text{ g/cm}^3$ .

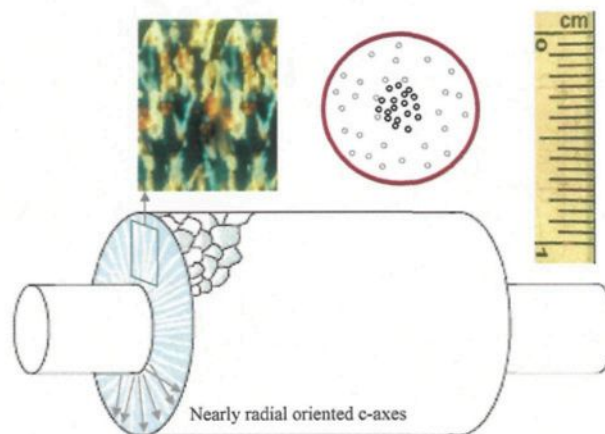


**Fig. 6.12:** Texture, fabric and Wulff net of feathery atmospheric ice, accreted at  $T_a = -10^\circ\text{C}$ ,  $LWC = 1.0 \text{ g/m}^3$ , and air speed =  $10 \text{ m/s}$ .

The c-axis orientation is in the preferred columnar direction and becomes randomly oriented as the deposit temperature decreases (soft rime). The feathery ice has a structure which is columnar to granular, so that it should be considered as a material being between transversely isotropic (hard rime) and nearly isotropic (soft rime). Feathery ice is formed usually at air temperatures below  $-10^\circ\text{C}$ , under a dry growth regime when the deposit temperature is normally around  $-4^\circ\text{C}$ .

### 6.4.2.3 Granular atmospheric ice

The texture and c-axes orientation of granular ice is shown in Fig. 6.13. The c-axes are randomly oriented, so it can be considered as an isotropic material. This type of ice may be found under a very dry growth regime producing a very fine structure, as seen in very soft rime. In this situation, the ice has a rough and opaque appearance, and contains many air bubbles, with a density usually lower than  $0.6 \text{ g/cm}^3$ . Granular ice is formed at very low air temperatures, usually below  $-15^\circ\text{C}$ , with a deposit temperature normally below  $-10^\circ\text{C}$ .

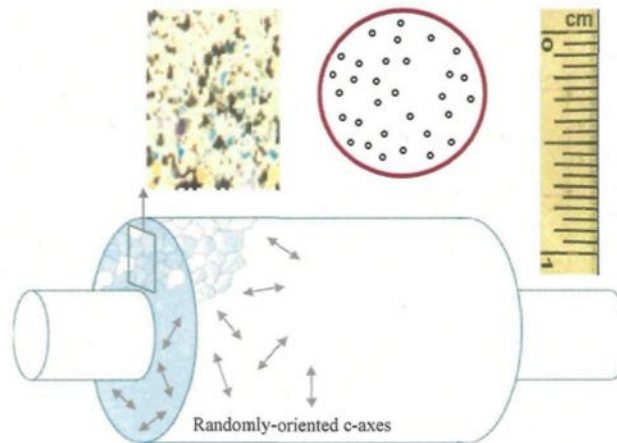


**Fig. 6.13:** Texture, fabric and Wulff net of feathery atmospheric ice, accreted at  $T_a = -20^\circ\text{C}$ ,  $LWC = 0.5 \text{ g/m}^3$ , and air speed =  $5 \text{ m/s}$ .

### 6.4.3 Air bubbles in atmospheric ice

The bubbles nucleate when the concentration of dissolved air in the liquid reaches a critical value at the growth front. Therefore, the air bubble content of atmospheric ice deposits depends on growth conditions, including air temperature, droplet size, and LWC. It may also be related to ice deposit temperature, as shown in Fig. 6.14.

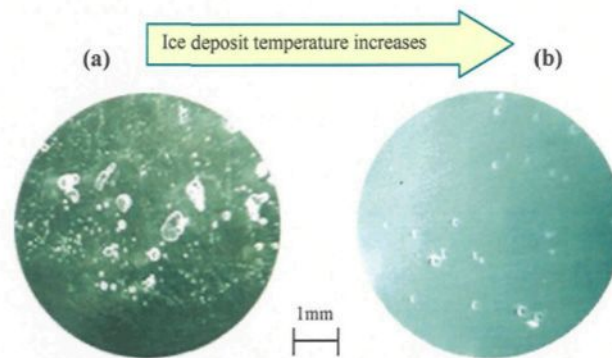


**Fig. 6.14:** Air bubble content at two different deposit temperatures,  
 (a) Transition condition, deposit surface temperature slightly below  $0^{\circ}\text{C}$ ,  
 (b) Wet growth regime, deposit surface temperature  $0^{\circ}\text{C}$ .

## 6.5 Conclusions

In this chapter, the three distinct textures of atmospheric ice observed on power lines are qualitatively described. They are characterized as columnar, feathery, and granular textures, each having its own fabric and mechanical behaviour. External factors such as degree of super-cooling, air temperature, precipitation rate, and impurities affect the growth of ice crystals producing a variety of textures and fabrics for atmospheric ice. On the basis of laboratory observations of this research work, the following conclusions could be drawn:

- 1) Following the rules set by Michel and Ramseier, the texture and fabric of individual grain in atmospheric ice deposits on electrical power lines is classified as columnar (S1, S2, and S3), feathery, and granular based on its grain shape.
- 2) Glaze belongs to the family of columnar ice, S2 in very wet conditions and S1 in transition from wet to dry regime of ice accretion. Hard rime has a feathery structure closer to S1 ice, with granular preference behaviour in very dry situation for soft rime.

- 3) Grain structures up to a maximum width of a few millimeters and normally less than 5 mm were observed for different growth conditions in the icing laboratories, fine to medium.
- 4) From a mechanical point of view, glaze (S2 to S1) and feathery hard rime (nearly S1) can be considered as transversely isotropic materials, while very soft rime with a fine granular or feathery structure may be assumed to be an isotropic material.
- 5) The air-bubble content of atmospheric ice varied from a very low level for glaze to the finer bubbles and higher air-content level characteristic of rime deposits.
- 6) Depending on ice porosity, the density of atmospheric ice varies in a range from 0.917 g/cm<sup>3</sup> for very clear glaze to about 0.6 g/cm<sup>3</sup> for soft rime.

The main contribution of this chapter is the classification of the atmospheric ice deposits on power lines by its grain shape and the c-axis orientations. By this classification, one may choose the appropriate poroelastic or cap-model material parameter formulations at a certain meteorological conditions; i.e. wet, transition, or dry regimes of ice accretion.

## CHAPTER 7

### MODEL ELABORATION AND NUMERICAL RESULTS

#### 7.1 Introduction

The viscoplastic behaviour of atmospheric ice was assumed to be governed by three distinct material deformation mechanisms in ductile region: instantaneous elastic, viscoelastic and plastic deformations. On the basis of test results, the theoretical formulations of each part were given in Chapters 3 to 5 as the functions of temperature, loading and strain rates, ice structure, ice porosity, and some internal state variables. The material descriptions in viscoplastic formulations are in rate form, and thus should be integrated versus time (backward or forward Euler method). In addition, an efficient linearization method (incremental procedure, in this case) should be implemented to solve the system of governing equations. The ABAQUS finite element program is used in this study to solve this system of equations, where the material constitutive equations are specified in ABAQUS by means of a user-defined material specification subroutine (UMAT); see Section 7.3. The next step is the elaboration of the model to some more realistic case studies for simulating the natural forces applied to a piece of accreted ice on overhead power lines. The ice structure observations of Chapter 6 provide good insight into the definition of those case studies.

In this chapter, the time-integration method, the incremental numerical procedures (linearization techniques), the application of UMAT subroutine of ABAQUS program, an introduction to the real loading conditions on power lines, and finally some numerical results, case studies, and model evaluation are presented. The case studies are selected for model elaboration in ductile region, i.e. in the limited ranges of temperature and strain rate.

## 7.2 Numerical implementations

The constitutive relations for infinitesimal viscoplastic deformation of atmospheric ice were given in Chapters 3, 4 and 5. Those equations are in rate form, and thus should be integrated by an efficient time-integration method. The constitutive relations then should be inserted into weak form of balance equations, and the whole system of equations should be spatially integrated over the elements at integration (Gauss) points. In the infinitesimal deformation of this study, however, an incremental procedure seems to be sufficient for time-integrating. In each step, the deformation increments are calculated by using the Jacobian matrix and then the stress increment and plastic variables must be updated. An acceptable algorithm, in any general inelastic problem, should satisfy:

- 1) Consistency with the constitutive relations,
- 2) Numerical stability,
- 3) Incremental plastic consistency,

The highest possible accuracy should be added to the above list; however, it is not strictly required for convergence, Ref. [45].

In the following sub-sections, the numerical considerations in this viscoplastic model are reviewed. The time-integration method is given first, then, the summary of model

formulations together with the numerical implementations of poroelastic, viscoelastic, and plastic models are outlined next. This section also gives a brief description on the model implementation into the UMAT subroutine.

### 7.2.1 Time-integration and incremental procedure

The total strain rate was decomposed into infinitesimal elastic, delayed-viscoelastic, and plastic contributions. The alternative forms of those constitutive equations for any viscoplastic material can be written as

$$\dot{\sigma}_{ij} = C_{ijkl}^x \dot{\epsilon}_{kl}^e = C_{ijkl}^x (\dot{\epsilon}_{kl} - \dot{\epsilon}_{kl}^{ve} - \dot{\epsilon}_{kl}^p) = C_{ijkl}^{ve} (\dot{\epsilon}_{kl} - \dot{\epsilon}_{kl}^p) = C_{ijkl}^{vp} \dot{\epsilon}_{kl} \quad (7.1)$$

in which, the fourth-order tensors  $C_{ijkl}^x$ ,  $C_{ijkl}^{ve}$ , and  $C_{ijkl}^{vp}$  denotes the elastic stiffness tensor and the time-dependent viscoelastic and viscoplastic tangent material stiffness tensors, respectively. The superscript “x”, for the elastic stiffness tensor, can be replaced by “d”, “u”, or “t” in drained, undrained, and transition poroelastic models. The reader is referred to Sections 4.2, 4.3, 3.4, and 5.3 for the terminology of those parameters.

To satisfy the above-mentioned consistency conditions, an incremental procedure seems to be sufficient for the infinitesimal strains of this study with the weak material nonlinearities. According to this algorithm, the discrete constitutive equations can be written as

$$\sigma_{ij}^{n+1} = \sigma_{ij}^n + \int_{t_n}^{t_{n+1}} C_{ijkl}^x (\dot{\epsilon}_{kl} - \dot{\epsilon}_{kl}^{ve} - \dot{\epsilon}_{kl}^p) dt = \sigma_{ij}^n + \int_{t_n}^{t_{n+1}} C_{ijkl}^{ve} (\dot{\epsilon}_{kl} - \dot{\epsilon}_{kl}^p) dt \quad (7.2)$$

$$\Delta \sigma_{ij}^{n+1} = C_{ijkl}^x (\Delta \epsilon_{kl} - \Delta \epsilon_{kl}^{ve} - \Delta \epsilon_{kl}^p) \Big|^{n+1} = C_{ijkl}^{ve} (\Delta \epsilon_{kl} - \Delta \epsilon_{kl}^p) \Big|^{n+1} = C_{ijkl}^{vp} \Delta \epsilon_{kl} \Big|^{n+1} \quad (7.3)$$

where the viscoelastic and plastic terms were given in Sections 3.4, and 5.3. The delayed-viscoelastic contribution is related to elastic strain by equation (3.36). The structural-change function  $\Delta \lambda^{ve}$  was also formulated as a function of initial and current von-Mises

deviatoric plastic strains in Section 2.4.2. Those plastic strains, in turn, must be determined in an iterative procedure. The incremental stress calculations are considered in an iteration procedure and are related with those delayed-viscoelastic and plastic strain formulations required to determine the terms  $\Delta\lambda^{ve}$  and  $\Delta\lambda_x^p$ , see Fig. 7.3 and the flowchart shown in Fig.

7.1. Considering, for example, the plastic strain that is related to the yield surface  $f_x$  by

$$\Delta\varepsilon_{ij}^p = \Delta\lambda_x^p \frac{\partial f_x}{\partial \sigma_{ij}} \quad (7.4)$$

the plastic incremental flow and hardening rules, for this iterative procedure, can be determined from

$$\Delta\varepsilon_{ij}^p|^{n+1} = \varepsilon_{ij}^p|^{n+1} - \varepsilon_{ij}^p|^{n+1} = \Delta\lambda_x^p|^{n+1} \left[ (1-\alpha) \left( \frac{\partial f_x}{\partial \sigma_{ij}} \right)^n + \alpha \left( \frac{\partial f_x}{\partial \sigma_{ij}} \right)^{n+1} \right] \quad (7.5)$$

$$\Delta H_x^{n+1} = \Delta\lambda_x^p|^{n+1} \left[ (1-\alpha) h_x^n + \alpha h_x^{n+1} \right] \quad (7.6)$$

where  $\alpha$  is a parameter ranging from 0 to 1. The method remains explicit by choosing  $\alpha = 0$  (Forward Euler integration scheme), while it is implicit when  $\alpha = 1$  (Backward Euler integration scheme). The latter case is unconditionally stable, while the stability of the former case can be achieved by less number of iterations at very short time-steps. The midpoint rule ( $\alpha = 0.5$ ) known as the Crank-Nicholson scheme are also used frequently for time-integrations. In this study, small time steps are selected to ensure the accuracy of delayed-viscoelastic formulations; thus, the stability of the Backward Euler integration scheme is guaranteed, and implemented. The general incremental procedure of this study is shown as a flowchart in Fig. 7.16.

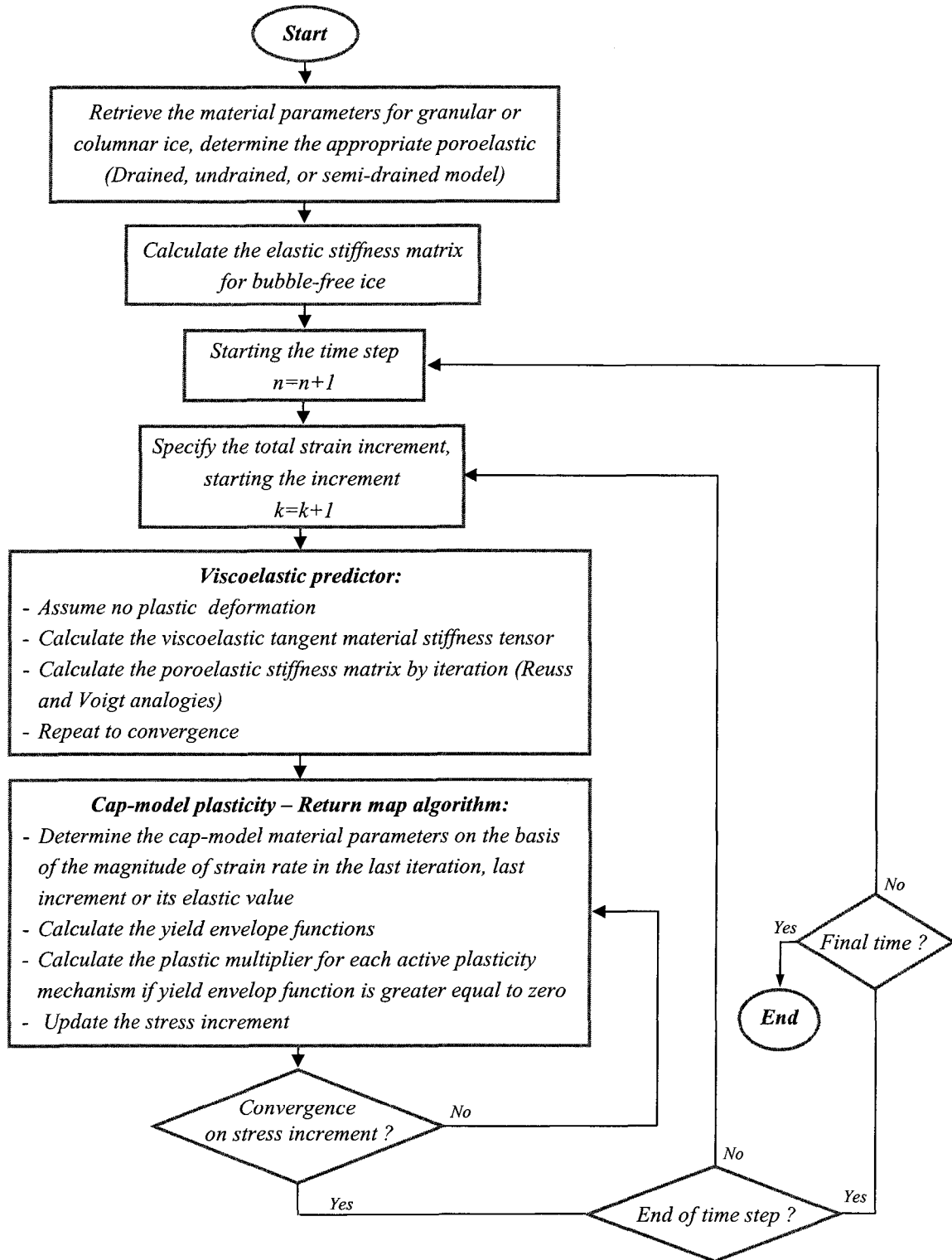


Fig. 7.1: Flowchart of the incremental solution procedure of ice viscoplastic model.

## 7.2.2 Poroelastic model implementation

The influence of ice porosity was applied to the elastic formulations of freshwater ice by means of two extreme situations, namely drained and undrained, see Section 4.3. Two set of poroelastic moduli were determined for each situations by using the Reuss and Voigt analogies. The averaged values were considered as the poroelastic moduli of atmospheric ice at drained or undrained situations. A summary of poroelastic formulations with original equation numbers, as well as the numerical implementation are given as follows:

### Freshwater ice:

(The columnar structure are formed in  $x_3$ -axis direction)

$$\begin{bmatrix} d\varepsilon_{11}^e \\ d\varepsilon_{22}^e \\ d\varepsilon_{33}^e \\ d\gamma_{23}^e \\ d\gamma_{13}^e \\ d\gamma_{12}^e \end{bmatrix} = \begin{bmatrix} \frac{1}{E_1} & -\frac{\nu_{21}}{E_2} & -\frac{\nu_{31}}{E_3} & 0 & 0 & 0 \\ -\frac{\nu_{12}}{E_1} & \frac{1}{E_2} & -\frac{\nu_{32}}{E_3} & 0 & 0 & 0 \\ -\frac{\nu_{13}}{E_1} & -\frac{\nu_{23}}{E_2} & \frac{1}{E_3} & 0 & 0 & 0 \\ 0 & 0 & 0 & \frac{1}{G_{23}} & 0 & 0 \\ 0 & 0 & 0 & 0 & \frac{1}{G_{13}} & 0 \\ 0 & 0 & 0 & 0 & 0 & \frac{1}{G_{12}} \end{bmatrix} \begin{bmatrix} d\sigma_{11} \\ d\sigma_{22} \\ d\sigma_{33} \\ d\sigma_{23} \\ d\sigma_{13} \\ d\sigma_{12} \end{bmatrix} = [S_{ik}^m] \{d\sigma_{kj}\} \quad (7.7)$$

$$E_1 = E_2 = E_p^{S1} = 9.470 (1 - 1.471 \times 10^{-3} \Theta)$$

Columnar S1 ice

$$E_3 = E_t^{S1} = 11.578 (1 - 1.471 \times 10^{-3} \Theta)$$

(for using in semi-drained model – glaze)

$$G_{12} = G_p^{S1} = 3.346 (1 - 1.471 \times 10^{-3} \Theta)$$

(for using in undrained model – hard rime)

$$G_{13} = G_{23} = G_t^{S1} = 2.946 (1 - 1.471 \times 10^{-3} \Theta)$$

$$\nu_{12} = \nu_{21} = \nu_p^{S1} = 0.415$$

$$\nu_{31} = \nu_{32} = \nu_{tp}^{S1} = 0.274$$

$$\nu_{13} = \nu_{23} = \nu_{pt}^{S1} = 0.224$$

(4.4)

$E_1 = E_2 = E_p^{S2} = 9.363 (1 - 1.471 \times 10^{-3} \Theta)$	<b>Columnar S2 ice</b>
$E_3 = E_t^{S2} = 9.551 (1 - 1.471 \times 10^{-3} \Theta)$	(for using in the drained model – glaze)
$G_{12} = G_p^{S2} = 3.528 (1 - 1.471 \times 10^{-3} \Theta)$	
$G_{13} = G_{23} = G_t^{S2} = 3.140 (1 - 1.471 \times 10^{-3} \Theta)$	
$\nu_{12} = \nu_{21} = \nu_p^{S2} = 0.327$	
$\nu_{31} = \nu_{32} = \nu_{tp}^{S2} = 0.319$	
$\nu_{13} = \nu_{23} = \nu_{pt}^{S2} = 0.312$	<b>(4.5)</b>

$E_1 = E_2 = E_3 = E^{iso} = 8.990 (1 - 1.471 \times 10^{-3} \Theta)$	<b>Granular ice</b>
$G_{12} = G_{13} = G_{23} = G^{iso} = 3.386 (1 - 1.471 \times 10^{-3} \Theta)$	(for using in drained model – soft rime)
$\nu_{12} = \nu_{13} = \nu_{23} = \nu_{21} = \nu_{31} = \nu_{32} = \nu^{iso} = 0.328$	<b>(4.3)</b>

**Porous ice:***Drained model:*

$d\varepsilon_{ij}^e = \frac{1}{1-\phi} S_{ijkl}^m d\sigma_{kl}$	<b>(4.22)</b>
$d\zeta = \frac{\phi}{1-\phi} L_{ij}^m d\sigma_{ij}$	<b>(4.23)</b>
$\phi_o = \phi \left[ 1 - \frac{L_{ij}^m d\sigma_{ij}}{1-\phi} \right]$	<b>(4.24)</b>

$d\sigma_{ij} = (1-\phi) C_{ijkl}^m d\varepsilon_{kl}^e$	<b>(4.36)</b>
$d\zeta = \phi C_{ijkl}^m L_{kl}^m d\varepsilon_{ij}^e$	<b>(4.37)</b>
$\phi_o = \phi \left( 1 - C_{ijkl}^m L_{kl}^m \varepsilon_{ij}^e \right)$	<b>(4.38)</b>

Reuss Analogy

Voigt Analogy

*Undrained model:*

$d\varepsilon_{ij}^c = \frac{1}{1-\phi} \left[ S_{ijkl}^m - \frac{\phi^2 K_{Rc}}{1-\phi} L_{ij}^m L_{kl}^m \right] d\sigma_{kl}$	<b>(4.25)</b>
$dp_v = -\frac{\phi K_{Rc}}{1-\phi} L_{ij}^m d\sigma_{ij}$	<b>(4.26)</b>
$\phi = \frac{\rho_{w_o}}{\rho_w} \phi_o$	<b>(4.27)</b>

$d\sigma_{ij} = (C_{ijkl}^d + K_{vc} \beta_{ij} \beta_{kl}) d\varepsilon_{kl}^c$	<b>(4.39)</b>
$dp_v = -K_{vc} \beta_{ij} d\varepsilon_{ij}^c$	<b>(4.40)</b>
$\phi = \frac{\rho_{w_o}}{\rho_w} \phi_o$	<b>(4.41)</b>

The parameters  $L_{ij}^m$ ,  $K_{Rc}$ ,  $K_{vc}$ ,  $K_{Rc}$ ,  $\rho_{w_o}$ ,  $\rho_w$ , and  $\beta_{ij}$  are formulated in Section 4.3, while

the undrained poroelastic implementation procedure is shown as a flowchart in Fig. 7.2.

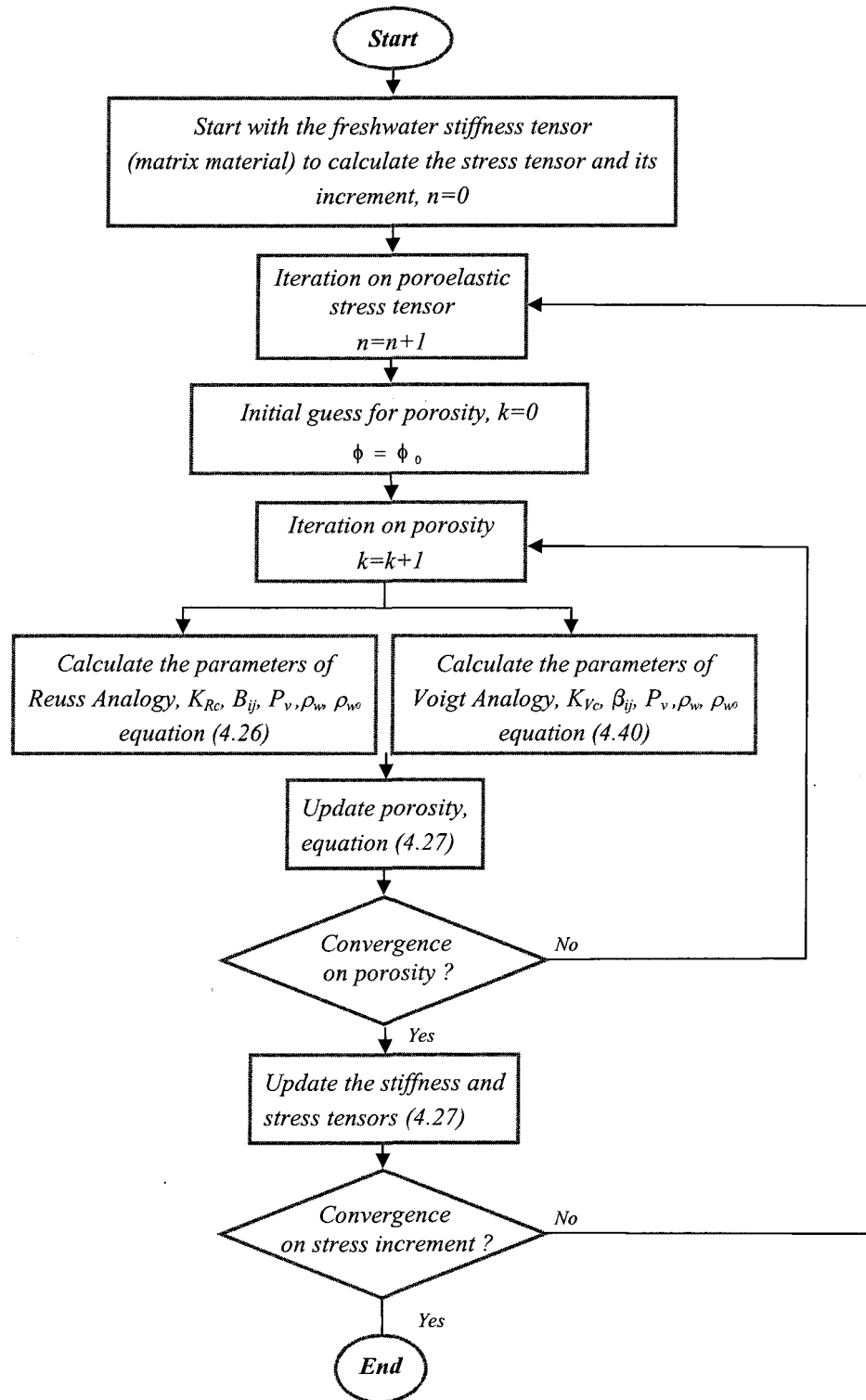


Fig. 7.2: Flowchart of the undrained poroelastic model implementation.

As shown in Fig. 7.2, the undrained poroelastic stiffness tensor is determined through an iterative procedure, on stress and porosity, because the current magnitude of porosity depends on the stress field in porous materials. The drained formulations, on the other hand, lead to a second order algebraic equation in terms of porosity, equation (4.24). The following solution is obtained for this equation, in which the positive sign is not acceptable.

$$\phi = \frac{1}{2} \left( 1 + \phi_0 - L_{ij}^m \sigma_{ij} - \sqrt{(1 + \phi_0 - L_{ij}^m \sigma_{ij})^2 - 4\phi_0} \right) \quad (7.8)$$

The drained stiffness poroelastic tensor then can be determined by using Reuss and Voigt analogies after substituting the porosity calculated from equation (7.9) into equations (4.22) to (4.24) and (4.36) to (4.38).

### 7.2.3 Delayed-viscoelastic model implementation

The delayed-viscoelastic model, as well as the cap-model plasticity (next section), must be implemented through an incremental procedure. A pure viscoelastic deformation is considered as initial guess with  $\Delta\lambda^{ve} = 0$ , equation (7.9), in which the material parameters are given in Table 2.2. The viscoelastic tangent material stiffness tensor  $C_{ijkl}^{ve}$  is then calculated using equation (7.10). Finally, the structural-change function is updated through the Return-mapping plasticity algorithm, see next section and flowchart in Fig. 7.1.

$$\Delta\varepsilon_{ij}^{ve} = \frac{(1 + \Delta\lambda^{ve}) C_1 \varepsilon_{ij}^e}{d_g} \left\{ 1 - \exp[-(a_\tau \Delta t)^b] \right\} \quad (7.9)$$

$$C_{ijkl}^{ve} = \frac{C_{ijkl}^x}{1 + \frac{(1 + d\lambda^{ve}) C_1}{d_g} \left\{ 1 - \exp[-(a_\tau dt)^b] \right\}} \quad (7.10)$$

The stress history of Fig. 7.3 is used as an illustrative example to show the numerical implementation of the delayed-viscoelastic and plastic formulations. The total time is divided into  $N$  (Step) time steps (left figure). The external loading is applied in the form of  $k$  (KInc) stress increments in each time step (right figure). The terms in the parenthesis denotes the corresponding variable names in UMAT subroutine.

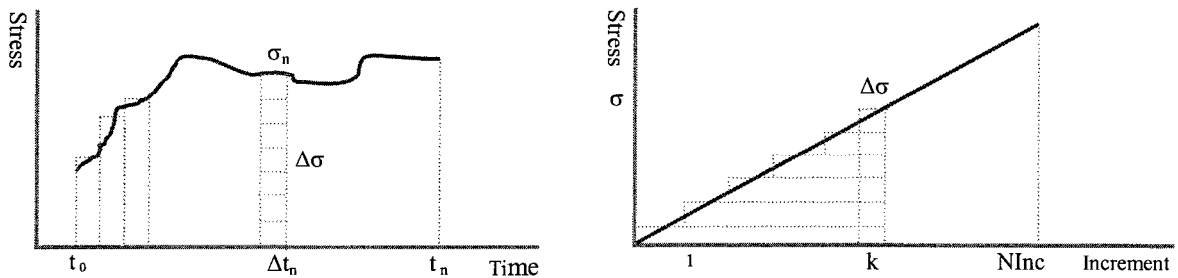


**Fig. 7.3:** Loading scenario and time steps (left), and incremental stress within each time step (right).

The delayed-viscoelastic strain increment was given by equation (7.9). The total viscoelastic strain at time step  $n$ , however, can be determined by following equation by considering the loading memory of last increments.

$$\varepsilon_{ij}^{ve}|^n = \frac{C_1}{d_g} \sum_{k=1}^{Ninc} \left\{ (1 + \Delta\lambda^{ve}) \varepsilon_{ij}^e|^n \left[ 1 - \exp \left[ -\left( a_T \sum_{\ell=k}^{Ninc} \Delta t_\ell \right)^b \right] \right] \right\} \quad (7.11)$$

Equation (7.11) for time step “ $n-1$ ” represents a memory tensor  $\Xi_{ij}^{history}$  for the calculations of next stress increment. In each increment the memory tensor is updated and saved as a state variable for the viscoelastic calculations of next increment, see Section 7.3. An alternative form of equation (7.11) suitable for numerical implementation can be written as

$$\varepsilon_{ij}^{ve}|^k = \Xi_{ij}^{history} + \frac{C_1}{d_g} (1 + \Delta\lambda^{ve}) \varepsilon_{ij}^e|^k \left[ 1 - \exp \left[ -\left( a_T \Delta t \right)^b \right] \right] \quad (7.12)$$

$$\Xi_{ij}^{history} = \frac{C_1}{d_g} \sum_{j=1}^{k-1} \left\{ (1 + \Delta\lambda^{ve}) \varepsilon_{ij}^e|^j \left[ 1 - \exp \left[ -\left( a_T \sum_{\ell=j}^{k-1} \Delta t_\ell \right)^b \right] \right] \right\} \quad (7.13)$$

### 7.2.4 Cap-model plasticity algorithm

The cap-model plasticity is implemented by an iterative procedure in each increment of every time step. The stress or strain increment is first calculated by a viscoelastic predictor algorithm. The material parameters of the cap-model, as well as the yield functions are determined to calculate the plastic multiplier of each active plasticity mechanism. The stress tensor then is calculated and its location in yield envelope is specified, star points in Fig. 7.4. This iterative procedure will end for the negative yield functions as the stress point is lied down in viscoelastic region 6. The return-mapping algorithm will be started for the plasticity mechanisms for which the yield functions are zero or positive. In Fig. 7.4, the tension yield mechanism is the only active plastic model if the stress point lies down in region 1, while the shear or cap yielding mechanism is active if the stress point lies down in regions 3 or 5, respectively. Two yielding mechanisms are simultaneously active in other regions, the tension and shear yielding in region 2, and the shear and cap yielding mechanisms in region 4.

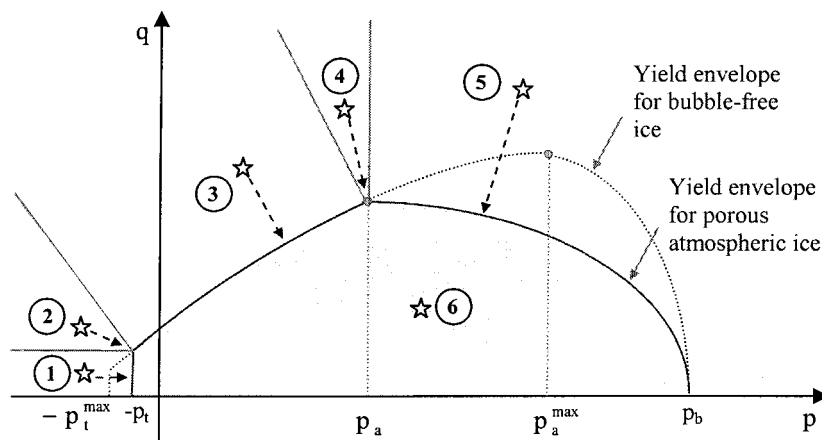


**Fig. 7.4:** The modes of cap-model: (1) pure tension yield, (2) tension-shear yields, (3) pure shear yield, (4) shear-cap yields, (5) pure cap yield, and (6) pure viscoelastic deformation.

A summary of the cap-model formulations is given below, while the iterative flowchart for this incremental plasticity model is presented in Fig. 7.5.

**Ice failure (yield) envelope :**

*Shear-yield curve:*

$$f_s(\sigma_{ij}, p_a^{\max}, d, b) = q - d - bp + \frac{b}{2p_a^{\max}} p^2 = 0 \quad \text{for} \quad -p_t \leq p \leq p_a \quad (5.2)$$

*Cap-yield curve:*

$$f_c(\sigma_{ij}, p_a, p_b) = q - \frac{q_a}{p_b - p_a} \sqrt{(p_b - p_a)^2 - (p - p_a)^2} = 0 \quad \text{for} \quad p_a \leq p \leq p_b \quad (5.11)$$

*Tension-yield curve:*

$$f_t = -p_t - p = 0 \quad (5.15)$$

*Material parameters of shear-yield curve:*

$$d(T) = d_0 \exp\left(\alpha \left[1 - \frac{T}{T_m}\right]\right) \quad (5.3)$$

$$b(T, \dot{\epsilon}) = b_1(T) \left(\frac{\dot{\epsilon}}{\dot{\epsilon}_1}\right)^{\frac{1}{\mu}}, \quad b_1(T) = b_0 \exp\left(\gamma \left[1 - \frac{T}{T_m}\right]^{\nu}\right) \quad (5.6), (5.7)$$

$$p_a^{\max}(T, \dot{\epsilon}) = p_{a1}^{\max}(T) \left\{1 - \exp\left(-\frac{\dot{\epsilon}}{\dot{\epsilon}_1}\right)\right\}^{\eta}, \quad p_{a1}^{\max}(T) = p_{a0}^{\max} \exp\left(\lambda \left[1 - \frac{T}{T_m}\right]^{\delta}\right) \quad (5.9), (5.10)$$

*Material parameters of cap-yield curve:*

$$q_a = d + b p_a - \frac{b}{2p_a^{\max}} p_a^2 \quad (5.12)$$

$$p_a = (1 - \phi) p_a^{\max} + 3 \beta_{kk} p_v, \quad p_a^0 = (1 - \phi_0) p_a^{\max} \quad (5.13)$$

$$p_b = \frac{T_m - T}{A} \quad (5.14)$$

*Material parameters of cap-yield curve:*

$$p_t = (1 - \phi) p_t^{\max} \quad (5.16)$$

in which the material constants are tabulated in Table 5.1 to Table 5.4.

**Plastic flow rules :**

$$d\epsilon_{ij}^p = \sum_{x=s,c,t} d\lambda_x^p \frac{\partial f_x}{\partial \sigma_{ij}}, \quad (5.17)$$

$$d\lambda_x^p = \frac{1}{\mu_x(t)} \int_0^t \mu_x(\tau) Q_x(\tau) d\tau, \quad \mu_x(t) = \text{EXP} \left[ \int_0^t P_x(\tau) d\tau \right] \quad (5.46), (5.64), (5.78)$$

in which the subscript “x” should be replaced by “s”, “c”, or “t” for shear-, cap-, or tension-yielding mechanism, respectively. The time-dependent functions  $P_x(t)$  and  $Q_x(t)$  are given for shear-, cap-, and tension-yielding by equations (5.44), (5.45), (5.62), (5.63), and (5.78), Sections 5.3.1 to 5.3.3.

**Plastic hardening rules :***Cap-yield:*

$$dp_a = 3 d\lambda_c^p K_{vc} \beta_{kk}^2 \frac{\partial f_c}{\partial p} + (1-\phi) d\lambda_c^p \left[ -\frac{\partial p_a^{\max}}{\partial \dot{\epsilon}_{vol}^p} \frac{\partial f_c}{\partial p} + \frac{\partial p_a^{\max}}{\partial \dot{\epsilon}_{dev}^p} \frac{\partial f_c}{\partial q} \right] \quad (5.66)$$

*Tension-yield:*

$$dp_t = d\lambda_t^p \left\{ (1-\phi) \frac{\partial p_t^{\max}}{\partial \dot{\epsilon}_{dev}^p} \frac{\partial f_t}{\partial q} \right\} \quad (5.79)$$

The time integrals in the above equations (5.46), (5.64), and (5.78) are replaced by summation terms in numerical implementation procedure, equations (7.14) and (7.15). Two memory functions then should be considered for each yielding mechanism as state variables in UMAT subroutine to take the plastic deformation history into account.

$$\mu_x^n(t) = \text{EXP} \left[ \sum_{n=1}^N P_x^n(t) \Delta t_n \right] = \text{EXP} \left[ P_x^{\text{history}} + P_x^n(t) \Delta t_n \right] \quad (7.14)$$

$$d\lambda_x^p = \frac{1}{\mu_x^n(t)} \sum_{n=1}^N \mu_x^n(t) Q_x^n(t) \Delta t_n = \frac{1}{\mu_x^n(t)} \Gamma_x^{\text{history}} + Q_x^n(t) \Delta t_n \quad (7.15)$$

$$\text{in which } P_x^{\text{history}} = \sum_{\ell=1}^{n-1} P_x^\ell(t) \Delta t_\ell \quad \text{and} \quad \Gamma_x^{\text{history}} = \sum_{\ell=1}^{n-1} \mu_x^\ell(t) Q_x^\ell(t) \Delta t_\ell .$$

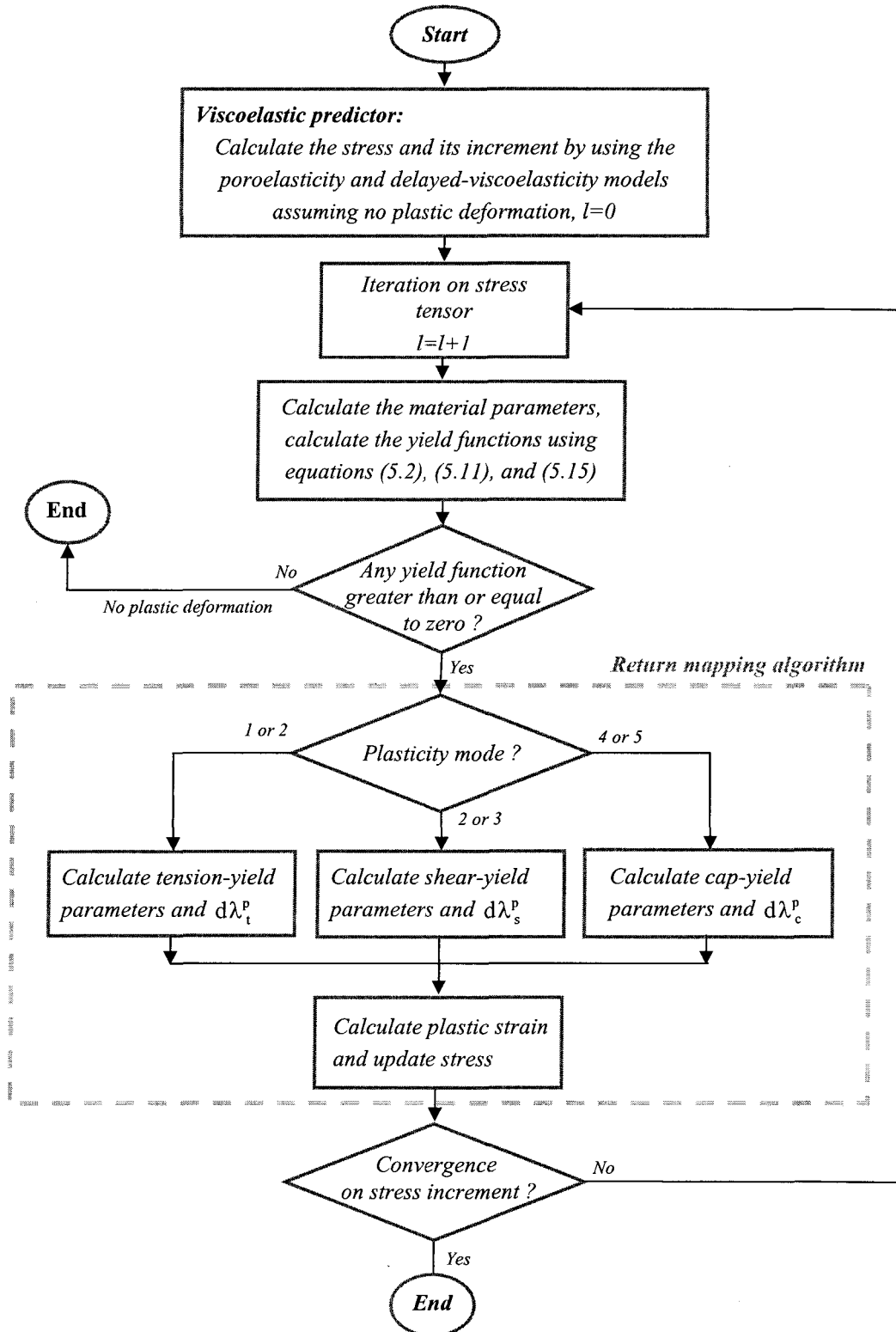


Fig. 7.5: Flowchart of the incremental cap-model numerical implementation.

### 7.3 UMAT Subroutine in ABAQUS Program

The viscoplastic constitutive equations of porous ice are applied to ABAQUS Finite Element Program by means of a user-defined subroutine (UMAT) in FORTRAN programming language. This UMAT subroutine is listed in Appendix 2. The numerical computations are performed by ABAQUS/Standard for static and dynamic simulations. For impulse loading, on the other hand, the material subroutine VUMAT of ABAQUS/Explicit could be used in future. The brief explanation of the UMAT subroutine including the utility interface and the derivation of material Jacobian matrix are given in this section. This subroutine will be called at every material point in each iteration of every increment. Storage space should be allocated for material constants (PROPS) and solution-dependent state variables (STATEV). Any other mechanical material properties included in the same material definition (except thermal expansion, heat transfer properties, and density) will be ignored. The following option can be used to specify a user-defined material specification in ABAQUS input file, Ref. [2]:

```
*USER MATERIAL, TYPE=MECHANICAL,
CONSTANTS = number_of_constants, UNSYMM
```

where “number\_of\_constants” is the total number of material constants appearing in the material constitutive equations (NPROPS variable), and the option “UNSYMM” should be used when the Jacobian matrix  $\partial\Delta\sigma/\partial\Delta\varepsilon$  is not symmetric, for example when non-associate flow rule is implemented to the plasticity model that is not the case of this study. The material parameters should be entered right after the above-mentioned lines, eight data

per line. The values of the following variables are passed into UMAT at the beginning of every increment:

- 1) Total time, step time, and time increment (*TIME (1)*, *TIME (2)*, and *DTIME*).
- 2) Cauchy stress tensor (effective stress, for porous materials) (*STRESS (NTENS)*), in which *NTENS* refers to the number of stress component entered into formulation.
- 3) Solution-dependent state variables and their increments (*STATEV (NSTATV)*),  
     \**Depvar*  
     *number\_of\_state\_variables*
- 4) Pre-defined field variables (Temperature, in this case) and its increment (*TEMP*, *DTEMP*).
- 5) Strain and strain increment (*STRAN (NTENS)*, *DSTRAN (NTENS)*).

The following quantities have to be updated in the UMAT subroutine in each increment:

- 1) The state of stress (*STRESS (NTENS)*),  $\sigma_{ij}^{n+1} = \sigma_{ij}^n + \Delta\sigma_{ij}^{n+1}$ .
- 2) The values of solution-dependent state variables (*STATEV (NSTATV)*).
- 3) Material Jacobian matrix (*DDSDDE (NTENS, NTENS)*),  $\partial\Delta\sigma/\partial\Delta\varepsilon$ .

The magnitude of specific elastic strain energy, and creep and plastic dissipations can be updated in UMAT subroutine without any influence on the numerical solution.

The material constants (*PROPS*) and the state variables (*STATEV*) defined in the UMAT subroutine of this study are tabulated in Table 7.1

**Table 7.1:** Material constants (PROPS) defined in UMAT subroutine.

Description	Symbol	Number	Granular ice	Columnar S1 ice	Columnar S2 ice	Unit
Young's modulus at 0°C, column direction	$E_{11}$	PROPS (1)	$8.990 \times 10^9$	$11.578 \times 10^9$	$9.551 \times 10^9$	Pa
Young's modulus at 0°C, in isotropic plane	$E_{22}$	PROPS (2)	$8.990 \times 10^9$	$9.470 \times 10^9$	$9.363 \times 10^9$	Pa
Young's modulus at 0°C, in isotropic plane	$E_{33}$	PROPS (3)	$8.990 \times 10^9$	$9.470 \times 10^9$	$9.363 \times 10^9$	Pa
Shear modulus at 0°C, lateral plane	$G_{12}$	PROPS (4)	$3.386 \times 10^9$	$2.946 \times 10^9$	$3.140 \times 10^9$	Pa
Shear modulus at 0°C, lateral plane	$G_{13}$	PROPS (5)	$3.386 \times 10^9$	$2.946 \times 10^9$	$3.140 \times 10^9$	Pa
Shear modulus at 0°C, isotropic plane	$G_{23}$	PROPS (6)	$3.386 \times 10^9$	$3.346 \times 10^9$	$3.528 \times 10^9$	Pa
Poisson's ratio at 0°C, lateral plane	$\nu_{12}$	PROPS (7)	0.328	0.274	0.319	---
Poisson's ratio at 0°C, lateral plane	$\nu_{21}$	PROPS (8)	0.328	0.224	0.312	---
Poisson's ratio at 0°C, lateral plane	$\nu_{13}$	PROPS (9)	0.328	0.274	0.319	---
Poisson's ratio at 0°C, lateral plane	$\nu_{31}$	PROPS (10)	0.328	0.224	0.312	---
Poisson's ratio at 0°C, isotropic plane	$\nu_{23}$	PROPS (11)	0.328	0.415	0.327	---
Poisson's ratio at 0°C, isotropic plane	$\nu_{32}$	PROPS (12)	0.328	0.415	0.327	---
Elastic temperature coefficient in (4.3) ...	---	PROPS (13)	$1.471 \times 10^{-3}$	$1.471 \times 10^{-3}$	$1.471 \times 10^{-3}$	$^{\circ}\text{C}^{-1}$
Initial porosity	$\phi_0$	PROPS (14)	0.13 - 0.35	0.05 - 0.13	0 - 0.05	---
Poroeastic mode, 1 drained, 2 undrained,	---	PROPS (15)	1	2 or 3	1	---
Grain size	$d_g$	PROPS (16)	< 1.0	1.0 - 5.0	1.0 - 5.0	mm
Iteration factor	$\alpha$	PROPS (17)	1.0	1.0	1.0	---
Material constant in delayed-viscoelasticity	$C_1$	PROPS (18)	$9.0 \times 10^{-3}$	$9.0 \times 10^{-3}$	$9.0 \times 10^{-3}$	---
Material constant in delayed-viscoelasticity	b	PROPS (19)	0.34	0.34	0.34	---
Material constant in delayed-viscoelasticity	$a_{T_0}$	PROPS (20)	$2.5 \times 10^{-4}$	$2.5 \times 10^{-4}$	$2.5 \times 10^{-4}$	$\text{s}^{-1}$
Activation creep energy	$Q_a$	PROPS (21)	$66.9 \times 10^3$	$66.9 \times 10^3$	$66.9 \times 10^3$	J.mole <sup>-1</sup>
Material constant in structural-change func.	$A_\lambda$	PROPS (22)	$7.5 \times 10^5$	$7.5 \times 10^5$	$7.5 \times 10^5$	s
Material constant in structural-change func.	$B_\lambda$	PROPS (23)	$1.9 \times 10^4$	$1.9 \times 10^4$	$1.9 \times 10^4$	s
Ref. temperature in viscoelasticity model	$T_0$	PROPS (24)	263.16	263.16	263.16	$^{\circ}\text{K}$
Ice cohesion at melting point	$d_0$	PROPS (25)	$0.875 \times 10^6$	$3.10 \times 10^6$	$3.10 \times 10^6$	Pa
Material constant in ice cohesion	$\alpha$	PROPS (26)	12.78	9.61	9.61	---
Melting temperature	$T_m$	PROPS (27)	273.16	273.16	273.16	$^{\circ}\text{K}$
Material constant in ice friction parameter	$b_0$	PROPS (28)	0.10	0.15	0.15	---
Ref. temperature in cap-model plasticity	$T_0$	PROPS (29)	261.36	261.36	261.36	$^{\circ}\text{K}$
Material constant in ice friction parameter	$\gamma$	PROPS (30)	2.70	4.05	4.05	---

Material constant in ice friction parameter	$\nu$	PROPS (31)	0.35	0.25	0.25	---
Material constant in ice friction parameter	$\mu$	PROPS (32)	4.20	5.20	5.20	---
Ref. strain rate in cap-plasticity model	$\dot{\epsilon}_1$	PROPS (33)	$1.4 \times 10^{-4}$	$5.4 \times 10^{-3}$	$5.4 \times 10^{-3}$	$s^{-1}$
Material constant in ice pressure at max. st.	$p_{a0}^{\max}$	PROPS (34)	$21.50 \times 10^6$	$25.50 \times 10^6$	$25.50 \times 10^6$	Pa
Material constant in ice pressure at max. st.	$\lambda$	PROPS (35)	1.75	1.95	1.95	---
Material constant in ice pressure at max. st.	$\delta$	PROPS (36)	0.55	0.50	0.50	---
Material constant in ice pressure at max. st.	$\eta$	PROPS (37)	0.40	0.25	0.25	---
Material constant in melting pressure	A	PROPS (38)	$0.0908 \times 10^{-6}$	$0.0908 \times 10^{-6}$	$0.0908 \times 10^{-6}$	$^{\circ}K Pa^{-1}$
Tension strength pressure of freshwater ice	$p_t^{\max}$	PROPS (39)	$1.0 \times 10^6$	$1.0 \times 10^6$	$1.0 \times 10^6$	Pa

**Table 7.2:** State variables (STATEV) defined in UMAT subroutine.

Description	Symbol	Number	Initial value	Unit
Component of viscoelastic memory tensor	$\Xi_{11}^{\text{history}}$	STATEV (1)	0.0	---
Component of viscoelastic memory tensor	$\Xi_{22}^{\text{history}}$	STATEV (2)	0.0	---
Component of viscoelastic memory tensor	$\Xi_{33}^{\text{history}}$	STATEV (3)	0.0	---
Component of viscoelastic memory tensor	$\Xi_{12}^{\text{history}}$	STATEV (4)	0.0	---
Component of viscoelastic memory tensor	$\Xi_{13}^{\text{history}}$	STATEV (5)	0.0	---
Component of viscoelastic memory tensor	$\Xi_{23}^{\text{history}}$	STATEV (6)	0.0	---
Memory function in shear-yield mechanism	$P_s^{\text{history}}$	STATEV (7)	0.0	---
Memory function in shear-yield mechanism	$\Gamma_s^{\text{history}}$	STATEV (8)	0.0	---
Memory function in cap-yield mechanism	$P_c^{\text{history}}$	STATEV (9)	0.0	---
Memory function in cap-yield mechanism	$\Gamma_c^{\text{history}}$	STATEV (10)	0.0	---
Memory function in tension-yield mechanism	$P_t^{\text{history}}$	STATEV (11)	0.0	---
Memory function in tension-yield mechanism	$\Gamma_t^{\text{history}}$	STATEV (12)	0.0	---
The structural change function of viscoelasticity	$d\lambda^{\text{ve}}$	STATEV (13)	0.0	---
Elastic strain at the end of increment	$\epsilon_{ij}^e$	STATEV (14) – (19)	0.0	---
Viscoelastic strain at the end of increment	$\epsilon_{ij}^{\text{ve}}$	STATEV (20) – (25)	0.0	---
Plastic strain at the end of increment	$\epsilon_{ij}^p$	STATEV (26) – (31)	0.0	---

## 7.4 Numerical results and model evaluation

The theoretical formulations of this model, Chapters 3, 4, and 5, are implemented into ABAQUS Finite Element Program by using a user material specification subroutine UMAT in FORTRAN language. In two subsequent sections, some of the results are reviewed and compared with available test data for freshwater and porous ice types. The variations of poroelastic moduli with porosity are given first. The freshwater and porous ice failure (yield) envelopes of this study are presented next. The effects of porosity on cap-yield are also given in this section. The cap-model yield (failure) envelope of this study shows a good agreement with the available test data of Jones (1982), Rist and Murrell (1994), and Gagnon and Gammon (1995). In this section, the strain-rate, temperature, and porosity dependencies of granular and columnar ice yield envelopes are investigated.

### 7.4.1 Strain-rate dependency of ice yield envelope

The strain-rate dependency of the yield curves for granular ice in the range of  $10^{-6}$  to  $10^{-2}$  at  $-11.8^{\circ}\text{C}$  (ductile to transient) is shown in Fig. 7.6. The curves are in the good agreements with the tests data of Jones (1982) for isotropic ice.

The similar trend for strain-rate dependency of columnar S2 ice is shown in Fig. 7.7 for the same range of strain rates and at the temperature of  $-11.8^{\circ}\text{C}$ . The rate of this variation is higher for the yield envelope of columnar ice, in such a way that the maximum shear strength (or von-Mises stress) is about 26.0 MPa at a strain rate of  $1.4 \times 10^{-2} \text{ s}^{-1}$ , while the similar value for granular ice is 12.2 MPa. It is interesting to note that the shear strengths of those ice types are almost at the same level when a strain rate of  $1.4 \times 10^{-6} \text{ s}^{-1}$  is applied.

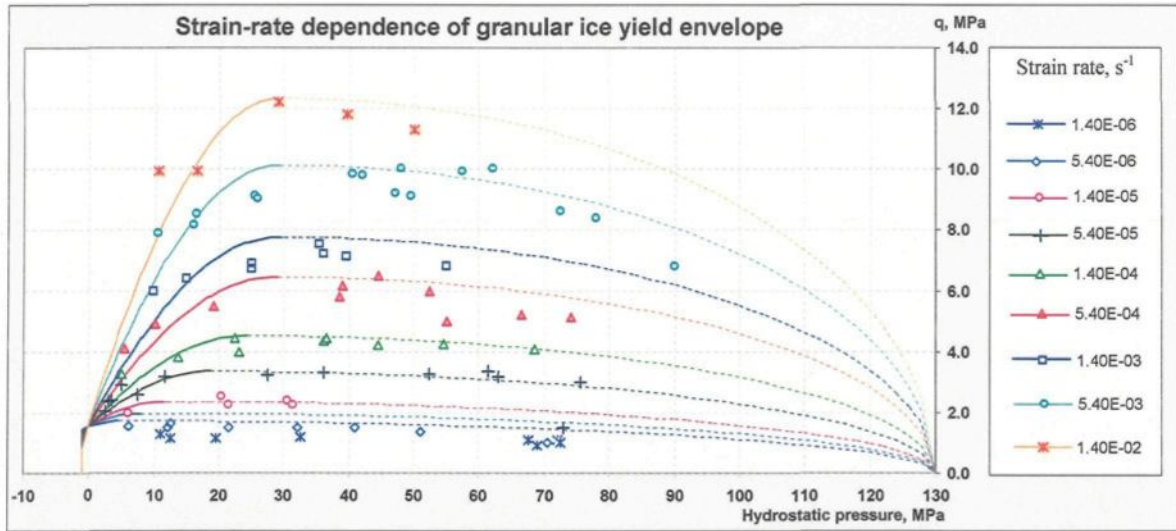


**Fig. 7.6:** Strain-rate dependency of granular ice yield envelope, the tests data are adopted from Jones (1982) at  $-11.8^{\circ}\text{C}$ .

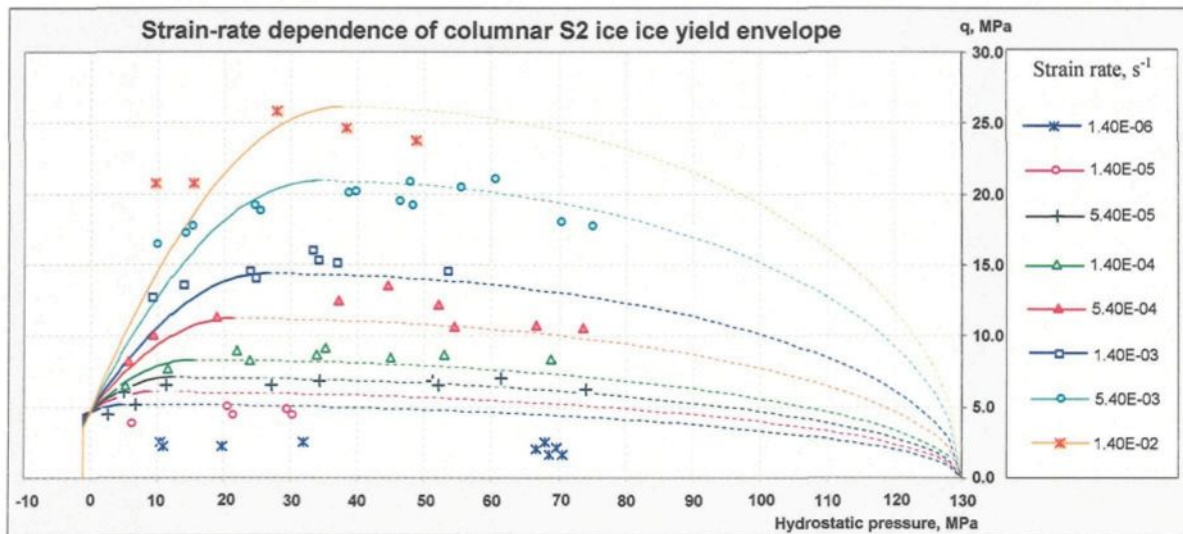


**Fig. 7.7:** Strain-rate dependency of columnar S2 ice ice yield envelope, the tests data are adopted from Jones (1982) at  $-11.8^{\circ}\text{C}$ .

#### 7.4.2 Temperature dependency of ice yield envelope

In Fig. 7.8 and Fig. 7.9, the temperature dependencies of the yield curves are shown for granular and columnar S2 ice at three different temperatures. The curves are in the good agreement with the test data of Jones (1982) for isotropic ice and Gagnon and Gammon

(1995) for columnar S2 ice. The maximum shear strength (or von-Mises stress) of columnar ice is higher than the corresponding value for granular ice, e.g. 21.0 MPa and 10.0 MPa for columnar and granular ice types, respectively.

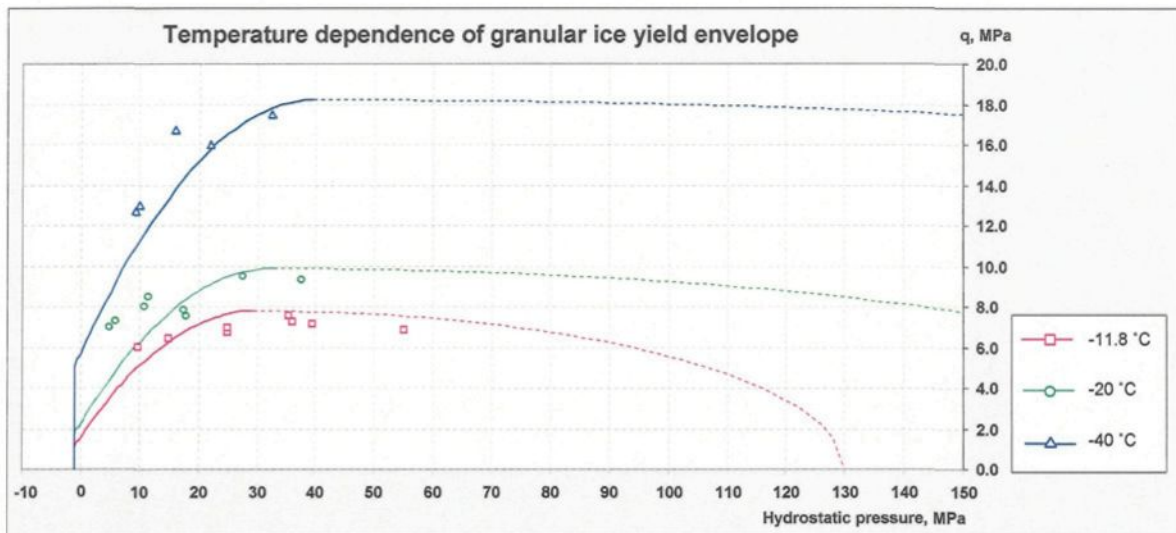


**Fig. 7.8:** Temperature dependency of granular ice yield envelope, the tests data are adopted from Jones (1982) at  $-11.8^{\circ}\text{C}$  for strain rate  $1.4 \times 10^{-3} \text{ s}^{-1}$ , and Rist and Murrell (1994) at  $-20^{\circ}\text{C}$  and  $-40^{\circ}\text{C}$  for strain rate  $1.0 \times 10^{-3} \text{ s}^{-1}$ .

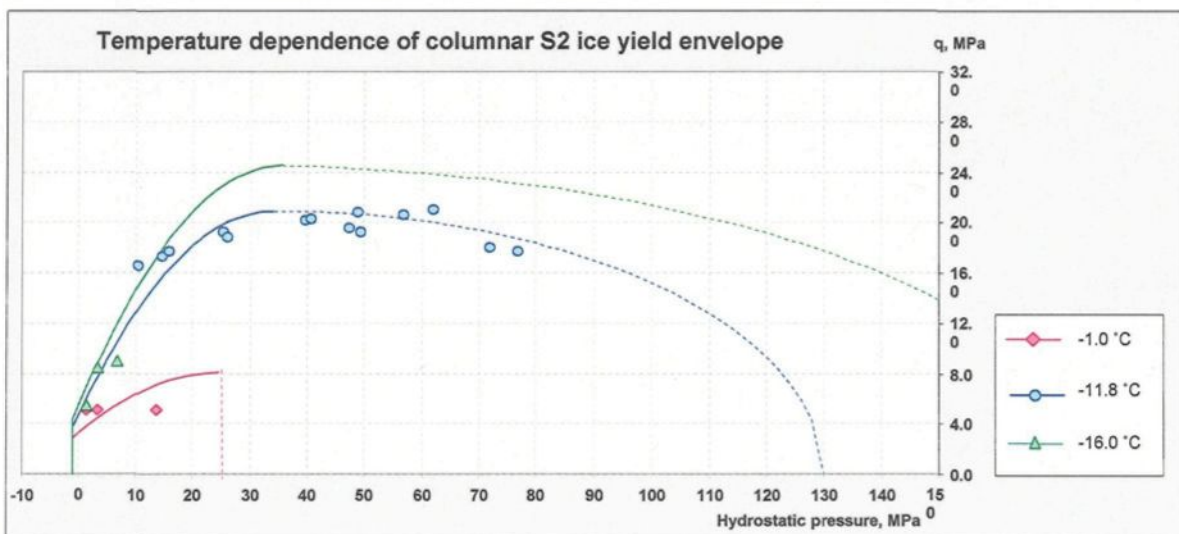


**Fig. 7.9:** Temperature dependency of columnar S2 ice yield envelope, the tests data are adopted from Jones (1982) at  $-11.8^{\circ}\text{C}$  for strain rate  $4.7 \times 10^{-3} \text{ s}^{-1}$ , and Gagnon and Gammon (1995) at  $-1.0^{\circ}\text{C}$  and  $-16.0^{\circ}\text{C}$  for strain rates  $5.4 \times 10^{-3} \text{ s}^{-1}$  and  $4.3 \times 10^{-3} \text{ s}^{-1}$ , respectively.

### 7.4.3 Porosity dependency of ice yield envelope

A typical influence of porosity on cap-yield envelope of granular and columnar ice types are shown in Fig. 7.10 and Fig. 7.11, respectively. Lower porosity dependency is observed for columnar atmospheric ice, which contains less air bubbles giving raise of the porosity to vary between 2 to 13%.

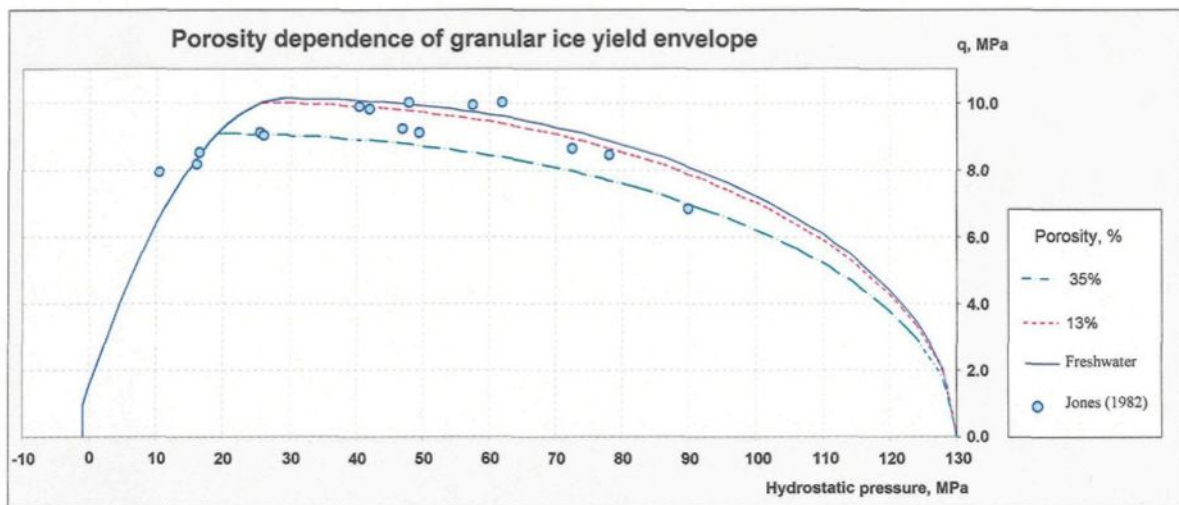


**Fig. 7.10:** Porosity dependence of granular atmospheric ice yield envelope, the tests data of freshwater ice are adopted from Jones (1982) at  $-11.8^{\circ}\text{C}$  for strain rate of  $5.4 \times 10^{-3} \text{ s}^{-1}$ .

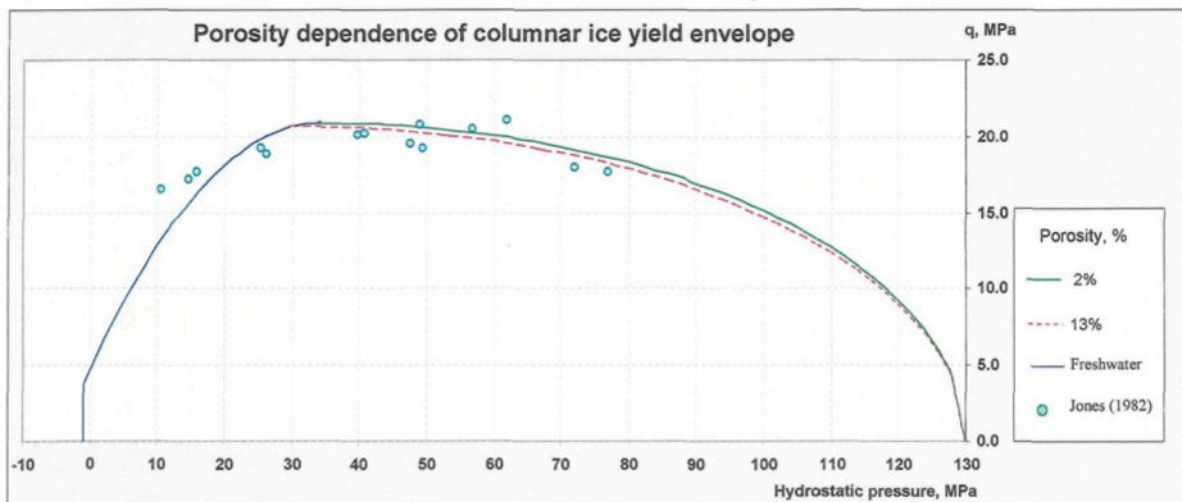


**Fig. 7.11:** Porosity dependence of columnar atmospheric ice yield envelope, the tests data of freshwater ice are adopted from Jones (1982) at  $-11.8^{\circ}\text{C}$  for strain rate of  $5.4 \times 10^{-3} \text{ s}^{-1}$ .

The porosity of granular atmospheric ice, on the other hand, is assumed to vary in the range of 13 to 35% based on meteorological conditions. As shown in figures, the shear yield curve is assumed to be unaffected by porosity, while the effects of porosity are applied to cap- and tension-yield envelopes. The porosity dependency of the shear curve may also be added in future works by performing some material test at various temperatures and strain rates.

#### 7.4.4 Ice yield envelope evaluation

The yield envelopes of this model are compared with Derradji's model (2000) in Fig. 7.12 for freshwater granular ice at temperature  $-11.8^{\circ}\text{C}$  at different strain rates. Another comparison is made in the same conditions but at temperature  $-40^{\circ}\text{C}$  in Fig. 7.13, in which the yield envelope of this model shows a very good agreement with the available test data.

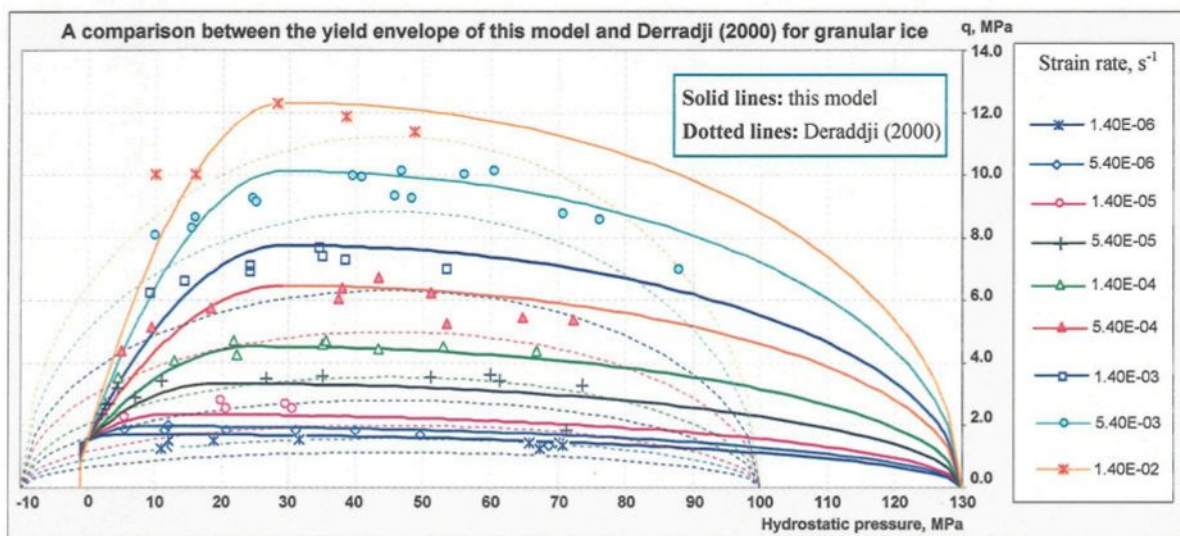


**Fig. 7.12:** A comparison between the yield (failure) envelopes of this model and Derradji (2000) for freshwater granular ice, the tests data are adopted from Jones (1982) at  $-11.8^{\circ}\text{C}$ .

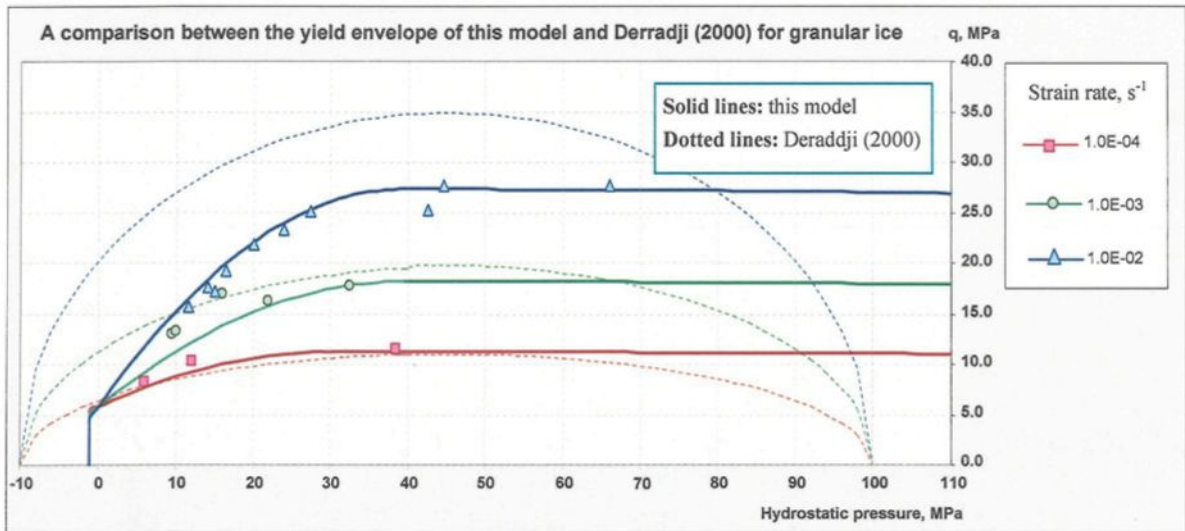


**Fig. 7.13:** A comparison between the yield (failure) envelopes of this model and Derradji (2000) for freshwater granular ice, the tests data are adopted from Rist and Murrell (1994) at  $-40^{\circ}\text{C}$ .

The yield envelopes are also compared with the model of Fish *et al.* (1997) for columnar S2 ice. The results of this comparison are shown in Fig. 7.14 and Fig. 7.15 at the temperatures of  $-11.8^{\circ}\text{C}$  and  $-16^{\circ}\text{C}$  at different strain rates.

It should be noted that the strain-rate dependency of ice cohesion is ignored in this model. A little dependence of ice cohesion to strain rate can be applied to the model by a little effort in future. However, it seems to have a minor effect at lower temperatures, see Fig. 7.15, as well as lower strain rates, see Fig. 7.14.

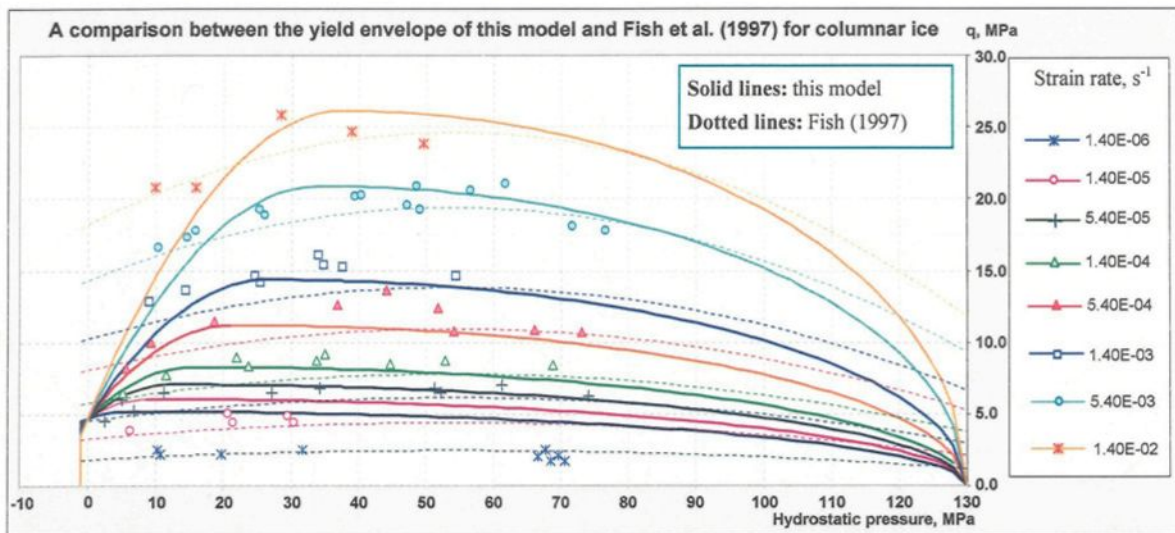


Fig. 7.14: A comparison between the yield (failure) envelopes of this model and Fish *et al.* (1997) for columnar S2 ice, the tests data are adopted from Jones (1982) at  $-11.8^{\circ}\text{C}$ .

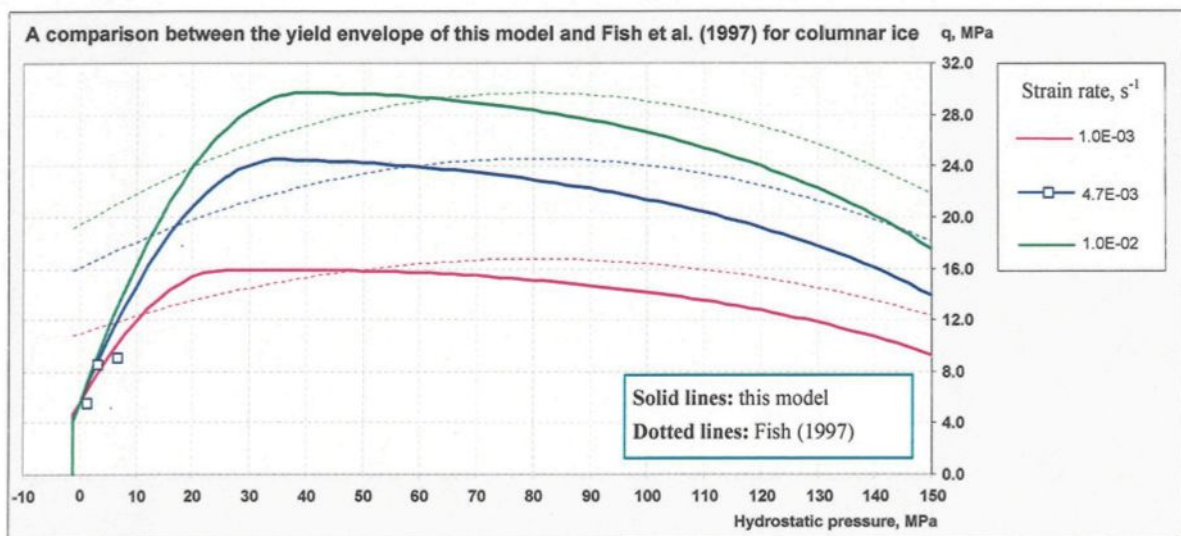


Fig. 7.15: A comparison between the yield (failure) envelopes of this model and Fish *et al.* (1997) for columnar S2 ice, the tests data are adopted from Gagnon and Gammon (1995) at  $-16^{\circ}\text{C}$ .

## 7.5 Case studies for natural loading conditions

External mechanical forces acting on the system of power lines and the ice deposits can be categorized into (a) static loads due to thermal stresses, and the weight of line components and the accreted ice, and (b) dynamic and impulse forces acting on lines resulting from wind and sudden ice shedding, see Fig. 1.1 and Fig. 1.3. The wind force, in the latter category, has a fluctuating nature that depends on the direction of power line, ice geometry, elevation and many other factors. It may also cause galloping of the lines in the case of asymmetric ice shape when the wind force is strong enough. The impulse loads induced by sudden ice shedding, on the other hand, is the most critical loading condition for the power-line that should be considered in future studies.

In this work, however, the static loading condition is considered as a series of case studies for model elaboration purposes, which consist of a constant wind pressure, gravity force, the internal ice pressures (confining), the thermal stresses due to temperature gradient in ice deposit, the bending moment resulting from gradual ice accretion and the twisting torque from the rotation of power lines due to asymmetrical ice shape. Application of the model to a more realistic situation requires the modification of the model for high-rate deformation, as well as the natural loading, the adhesive contact boundary condition, and the displacement boundary condition due to galloping to be well-defined, see Section 1.2 and Fig. 1.3 for more details. The schematic representation of the external forces and the relevant force balance are shown in Fig. 7.16.

The bending moment due to gradual ice accretion can be explained by considering the following equation for the Catenary cable curve, which is obtained by this assumption that the cable hangs under the action of uniform weight per its length ( $w$ ), see Fig. 7.16.

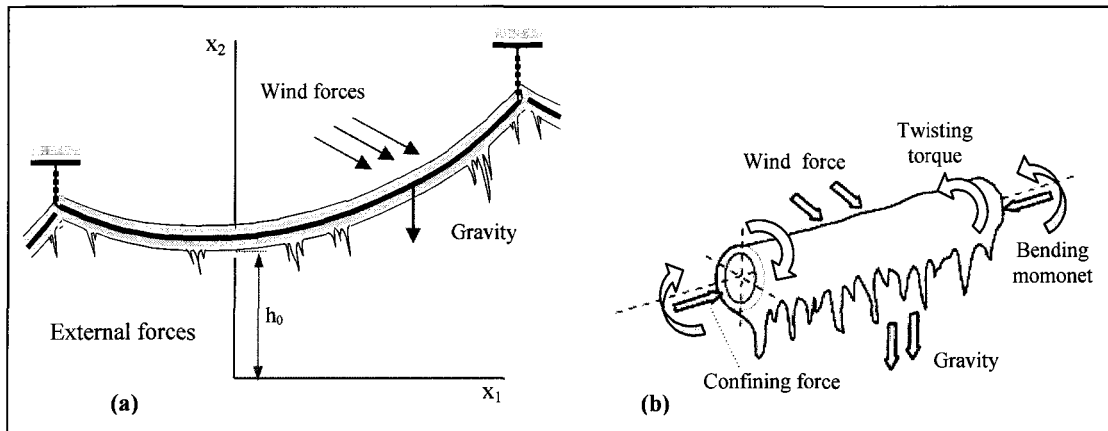


Fig. 7.16: External forces and the force balance diagram for ice deposits on electrical power lines.

$$x_2 = h_0 + \frac{T_0}{w_c + w_{ice}} \left[ \cosh \left( \frac{w_c + w_{ice}}{T_0} x_1 \right) - 1 \right] \quad (7.16)$$

In equation (7.16), the slope of curve is a function of the cable weight ( $w_c$ ) plus the weight of accreted ice ( $w_{ice}$ ), in which  $T_0$  denotes the constant horizontal component of cable tension, and  $h_0$  the minimum distance between the cable curve and the ground. Now, consider that the layers of ice are accreted gradually on the power line. In this case, the line starts to sag gradually, thus producing a bending moment in the previous layers of accreted ice closer to the line surface. This gradual bending moment, the ice confining pressure due to ice weight, the thermal stresses induced by temperature changes, gravity, and the twisting torque due to asymmetrical ice shape are the various types of static loads normally applied to atmospheric ice deposits accreted on power lines. Based on this brief discussion, the following case studies are selected for model elaboration: (a) wind force, (b) ice

confining pressure, (c) bending moments, and (d) twisting torques, which are considered to be static, see Fig. 7.17. In all these case studies, however, the magnitude of loads is considered to be limited to a maximum value of 0.5 MPa, which is the normal loading range for the ductile behaviour of ice. The results of these case studies can also be used to validate the model accuracy for predicting the mechanical behaviour of an ice deposit when the effects of crack activity are considered in the model.

In the next section, the anisotropic behaviour of various types of atmospheric ice is investigated. The external loads are applied in a short period of time (one second), so the results can be interpreted as elastic deformation. The viscoelastic and plastic contributions are small in such a limited loading period. These case studies are selected for this survey to show the effects of anisotropy and texture-change on the mechanical behaviour of atmospheric ice on power lines. The results could be extended for larger loading times to consider the failure behaviour of ice in future works. The effects of mesh size in solution convergence, and the temperature and ice-structure dependency of the solutions are also investigated in this section.

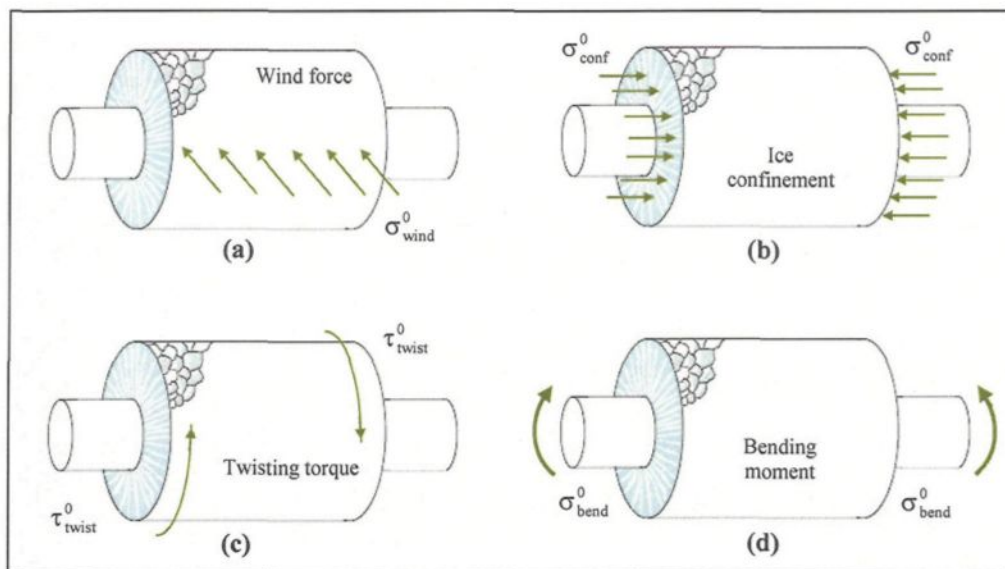


**Fig. 7.17:** Selected case studies for model elaboration at static load condition,  
 (a) Radial compression (wind load), (b) Axial compression (ice confinement),  
 (c) Torsion (cable twist), (d) Bending moments (gradual ice accretion or galloping)

### 7.5.1 Anisotropic behaviour of atmospheric ice deposit

The short-term anisotropic behaviour of columnar ice deposits are studied here on the basis of the matters presented in Section 4.2.4. In that section, a comparison was made between the anisotropy of various types of columnar ice, see Fig. 4.10. A maximum anisotropy of 29.2% and 41.8% were determined for  $E_{33}$  and  $G_{13}$  moduli of S1 ice through a 90-degree rotation around the normal axis to the column.

In this section, the influence of this anisotropic behaviour is studied for the atmospheric ice deposit on power lines by running a few simulations with ABAQUS. The ice structures are selected as a combination of different ice textures. An ice deposit of 55mm in thickness is accumulated on power line, which is modeled by a rigid body or a deformable aluminum cylinder (35mm in diameter). The plane strain assumption is

considered for the lateral loading scenario, while axisymmetric modeling is applied for axial loading conditions. In a real situation, the ice deposit has an asymmetric geometry with a granular structure very close to the electrical line and a columnar (S1 or S2) structure far from the cable surface. Three distinct structures are considered in these models: granular ice deposit (Case-G), thin layer of granular ice (5mm in thickness) followed by another 50mm thick layer of glaze (ice S2) (Case-GS2), or the same granular thin layer followed by a similar thick deposit of hard rime (ice S1) (Case-GS1). Different loading scenarios are modeled: pressure force applied by a static wind force, torsion induced by cable twist, axial loading due to ice confinement, and bending moment resulting from the gradual ice accretion. In the next sections, those loading conditions are applied to the system of ice deposits and electrical conductor by means of a few ABAQUS models. The effects of mesh size and temperature are also studied in the next sections.

#### 7.5.1.1 The anisotropy induced by wind load

Wind applies a fluctuating and complex loading scenario on a power line system and the accreted ice, which depends on many factors. In this section, however, a static load pressure of 0.5 MPa is applied to a part of the electrical line to investigate the state of anisotropy in the ice deposit. The electrical line, in this case, is modeled by a discrete rigid body and a plane strain assumption is considered. In this section, all three ice structures are modeled at a temperature of  $-10^{\circ}\text{C}$ , see Fig. 7.18. A scale factor of 3000 is chosen in deformed shape presentations for all modeling of this section.

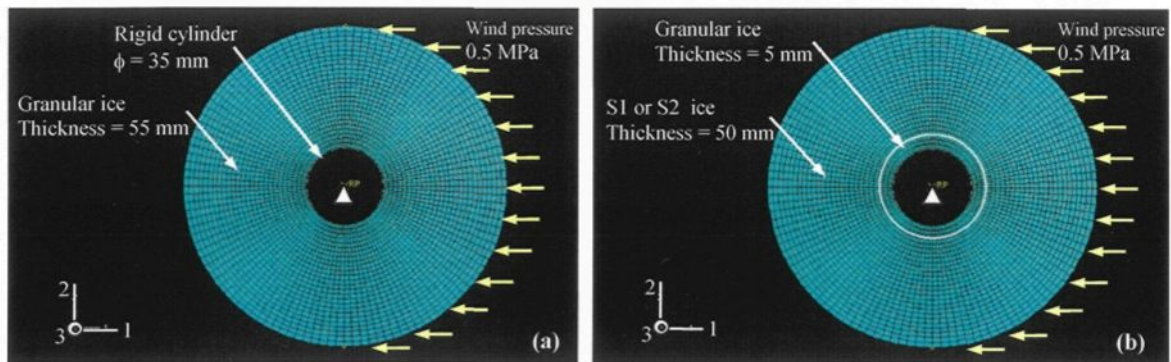


**Fig. 7.18:** Selected case study for determining the ice anisotropy due to static wind pressure, (a) Case-G, (b) Case G-S2 and G-S1.

The contours of  $x_1$ -displacements ( $U_1$ ) and  $x_2$ -displacements ( $U_2$ ) for this loading condition and Case-G are shown in Fig. 7.19. The maximum magnitude of  $U_1$  ( $3.303 \times 10^{-3}$  mm) is produced at front of the ice deposit, and the maximum value of  $U_2$  ( $1.329 \times 10^{-3}$  mm) and its location are shown in the same figure.

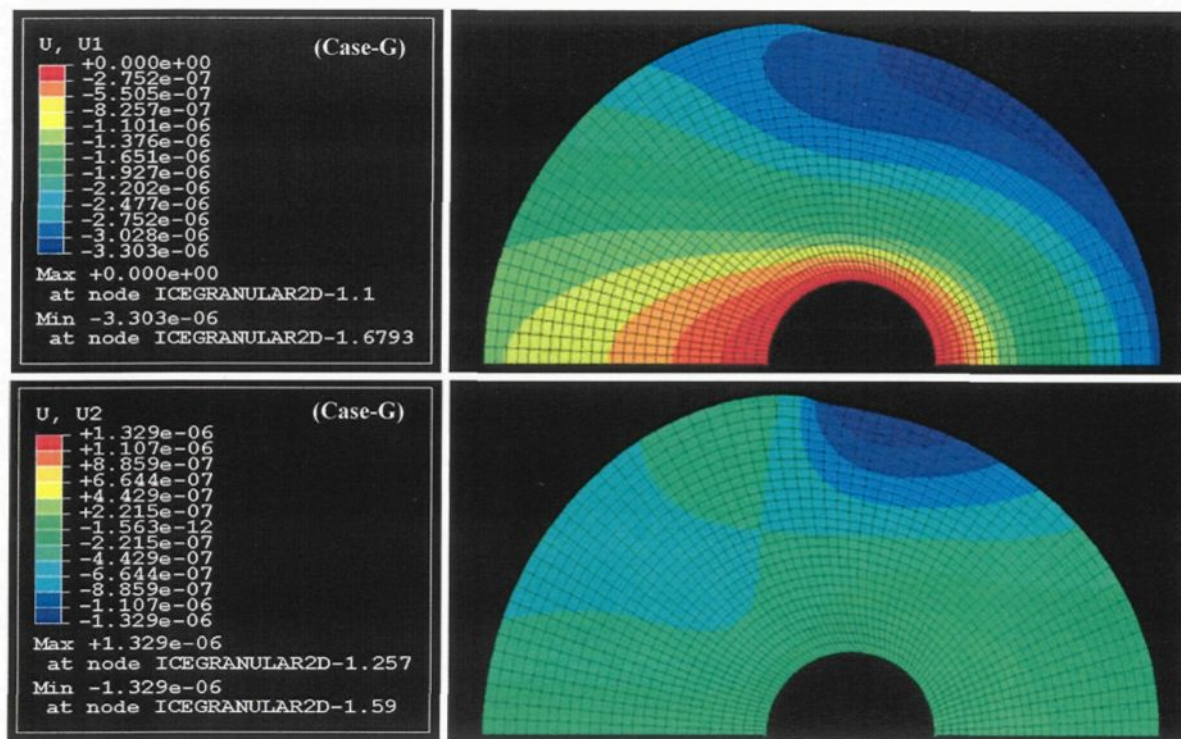


**Fig. 7.19:** Displacement contours in  $x_1$ -direction ( $U_1$ ) and  $x_2$ -directions ( $U_2$ ) and the corresponding legends for wind pressure  $0.5 \times 10^6$  Pa (Case-G),  $U_1$  and  $U_2$  are given in meter.

A comparison of the variation of von-Mises stress for different structure cases are shown in Fig. 7.20 and Fig. 7.21.

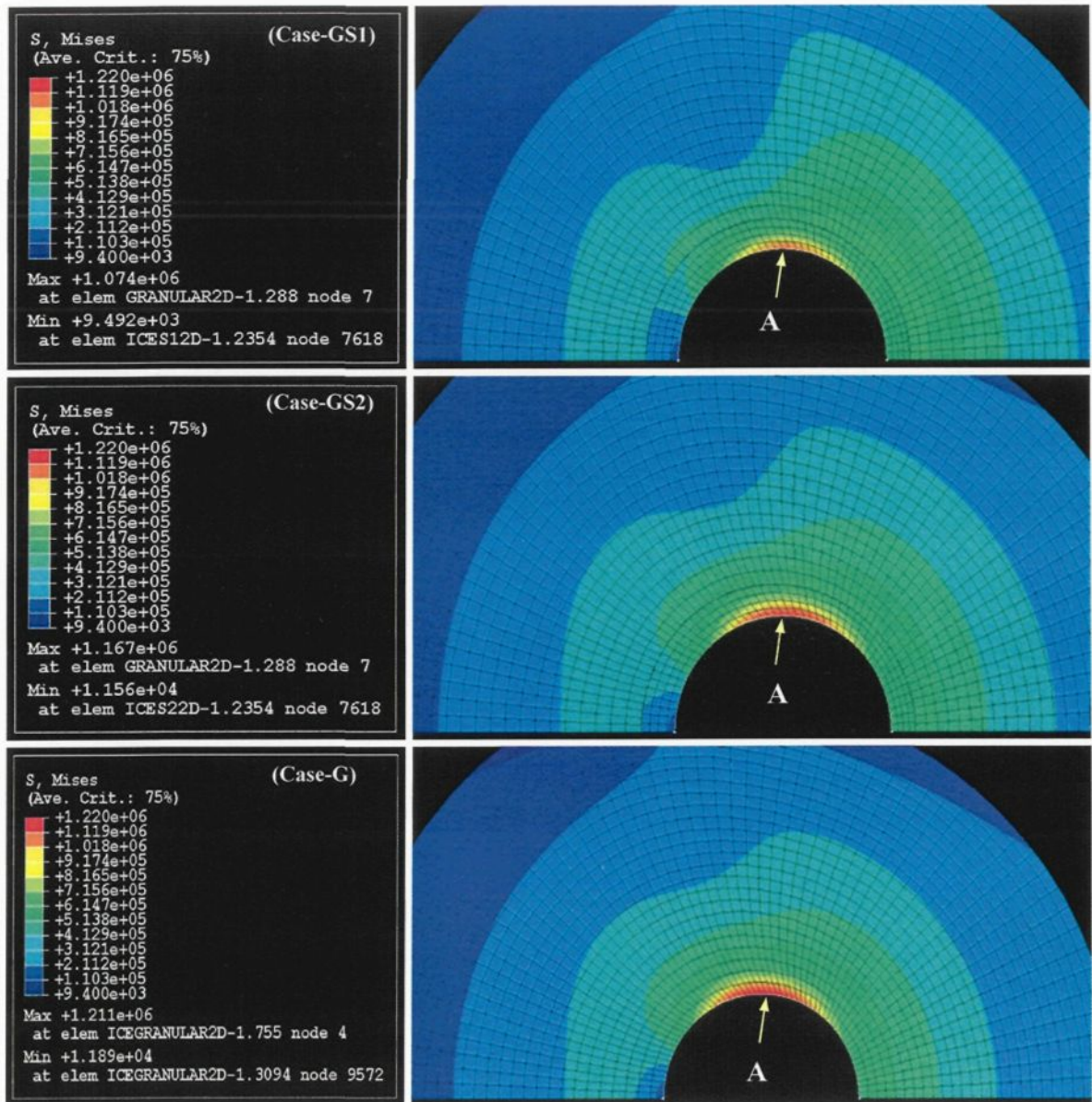


**Fig. 7.20:** The comparison between the von-Mises stress contours in Pa for ice structures of cases GS1, GS2, and G at static wind pressure  $0.5 \times 10^6$  Pa.

The maximum von-Mises stress for this loading scenario occurs at the upper and lower parts of ice-conductor interface for the cases G, GS1 and GS2. The points of maximum von-Mises stress are indicated by “A” followed by a flash in those figures.

The von-Mises stress in the granular ice deposit (Case-G) has the maximum magnitude (1.211 MPa), which is close to Case-GS2. Along the  $x_1$ -axis, however, the maximum von-Mises stress belongs to Case-GS1 with a jump at the interface between granular and S1 ice.

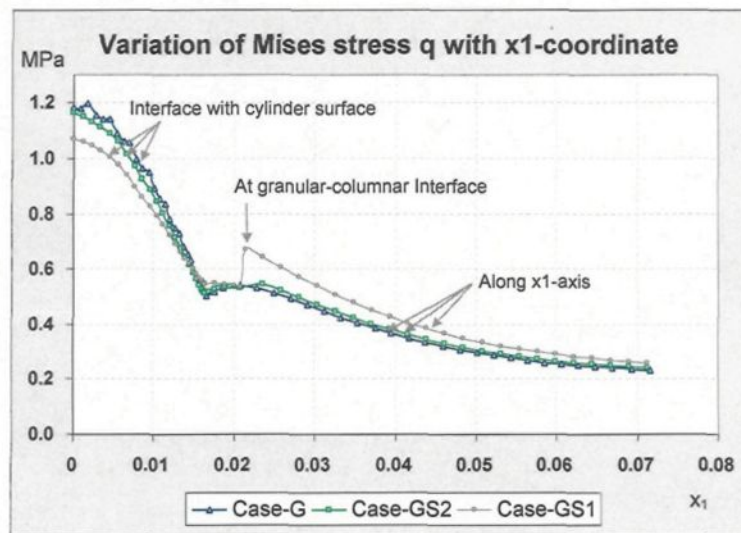


**Fig. 7.21:** The comparison of the von-Mises stress variations along the cylinder surface and along the  $x_1$ -axis at wind pressure 0.5MPa in the cases G, GS1, and GS2.

A similar comparison for the variation of hydrostatic pressure, in this case, is given for the different structure cases as shown in Fig. 7.22 and Fig. 7.23. The maximum hydrostatic pressure for this loading scenario occurs at the front face of the conductor surface for all three structures ( $x_1 = 0.0175\text{m}$ ).

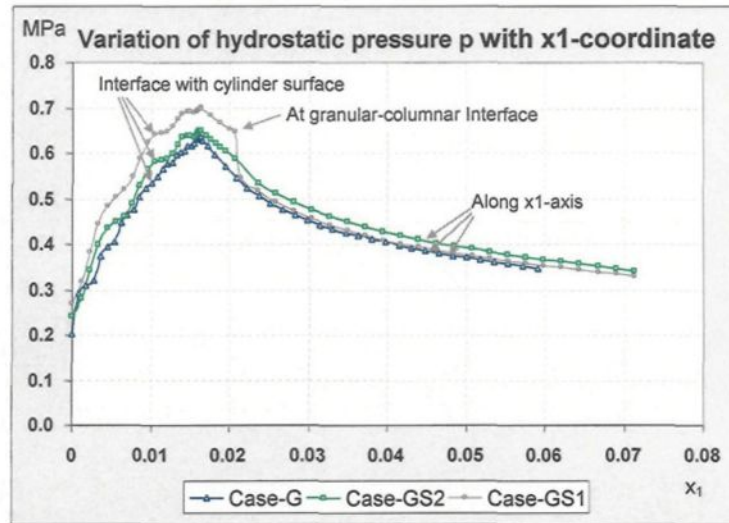


**Fig. 7.22:** The comparison of the hydrostatic pressure variations along the cylinder surface and along the  $x_1$ -axis at wind pressure 0.5MPa in the cases G, GS1, and GS2.

In Fig. 7.22, the pressure in the granular layer of Case-GS1 has the maximum magnitude (0.710 MPa). Along the  $x_1$ -axis, the magnitude of hydrostatic pressure is changed suddenly to a lower level at the interface of granular and S1 ice. The maximum pressure induced along this axis, however, belongs to the Case-GS2 with a minor change at the interface of granular and S2 ice. The jump in von-Mises and pressure stresses causes the interface to be a good location for stress concentration and crack initiation.

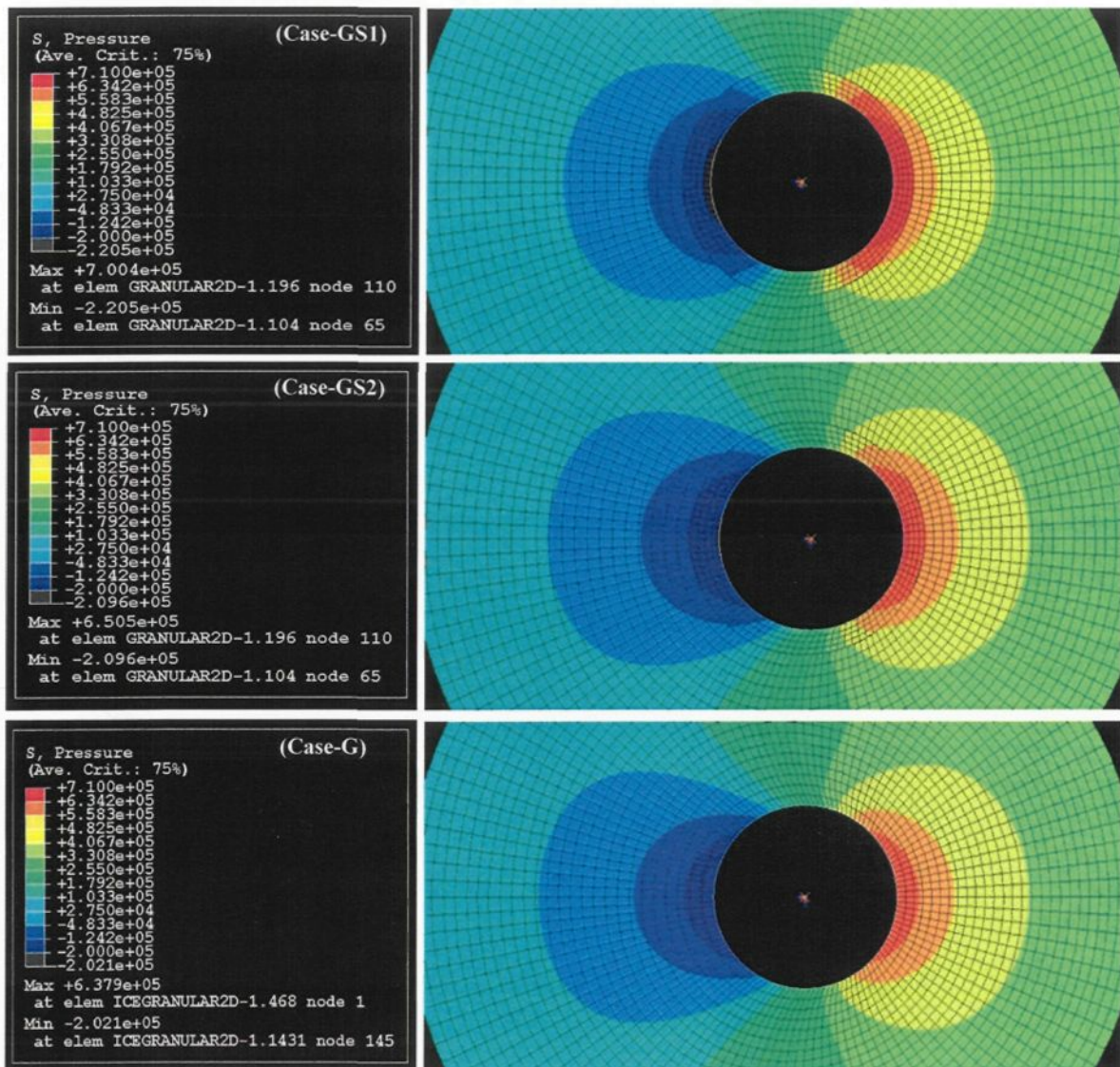


Fig. 7.23: The comparison of the hydrostatic pressure in Pa contours and the corresponding legends for ice structures of the cases GS1, GS2, and G at wind pressure  $0.5 \times 10^6$  Pa.

#### 7.5.1.2 The influence of mesh size and element type in solution accuracy

In finite element analysis, it is always required to study the mesh-size dependency of the solutions to find out the optimum mesh size for analysis. It is important to be sure of the accuracy of the results, at the same time, to reduce the computation time and round-off

errors. In this work, this dependency is studied by running the analysis for similar loading conditions with five different mesh sizes and two linear and quadratic elements. The five mesh sizes are produced by selecting different magnitudes of seed numbers for a quarter of cylinder surface. This means that the number of seeds 6, 8, 12, 16, and 20 that are selected here correspond to the total number of seeds 24, 32, 48, 64 and 80 selected on the cylinder surface. Two reduced-integration plane-strain elements CPE4R (linear) and CPE8R (quadratic) are selected in this part to investigate the influence of element type on von-Mises stress, hydrostatic pressure, and  $x_1$ -displacement induced in the material. The magnitude of von-Mises stress is determined for the upper point close to the cylinder surface, flashed point in Fig. 7.20, while pressure and magnitude of displacement are calculated for the front face of cylinder and ice on the  $x_1$ -axis, respectively.

The convergence of von-Mises stress, hydrostatic pressure, and the magnitude of displacement (U1) to the final solution are shown in Fig. 7.24.

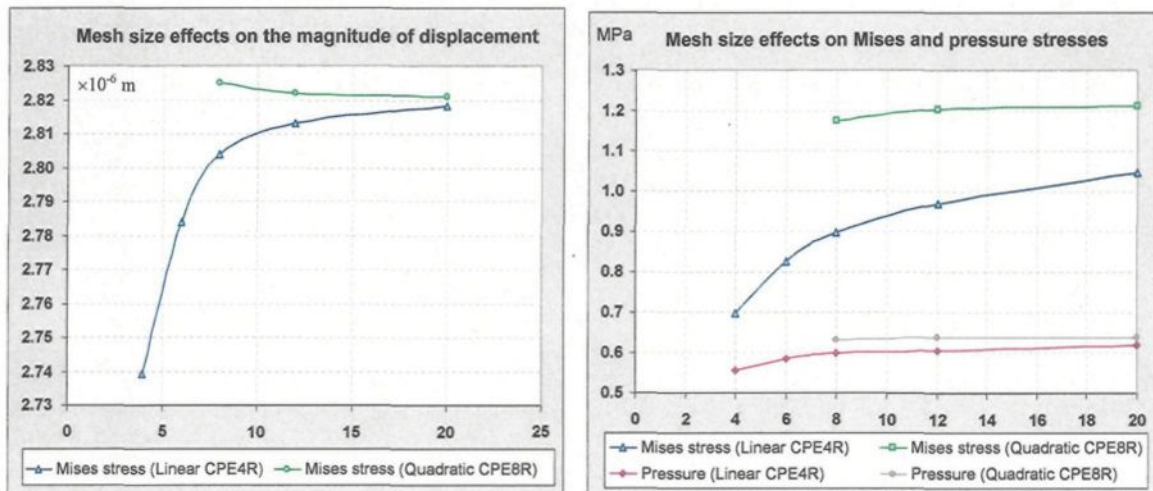


**Fig. 7.24:** The effects of mesh size and element type on the accuracy of displacement, von-Mises stress and hydrostatic pressure in case G at wind pressure 0.5MPa.

As it can be seen from these figures, the rate of convergence is higher for quadratic elements. Hence, the quadratic plane strain or axisymmetric elements of CPE8R or CAX8R are selected for these models. In the following case studies, twenty seeds are considered on a quarter of cylinder surface.

### 7.5.1.3 The anisotropy due to cable torsion

In this model, the torsion traction of 0.5 MPa is applied to the two ice structures of Case-GS1 and Case-GS2, Fig. 7.25. The von-Mises stress and displacement contours for Case-GS1 are shown in Fig. 7.26, which are almost the same for the other cases also. In these figures, the von-Mises stress varies from 0.866 MPa for the outer surface to the maximum value of 14.94 MPa in the layers closer to the cylinder surface. The magnitude of displacement, on the other hand, varies from zero to the maximum value of 0.0928 mm, inversely.

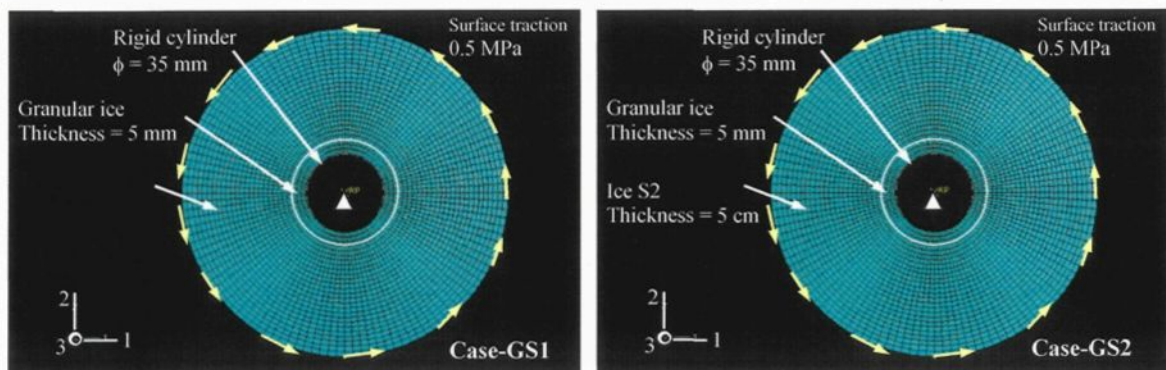


**Fig. 7.25:** Selected case study for determining the ice anisotropy due to torsion traction of 0.5 MPa applied to the outer surface of ice deposit, in the cases GS1 (left) and GS2 (right).

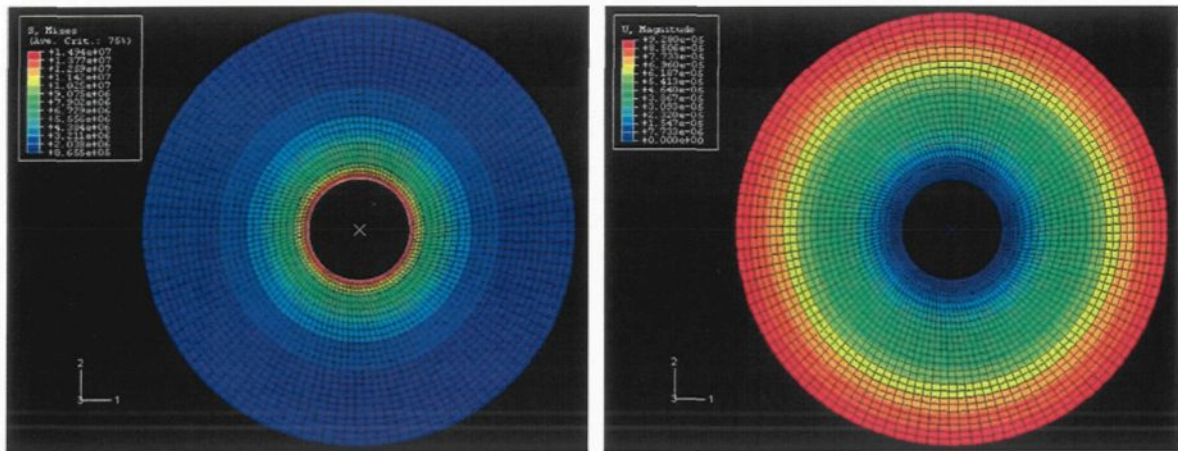


**Fig. 7.26:** The comparison of von-Mises stress in Pa (left) and displacement contours in meter (right) at torsion traction of 0.5 MPa in the case GS1.

The variations of von-Mises stress and displacement magnitude are compared for both cases in Fig. 7.27, where no significant differences in torsion behaviour were observed. As it can be seen from Fig. 7.27, the maximum von-Mises stress occurs in the first layer of accreted ice adjacent to the cylinder surface, while the maximum deformation takes place on the outer surface of the ice deposit.

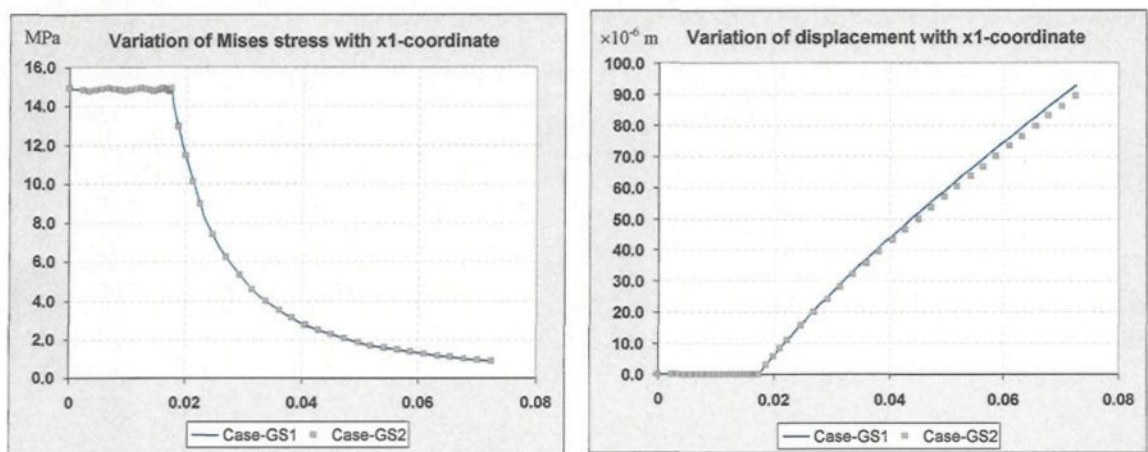


**Fig. 7.27:** The variation of von-Mises stress and displacement magnitude with  $x_1$ -coordinate at torsion traction of 0.5 MPa in the cases GS1 and GS2.

#### 7.5.1.4 The anisotropy resulting from ice confinement

In this model, the confinement force of 0.5 MPa is applied to the axisymmetric structures of Case-GS1 and Case-GS3-0-10, Fig. 7.28. The latter structure refers to a 5 mm thick-layer of granular ice deposit plus another thick-layer of 50 mm of S3 ice, in which the c-axes are oriented in the z-axis with a scatter angle of 10 degrees. The c-axes in these structures are oriented normal and parallel to the direction of confining pressure, respectively. The system of electrical line and ice deposit is modeled as an axisymmetric geometry. The system of electrical line and ice deposit is modeled as an axisymmetric geometry. The axisymmetric elements of CAX8R are used for this simulation for both ice structures.

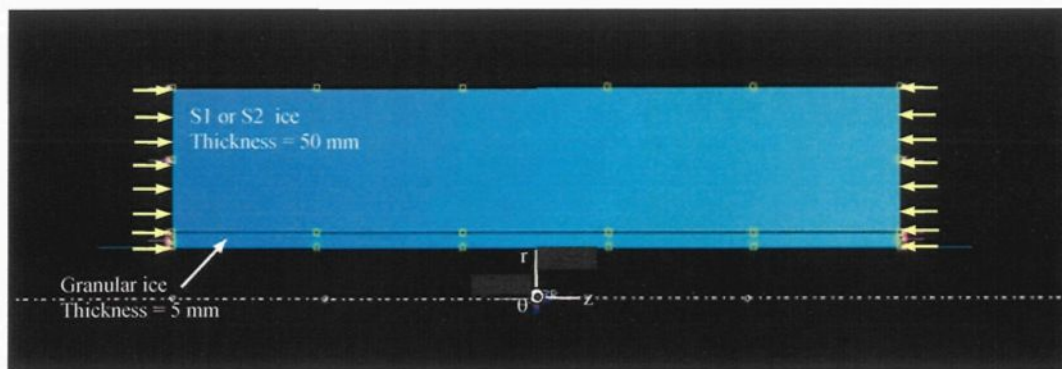


**Fig. 7.28:** Selected case study for determining the ice anisotropy due to confinement of 0.5 MPa applied to the ice deposit in the cases GS1 and GS2.

The contours of von-Mises stress, pressure and axial displacement for both cases are shown in Fig. 7.29. The maximum magnitudes of these parameters are 0.228 MPa (Case-GS3-0-10 at interfaces of cylinder with granular ice, and granular ice to S3 ice), 0.115 MPa (Case-GS3-0-10 at interfaces of cylinder with granular ice, and granular ice to S3 ice), and  $6.015 \times 10^{-4}$  mm (Case-GS1 at outer surface of S1 ice).

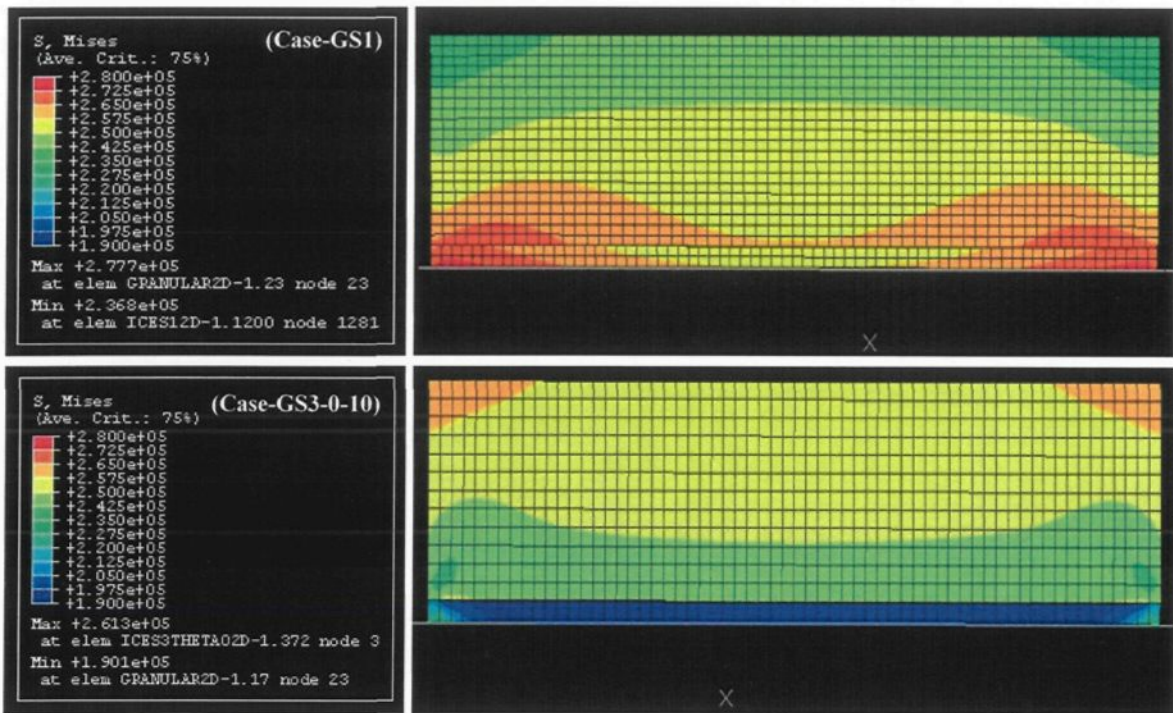


Fig. 7.29: The comparison of the von-Mises stress contours in Pa and the corresponding legends for the ice structures of cases GS1 and GS3-0-10 at confining pressure of  $0.5 \times 10^6$  Pa.

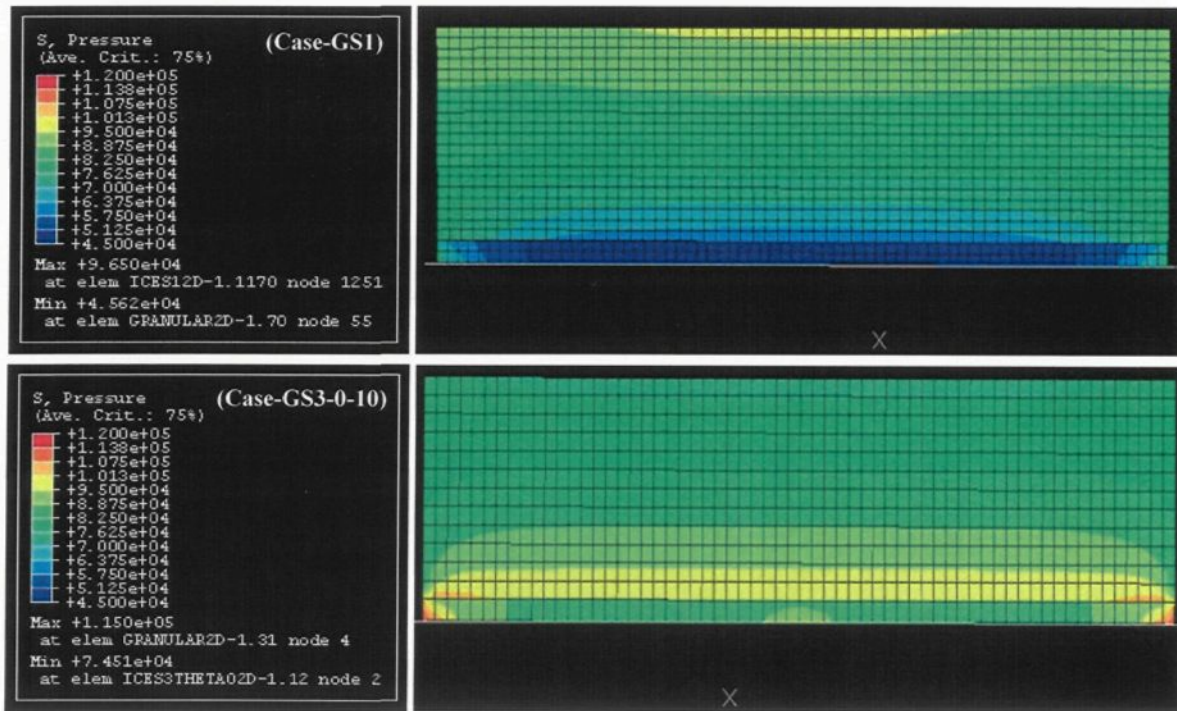


Fig. 7.30: The comparison of the hydrostatic pressure contours in Pa and the corresponding legends for the ice structures of the cases GS1 and GS3-0-10 at confining pressure of  $0.5 \times 10^6$  Pa.

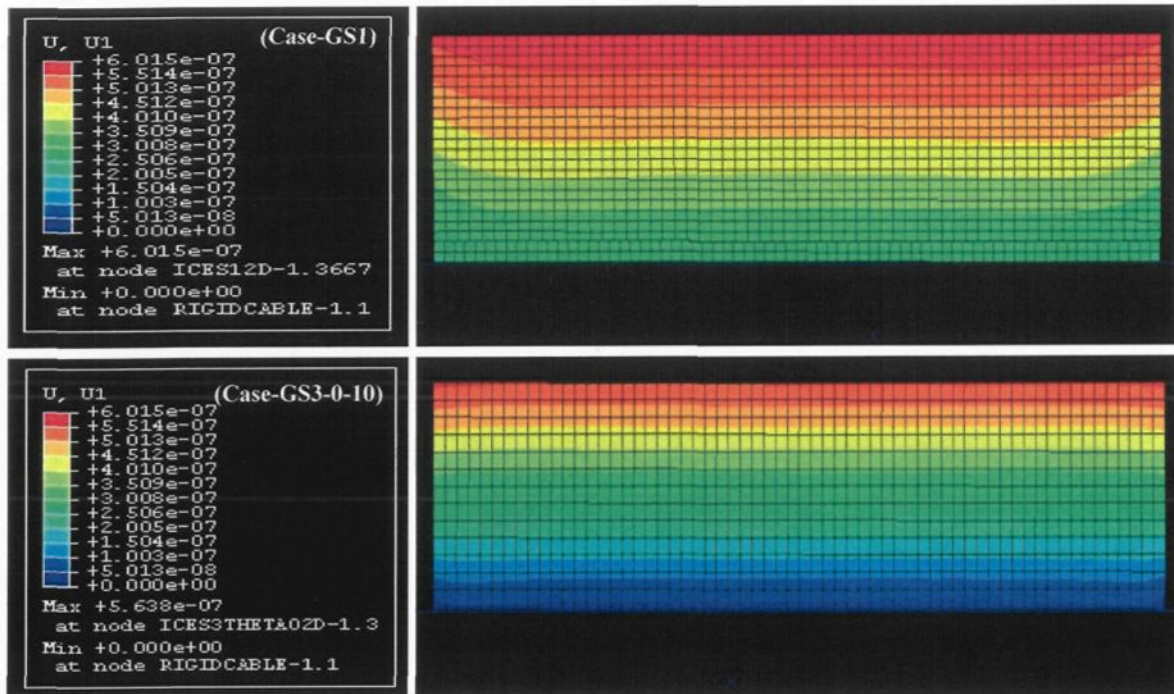


Fig. 7.31: The comparison of the contours of displacement (in meter) in x1-direction (U1) and the corresponding legends for the ice structures of the cases GS1 and GS3-0-10 at confining pressure of  $0.5 \times 10^6$  Pa.

### 7.5.2 Temperature dependency of ice behaviour

As it was seen in Section 4.2, the elastic moduli of freshwater ice vary by 7.4% for a change in ice temperature within the range of  $0^\circ\text{C}$  to  $-50^\circ\text{C}$ . In the above case studies, however, the results were not affected by temperature that's much in those loading conditions and in a short period of time. As it was stated before, the viscoelastic and plastic contributions are negligible in ice behaviour for this short period of time. The main temperature dependency, on the other hand, is related to those contributions. Even the elastic moduli are not affected so much by temperature because of the low level of loadings in those case studies; compare the load magnitude (in a scale of MPa) to the elastic moduli of ice (in a scale of GPa).

## 7.6 Conclusions

In this chapter, the numerical considerations and the manner of implementing the model as a UMAT subroutine of the ABAQUS finite element program are detailed. The time-integration of the rate form of constitutive equations are described and the UMAT interface is explained. The natural loading scenarios for atmospheric ice deposits on overhead power lines are briefly reviewed and a few case studies are selected for model elaboration.

On the basis of the analysis of this chapter, the following conclusions could be drawn:

- 1) Four types of static loading scenarios (case studies) are considered for simulating the natural static loads applied to the electrical power lines during an atmospheric icing event. In those case studies, a static wind pressure, a compressive pressure due to ice confinement, and a torsion traction resulting from the twist of conductor in a limited magnitude of 0.5 MPa are applied to a symmetric geometry of accreted ice on electrical line for numerical simulation.
- 2) Three ice structures are considered in the numerical models. They are granular ice deposits, the combination of granular (first layers of deposit near conductor surface) and glaze (S2 ice), and finally another combination of granular ice with hard rime (S1 ice). In the two combination cases, the ice structure exhibits anisotropic mechanical behaviour, which can be assumed as one of the sources of crack propagation, and thus failure.
- 3) Cable twist induced the maximum magnitude of von-Mises stress, which is the shear stress measure (about 15MPa when torsion surface traction of 0.5 MPa is applied). This means that the shear failure of ice is easier in torsion rather than bending, wind force or

confining forces. The maximum magnitude of von-Mises stress corresponds to granular ice deposits, which is the weakest ice structure for shear forces.

- 4) Wind force induced the maximum magnitude of hydrostatic pressure to the ice deposit (0.7 MPa for a wind pressure of 0.5 MPa) at the ice layers close to the conductor surface. This maximum magnitude corresponds to the ice structure Case-GS1 that consists of a granular layer near the conductor surface followed by the S1 ice layers.
- 5) The maximum magnitude of deformation is induced in the outer layers of ice deposits when subjected to torsion traction (0.0928 mm for the torsion traction of 0.5 MPa).

## CHAPTER 8

### GENERAL CONCLUSIONS AND RECOMMENDATIONS

#### 8.1 General conclusions

The viscoplastic constitutive equations of various types of atmospheric ice were presented in ductile deformation. The effects of microcrack-activity could be added to this model in future works. By defining the real state of loading (wind, temperature changes, and so on), the mathematical model of this study could be used to describe the atmospheric ice breaking phenomenon in the full range of temperature and strain rate. The UMAT subroutine, written in FORTRAN language, should be modified to cover the transition and brittle regions of ice deformation. The final results are then useful in explaining the natural mechanisms of ice breaking and also for improving the mechanical de-icing techniques. On the basis of literature review and the analyses of this work, the following conclusions have been drawn:

- 1) The mechanical behaviour of atmospheric ice depends on temperature and strain rate, and thus should be described in three distinct regions (ductile, brittle, and the transition region from ductile to brittle). The failure and yield surfaces, thus, should be determined for various ice structures subjected to different temperature and strain rate conditions.

- 2) Ice structure, grain size, and porosity are the other critical parameters having influence on the mechanical behaviour of atmospheric ice. These parameters, in turn, are affected by meteorological factors such as liquid water content (LWC), air temperature, and the size of super-cooled water droplets.
- 3) At natural temperatures, atmospheric ice undergoes creep deformation, while similar behaviour can be observed in metals at high temperatures. Three stages of creep deformation are involved in ice deformation.
- 4) For this viscoplastic deformation, the total strain consists of four distinct components, a recoverable instantaneous elastic part, a viscoelastic part, a plastic flow, and a crack activity strain. The cracking component, however, could be ignored if the effects of crack-activities in elastic moduli and viscoplastic characteristics are taken into account.
- 5) Glaze and hard rime are two more important types of atmospheric ice for the case of power-line icing. The porosity of these types of atmospheric ice reaches a maximum value of 35%, and thus cannot be ignored in material constitution.
- 6) The effects of porosity are considered in elastic deformation by using the drained and undrained poroelastic models, as well as the definition of effective stress, which consists of the stress in solid-state and pore pressure. The drained model is a better representation of poroelastic deformation of glaze (similar formulations are used for dry soft rime), while the undrained model is used for hard rime.
- 7) The temperature dependency of ice elastic moduli is almost 7.4% that is considered in elasticity model. This dependency in viscoelastic and plastic models, on the other hand, is

considered by means of a shift function and using the temperature-dependent material parameters, respectively.

8) The anisotropy in mechanical behaviour of ice deposit is also important. This anisotropy is induced by the variation in ice structure from granular, at layers close to the conductor surface, to columnar for the rest of ice layer. The maximum anisotropy belongs to Poisson's ratios of S1 ice that varies 80.2% with rotation angle; while the other maximum anisotropy of 29.2% and 41.8% were observed for Young's and shear moduli.

9) The shear yielding of atmospheric ice is assumed to be unaffected by porosity, while it has a significant effect on cap yielding mechanism of ice deformation.

10) The shear yielding is characterized by three material parameters, cohesion, friction angle, and the hydrostatic pressure at maximum shear strength. Those are the functions of temperature and strain rate. The available data for freshwater ice is used to determine these dependencies, even for shear yielding of porous ice.

11) The cap yielding, on the other hand, is characterized by two material parameters, the hydrostatic pressure at maximum shear strength, and ice melting pressure, which are functions of temperature, strain rate, and porosity.

12) Ice yield surface is strongly affected by ice structure, but no significant grain-size dependence is reported.

13) Four types of loading scenarios are considered in the case of atmospheric icing of power lines. They are wind force, bending moment due to gradual ice accretion, thermal stresses due to temperature gradient in ice deposit, and torsion traction resulting from the twist of conductor.

14) Cable twist induces the maximum magnitude of von-Mises stress (about 15MPa when torsion surface traction of 0.5 MPa is applied). This means that the shear failure of ice is easier in torsion rather than bending, wind force or confining forces. The maximum magnitude of von-Mises stress corresponds to granular ice deposits (Case-G), which is the weakest ice structure for shear forces.

15) Wind force induces the maximum magnitude of hydrostatic pressure (0.7 MPa for a wind pressure of 0.5 MPa) on the ice layers closest to the conductor surface. The maximum magnitude corresponds to the ice structure Case-GS1.

16) The maximum magnitude of deformation is induced in the outer layers of ice deposits when subjected to torsion traction (0.0928 mm for torsion traction 0.5 MPa in Case-G).

## 8.2 Recommendations for future work

Based on the strain decomposition, a complementary work is required to include the effects of crack-activity to this model. This can be done by considering a distinct crack-activity strain or by considering those effects in elastic, viscoelastic, and plastic strains. The latter choice, however, is preferred because the plastic formulations presented in this work could be implemented in those cracking models. In addition, the effects of microcracks in elastic moduli are also a well-documented theory. The accuracy and consistency of the model of this study could be increased by following improvements:

- 1) The elastic moduli and viscoelastic flow could be modified to take the minor crack activities into account in ductile region.
- 2) The effects of viscoelastic and plastic deformation on the pore pressure calculation should be considered in the Voigt analogy of poroelastic model.
- 3) The Sinha's viscoelastic model is modified for atmospheric ice by replacing the deviatoric elastic with the effective poroelastic strain to consider the effects of porosity into the viscoelastic formulations. However, this model requires to be validated by laboratory works. The accuracy of the original model, for freshwater ice, depends highly on the size of time step, normally must be smaller than one second. The accuracy of the results requires much of the computational time. It is recommended to use a more recent viscoelastic model in future works after modifying those models to take porosity into account, see Refs. [55].
- 4) In plasticity formulation, a non-associated flow rule could be considered based on Glen's model for the ductile deformation of ice and Michel's model for brittle fracture.
- 5) A hardening rule could be applied in the shear-failure of cap-model plasticity.

- 6) The Bauschinger effects could be applied to the cap-model plasticity in future works.
- 7) In shear-yield envelope, the parameter  $K$  could be assumed to be not equal to one for including the dependence on the third deviatoric stress invariant in shear failure of ice.
- 8) The available test results on freshwater granular and columnar S2 ice types are limited to a certain strain-rates and temperatures. A series of complementary material tests are required for other ranges of temperatures and strain rates. In addition, the similar failure curves should also be obtained for the case of columnar S1 ice, as well for the various types of ice at higher strain rates for extending the formulations beyond the ductile region.
- 9) The ice cohesion, in this study, is assumed to be independent from strain rate, so a function of temperature only, equation (5.3). A little strain-rate dependency, however, is observed for this parameter in the existing test data. This can be applied to the formulations of ice fixed-yield envelope in future works.
- 10) In the UMAT subroutine presented here, no strain-rate dependency is considered for the tensile strength of bubble-free ice  $p_t^{\max}$ , see Section 5.2.3. The small strain-rate dependency, however, can be applied to the fixed-yield envelope of ice in future works. The cap-model formulations presented in this study, however, takes this dependency into consideration; see equations (5.73) to (5.75).
- 11) Some other experimental tests are also required for relating the material parameters of shear yielding to meteorological parameters (LWC, ice type, droplet size, wind velocity, air temperature).
- 12) The lack of results of material tests on various types of atmospheric ice (with confinement) hinders the complete evaluation of the model. Further investigation is needed

to evaluate the model accuracy for predicting the pressure-dependency of atmospheric ice behaviour when subjected to arbitrary loading conditions.

13) Further studies are still required to describe the real loading scenarios exerted on the system of lines and towers. The results could be assumed to be the boundary conditions for this model.

14) The presence of air bubbles are considered in the cap-model plasticity by using the definition of the term “porosity” to take the size and the density of the bubbles into consideration. The size and the shape of air bubbles, however, play a very important role in cracking activities, particularly in tension. Hence, the porosity should be replaced by the size and the density of air bubbles in those cracking models.

15) The coupled temperature-deformation problem could be defined to investigate the influence of thermal stresses in ice shedding phenomena.

## REFERENCES

- [1] *ABAQUS theory manual (2003)*; Version 6.4, ABAQUS Incorporation.
- [2] *ABAQUS users manual (2003)*; User subroutine & parametric studies, Version 6.4, ABAQUS Incorporation, VI: 25.20.30-1-14.
- [3] *Arakawa, M., and Maeno, N. (1997)*; Mechanical strength of polycrystalline ice under uniaxial compression, *Cold region science and technology*, **26**: 215-229.
- [4] *Bentley, C.R., Pomeroy, P.W., and Dorman, H.J. (1957)*; Seismic measurements on the Greenland ice-cap, *Annales de Géophysique*, **13**: 253-285.
- [5] *Bouamoul, A. (2002)*; Étude expérimentale et théorique sur le processus de délestage par fonte de la glace accumulée autour d'un cylindre, Thèse de doctorat, Université du Québec à Chicoutimi (UQAC).
- [6] *Budd, W.F., and Jacka, T.H. (1989)*; A review of ice rheology for ice sheet modeling, *Cold region science and technology*, **16** (139): 107-144.
- [7] *Chtourou, H., Guillot, M., and Gakwaya, A. (2002)*; Modeling of the metal powder compaction process using the cap model, Part I: Experimental material characterization and validation, *International Journal of Solids and Structures*, **39**: 1059-1075.
- [8] *Chtourou, H., Gakwaya, A., and Guillot, M. (2002)*; Modeling of the metal powder compaction process using the cap model, Part II: Numerical implementation and practical applications, *International Journal of Solids and Structures*, **39**: 1077-1096.
- [9] *Cole, D.M. (1987)*; Strain-rate and grain-size effects in ice, *Journal of Glaciology*, **33** (155): 274-280.
- [10] *Colle, J.J. (2000)*; Compressed-water pulse generators and applications, Tempress Technologies Incorporation.
- [11] *Cowin, S.C. (2004)*; Anisotropic poroelasticity - fabric tensor formulation, *Mechanics of Material*, **36**: 665-677.
- [12] *Cox, G.F.N., Richter-Menge, J.A. (1985)*; Tensile strength of multi-year pressure ridge ice samples, Proc. 4<sup>th</sup> Int'l Symposium on Offshore Mechanics and Arctic Engineering, Dallas, Texas.
- [13] *Dantl, G. (1969)*; Elastic moduli of ice, in *Physics of ice*, by Riehl, N., Bullemer, B., and Engelhardt, H., Cambridge University Press, Cambridge: 223-230.
- [14] *Derradji-Aouat, A. (1992)*; Mathematical modeling of monotonic and cyclic behaviour of freshwater ice, doctorate thesis, Ottawa University, Ottawa.
- [15] *Derradji-Aouat, A., Sinha, N.K., Evgin, E. (2000)*; Mathematical modeling of monotonic and cyclic behaviour of freshwater columnar grained S-2 ice, *Journal of Cold Region Engineering*, **31**: 59-81.

- [16] *Drucker, D.C., Gibson, R.E., and Henkel, D.J. (1957); Soil mechanics and work-hardening theories of plasticity, Transactions American Society of Civil Engineers, 122.*
- [17] *Druez, J., Nguyen, D.D., and Lavoie, Y. (1986); Mechanical properties of atmospheric ice, Cold region science and technology, 13: 67-74.*
- [18] *Druez, J., Louchez, S., and Bouchard, G. (1990); Study of ice shedding phenomenon on cables, Proceedings of 9<sup>th</sup> International Conference of Offshore Mechanics and Arctic Engineering, 143-148.*
- [19] *Druez, J., and McComber, P. (1997); Ice accretion and shedding on overhead line cables, Proceedings of the 7<sup>th</sup> International Offshore and Polar Engineering Conference, 2: 647-655.*
- [20] *Fish, A.M. (1991); Creep and yield model of ice under combined stress, CRREL report 91-31.*
- [21] *Fish, A.M., and Zaretsky, Y.K. (1997); Ice strength as a function of hydrostatic pressure and temperature, Cold Region Research and Engineering Laboratory, Tech. Report 97-6.*
- [22] *Frederking, R.M.W. (1977); Plain strain compressible strength of columnar-grained and granular-snow ice, Journal of glaciology, 18 (80): 505-516.*
- [23] *Frederking, R.M.W., and Timco, G.W. (1986); Field measurement of the shear strength of columnar-grained sea ice, Proc. IAHR Symp., Iowa City, 1: 279-292.*
- [24] *Gagnon, R.E., Kieft, H., and Clouter, M.J. (1988); Pressure dependence of the elastic constants of ice  $I_h$  to 2.8 kbar by Brillouin Spectroscopy, Journal of Chem. Phys., 89 (8): 4522-4528.*
- [25] *Gagnon, R.E., and Gammon, P.H. (1995); Triaxial experiments on iceberg and glacier ice, Journal of Glaciology, 41 (139): 538-540.*
- [26] *Gammon, P.H., Kieft, H., Clouter, M.J., and Denner, W.W. (1983); Elastic constants of artificial and natural ice samples by Brillouin Spectroscopy, Journal of Glaciology, 29 (103): 433-460.*
- [27] *Gold, L.W. (1970); Process of failure in ice, National research council of Canada (NRC), Division of building research.*
- [28] *Gold, L.W. (1978); Engineering properties of freshwater ice, Journal of glaciology, 19 (81): 197-212.*
- [29] *Graham, B.W., Chabot, L.G., and Pilkington, G.R. (1983); Ice load sensors for offshore Arctic structures, Proc. POAC'83, Helsinki, Finland, 4: 547-562.*
- [30] *Hausler, F.U. (1983); Comparison between different yield functions of saline ice, Annals of Glaciology, 4: 105-109.*

- [31] *Hill, R. (1952)*; The elastic behaviour of a crystalline aggregate, Proc. Phys. Soc., **65(A)**, 349-354.
- [32] *Jacka, T.H. (1984)*; Laboratory studies on relationships between ice crystal size and flow rate, Cold region science and technology, **10 (1)**: 31-42.
- [33] *Jones, S.J. (1982)*; The confined compressive strength of polycrystalline ice, Journal of Glaciology, **28 (98)**: 171-177.
- [34] *Jordaan, I.J., and McKenna, R.F. (1989)*; Processes of deformation and fracture of ice in compression, proceeding of Symposium on ice-structure interaction, St. John's, Newfoundland, 283-310.
- [35] *Kim, J., and Sunder, S.S. (1997)*; Statistical effects on the evolution of compliance and compressive fracture stress of ice, Cold region science and technology, **26**: 137-152.
- [36] *Laforte, J.-L., and Phan, L.C. (1983)*; Microstructure of ice accretions grown on aluminum conductors, Journal of Climate and Applied Meteorology, **22 (7)**: 1175-1189.
- [37] *Lu, M.L., Popplewell, N., and Shah, A.H. (2000)*; Freezing rain simulations for fixed and unheated conductor samples, University of Manitoba, Manitoba.
- [38] *Michel, B., and Ramseier, R.O. (1971)*; Classification of river and lake ice, Canadian geotechnical journal, **8**: 36-45.
- [39] *Michel, B. (1978)*; Ice Mechanics, Presses de l'Université Laval, Québec.
- [40] *Michel, B., and Blanchet, D. (1983)*; Indentation of an S2 floating ice sheet in the brittle range, Annals of Glaciology, **4**: 180-187.
- [41] *Nadreau, J.P., and Michel, B. (1986)*; Yield and failure envelope for ice under multiaxial compressive stresses, Cold region science and technology, **12**: 75-82.
- [42] *Nadreau, J.P., Nawwar, A.M., and Wang, Y.S. (1991)*; Triaxial testing of freshwater ice at low confining pressure, Transactions of ASME, **113**: 260-265.
- [43] *Nanthikesan, S., and Sunder, S.S. (1994)*; Anisotropic elasticity of polycrystalline ice  $I_h$ , Cold region science and technology, **22**: 149-169.
- [44] *Nowick, A.S., and Berry, B.S. (1972)*; Anelastic relaxation in crystalline solids, Academic Press, New York.
- [45] *Ortiz, M., and Popov, E. P. (1985)*; Accuracy and stability of integration algorithms for elastoplastic constitutive relations, International Journal for Numerical Methods in Engineering, **21**: 1561-1576.
- [46] *Ramseier, R.O. (1976)*; Growth and mechanical properties of river and lake ice, Ph.D. thesis at Civil engineering department, Laval University, Quebec.
- [47] *Reuss, A. (1929)*; Z. Angew. Math. Mech., **9**: 49.

- [48] *Richter-Menge, J.A., Cox, G.F.N., Perron, N., Durell, G., Bosworth, H.W. (1986);* Triaxial testing of first-year sea ice, USA Cold Regions Research and Engineering Laboratory, CRREL Report 86-16.
- [49] *Richter-Menge, J.A. (1992);* US research in ice mechanics: 1987-1990, Cold region science and technology, **20**: 231-246.
- [50] *Rist, M.A., and Murrell, S.A.F. (1994);* Ice triaxial deformation and fracture, Journal of Glaciology, **40** (135): 305-318.
- [51] *Rogachko, S. I. et al. (1997);* The influence of porosity on mechanical strength of hummocks, Proc. 16<sup>th</sup> Int. Conf. Offshore Mechanics and Arctic Eng., Yokohama, **IV**: 151-157.
- [52] *Roshan-Fekr, M., and McClure, G. (1998);* Numerical modeling of the dynamic response of ice shedding on electrical transmission lines, Atmospheric Research Special Issue, **46** (1-2): 538-540.
- [53] *Sandler, I.S., and Rubin, D. (1979);* An algorithm and a modular subroutine for the cap model, International Journal for Numerical and Analytical Methods in Geomechanics, **3**: 173-186.
- [54] *Sayles, F.H. (1974);* Triaxial constant strain rate tests and triaxial creep tests on frozen Ottawa sand, USA Cold Regions Research and Engineering Laboratory, Technical Report 23.
- [55] *Schapery, R.A. (1997);* Linear elastic and viscoelastic deformation behaviour of ice, Journal of Cold Region Engineering, **11**(4): 271-289.
- [56] *Sinha, N.K. (1977);* Technique for studying structure of sea ice, Journal of glaciology, **18** (79): 315-323.
- [57] *Sinha, N.K. (1978a);* Observation of basal dislocations in ice by etching and replicating, Journal of glaciology, **21** (85): 385-395.
- [58] *Sinha, N.K. (1978b);* Short-term rheology of polycrystalline ice, Journal of glaciology, **21** (85): 457-473.
- [59] *Sinha, N.K. (1981);* Deformation behaviour of ice like material in engineering application, Int. sym. on mech. behaviour of the structured media, Ottawa, 419-430.
- [60] *Sinha, N.K. (1983);* Creep model of ice for monotonically increasing stress, Cold region science and technology, **8**: 25-33.
- [61] *Sinha, N.K. (1984);* Inter crystalline cracking, grain boundary sliding and delayed elasticity at high temperatures, Journal of material science, **19** (2): 359-376.
- [62] *Sinha, N.K. (1985);* Confined strength and deformation of second-year columnar-grained sea ice in Mould Bay, Proc. 4<sup>th</sup> OMAE Symp., Dallas, Texas, **II**: 209-219.
- [63] *Sinha, N.K. (1986);* Young arctic frazil sea ice: field and laboratory strength tests, Journal of Materials Science, **21**(5): 1533-1546.

- [64] *Sinha, N.K., Timco, G.W., and Frederking, R. (1987)*; Recent advances in ice mechanics in Canada, National Research Council of Canada (NRC).
- [65] *Sinha, N.K. (1989)*; Elasticity of natural types of polycrystalline ice, Cold region science and technology, **17**: 127-135.
- [66] *Sjolind, S.G. (1987)*; A constitutive model for ice as damaging-viscoelastic material, Cold region science and technology, **14**: 247-262.
- [67] *Structure group of ice storm commission (2002)*; Lessons from the ice storm of 1998, Proceeding of International Workshop of Atmospheric Icing Structures, IW AIS 2002.
- [68] *Sunder, S.S., and Wu, M.S. (1989)*; A multiaxial differential model of flow in orthotropic polycrystalline ice, Cold region science and technology, **16**: 223-235.
- [69] *Sunder, S.S., and Wu, M.S. (1990a)*; Crack nucleation due to elastic anisotropy in polycrystalline ice, Cold region science and technology, **18**: 29-47.
- [70] *Sunder, S.S., and Wu, M.S. (1990b)*; On the constitutive modeling of transient creep in polycrystalline ice, Cold region science and technology, **18**: 267-294.
- [71] *Sunder, S.S., and Nanthikesan, S. (1990c)*; Crack nucleation due to elastic anisotropy in porous ice, Cold region science and technology, **18**: 249-265.
- [72] *Timco, G.W., and Frederking, R.M.W. (1984)*; An investigation of the failure envelope of granular/discontinuous-columnar sea ice, Cold region science and technology, **9**: 17-27.
- [73] *Timco, G.W., and Frederking, R.M.W. (1986)*; Confined compression tests: Outlining the failure envelope of columnar sea ice, Cold region science and technology, **12**: 13-28.
- [74] *Voigt, W. (1910)*; Lehrbuch Der Krystallphysik, Feubner, Berlin.
- [75] *Weiss, J., and Schulson, E.M. (1995)*; The failure of freshwater granular ice under compressive loading, Acta Metallurgica Material, **43** (6): 2303-2315.
- [76] *Witney, K.C., Frederking, R.M.W., and Weir-Jones, I. (1986)*; Field performance of an ice force panel for in-situ and structural measurements, Polar Tech'86, Helsinki, Finland: 27-30.
- [77] *Xiao, J., and Jordaan, I.J. (1996)*; Application of damage mechanics to ice failure in compression, Cold region science and technology, **24**: 305-322.
- [78] *Zener, C. (1948)*; Elasticity and anelasticity of metals, The University of Chicago Press: 170.
- [79] *Zhan, C., Evgin, E., and Sinha, N.K. (1994)*; A three dimensional anisotropic constitutive model for ductile behaviour of columnar grained ice, Cold region science and technology, **22**: 269-284.

## **APPENDIX 1**

### **MAPLE CODE FOR ICE ELASTIC MODULI**

## *Ice elasticity - Granular*

```
> restart:  
with(linalg):  
with(tensor):  
Digits:= Digits+10:  
pi:=3.14159265358979332384:
```

- ▣ Rotation matrices
- ▣ Stress tensors in rotated coordinates
- ▣ Strain tensors in rotated coordinates
- ▣ Monocrystal elastic stiffness constants for hexagonal ice I<sub>h</sub>
- ▣ Monocrystal elastic compliance constants for hexagonal ice I<sub>h</sub>
- ▣ Isotropic elastic moduli for granular ice -- Voigt assumption
- ▣ Isotropic elastic moduli for granular ice -- Reuss assumption
- ▣ Isotropic elastic moduli for granular ice -- Hill's averaging technique

## ***Ice elasticity - Granular***

```
> restart:
with(linalg):
with(tensor):
Digits:= Digits+10:
pi:=3.14159265358979332384:
```

### ☒ Rotation matrices

A general rotation around Cartesian axes from global to principal coordinates (c.c.w. rotation is positive):

```
> angle2:= phi:
angle3:= theta:
```

#### **A positive rotation around 3-axis**

3-axis in principal coordinates is in direction of c-axis

```
> Q3:= matrix(3,3,[cos(angle3),sin(angle3),0,-sin(angle3),cos(angle3),0,0,0,1]);
```

$$Q^3 := \begin{bmatrix} \cos(\theta) & \sin(\theta) & 0 \\ -\sin(\theta) & \cos(\theta) & 0 \\ 0 & 0 & 1 \end{bmatrix}$$

```
> Q3tran:= transpose(Q3):
> Q3inv:= simplify(inverse(Q3),trig):
```

#### **A positive rotation around 2-axis**

2-axis in principal coordinates is normal to c-axis

```
> Q2:= matrix(3,3,[cos(angle2),0,-sin(angle2),0,1,0,sin(angle2),0,cos(angle2)]);
```

$$Q^2 := \begin{bmatrix} \cos(\phi) & 0 & -\sin(\phi) \\ 0 & 1 & 0 \\ \sin(\phi) & 0 & \cos(\phi) \end{bmatrix}$$

```
> Q2tran:= transpose(Q2):
> Q2inv:= simplify(inverse(Q2),trig):
```

### **The general rotation from global to principal coordinates (angle3, angle2)**

```
> Q:= simplify(evalm(Q2 &* Q3),trig);
Qtran:= transpose(Q):
Qinv:= simplify(inverse(Q),trig):
```

$$Q := \begin{bmatrix} \cos(\phi)\cos(\theta) & \cos(\phi)\sin(\theta) & -\sin(\phi) \\ -\sin(\theta) & \cos(\theta) & 0 \\ \sin(\phi)\cos(\theta) & \sin(\phi)\sin(\theta) & \cos(\phi) \end{bmatrix}$$

### ☒ Stress tensor in rotated coordinates

#### **Tensorial format:**

Stress components in principal coordinates of orthotropic material

(3-axis in direction of c-axis)

```
> Tt:= matrix(3,3,[T11,T12,T13,T12,T22,T23,T13,T23,T33]):
```

Stress components in global axes

(after two consequence rotations around 3 and 2-axis)

```
> t:= matrix(3,3,[t11,t12,t13,t12,t22,t23,t13,t23,t33]):
t:= evalm(Qtran &* Tt &* Q):
t11:= simplify(t[1,1],trig):
t12:= simplify(t[1,2],trig):
t13:= simplify(t[1,3],trig):
t22:= simplify(t[2,2],trig):
t23:= simplify(t[2,3],trig):
t33:= simplify(t[3,3],trig):
t:= matrix(3,3,[t11,t12,t13,t12,t22,t23,t13,t23,t33]):
```

**Engineering format:**

Stress components in principal coordinates of orthotropic material

(3-axis in direction of c-axis)

```
> Sigma:= vector(6,[Sigma11,Sigma22,Sigma33,Tau23,Tau13,Tau12]):
```

Rotation matrix for stress tensor in engineering notation ( $\sigma=[L]^T \Sigma$ ):

```
> Lt:=matrix(6,6,[Lt11,Lt12,Lt13,Lt14,Lt15,Lt16,Lt12,Lt22,Lt23,Lt24,Lt25,Lt26,
Lt13,Lt23,Lt33,Lt34,Lt35,Lt36,Lt14,Lt24,Lt34,Lt44,Lt45,Lt46,
Lt15,Lt25,Lt35,Lt45,Lt55,Lt56,Lt16,Lt26,Lt36,Lt46,Lt56,Lt66]):
```

```
Lt:=matrix(6,6,[
Q[1,1]^2,Q[1,2]^2,Q[1,3]^2,Q[1,3]*Q[1,2],Q[1,3]*Q[1,1],Q[1,2]*Q[1,1],
Q[2,1]^2,Q[2,2]^2,Q[2,3]^2,Q[2,3]*Q[2,2],Q[2,3]*Q[2,1],Q[2,2]*Q[2,1],
Q[3,1]^2,Q[3,2]^2,Q[3,3]^2,Q[3,3]*Q[3,2],Q[3,3]*Q[3,1],Q[3,2]*Q[3,1],
2*Q[2,1]*Q[3,1],2*Q[2,2]*Q[3,2],2*Q[2,3]*Q[3,3],Q[2,3]*Q[3,2]+Q[3,3]*Q[2,2],Q[2
,3]*Q[3,1]+Q[3,3]*Q[2,1],Q[2,2]*Q[3,1]+Q[3,2]*Q[2,1],
2*Q[1,1]*Q[3,1],2*Q[1,2]*Q[3,2],2*Q[1,3]*Q[3,3],Q[1,3]*Q[3,2]+Q[3,3]*Q[1,2],Q[1
,3]*Q[3,1]+Q[3,3]*Q[1,1],Q[1,2]*Q[3,1]+Q[3,2]*Q[1,1],
2*Q[1,1]*Q[2,1],2*Q[1,2]*Q[2,2],2*Q[1,3]*Q[2,3],Q[1,3]*Q[2,2]+Q[2,3]*Q[1,2],Q[1
,3]*Q[2,1]+Q[2,3]*Q[1,1],Q[1,2]*Q[2,1]+Q[2,2]*Q[1,1]):
```

Lt11:=Lt [1, 1];

Lt14:=Lt [1, 4];

Lt21:=Lt [2, 1];

Lt24:=Lt [2, 4];

Lt31:=Lt [3, 1];

Lt34:=Lt [3, 4];

Lt41:=Lt [4, 1];

Lt44:=Lt [4, 4];

Lt51:=Lt [5, 1];

Lt54:=Lt [5, 4];

Lt61:=Lt [6, 1];

Lt64:=Lt [6, 4];

Lt12:=Lt [1, 2];

Lt15:=Lt [1, 5];

Lt22:=Lt [2, 2];

Lt25:=Lt [2, 5];

Lt32:=Lt [3, 2];

Lt35:=Lt [3, 5];

Lt42:=Lt [4, 2];

Lt45:=Lt [4, 5];

Lt52:=Lt [5, 2];

Lt55:=Lt [5, 5];

Lt62:=Lt [6, 2];

Lt65:=Lt [6, 5];

Lt13:=Lt [1, 3];

Lt16:=Lt [1, 6];

Lt23:=Lt [2, 3];

Lt26:=Lt [2, 6];

Lt33:=Lt [3, 3];

Lt36:=Lt [3, 6];

Lt43:=Lt [4, 3];

Lt46:=Lt [4, 6];

Lt53:=Lt [5, 3];

Lt56:=Lt [5, 6];

Lt63:=Lt [6, 3];

Lt66:=Lt [6, 6];

Lt11 :=  $\cos(\phi)^2 \cos(\theta)^2$

Lt14 :=  $-\sin(\phi) \cos(\phi) \sin(\theta)$

Lt21 :=  $\sin(\theta)^2$

Lt24 := 0

Lt31 :=  $\sin(\phi)^2 \cos(\theta)^2$

Lt34 :=  $\sin(\phi) \cos(\phi) \sin(\theta)$

Lt41 :=  $-2 \sin(\theta) \sin(\phi) \cos(\theta)$

Lt44 :=  $\cos(\phi) \cos(\theta)$

Lt12 :=  $\cos(\phi)^2 \sin(\theta)^2$

Lt15 :=  $-\sin(\phi) \cos(\phi) \cos(\theta)$

Lt22 :=  $\cos(\theta)^2$

Lt25 := 0

Lt32 :=  $\sin(\phi)^2 \sin(\theta)^2$

Lt35 :=  $\sin(\phi) \cos(\phi) \cos(\theta)$

Lt42 :=  $2 \sin(\theta) \sin(\phi) \cos(\theta)$

Lt45 :=  $-\cos(\phi) \sin(\theta)$

Lt13 :=  $\sin(\phi)^2$

Lt16 :=  $\cos(\phi)^2 \sin(\theta) \cos(\theta)$

Lt23 := 0

Lt26 :=  $-\cos(\theta) \sin(\theta)$

Lt33 :=  $\cos(\phi)^2$

Lt36 :=  $\sin(\phi)^2 \sin(\theta) \cos(\theta)$

Lt43 := 0

Lt46 :=  $\cos(\theta)^2 \sin(\phi) - \sin(\theta)^2 \sin(\phi)$

```

Lt51 := 2 cos(phi) cos(theta)^2 sin(phi)      Lt52 := 2 cos(phi) sin(theta)^2 sin(phi)      Lt53 := -2 sin(phi) cos(phi)
Lt54 := -sin(phi)^3 sin(theta) + cos(phi)^2 sin(theta)  Lt55 := -sin(phi)^2 cos(theta) + cos(phi)^2 cos(theta)  Lt56 := 2 cos(phi) cos(theta) sin(phi) sin(theta)
Lt61 := -2 cos(phi) cos(theta) sin(theta)      Lt62 := 2 cos(phi) cos(theta) sin(theta)      Lt63 := 0
Lt64 := -sin(phi) cos(theta)                  Lt65 := sin(phi) sin(theta)                  Lt66 := -cos(phi) sin(theta)^2 + cos(phi) cos(theta)^2

```

```

> Lttran:= simplify(transpose(Lt),trig):
Lttraninv:= simplify(inverse(Lttran),trig):

```

### Stress components in global axes

(after two consequence rotations around 3 and 2-axis)

```

> sigma:= vector(6, [sigma11, sigma22, sigma33, tau23, tau13, tau12]):
sigma:= evalm(Lttran &* Sigma):
sigma11:= simplify(sigma[1],trig):
sigma22:= simplify(sigma[2],trig):
sigma33:= simplify(sigma[3],trig):
tau23:= simplify(sigma[4],trig):
tau13:= simplify(sigma[5],trig):
tau12:= simplify(sigma[6],trig):
sigma:= vector(6, [sigma11, sigma22, sigma33, tau23, tau13, tau12]):

```

## ☒ Strain tensor in rotated coordinates

### Tensorial format:

Strain components in principal coordinates of orthotropic material

(3-axis in direction of c-axis)

```

> E:= matrix(3,3, [E11,E12,E13,E12,E22,E23,E13,E23,E33]):

```

Strain components in global axes

(after two consequence rotations around 3 and 2-axis)

```

> e:= matrix(3,3, [e11,e12,e13,e12,e22,e23,e13,e23,e33]):
e:= evalm(Qtran &* E &* Q):
e11:= simplify(e[1,1],trig):
e12:= simplify(e[1,2],trig):
e13:= simplify(e[1,3],trig):
e22:= simplify(e[2,2],trig):
e23:= simplify(e[2,3],trig):
e33:= simplify(e[3,3],trig):
e:= matrix(3,3, [e11,e12,e13,e12,e22,e23,e13,e23,e33]):

```

### Engineering format:

Strain components in principal coordinates of orthotropic material

(3-axis in direction of c-axis)

```

> Gamma:= vector(6, [Epsilon11,Epsilon22,Epsilon33,Gamma23,Gamma13,Gamma12]):

```

Rotation matrix for strain in engineering notation (epsilon=[Le]<sup>T</sup>\*Gamma):

```

> Le:=matrix(6,6, [Le11,Le12,Le13,Le14,Le15,Le16,Le12,Le22,Le23,Le24,Le25,Le26,
                  Le13,Le23,Le33,Le34,Le35,Le36,Le14,Le24,Le34,Le44,Le45,Le46,
                  Le15,Le25,Le35,Le45,Le55,Le56,Le16,Le26,Le36,Le46,Le56,Le66]):

```

```

Le:=matrix(6,6, [
Q[1,1]^2,Q[1,2]^2,Q[1,3]^2,2*Q[1,3]*Q[1,2],2*Q[1,3]*Q[1,1],2*Q[1,2]*Q[1,1],
Q[2,1]^2,Q[2,2]^2,Q[2,3]^2,2*Q[2,3]*Q[2,2],2*Q[2,3]*Q[2,1],2*Q[2,2]*Q[2,1],
Q[3,1]^2,Q[3,2]^2,Q[3,3]^2,2*Q[3,3]*Q[3,2],2*Q[3,3]*Q[3,1],2*Q[3,2]*Q[3,1],

```

```

Q[2,1]*Q[3,1],Q[2,2]*Q[3,2],Q[2,3]*Q[3,3],Q[2,3]*Q[3,2]+Q[3,3]*Q[2,2],Q[2,3]*Q[
3,1]+Q[3,3]*Q[2,1],Q[2,2]*Q[3,1]+Q[3,2]*Q[2,1],
Q[1,1]*Q[3,1],Q[1,2]*Q[3,2],Q[1,3]*Q[3,3],Q[1,3]*Q[3,2]+Q[3,3]*Q[1,2],Q[1,3]*Q[
3,1]+Q[3,3]*Q[1,1],Q[1,2]*Q[3,1]+Q[3,2]*Q[1,1],
Q[1,1]*Q[2,1],Q[1,2]*Q[2,2],Q[1,3]*Q[2,3],Q[1,3]*Q[2,2]+Q[2,3]*Q[1,2],Q[1,3]*Q[
2,1]+Q[2,3]*Q[1,1],Q[1,2]*Q[2,1]+Q[2,2]*Q[1,1]))):

```

```

Le11:=Le[1,1];           Le12:=Le[1,2];           Le13:=Le[1,3];
Le14:=Le[1,4];           Le15:=Le[1,5];           Le16:=Le[1,6];
Le21:=Le[2,1];           Le22:=Le[2,2];           Le23:=Le[2,3];
Le24:=Le[2,4];           Le25:=Le[2,5];           Le26:=Le[2,6];
Le31:=Le[3,1];           Le32:=Le[3,2];           Le33:=Le[3,3];
Le34:=Le[3,4];           Le35:=Le[3,5];           Le36:=Le[3,6];
Le41:=Le[4,1];           Le42:=Le[4,2];           Le43:=Le[4,3];
Le44:=Le[4,4];           Le45:=Le[4,5];           Le46:=Le[4,6];
Le51:=Le[5,1];           Le52:=Le[5,2];           Le53:=Le[5,3];
Le54:=Le[5,4];           Le55:=Le[5,5];           Le56:=Le[5,6];
Le61:=Le[6,1];           Le62:=Le[6,2];           Le63:=Le[6,3];
Le64:=Le[6,4];           Le65:=Le[6,5];           Le66:=Le[6,6];

```

```

Le11 := cos(phi)^2*cos(theta)^2           Le12 := cos(phi)^2*sin(theta)^2           Le13 := sin(phi)^2
Le14 := -2*sin(phi)*cos(phi)*sin(theta)   Le15 := -2*sin(phi)*cos(phi)*cos(theta)   Le16 := 2*cos(phi)^2*sin(theta)*cos(theta)
Le21 := sin(theta)^2                       Le22 := cos(theta)^2                       Le23 := 0
Le24 := 0                                  Le25 := 0                                  Le26 := -2*cos(theta)*sin(theta)
Le31 := sin(phi)^3*cos(theta)^2           Le32 := sin(phi)^2*sin(theta)^2           Le33 := cos(phi)^2
Le34 := 2*sin(phi)*cos(phi)*sin(theta)    Le35 := 2*sin(phi)*cos(phi)*cos(theta)    Le36 := 2*sin(phi)^2*sin(theta)*cos(theta)
Le41 := -sin(theta)*sin(phi)*cos(theta)   Le42 := sin(theta)*sin(phi)*cos(theta)   Le43 := 0
Le44 := cos(phi)*cos(theta)               Le45 := -cos(phi)*sin(theta)             Le46 := cos(theta)^2*sin(phi) - sin(theta)^2*sin(phi)
Le51 := cos(phi)*cos(theta)^2*sin(phi)    Le52 := cos(phi)*sin(theta)^2*sin(phi)   Le53 := -sin(phi)*cos(phi)
Le54 := -sin(phi)^2*sin(theta) + cos(phi)^2*sin(theta)
Le55 := -sin(phi)^2*cos(theta) + cos(phi)^2*cos(theta)
Le56 := 2*cos(phi)*cos(theta)*sin(phi)*sin(theta)
Le61 := -cos(phi)*cos(theta)*sin(theta)   Le62 := cos(phi)*cos(theta)*sin(theta)   Le63 := 0
Le64 := -sin(phi)*cos(theta)              Le65 := sin(phi)*sin(theta)              Le66 := -cos(phi)*sin(theta)^2 + cos(phi)*cos(theta)^2

```

```

> Letran:= simplify(transpose(Le),trig):
Letraninv:= simplify(inverse(Letran),trig):

```

Stress components in global axes

(after two consequence rotations around 3 and 2-axis)

```

> epsilon:= vector(6,[epsilon11,epsilon22,epsilon33,gamma23,gamma13,gamma12]):
epsilon:= evalm(Letran &* Gamma):
epsilon11:= simplify(epsilon[1],trig):
epsilon22:= simplify(epsilon[2],trig):
epsilon33:= simplify(epsilon[3],trig):
gamma23:= simplify(epsilon[4],trig):
gamma13:= simplify(epsilon[5],trig):
gamma12:= simplify(epsilon[6],trig):
epsilon:= vector(6,[epsilon11,epsilon22,epsilon33,gamma23,gamma13,gamma12]):

```

### ☒ Monocrystal elastic stiffness constants for hexagonal ice $I_h$

#### Monocrystal principals constants

The independant coefficients in  $[C_{ij}]$  are  $C_{11}=C_{22}$ ,  $C_{12}$ ,  $C_{13}=C_{23}$ ,  $C_{33}$ ,  $C_{44}=C_{55}$  for a hexagonal crystal.

We have also  $C_{66}=0.5(C_{11}-C_{12})$  where c-axis is in the direction of 3-axis.

Stiffness matrix in local principal axes is:

```
> C:=matrix(6,6,[C11,C12,C13,0,0,0,C12,C11,C13,0,0,0,
                C13,C13,C33,0,0,0,0,0,0,C44,0,0,0,0,0,C44,0,0,0,0,0,C66]);
```

$$C = \begin{bmatrix} C_{11} & C_{12} & C_{13} & 0 & 0 & 0 \\ C_{12} & C_{11} & C_{13} & 0 & 0 & 0 \\ C_{13} & C_{13} & C_{33} & 0 & 0 & 0 \\ 0 & 0 & 0 & C_{44} & 0 & 0 \\ 0 & 0 & 0 & 0 & C_{44} & 0 \\ 0 & 0 & 0 & 0 & 0 & C_{66} \end{bmatrix}$$

#### Gammon (1983) measurements for ice monocrystal $I_h$

The adiabatic values (GPa) at a reference temperature ( $T_m=-16C$ ) are measured as below:

```
> C0:= vector(5,[13.929,7.082,5.765,15.010,3.014]);
#C0:= vector(5,[13.675,6.828,5.514,14.761,3.014]);
```

The Isothermal values (GPa) at a reference temperature ( $T_m=-16C$ ) are measured as above.

The results can be presented in the form of  $C=C_0(1-a*T)/(1-a*T_m)$  where:

```
> a:= 1.418e-3:
Tm:= -16:
```

The temperature-dependence of elastic stiffness constants:

```
> Ct11:= T->C0[1]*(1-a*T)/(1-a*Tm):
Ct12:= T->C0[2]*(1-a*T)/(1-a*Tm):
Ct13:= T->C0[3]*(1-a*T)/(1-a*Tm):
Ct33:= T->C0[4]*(1-a*T)/(1-a*Tm):
Ct44:= T->C0[5]*(1-a*T)/(1-a*Tm):
Ct66:= T->0.5*(Ct11(T)-Ct12(T)):
```

```
Digits:= Digits-15:
```

```
Ct:=matrix(6,6,[Ct11(T),Ct12(T),Ct13(T),0,0,0,Ct12(T),Ct11(T),Ct13(T),0,0,0,
                Ct13(T),Ct13(T),Ct33(T),0,0,0,0,0,0,Ct44(T),0,0,0,0,0,Ct44(T),0,0,0,0,0,0,
                Ct66(T)]);
```

```
Ct:= [[13.620 - 0.019313 T, 6.9248 - 0.0098194 T, 5.6370 - 0.0079933 T, 0, 0, 0],
      [6.9248 - 0.0098194 T, 13.620 - 0.019313 T, 5.6370 - 0.0079933 T, 0, 0, 0],
      [5.6370 - 0.0079933 T, 5.6370 - 0.0079933 T, 14.677 - 0.020812 T, 0, 0, 0],
      [0, 0, 0, 2.9471 - 0.0041790 T, 0, 0], [0, 0, 0, 2.9471 - 0.0041790 T, 0, 0],
      [0, 0, 0, 0, 3.3476 - 0.0047468 T]]
```

Elastic constants at  $0^\circ C$ :

```
> Temp:=0:
Ctemp:= eval(Ct,T=Temp);
Stemp:= inverse(Ctemp);
Digits:= Digits+15:
```

$$C_{temp} := \begin{bmatrix} 13.620 & 6.9248 & 5.6370 & 0 & 0 & 0 \\ 6.9248 & 13.620 & 5.6370 & 0 & 0 & 0 \\ 5.6370 & 5.6370 & 14.677 & 0 & 0 & 0 \\ 0 & 0 & 0 & 2.9471 & 0 & 0 \\ 0 & 0 & 0 & 0 & 2.9471 & 0 \\ 0 & 0 & 0 & 0 & 0 & 3.3476 \end{bmatrix}$$

$$S_{temp} := \begin{bmatrix} 0.10552 & -0.043844 & -0.023686 & 0. & 0. & 0. \\ -0.043844 & 0.10552 & -0.023686 & 0. & 0. & 0. \\ -0.023686 & -0.023686 & 0.086328 & 0. & 0. & 0. \\ 0. & 0. & 0. & 0.33932 & 0. & 0. \\ 0. & 0. & 0. & 0. & 0.33932 & 0. \\ 0. & 0. & 0. & 0. & 0. & 0.29872 \end{bmatrix}$$

### Rotated monocrystal stiffness constants

$$[Cg] = [Lt]^T [C] [Le]^{-T}$$

```
> Cg := evalm(Lttran &* C &* Letraninv):
```

```
Cg11:= simplify(Cg[1,1],trig):
```

```
Cg12:= simplify(Cg[1,2],trig):
```

```
Cg13:= simplify(Cg[1,3],trig):
```

```
Cg14:= simplify(Cg[1,4],trig):
```

```
Cg15:= simplify(Cg[1,5],trig):
```

```
Cg16:= simplify(Cg[1,6],trig):
```

```
Cg22:= simplify(Cg[2,2],trig):
```

```
Cg23:= simplify(Cg[2,3],trig):
```

```
Cg24:= simplify(Cg[2,4],trig):
```

```
Cg25:= simplify(Cg[2,5],trig):
```

```
Cg26:= simplify(Cg[2,6],trig):
```

```
Cg33:= simplify(Cg[3,3],trig):
```

```
Cg34:= simplify(Cg[3,4],trig):
```

```
Cg35:= simplify(Cg[3,5],trig):
```

```
Cg36:= simplify(Cg[3,6],trig):
```

```
Cg44:= simplify(Cg[4,4],trig):
```

```
Cg45:= simplify(Cg[4,5],trig):
```

```
Cg46:= simplify(Cg[4,6],trig):
```

```
Cg55:= simplify(Cg[5,5],trig):
```

```
Cg56:= simplify(Cg[5,6],trig):
```

```
Cg66:= simplify(Cg[6,6],trig):
```

```
Cg := matrix(6,6,[Cg11,Cg12,Cg13,Cg14,Cg15,Cg16,Cg12,Cg22,Cg23,Cg24,Cg25,Cg26,
Cg13,Cg23,Cg33,Cg34,Cg35,Cg36,Cg14,Cg24,Cg34,Cg44,Cg45,Cg46,
Cg15,Cg25,Cg35,Cg45,Cg55,Cg56,Cg16,Cg26,Cg36,Cg46,Cg56,Cg66]):
```

```
Cgt := evalm(Lttran &* Ct &* Letraninv):
```

```
Cgt11:= simplify(Cgt[1,1],trig):
```

```
Cgt12:= simplify(Cgt[1,2],trig):
```

```
Cgt13:= simplify(Cgt[1,3],trig):
```

```
Cgt14:= simplify(Cgt[1,4],trig):
```

```
Cgt15:= simplify(Cgt[1,5],trig):
```

```
Cgt16:= simplify(Cgt [1,6], trig):
Cgt22:= simplify(Cgt [2,2], trig):
Cgt23:= simplify(Cgt [2,3], trig):
Cgt24:= simplify(Cgt [2,4], trig):
Cgt25:= simplify(Cgt [2,5], trig):
Cgt26:= simplify(Cgt [2,6], trig):
Cgt33:= simplify(Cgt [3,3], trig):
Cgt34:= simplify(Cgt [3,4], trig):
Cgt35:= simplify(Cgt [3,5], trig):
Cgt36:= simplify(Cgt [3,6], trig):
Cgt44:= simplify(Cgt [4,4], trig):
Cgt45:= simplify(Cgt [4,5], trig):
Cgt46:= simplify(Cgt [4,6], trig):
Cgt55:= simplify(Cgt [5,5], trig):
Cgt56:= simplify(Cgt [5,6], trig):
Cgt66:= simplify(Cgt [6,6], trig):

Cgt:= matrix(6,6, [Cgt11, Cgt12, Cgt13, Cgt14, Cgt15, Cgt16,
  Cgt12, Cgt22, Cgt23, Cgt24, Cgt25, Cgt26, Cgt13, Cgt23, Cgt33, Cgt34, Cgt35, Cgt36,
  Cgt14, Cgt24, Cgt34, Cgt44, Cgt45, Cgt46, Cgt15, Cgt25, Cgt35, Cgt45, Cgt55, Cgt56,
  Cgt16, Cgt26, Cgt36, Cgt46, Cgt56, Cgt66] ):
```

### ☒ Monocrystal elastic compliance constants for hexagonal ice $I_h$

#### Monocrystal principals constants

The independant coefficients in  $[S_{ij}]$  are  $S_{11}=S_{22}$ ,  $S_{12}$ ,  $S_{13}=S_{23}$ ,  $S_{33}$ ,  $S_{44}=S_{55}$  for a hexagonal crystal.

We have also  $S_{66}=2(S_{11}-S_{12})$  where c-axis is in the direction of 3-axis.

Compliance matrix in local principal axes is:

```
> S:=matrix(6,6,[S11,S12,S13,0,0,0,S12,S11,S13,0,0,0,
                S13,S13,S33,0,0,0,0,0,0,S44,0,0,0,0,0,S44,0,0,0,0,0,S66]);
```

$$S := \begin{bmatrix} S_{11} & S_{12} & S_{13} & 0 & 0 & 0 \\ S_{12} & S_{11} & S_{13} & 0 & 0 & 0 \\ S_{13} & S_{13} & S_{33} & 0 & 0 & 0 \\ 0 & 0 & 0 & S_{44} & 0 & 0 \\ 0 & 0 & 0 & 0 & S_{44} & 0 \\ 0 & 0 & 0 & 0 & 0 & S_{66} \end{bmatrix}$$

#### Gammon (1983) measurements for ice monocrystal $I_h$

The *adiabatic* values (GPa) at a reference temperature ( $T_m=-16C$ ) are measured as below:

```
> S0:= vector(5,[10.318,-4.287,-2.316,8.441,33.179]);
#S0:= vector(5,[10.350,-4.250,-2.280,8.480,33.180]);
S0:= evalm(S0*1e-2);
```

The *Isothermal* values (GPa) at a reference temperature ( $T_m=-16C$ ) are measured as above.

The results can be presented in the form of  $S=S_0(1+a*T)/(1+a*T_m)$  where:

```
> a:= 1.418e-3;
Tm:= -16;
```

The temperature-dependence of elastic compliance constants:

```
> St11:= T->S0[1]*(1+a*T)/(1+a*Tm);
St12:= T->S0[2]*(1+a*T)/(1+a*Tm);
St13:= T->S0[3]*(1+a*T)/(1+a*Tm);
St33:= T->S0[4]*(1+a*T)/(1+a*Tm);
St44:= T->S0[5]*(1+a*T)/(1+a*Tm);
St66:= T->2*(St11(T)-St12(T));
```

```
Digits:= Digits-16;
```

```
St:=matrix(6,6,[St11(T),St12(T),St13(T),0,0,0,St12(T),St11(T),St13(T),0,0,0,
                St13(T),St13(T),St33(T),0,0,0,0,0,0,St44(T),0,0,
                0,0,0,0,St44(T),0,0,0,0,0,0,St66(T)]);
```

```
S:= [[0.1056+0.0001497 T,-0.04387-0.00006221 T,-0.02370-0.00003361 T,0,0,0],
     [-0.04387-0.00006221 T,0.1056+0.0001497 T,-0.02370-0.00003361 T,0,0,0],
     [-0.02370-0.00003361 T,-0.02370-0.00003361 T,0.08637+0.0001225 T,0,0,0],
     [0,0,0,0.3395+0.0004814 T,0,0], [0,0,0,0,0.3395+0.0004814 T,0],
     [0,0,0,0,0.2989+0.0004238 T]]
```

Elastic constants at  $0^\circ C$ :

```
> Temp:=0;
Stemp:= eval(St,T=Temp);
Ctemp:= inverse(Stemp);
Digits:= Digits+16;
```

$$S_{temp} := \begin{bmatrix} 0.1056 & -0.04387 & -0.02370 & 0 & 0 & 0 \\ -0.04387 & 0.1056 & -0.02370 & 0 & 0 & 0 \\ -0.02370 & -0.02370 & 0.08637 & 0 & 0 & 0 \\ 0 & 0 & 0 & 0.3395 & 0 & 0 \\ 0 & 0 & 0 & 0 & 0.3395 & 0 \\ 0 & 0 & 0 & 0 & 0 & 0.2989 \end{bmatrix}$$

$$C_{temp} := \begin{bmatrix} 13.61 & 6.917 & 5.632 & 0. & 0. & 0. \\ 6.917 & 13.61 & 5.632 & 0. & 0. & 0. \\ 5.632 & 5.632 & 14.67 & 0. & 0. & 0. \\ 0. & 0. & 0. & 2.946 & 0. & 0. \\ 0. & 0. & 0. & 0. & 2.946 & 0. \\ 0. & 0. & 0. & 0. & 0. & 3.346 \end{bmatrix}$$

### Rotated monocystal stiffness constants

$$[Sg]=[Le]^T [S] [Lt]^T$$

```
> Sg:= evalm(Letran &* S &* Lttraninv):
```

```
Sg11:= simplify(Sg[1,1],trig):
```

```
Sg12:= simplify(Sg[1,2],trig):
```

```
Sg13:= simplify(Sg[1,3],trig):
```

```
Sg14:= simplify(Sg[1,4],trig):
```

```
Sg15:= simplify(Sg[1,5],trig):
```

```
Sg16:= simplify(Sg[1,6],trig):
```

```
Sg22:= simplify(Sg[2,2],trig):
```

```
Sg23:= simplify(Sg[2,3],trig):
```

```
Sg24:= simplify(Sg[2,4],trig):
```

```
Sg25:= simplify(Sg[2,5],trig):
```

```
Sg26:= simplify(Sg[2,6],trig):
```

```
Sg33:= simplify(Sg[3,3],trig):
```

```
Sg34:= simplify(Sg[3,4],trig):
```

```
Sg35:= simplify(Sg[3,5],trig):
```

```
Sg36:= simplify(Sg[3,6],trig):
```

```
Sg44:= simplify(Sg[4,4],trig):
```

```
Sg45:= simplify(Sg[4,5],trig):
```

```
Sg46:= simplify(Sg[4,6],trig):
```

```
Sg55:= simplify(Sg[5,5],trig):
```

```
Sg56:= simplify(Sg[5,6],trig):
```

```
Sg66:= simplify(Sg[6,6],trig):
```

```
Sg:= matrix(6,6,[Sg11,Sg12,Sg13,Sg14,Sg15,Sg16,Sg12,Sg22,Sg23,Sg24,Sg25,Sg26,
Sg13,Sg23,Sg33,Sg34,Sg35,Sg36,Sg14,Sg24,Sg34,Sg44,Sg45,Sg46,
Sg15,Sg25,Sg35,Sg45,Sg55,Sg56,Sg16,Sg26,Sg36,Sg46,Sg56,Sg66]):
```

```
Sgt:= evalm(Letran &* St &* Lttraninv):
```

```
Sgt11:= simplify(Sgt[1,1],trig):
```

```
Sgt12:= simplify(Sgt[1,2],trig):
```

```
Sgt13:= simplify(Sgt[1,3],trig):
```

```
Sgt14:= simplify(Sgt[1,4],trig):
```

```
Sgt15:= simplify(Sgt[1,5],trig):
```

```
Sgt16:= simplify(Sgt[1,6],trig):
```

```
Sgt22:= simplify(Sgt [2,2], trig) :
Sgt23:= simplify(Sgt [2,3], trig) :
Sgt24:= simplify(Sgt [2,4], trig) :
Sgt25:= simplify(Sgt [2,5], trig) :
Sgt26:= simplify(Sgt [2,6], trig) :
Sgt33:= simplify(Sgt [3,3], trig) :
Sgt34:= simplify(Sgt [3,4], trig) :
Sgt35:= simplify(Sgt [3,5], trig) :
Sgt36:= simplify(Sgt [3,6], trig) :
Sgt44:= simplify(Sgt [4,4], trig) :
Sgt45:= simplify(Sgt [4,5], trig) :
Sgt46:= simplify(Sgt [4,6], trig) :
Sgt55:= simplify(Sgt [5,5], trig) :
Sgt56:= simplify(Sgt [5,6], trig) :
Sgt66:= simplify(Sgt [6,6], trig) :

Sgt:= matrix(6,6, [Sgt11,Sgt12,Sgt13,Sgt14,Sgt15,Sgt16,
    Sgt12,Sgt22,Sgt23,Sgt24,Sgt25,Sgt26,Sgt13,Sgt23,Sgt33,Sgt34,Sgt3
    5,Sgt36,
    Sgt14,Sgt24,Sgt34,Sgt44,Sgt45,Sgt46,Sgt15,Sgt25,Sgt35,Sgt45,Sgt5
    5,Sgt56,
    Sgt16,Sgt26,Sgt36,Sgt46,Sgt56,Sgt66] ) :
```

### ☒ Isotropic elastic moduli for granular ice -- Voigt assumption

Elastic constants versus corresponding monocystal values

```

> Cv11:= simplify(int(int(Cg11*sin(phi), phi=0..Pi), theta=0..2*Pi)/(4*Pi));
Cv12:= simplify(int(int(Cg12*sin(phi), phi=0..Pi), theta=0..2*Pi)/(4*Pi));
Cv13:= simplify(int(int(Cg13*sin(phi), phi=0..Pi), theta=0..2*Pi)/(4*Pi));
Cv14:= simplify(int(int(Cg14*sin(phi), phi=0..Pi), theta=0..2*Pi)/(4*Pi));
Cv15:= simplify(int(int(Cg15*sin(phi), phi=0..Pi), theta=0..2*Pi)/(4*Pi));
Cv16:= simplify(int(int(Cg16*sin(phi), phi=0..Pi), theta=0..2*Pi)/(4*Pi));
Cv22:= simplify(int(int(Cg22*sin(phi), phi=0..Pi), theta=0..2*Pi)/(4*Pi));
Cv23:= simplify(int(int(Cg23*sin(phi), phi=0..Pi), theta=0..2*Pi)/(4*Pi));
Cv24:= simplify(int(int(Cg24*sin(phi), phi=0..Pi), theta=0..2*Pi)/(4*Pi));
Cv25:= simplify(int(int(Cg25*sin(phi), phi=0..Pi), theta=0..2*Pi)/(4*Pi));
Cv26:= simplify(int(int(Cg26*sin(phi), phi=0..Pi), theta=0..2*Pi)/(4*Pi));
Cv33:= simplify(int(int(Cg33*sin(phi), phi=0..Pi), theta=0..2*Pi)/(4*Pi));
Cv34:= simplify(int(int(Cg34*sin(phi), phi=0..Pi), theta=0..2*Pi)/(4*Pi));
Cv35:= simplify(int(int(Cg35*sin(phi), phi=0..Pi), theta=0..2*Pi)/(4*Pi));
Cv36:= simplify(int(int(Cg36*sin(phi), phi=0..Pi), theta=0..2*Pi)/(4*Pi));
Cv44:= simplify(int(int(Cg44*sin(phi), phi=0..Pi), theta=0..2*Pi)/(4*Pi));
Cv45:= simplify(int(int(Cg45*sin(phi), phi=0..Pi), theta=0..2*Pi)/(4*Pi));
Cv46:= simplify(int(int(Cg46*sin(phi), phi=0..Pi), theta=0..2*Pi)/(4*Pi));
Cv55:= simplify(int(int(Cg55*sin(phi), phi=0..Pi), theta=0..2*Pi)/(4*Pi));
Cv56:= simplify(int(int(Cg56*sin(phi), phi=0..Pi), theta=0..2*Pi)/(4*Pi));
Cv66:= simplify(int(int(Cg66*sin(phi), phi=0..Pi), theta=0..2*Pi)/(4*Pi));

```

```

Cv:=matrix(6,6,[Cv11,Cv12,Cv13,Cv14,Cv15,Cv16,Cv12,Cv22,Cv23,Cv24,Cv25,Cv26,
Cv13,Cv23,Cv33,Cv34,Cv35,Cv36,Cv14,Cv24,Cv34,Cv44,Cv45,Cv46,
Cv15,Cv25,Cv35,Cv45,Cv55,Cv56,Cv16,Cv26,Cv36,Cv46,Cv56,Cv66]):

```

$$Cv11 = \frac{9}{20} C11 + \frac{4}{15} C13 + \frac{8}{15} C44 + \frac{1}{12} C12 + \frac{1}{6} C66 + \frac{1}{5} C33$$

$$Cv12 = \frac{8}{15} C13 + \frac{1}{15} C33 + \frac{3}{20} C11 - \frac{1}{6} C66 - \frac{4}{15} C44 + \frac{1}{4} C12$$

$$Cv13 = \frac{1}{3} C12 - \frac{4}{15} C44 + \frac{1}{15} C11 + \frac{1}{15} C33 + \frac{8}{15} C13$$

$$Cv14 = 0$$

$$Cv15 = 0$$

$$Cv16 = 0$$

$$Cv22 = \frac{9}{20} C11 + \frac{4}{15} C13 + \frac{8}{15} C44 + \frac{1}{12} C12 + \frac{1}{6} C66 + \frac{1}{5} C33$$

$$Cv23 = \frac{1}{3} C12 - \frac{4}{15} C44 + \frac{1}{15} C11 + \frac{1}{15} C33 + \frac{8}{15} C13$$

$$Cv24 = 0$$

$$Cv25 = 0$$

$$Cv26 = 0$$

$$Cv33 = \frac{1}{5} C33 + \frac{4}{15} C13 + \frac{8}{15} C44 + \frac{8}{15} C11$$

$$Cv34 = 0$$

$$Cv35 = 0$$

$$Cv36 = 0$$

$$Cv44 = -\frac{2}{15} C13 + \frac{1}{15} C11 + \frac{1}{3} C66 + \frac{1}{15} C33 + \frac{2}{5} C44$$

$$Cv45 = 0$$

$$Cv46 = 0$$

$$C_{55} := -\frac{2}{15} C_{13} + \frac{1}{15} C_{11} + \frac{1}{3} C_{66} + \frac{1}{15} C_{33} + \frac{2}{5} C_{44}$$

$$C_{56} := 0$$

$$C_{66} := \frac{2}{5} C_{44} + \frac{1}{15} C_{33} + \frac{3}{20} C_{11} - \frac{2}{15} C_{13} - \frac{1}{12} C_{12} + \frac{1}{6} C_{66}$$

### Practical formulation of temperature dependence of elastic constants

```

> Digits:= Digits-15:
Cvt11:= simplify(int(int(Cgt11*sin(phi), phi=0..Pi), theta=0..2*Pi)/(4*Pi));
Cvt12:= simplify(int(int(Cgt12*sin(phi), phi=0..Pi), theta=0..2*Pi)/(4*Pi));
Cvt13:= simplify(int(int(Cgt13*sin(phi), phi=0..Pi), theta=0..2*Pi)/(4*Pi));
Cvt14:= simplify(int(int(Cgt14*sin(phi), phi=0..Pi), theta=0..2*Pi)/(4*Pi));
Cvt15:= simplify(int(int(Cgt15*sin(phi), phi=0..Pi), theta=0..2*Pi)/(4*Pi));
Cvt16:= simplify(int(int(Cgt16*sin(phi), phi=0..Pi), theta=0..2*Pi)/(4*Pi));
Cvt22:= simplify(int(int(Cgt22*sin(phi), phi=0..Pi), theta=0..2*Pi)/(4*Pi));
Cvt23:= simplify(int(int(Cgt23*sin(phi), phi=0..Pi), theta=0..2*Pi)/(4*Pi));
Cvt24:= simplify(int(int(Cgt24*sin(phi), phi=0..Pi), theta=0..2*Pi)/(4*Pi));
Cvt25:= simplify(int(int(Cgt25*sin(phi), phi=0..Pi), theta=0..2*Pi)/(4*Pi));
Cvt26:= simplify(int(int(Cgt26*sin(phi), phi=0..Pi), theta=0..2*Pi)/(4*Pi));
Cvt33:= simplify(int(int(Cgt33*sin(phi), phi=0..Pi), theta=0..2*Pi)/(4*Pi));
Cvt34:= simplify(int(int(Cgt34*sin(phi), phi=0..Pi), theta=0..2*Pi)/(4*Pi));
Cvt35:= simplify(int(int(Cgt35*sin(phi), phi=0..Pi), theta=0..2*Pi)/(4*Pi));
Cvt36:= simplify(int(int(Cgt36*sin(phi), phi=0..Pi), theta=0..2*Pi)/(4*Pi));
Cvt44:= simplify(int(int(Cgt44*sin(phi), phi=0..Pi), theta=0..2*Pi)/(4*Pi));
Cvt45:= simplify(int(int(Cgt45*sin(phi), phi=0..Pi), theta=0..2*Pi)/(4*Pi));
Cvt46:= simplify(int(int(Cgt46*sin(phi), phi=0..Pi), theta=0..2*Pi)/(4*Pi));
Cvt55:= simplify(int(int(Cgt55*sin(phi), phi=0..Pi), theta=0..2*Pi)/(4*Pi));
Cvt56:= simplify(int(int(Cgt56*sin(phi), phi=0..Pi), theta=0..2*Pi)/(4*Pi));
Cvt66:= simplify(int(int(Cgt66*sin(phi), phi=0..Pi), theta=0..2*Pi)/(4*Pi));

Cvt:=matrix(6,6,[Cvt11,Cvt12,Cvt13,Cvt14,Cvt15,Cvt16,
                 Cvt12,Cvt22,Cvt23,Cvt24,Cvt25,Cvt26,Cvt13,Cvt23,Cvt33,Cvt34,Cvt3
                 5,Cvt36,
                 Cvt14,Cvt24,Cvt34,Cvt44,Cvt45,Cvt46,Cvt15,Cvt25,Cvt35,Cvt45,Cvt5
                 5,Cvt56,
                 Cvt16,Cvt26,Cvt36,Cvt46,Cvt56,Cvt66]):
Digits:= Digits+15:

Cvt11 := -0.018824 T+13.274
Cvt12 := -0.0090965 T+6.4155
Cvt13 := -0.0090965 T+6.4152
Cvt14 := 0.
Cvt15 := 0.
Cvt16 := 0.
Cvt22 := -0.018823 T+13.274
Cvt23 := -0.0090965 T+6.4152
Cvt24 := 0.
Cvt25 := 0.
Cvt26 := 0.
Cvt33 := -0.018824 T+13.274
Cvt34 := 0.
Cvt35 := 0.
Cvt36 := 0.

```

```

Cvt44 := -0.0048630 T + 3.4295
Cvt45 := 0.
Cvt46 := 0.
Cvt55 := -0.0048630 T + 3.4295
Cvt56 := 0.
Cvt66 := -0.0048630 T + 3.4295

```

### ☒ Isotropic elastic moduli for granular ice -- Reuss assumption

#### Elastic constants versus corresponding monocrystal values

```

> Sr11:= simplify(int(int(Sg11*sin(phi), phi=0..Pi), theta=0..2*Pi)/(4*Pi));
Sr12:= simplify(int(int(Sg12*sin(phi), phi=0..Pi), theta=0..2*Pi)/(4*Pi));
Sr13:= simplify(int(int(Sg13*sin(phi), phi=0..Pi), theta=0..2*Pi)/(4*Pi));
Sr14:= simplify(int(int(Sg14*sin(phi), phi=0..Pi), theta=0..2*Pi)/(4*Pi));
Sr15:= simplify(int(int(Sg15*sin(phi), phi=0..Pi), theta=0..2*Pi)/(4*Pi));
Sr16:= simplify(int(int(Sg16*sin(phi), phi=0..Pi), theta=0..2*Pi)/(4*Pi));
Sr22:= simplify(int(int(Sg22*sin(phi), phi=0..Pi), theta=0..2*Pi)/(4*Pi));
Sr23:= simplify(int(int(Sg23*sin(phi), phi=0..Pi), theta=0..2*Pi)/(4*Pi));
Sr24:= simplify(int(int(Sg24*sin(phi), phi=0..Pi), theta=0..2*Pi)/(4*Pi));
Sr25:= simplify(int(int(Sg25*sin(phi), phi=0..Pi), theta=0..2*Pi)/(4*Pi));
Sr26:= simplify(int(int(Sg26*sin(phi), phi=0..Pi), theta=0..2*Pi)/(4*Pi));
Sr33:= simplify(int(int(Sg33*sin(phi), phi=0..Pi), theta=0..2*Pi)/(4*Pi));
Sr34:= simplify(int(int(Sg34*sin(phi), phi=0..Pi), theta=0..2*Pi)/(4*Pi));
Sr35:= simplify(int(int(Sg35*sin(phi), phi=0..Pi), theta=0..2*Pi)/(4*Pi));
Sr36:= simplify(int(int(Sg36*sin(phi), phi=0..Pi), theta=0..2*Pi)/(4*Pi));
Sr44:= simplify(int(int(Sg44*sin(phi), phi=0..Pi), theta=0..2*Pi)/(4*Pi));
Sr45:= simplify(int(int(Sg45*sin(phi), phi=0..Pi), theta=0..2*Pi)/(4*Pi));
Sr46:= simplify(int(int(Sg46*sin(phi), phi=0..Pi), theta=0..2*Pi)/(4*Pi));
Sr55:= simplify(int(int(Sg55*sin(phi), phi=0..Pi), theta=0..2*Pi)/(4*Pi));
Sr56:= simplify(int(int(Sg56*sin(phi), phi=0..Pi), theta=0..2*Pi)/(4*Pi));
Sr66:= simplify(int(int(Sg66*sin(phi), phi=0..Pi), theta=0..2*Pi)/(4*Pi));

Sr:=matrix(6,6,[Sr11,Sr12,Sr13,Sr14,Sr15,Sr16,Sr12,Sr22,Sr23,Sr24,Sr25,Sr26,
                Sr13,Sr23,Sr33,Sr34,Sr35,Sr36,Sr14,Sr24,Sr34,Sr44,Sr45,Sr46,
                Sr15,Sr25,Sr35,Sr45,Sr55,Sr56,Sr16,Sr26,Sr36,Sr46,Sr56,Sr66]):

```

$$S_{*11} := \frac{2}{15} S_{44} + \frac{4}{15} S_{13} + \frac{1}{5} S_{33} + \frac{9}{20} S_{11} + \frac{1}{24} S_{66} + \frac{1}{12} S_{12}$$

$$S_{*12} := \frac{3}{20} S_{11} + \frac{1}{4} S_{12} - \frac{1}{24} S_{66} + \frac{1}{15} S_{33} - \frac{1}{15} S_{44} + \frac{8}{15} S_{13}$$

$$S_{*13} := \frac{1}{3} S_{12} - \frac{1}{15} S_{44} + \frac{1}{15} S_{11} + \frac{1}{15} S_{33} + \frac{8}{15} S_{13}$$

$$S_{*14} := 0$$

$$S_{*15} := 0$$

$$S_{*16} := 0$$

$$S_{*22} := \frac{2}{15} S_{44} + \frac{4}{15} S_{13} + \frac{1}{5} S_{33} + \frac{9}{20} S_{11} + \frac{1}{24} S_{66} + \frac{1}{12} S_{12}$$

$$S_{*23} := \frac{1}{3} S_{12} - \frac{1}{15} S_{44} + \frac{1}{15} S_{11} + \frac{1}{15} S_{33} + \frac{8}{15} S_{13}$$

$$S_{*24} := 0$$

```

S<25 := 0
S<26 := 0
S<33 :=  $\frac{1}{5}S33 + \frac{4}{15}S13 + \frac{2}{15}S44 + \frac{8}{15}S11$ 
S<34 := 0
S<35 := 0
S<36 := 0
S<44 :=  $\frac{4}{15}S11 - \frac{8}{15}S13 + \frac{4}{15}S33 + \frac{2}{5}S44 + \frac{1}{3}S66$ 
S<45 := 0
S<46 := 0
S<55 :=  $\frac{4}{15}S11 - \frac{8}{15}S13 + \frac{4}{15}S33 + \frac{2}{5}S44 + \frac{1}{3}S66$ 
S<56 := 0
S<66 :=  $\frac{2}{5}S44 - \frac{8}{15}S13 + \frac{4}{15}S33 + \frac{1}{6}S66 + \frac{3}{5}S11 - \frac{1}{3}S12$ 

```

### Practical formulation of temperature dependence of elastic constants

```

> Digits:= Digits-16:
Srt11:= simplify(int(int(Sgt11*sin(phi), phi=0..Pi), theta=0..2*Pi)/(4*Pi));
Srt12:= simplify(int(int(Sgt12*sin(phi), phi=0..Pi), theta=0..2*Pi)/(4*Pi));
Srt13:= simplify(int(int(Sgt13*sin(phi), phi=0..Pi), theta=0..2*Pi)/(4*Pi));
Srt14:= simplify(int(int(Sgt14*sin(phi), phi=0..Pi), theta=0..2*Pi)/(4*Pi));
Srt15:= simplify(int(int(Sgt15*sin(phi), phi=0..Pi), theta=0..2*Pi)/(4*Pi));
Srt16:= simplify(int(int(Sgt16*sin(phi), phi=0..Pi), theta=0..2*Pi)/(4*Pi));
Srt22:= simplify(int(int(Sgt22*sin(phi), phi=0..Pi), theta=0..2*Pi)/(4*Pi));
Srt23:= simplify(int(int(Sgt23*sin(phi), phi=0..Pi), theta=0..2*Pi)/(4*Pi));
Srt24:= simplify(int(int(Sgt24*sin(phi), phi=0..Pi), theta=0..2*Pi)/(4*Pi));
Srt25:= simplify(int(int(Sgt25*sin(phi), phi=0..Pi), theta=0..2*Pi)/(4*Pi));
Srt26:= simplify(int(int(Sgt26*sin(phi), phi=0..Pi), theta=0..2*Pi)/(4*Pi));
Srt33:= simplify(int(int(Sgt33*sin(phi), phi=0..Pi), theta=0..2*Pi)/(4*Pi));
Srt34:= simplify(int(int(Sgt34*sin(phi), phi=0..Pi), theta=0..2*Pi)/(4*Pi));
Srt35:= simplify(int(int(Sgt35*sin(phi), phi=0..Pi), theta=0..2*Pi)/(4*Pi));
Srt36:= simplify(int(int(Sgt36*sin(phi), phi=0..Pi), theta=0..2*Pi)/(4*Pi));
Srt44:= simplify(int(int(Sgt44*sin(phi), phi=0..Pi), theta=0..2*Pi)/(4*Pi));
Srt45:= simplify(int(int(Sgt45*sin(phi), phi=0..Pi), theta=0..2*Pi)/(4*Pi));
Srt46:= simplify(int(int(Sgt46*sin(phi), phi=0..Pi), theta=0..2*Pi)/(4*Pi));
Srt55:= simplify(int(int(Sgt55*sin(phi), phi=0..Pi), theta=0..2*Pi)/(4*Pi));
Srt56:= simplify(int(int(Sgt56*sin(phi), phi=0..Pi), theta=0..2*Pi)/(4*Pi));
Srt66:= simplify(int(int(Sgt66*sin(phi), phi=0..Pi), theta=0..2*Pi)/(4*Pi));

Srt:= matrix(6,6,[Srt11,Srt12,Srt13,Srt14,Srt15,Srt16,
                  Srt12,Srt22,Srt23,Srt24,Srt25,Srt26,Srt13,Srt23,Srt33,Srt34,Srt3
                  5,Srt36,
                  Srt14,Srt24,Srt34,Srt44,Srt45,Srt46,Srt15,Srt25,Srt35,Srt45,Srt5
                  5,Srt56,
                  Srt16,Srt26,Srt36,Srt46,Srt56,Srt66]):

S<t11 := 0.1125 + 0.0001595 T
S<t12 := -0.00005260 T - 0.03710
S<t13 := -0.00005265 T - 0.03712
S<t14 := 0.
S<t15 := 0.
S<t16 := 0.

```

```

Srt22 := 0.0001595 T + 0.1126
Srt23 := -0.00005265 T - 0.03712
Srt24 := 0.
Srt25 := 0.
Srt26 := 0.
Srt33 := 0.0001595 T + 0.1126
Srt34 := 0.
Srt35 := 0.
Srt36 := 0.
Srt44 := 0.0004243 T + 0.2993
Srt45 := 0.
Srt46 := 0.
Srt55 := 0.0004243 T + 0.2993
Srt56 := 0.
Srt66 := 0.0004243 T + 0.2993

```

### ☒ Isotropic elastic moduli for granular ice -- Hill's averaging

#### Lower bound of elastic modulus (Reuss) at 0C

```

> Temp := 0:
Srtemp := eval(Srt, T=Temp);
Er := 3 / (Srtemp[1,1] + Srtemp[2,2] + Srtemp[3,3]);
vr := - (Srtemp[1,2] + Srtemp[1,3] + Srtemp[2,3]) * Er / 3;
Gr := 3 / (Srtemp[4,4] + Srtemp[5,5] + Srtemp[6,6]);

```

$$Srtemp = \begin{bmatrix} 0.1125 & -0.03710 & -0.03712 & 0. & 0. & 0. \\ -0.03710 & 0.1126 & -0.03712 & 0. & 0. & 0. \\ -0.03712 & -0.03712 & 0.1126 & 0. & 0. & 0. \\ 0. & 0. & 0. & 0.2993 & 0. & 0. \\ 0. & 0. & 0. & 0. & 0.2993 & 0. \\ 0. & 0. & 0. & 0. & 0. & 0.2993 \end{bmatrix}$$

Er = 8.883

vr = 0.3296

Gr = 3.342

#### Upper bound of elastic modulus (Voigt) at 0C

```

> Temp := 0:
Cvtemp := eval(Cvt, T=Temp);
Cvtempinv := inverse(Cvtemp);
evalm(Cvtemp &* Cvtempinv):
Ev := 3 / (Cvtempinv[1,1] + Cvtempinv[2,2] + Cvtempinv[3,3]);
vv := - (Cvtempinv[1,2] + Cvtempinv[1,3] + Cvtempinv[2,3]) * Ev / 3;
Gv := 3 / (Cvtempinv[4,4] + Cvtempinv[5,5] + Cvtempinv[6,6]);

```

$$Cvtempinv := \begin{bmatrix} 0.1100 & -0.03587 & -0.03585 & 0. & 0. & 0. \\ -0.03587 & 0.1100 & -0.03585 & 0. & 0. & 0. \\ -0.03585 & -0.03585 & 0.1100 & 0. & 0. & 0. \\ 0. & 0. & 0. & 0.2915 & 0. & 0. \\ 0. & 0. & 0. & 0. & 0.2915 & 0. \\ 0. & 0. & 0. & 0. & 0. & 0.2915 \end{bmatrix}$$

```
Ev := 9.090
vv := 0.3260
Gv := 3.432
```

#### Effective elastic modulus of granular ice (Hill) at 0C

```
> E := (Ev+Er)/2;
v := (vv+vr)/2;
G := (Gv+Gr)/2;
```

```
E := 8.987
v := 0.3278
G := 3.387
```

#### Temperature dependence of elastic moduli for granular ice

The results are transformed into the text file "granular.out"

```
> fd := fopen("granular.out", WRITE);
fprintf(fd, "%q\n", 'Temperature', 'Ev', 'Gv', 'vv', 'Er', 'Gr', 'vr');
for Temp from -50 by 2 to 0 do
Cvtemp := eval(Cvt, T=Temp);
Cvtempinv := inverse(Cvtemp);
Ev := 3/(Cvtempinv[1,1]+Cvtempinv[2,2]+Cvtempinv[3,3]);
Gv := 3/(Cvtempinv[4,4]+Cvtempinv[5,5]+Cvtempinv[6,6]);
vv := Ev/(2*Gv)-1;

Srtemp := eval(Srt, T=Temp);
Er := 3/(Srtemp[1,1]+Srtemp[2,2]+Srtemp[3,3]);
Gr := 3/(Srtemp[4,4]+Srtemp[5,5]+Srtemp[6,6]);
vr := Er/(2*Gr)-1;

fprintf(fd, "%q\n", Temp, Ev, Gv, vv, Er, Gr, vr);
end do;
fclose(fd);

> Digits := Digits+16;
```

## **APPENDIX 2**

### **USER-DEFINED ABAQUS UMAT SUBROUTINE**

```

C *****
C *
C * ICE VISCOPLASTICITY MODEL FOR GRANULAR AND COLUMNAR ATMOSPHERIC ICE *
C * IN DUCTILE REGION *
C * *
C * This version uses: *
C * *
C * - Gammon mono-crystal elastic data *
C * - Hill's averaging scheme for elastic moduli of ice polycrystal *
C * - Drained and Undrained Poroelastic models *
C * - Viscoelasticity model of Sinha (1978) *
C * - Cap-model plasticity *
C * *
C * *
C * By:                      Mojtaba Eskandarian *
C *                      Université Québec à Chicoutimi (UQAC), 2005 *
C * *
C * Supervisors:           Prof. Masoud Farzaneh (CIGELE, UQAC) *
C *                      Prof. Augustin Gakwaya (Laval University) *
C * *
C *****
C
C   MAIN PROGRAM - ICE.FOR
C
C   PROGRAM Ice
C   IMPLICIT REAL*8 (A-H,O-Z)
C
C   MNStep: Number of time steps
C
C   PARAMETER NTENS=6,NSTATV=31,NPROPS=39,NDI=3,NSHR=3,MNStep=1
C   CHARACTER*80 CMNAME
C
C   DIMENSION STRESS(NTENS),STATEV(NSTATV),DDSDDE(NTENS,NTENS),
1     DDSDDT(NTENS),DRPLDE(NTENS),STRAN(NTENS),DSTRAN(NTENS),
2     TIME(2),PREDEF(1),DPRED(1),PROPS(NPROPS),COORDS(3),DROT(3,3),
3     DFGRD0(3,3),DFGRD1(3,3),DSTRESS(NTENS),ALoad(NTENS),
4     STRANe(NTENS),STRANve(NTENS),STRANp(NTENS),SNveOld(NTENS),
5     CM(NTENS,NTENS),SM(NTENS,NTENS)
C
C   OPEN(UNIT=2,FILE='IceOut.out',STATUS='OLD')
C
C   INITIALIZATION
C
C   DO i1=1,NTENS
       STRESS(i1) = 0.0
       DSTRESS(i1) = 0.0
       STRAN(i1) = 0.0
       STRANe(i1) = 0.0
       STRANve(i1) = 0.0
       STRANp(i1) = 0.0
       SNveOld(i1) = 0.0
   END DO

```

```

DO k1=1,NSTATV
  STATEV(k1) = 0.0
END DO
STE = 0.0
SSE = 0.0
SPD = 0.0
SCD = 0.0
PsHist = 0.0
GsHist = 0.0
PcHist = 0.0
GcHist = 0.0
PtHist = 0.0
GtHist = 0.0
C
C INPUTS - LOADING CONDITION
C Define the number of steps (MNStep) in Parameter section
C
C Total time
C TTime = 250.0
C Number of time steps
C NStep = MNStep
C Number of increments
C NInc = 40
C Step time increment
C STIME = TTime/NStep
C Time increment
C DTIME = STIME/NInc
C Temperature and its increment
C TEMP = 263.16
C DTEMP = 0.0
C Loads
C ALoad(1) = -2.0E+07
C ALoad(2) = 0.0
C ALoad(3) = ALoad(2)
C ALoad(4) = 0.0
C ALoad(5) = 0.0
C ALoad(6) = 0.0
C
C INPUTS - MATERIAL PROPERTIES AND OTHER PARAMETERS
C
C CALL PropGranular(PROPS,NPROPS)
C CALL PropIceS1(PROPS,NPROPS)
C CALL PropIceS2(PROPS,NPROPS)
C
C CALL Parameters2(STATEV,NSTATV,NTENS,SNveOld,
1 PsHist,GsHist,PcHist,GcHist,PtHist,GtHist,Dland,
2 STRANe,STRANve,STRANp)

```

```

C
C   START OF TIME STEP
C
C   TIME(1):Step time, TIME(2):Total time
C   TIME(2)=0.0
C   DO KSTEP=1,NStep
C     TIME(1)=0.0
C
C     DStress in each increment
C     DO k1=1,NTENS
C       STRESS(k1)=0.0
C       DSTRESS(k1)=ALoad(k1)/NInc
C     END DO
C
C     Initial DSTRAN of increment
C     CALL Elasticity(PROPS,NPROPS,NTENS,CM,SM,TEMP)
C     DO i1=1,NTENS
C       DSTRAN(i1)=0.0
C       DO j1=1,NTENS
C         DSTRAN(i1)=DSTRAN(i1)+SM(i1,j1)*DSTRESS(j1)
C       END DO
C     END DO
C
C   START OF INCREMENT
C   DO KINC=1,NInc
C
C     CALL UMAT(STRESS,STATEV,DDSDDE,SSE,SPD,SCD,
1     RPL,DDSDDT,DRPLDE,DRPLDT,
2     STRAN,DSTRAN,TIME,DTIME,TEMP,DTEMP,PRED,DPRED,CMNAME,
3     NDI,NSHR,NTENS,NSTATV,PROPS,NPROPS,COORDS,DROT,PNEWDT,
4     CELENT,DFGRD0,DFGRD1,NOEL,NPT,LAYER,KSPT,KSTEP,KINC)
C
C     Updating strain and times
C     DO k1=1,NTENS
C       STRAN(k1) = STRAN(k1)+DSTRAN(k1)
C     END DO
C     TIME(1)=TIME(1)+DTIME
C     TIME(2)=TIME(2)+DTIME
C     WRITE(*,*) ' Increment No. =',KINC,'/',NInc
C     CALL Parameters1(STATEV,NSTATV,NTENS,SNveOld,
1     PsHist,GsHist,PcHist,GcHist,PtHist,GtHist,Dland,
2     STRANe,STRANve,STRANp)
C     END DO
C     WRITE(*,*) ' Step No.   =',KSTEP,'/',NStep
C     WRITE(2,*) TIME(2),STRAN(1)
C     KINC=KINC-1
C   END DO
C
C   OUTPUTS
C
C   KSTEP=KSTEP-1

```

```

      CALL Parameters1(STATEV,NSTATV,NTENS,SNveOld,
1         PsHist,GsHist,PcHist,GcHist,PtHist,GtHist,Dland,
2         STRANe,STRANve,STRANp)
C
      CALL OUTWRITE(STRESS,DSTRESS,STRAN,DSTRAN,STRANe,
1         STRANve,STRANp,NTENS,KSTEP,NStep,KINC,
2         NInc,TIME,TEMP,SSE,SPD,SCD)
C
      END FILE(UNIT=2)
      CLOSE (UNIT=2)
      END PROGRAM
C
C
C
C -----
C *****
C ***** SUBROUTINES *****
C *****
C -----
C
C ***** MATERIAL PROPERTIES FOR GRANULAR ICE
C
      SUBROUTINE PropGranular(PROPS,NPROPS)
C
      IMPLICIT REAL*8 (A-H,O-Z)
      DIMENSION PROPS(NPROPS)
C      In order 11,22,33,12,13,23
C      Young's moduli, 1=E11:Column direction
      PROPS(1)=8.990E+09
      PROPS(2)=PROPS(1)
      PROPS(3)=PROPS(1)
C      Shear moduli, 6=G23:In isotropic plane
      PROPS(4)=3.386E+09
      PROPS(5)=PROPS(4)
      PROPS(6)=PROPS(4)
C      Poisson's ratio, 11=v23:In isotropic plane
      PROPS(7)=PROPS(1)/(2.0*PROPS(6))-1.0
      PROPS(8)=PROPS(7)
      PROPS(9)=PROPS(7)
      PROPS(10)=PROPS(7)
      PROPS(11)=PROPS(7)
      PROPS(12)=PROPS(7)
C      Temperature coefficient
      PROPS(13)=1.471E-03
C      Porosity
      PROPS(14)=0.35
C      MODE OF POROELASTIC MODEL PROPS(15)=1:Drained, =2:Undrained, =3:Transition
      PROPS(15)=1
C      Grain size in mm
      PROPS(16)=0.5
C      Time Integration factor
      PROPS(17)=1.0
C      Parameter C1 in viscoelasticity model

```

PROPS(18)=9.0E-03  
C Parameter b in viscoelasticity model  
PROPS(19)=0.34  
C Parameter aT0 in viscoelasticity model  
PROPS(20)=2.5E-04  
C Activation energy Qa in viscoelasticity model  
PROPS(21)=66.9E+03  
C Parameter Alanda in viscoelasticity model  
PROPS(22)=7.5E+05  
C Parameter Blanda in viscoelasticity model  
PROPS(23)=1.9E+04  
C Reference temperature T0 in viscoelasticity model  
PROPS(24)=263.16  
C Ice Cohesion at melting point d0 in plasticity model  
PROPS(25)=0.875E+06  
C Parameter Alpha in plasticity model  
PROPS(26)=12.78  
C Melting temperature  
PROPS(27)=273.16  
C Parameter b0 in plasticity model  
PROPS(28)=0.1  
C Reference temperature in plasticity model  
PROPS(29)=PROPS(27)-11.8  
C Parameter Gamma in plasticity model  
PROPS(30)=2.7  
C Parameter no in plasticity model  
PROPS(31)=0.35  
C Parameter mo in plasticity model  
PROPS(32)=4.20  
C Reference strain rate in plasticity model  
PROPS(33)=1.4E-04  
C Parameter pa0max in plasticity model  
PROPS(34)=21.5E+06  
C Parameter landa in plasticity model  
PROPS(35)=1.75  
C Parameter delta in plasticity model  
PROPS(36)=0.55  
C Parameter eta in plasticity model  
PROPS(37)=0.40  
C Parameter A in plasticity model  
PROPS(38)=0.0908E-06  
C Tension strength pressure ptmax in plasticity model  
PROPS(39)= 1.0E+06  
RETURN  
END

```

C
C ***** MATERIAL PROPERTIES FOR S1 ICE
C
C     SUBROUTINE PropIceS1(PROPS,NPROPS)
C
C     IMPLICIT REAL*8 (A-H,O-Z)
C     DIMENSION PROPS(NPROPS)
C     In order 11,22,33,12,13,23
C     Young's moduli, 1=E11:Column direction
C     PROPS(1)=11.578E+09
C     PROPS(2)=9.470E+09
C     PROPS(3)=PROPS(2)
C     Shear moduli, 6=G23:In isotropic plane
C     PROPS(4)=2.946E+09
C     PROPS(5)=PROPS(4)
C     PROPS(6)=3.346E+09
C     Poisson's ratio, 11=v23:In isotropic plane
C     PROPS(7)=0.2744
C     PROPS(8)=0.2244
C     PROPS(9)=0.2744
C     PROPS(10)=0.2244
C     PROPS(11)=PROPS(2)/(2.0*PROPS(6))-1.0
C     PROPS(12)=PROPS(11)
C     Temperature coefficient
C     PROPS(13)=1.471E-03
C     Porosity
C     PROPS(14)=0.13
C     MODE OF POROELASTIC MODEL PROPS(15)=1:Drained, =2:Undrained, =3:Transition
C     PROPS(15)=3
C     Grain size in mm
C     PROPS(16)=2.0
C     Time Integration factor
C     PROPS(17)=1.0
C     Parameter C1 in viscoelasticity model
C     PROPS(18)=9.0E-03
C     Parameter b in viscoelasticity model
C     PROPS(19)=0.34
C     Parameter aT0 in viscoelasticity model
C     PROPS(20)=2.5E-04
C     Activation energy Qa in viscoelasticity model
C     PROPS(21)=66.9E+03
C     Parameter Alanda in viscoelasticity model
C     PROPS(22)=7.5E+05
C     Parameter Blanda in viscoelasticity model
C     PROPS(23)=1.9E+04
C     Reference temprature T0 in viscoelasticity model
C     PROPS(24)=263.16
C     Ice Cohesion at melting point d0 in plasticity model
C     PROPS(25)=3.10E+06
C     Parameter Alpha in plasticity model
C     PROPS(26)=9.61
C     Melting temperature

```

```

PROPS(27)=273.16
C   Parameter b0 in plasticity model
PROPS(28)=0.15
C   Reference temperature in plasticity model
PROPS(29)=PROPS(27)-11.8
C   Parameter Gamma in plasticity model
PROPS(30)=4.05
C   Parameter no in plasticity model
PROPS(31)=0.25
C   Parameter mo in plasticity model
PROPS(32)=5.20
C   Reference strain rate in plasticity model
PROPS(33)=5.4E-03
C   Parameter pa0max in plasticity model
PROPS(34)=25.50E+06
C   Parameter landa in plasticity model
PROPS(35)=1.95
C   Parameter delta in plasticity model
PROPS(36)=0.50
C   Parameter eta in plasticity model
PROPS(37)=0.25
C   Parameter A in plasticity model
PROPS(38)=0.0908E-06
C   Tension strength pressure ptmax in plasticity model
PROPS(39)= 1.0E+06
RETURN
END

```

```

C
C ***** MATERIAL PROPERTIES FOR S2 ICE
C
C   SUBROUTINE PropIceS2(PROPS,NPROPS)
C
C   IMPLICIT REAL*8 (A-H,O-Z)
C   DIMENSION PROPS(NPROPS)
C   In order 11,22,33,12,13,23
C   Young's moduli, 1=E11:Column direction
PROPS(1)=9.551E+09
PROPS(2)=9.363E+09
PROPS(3)=PROPS(2)

```

- C Shear moduli,  $\mu = G_{23}$ : In isotropic plane  
PROPS(4)=3.140E+09  
PROPS(5)=PROPS(4)  
PROPS(6)=3.528E+09
- C Poisson's ratio,  $\nu = \nu_{23}$ : In isotropic plane  
PROPS(7)=0.3187  
PROPS(8)=0.3124  
PROPS(9)=0.3187  
PROPS(10)=0.3124  
PROPS(11)=PROPS(2)/(2.0\*PROPS(6))-1.0  
PROPS(12)=PROPS(11)
- C Temperature coefficient  
PROPS(13)=1.471E-03
- C Porosity  
PROPS(14)=0.05
- C MODE OF POROELASTIC MODEL PROPS(15)=1:Drained, =2:Undrained, =3:Transition  
PROPS(15)=1
- C Grain size in mm  
PROPS(16)=5.0
- C Time Integration factor  
PROPS(17)=1.0
- C Parameter C1 in viscoelasticity model  
PROPS(18)=9.0E-03
- C Parameter b in viscoelasticity model  
PROPS(19)=0.34
- C Parameter aT0 in viscoelasticity model  
PROPS(20)=2.5E-04
- C Activation energy Qa in viscoelasticity model  
PROPS(21)=66.9E+03
- C Parameter Alanda in viscoelasticity model  
PROPS(22)=7.5E+05
- C Parameter Blanda in viscoelasticity model  
PROPS(23)=1.9E+04
- C Reference temperature T0 in viscoelasticity model  
PROPS(24)=263.16
- C Ice Cohesion at melting point d0 in plasticity model  
PROPS(25)=3.10E+06
- C Parameter Alpha in plasticity model  
PROPS(26)=9.61
- C Melting temperature  
PROPS(27)=273.16
- C Parameter b0 in plasticity model  
PROPS(28)=0.15
- C Reference temperature in plasticity model  
PROPS(29)=PROPS(27)-11.8
- C Parameter Gamma in plasticity model  
PROPS(30)=4.05
- C Parameter no in plasticity model  
PROPS(31)=0.25
- C Parameter mo in plasticity model  
PROPS(32)=5.20
- C Reference strain rate in plasticity model

```

      PROPS(33)=5.4E-03
C   Parameter pa0max in plasticity model
      PROPS(34)=25.50E+06
C   Parameter landa in plasticity model
      PROPS(35)=1.95
C   Parameter delta in plasticity model
      PROPS(36)=0.50
C   Parameter eta in plasticity model
      PROPS(37)=0.25
C   Parameter A in plasticity model
      PROPS(38)=0.0908E-06
C   Tension strength pressure ptmax in plasticity model
      PROPS(39)= 1.0E+06
      RETURN
      END

```

```

C
C ***** OUTPUTS
C
      SUBROUTINE OUTWRITE(STRESS,DSTRESS,STRAN,DSTRAN,STRANe,
1         STRANve,STRANp,NTENS,KSTEP,NStep,KINC,
2         NInc,TIME,TEMP,SSE,SPD,SCD)
C
      IMPLICIT REAL*8 (A-H,O-Z)
      DIMENSION STRESS(NTENS),DSTRESS(NTENS),STRAN(NTENS),DSTRAN(NTENS),
1         STRANe(NTENS),STRANve(NTENS),STRANp(NTENS),TIME(2)
C
      WRITE(*,*)
      WRITE(*,*) ' Increment No. =',KINC,'/',NInc
      WRITE(*,*) ' Step No.   =',KSTEP,'/',NStep
      WRITE(*,*) ' Step time   =',TIME(1)
      WRITE(*,*) ' Total time  =',TIME(2)
      WRITE(*,*) ' Temperature =',TEMP
      WRITE(*,*) '-----'
      WRITE(*,*)
      WRITE(*,*) ' STRESS
      DO k1=1,NTENS
         WRITE(*,*) STRESS(k1)
      END DO
      WRITE(*,*)

```

```

WRITE(*,*) ' STRAIN          DSTRAIN',
1      '          ---- T O T A L ----'
      DO k1=1,NTENS
        WRITE(*,*) STRAN(k1),DSTRAN(k1)
      END DO
      WRITE(*,*)
      WRITE(*,*) ' STRAINe          ',
1      '          ----- ELASTIC -----'
      DO k1=1,NTENS
        WRITE(*,*) STRANe(k1)
      END DO
      WRITE(*,*)
      WRITE(*,*) ' STRAINve          ',
1      '          ---- VISCOELASTIC ----'
      DO k1=1,NTENS
        WRITE(*,*) STRANve(k1)
      END DO
      WRITE(*,*)
      WRITE(*,*) ' STRAINp          ',
1      '          ----- PLASTIC -----'
      DO k1=1,NTENS
        WRITE(*,*) STRANp(k1)
      END DO
      WRITE(*,*)
      WRITE(*,*) 'Energies:'
      WRITE(*,*) '-----'
      WRITE(*,*) 'Elastic=',SSE
      WRITE(*,*) 'Plastic=',SPD
      WRITE(*,*) ' Creep=',SCD
      WRITE(*,*) '-----'
      STE=SSE+SPD+SCD
      WRITE(*,*) ' Total=',STE
      WRITE(*,*)
      RETURN
      END

```

```

C
C
C-----
C*****
C***** U M A T *****
C*****
C-----
C
C
C      SUBROUTINE UMAT(STRESS,STATEV,DDSDDE,SSE,SPD,SCD,
1         RPL,DDSDDT,DRPLDE,DRPLDT,
2         STRAN,DSTRAN,TIME,DTIME,TEMP,DTEMP,PREDEF,DPRED,CMNAME,
3         NDI,NSHR,NTENS,NSTATV,PROPS,NPROPS,COORDS,DROT,PNEWDT,
4         CELENT,DFGRD0,DFGRD1,NOEL,NPT,LAYER,KSPT,KSTEP,KINC)
C
C      INCLUDE 'ABA_PARAM.INC'
C
C      IMPLICIT REAL*8 (A-H,O-Z)
C      CHARACTER*80 CMNAME
C      DIMENSION STRESS(NTENS),STATEV(NSTATV),
1         DDSDE(NTENS,NTENS),DDSDDT(NTENS),DRPLDE(NTENS),
2         STRAN(NTENS),DSTRAN(NTENS),TIME(2),PREDEF(1),DPRED(1),
3         PROPS(NPROPS),COORDS(3),DROT(3,3),DFGRD0(3,3),DFGRD1(3,3)
C
C      ADDED DECLARATIONS
C
C      INTEGER i1,j1,k1,kk
C      DIMENSION CM(NTENS,NTENS),SM(NTENS,NTENS),DSTRES(NTENS),
1         CX(NTENS,NTENS),SX(NTENS,NTENS),
2         STRANe(NTENS),DSTRANe(NTENS),STRANve(NTENS),
3         DSTRANve(NTENS),STRANp(NTENS),DSTRANp(NTENS),SNveOld(NTENS),
4         STRSdev(NTENS),DSTRSdev(NTENS),STRNdev(NTENS),DSTRNdev(NTENS),
5         STRSn1(NTENS),DpDSS(NTENS),DqDSS(NTENS),Cve(NTENS,NTENS),
6         DfDSSs(NTENS),DfDSSc(NTENS),DfDSSst(NTENS),Cve2(NTENS,NTENS)
C
C
C
C      INITIALIZATION
C
C      DO 1 i1=1,NTENS
          DSTRANe(i1) =0.0
          DSTRANve(i1) =0.0
          DSTRANp(i1) =0.0
          DSTRES(i1) =0.0
          DfDSSst(i1) =0.0
          DfDSSs(i1) =0.0
          DfDSSc(i1) =0.0
          DO 2 j1=1,NTENS
              CM(i1,j1) = 0.0
              SM(i1,j1) = 0.0
          
```

```

                DDSDE(i1,j1) = 0.0
2      CONTINUE
        IF (KINC .EQ. 1) THEN
            SSE=0.0
        END IF
1     CONTINUE
C
C
C     RETRIEVE PARAMETERS FROM STATEV ARRAY
C     =====
C
C     CALL Parameters1(STATEV,NSTATV,NTENS,SNveOld,
1       PsHist,GsHist,PcHist,GcHist,PtHist,GtHist,Dland,
2       STRANe,STRANve,STRANp)
C
C     INCOMING DATA FILTERING FOR VALUES SMALLER THAN 1.E-10
C
C     CALL InFilterV(STRAN,NTENS)
C     CALL InFilterV(DSTRAN,NTENS)
C     CALL InFilterV(STRESS,NTENS)
C     CALL InFilterV(DSTRES,NTENS)
C     CALL InFilterV(STATEV,NSTATV)
C     CALL InFilterV(PROPS,NPROPS)
C
C
C
C     ELASTIC MODULI
C     =====
C     CALL Elasticity(PROPS,NPROPS,NTENS,CM,SM,TEMP)
C
C
C
C     VISCOELASTIC PREDICTOR
C     =====
C     Viscoelastic parameters
C
C     Material parameter C1
C     VC1=PROPS(18)
C     Material parameter b
C     Vb=PROPS(19)
C     Universal gas constant
C     RUni=8.314
C     Material parameter Alanda
C     Aland=PROPS(22)
C     Material parameter Blanda
C     Bland=PROPS(23)
C     aT=PROPS(20)*EXP(PROPS(21)*(1.0/PROPS(24)-1.0/TEMP)/RUni)
C
C     TERM10 = (1.0+Dland)*VC1*(1.0-EXP(-(aT*DTIME)**Vb))/PROPS(16)
C     TERM10 = 1.0 + TERM10

```

```

DO 3 k1=1,NTENS
    DSTRANe(k1) = (DSTRAN(k1)-SNveOld(k1)+STRANve(k1))/TERM10
    DSTRANve(k1)= DSTRAN(k1)-DSTRANe(k1)
3 CONTINUE
C
C
C
C CAP-MODEL PLASTICITY
C =====
C
C Total Mises strain rate
CALL STRANDev(STRAN,DSTRAN,SNvol,DSNvol,STRNdev,DSTRNdev,
1 NTENS,NDI,NSHR)
CALL STNMises(STRNdev,DSTRNdev,SNMis,DSNMis,NDI,NSHR,NTENS)
SNrMis = DSNMis/DTIME
C
C Loop for calculating the plastic strain increment
kp=0
TERM20=1.0
Alpha=PROPS(17)
fS=0.0
fSold=0.0
fC=0.0
fCold=0.0
fT=0.0
fTold=0.0
dlandS0=0.0
dlandC0=0.0
dlandT0=0.0
Alpha=1E-8
DO WHILE ((TERM20.GT.1E-07).AND.(kp.LE.1000))
    kp=kp+1
    Pst=0.0
    Qst=0.0
    Ost=0.0
    Pct=0.0
    Qct=0.0
    Oct=0.0
    Ptt=0.0
    Qtt=0.0
    Ott=0.0
    dlandS=0.0
    dlandC=0.0
    dlandT=0.0
C
C POROELASTICITY
C -----
CALL PoroElasticity(PROPS(15),PROPS(14),Phi,PoreP,CM,SM,
1 CX,SX,STRESS,DSTRES,STRANe,DSTRANe,NTENS,NDI,NSHR,PROPS(17),
2 Betaii,BKcV)
C
C

```

```

C   DETERMINING THE YIELD ENVELOPE FUNCTIONS AND YIELD MODE
C   -----
C   Hydrostatic pressure and Mises stress
C   DO 4 k1=1,NTENS
C       STRSn1(k1)=STRESS(k1)+0.5*DSTRES(k1)
4   CONTINUE
C   CALL STRESDev(STRSn1,DSTRES,HP,DHP,STRSdev,DSTRSdev,NTENS,
1   NDI,NSHR)
C   CALL STSMises(STRSdev,QMis,NDI,NSHR,NTENS)
C
C   Yield functions and yield mode
C   CALL Yield(SNrMis,PROPS,NPROPS,HP,QMis,TEMP,Phi,Betaii,
1   PoreP,dT,bT,b1T,Pamax,Pa1max,Pa,QaMis,Pb,Pt,ft,fS,fC,ModYield)
C
C
C   RETURN MAPPING ALGORITHM
C   -----
C
C   Viscoelastic tangent matrix
C   TERM15 = (1.0+Dland)*VC1*(1.0-EXP(-((aT*DTIME)**Vb)))/PROPS(16)
C   TERM15 = 1.0+TERM15
C   DO 5 i1=1,NTENS
C       DO 6 j1=1,NTENS
C           TERM14=DSTRANe(j1)
C           IF (TERM14.EQ.0.0) THEN
C               TERM10=TERM15
C           ELSE
C               TERM10=1.0+DSTRANve(j1)/TERM14
C           END IF
C           Cve(i1,j1) = CX(i1,j1)/TERM10
C           Cve2(i1,j1) = CX(i1,j1)/TERM15
6       CONTINUE
5   CONTINUE
C
C   PLASTIC STRAIN AND MULTIPLIER
C
C   IF (ModYield .NE. 6) THEN
C   -----
C   Derivatives with respect of stress
C   TERM10 = 0.0
C   DO 7 k1=1,NDI
C       TERM10=TERM10+STRSdev(k1)/3.0
7   CONTINUE
C   DO 8 i1=1,NDI
C       DpDSS(i1)=-1.0/3.0
C       DqDSS(i1)=3.0*(STRSdev(i1)-TERM10)/(2.0*QMis)
8   CONTINUE
C   k1=NDI
C   DO 9 i1=1,NSHR
C       k1=k1+1
C       DpDSS(k1)=0.0

```

```

          DqDSS(k1)=3.0*STRSdev(k1)/(2.0*QMis)
9    CONTINUE
C
    IF ((ModYield.EQ.1).OR.(ModYield.EQ.2)) THEN
      CALL Tension(DpDSS,DqDSS,NTENS,Cve,DSTRAN,Ptt,Qtt,Ott,
1      DfDSSst,dlandT)
C      Cutting-plane algorithm
      CALL Cutting(dlandT,dlandT0,ft,fTold,Alpha)
    END IF
C
    IF ((ModYield.EQ.2).OR.(ModYield.EQ.3).OR.(ModYield.EQ.4)) THEN
      CALL Shear(SNrMis,PROPS,NPROPS,STATEV,NSTATV,DpDSS,DqDSS,
1      NTENS,HP,Cve,DSTRAN,dT,bT,b1T,Pamax,Pa1max,Pb,Pst,Qst,Ost,
2      DTIME,DfDSSs,dlandS)
C      Cutting-plane algorithm
      CALL Cutting(dlandS,dlandS0,fs,fSold,Alpha)
    END IF
C
    IF ((ModYield.EQ.4).OR.(ModYield.EQ.5)) THEN
      CALL Cap(SNrMis,PROPS,NPROPS,STATEV,NSTATV,DpDSS,DqDSS,
1      NTENS,HP,Cve,DSTRAN,Phi,Betaii,PoreP,BKcV,dT,bT,Pamax,
2      Pa1max,Pa,QaMis,Pb,fc,Pct,Qct,Oct,DTIME,DfDSSc,dlandC)
C      Cutting-plane algorithm
      CALL Cutting(dlandC,dlandC0,fc,fCold,Alpha)
    END IF
C
    dlandT0=dlandT
    dlandS0=dlandS
    dlandC0=dlandC
C
    Calculating the new increment in plastic strain
    DO 10 k1=1,NTENS
      TERM10 = dlandT*DfDSSst(k1) + dlandS*DfDSSs(k1)
      DSTRANp(k1) = TERM10 + dlandC*DfDSSc(k1)
10   CONTINUE
C
    Calculating the deviatoric plastic strain of increment (DSNMisP)
    CALL STRANdev(STRANp,DSTRANp,SNvol,DSNvol,STRNdev,DSTRNdev,
1    NTENS,NDI,NSHR)
    CALL STNMises(STRNdev,DSTRNdev,SNMisP,DSNMisP,NDI,NSHR,NTENS)
C
    Upating the structural change function (Dland)
    CALL Struct(Vb,TIME,DTIME,Aland,Bland,DSNMisP,SNMisP,Dland)
C
    -----
    END IF
C
    Updating strain components of increment
    TERM10 = (1.0+Dland)*VC1*(1.0-EXP(-(aT*DTIME)**Vb))/PROPS(16)
    TERM10 = 1.0+TERM10
    DO 100 k1=1,NTENS
      TERM14=(DSTRAN(k1)-DSTRANp(k1)-SNveOld(k1)+STRANve(k1))/TERM10
      DSTRANe(k1)=TERM14

```



```

C   WRITE(2,*)'Poroelastic moduli:'
C   WRITE(2,*)'-----'
C   WRITE(2,*)'Y11=',Y11
C   WRITE(2,*)'Y22=',Y22
C   WRITE(2,*)'Y33=',Y33
C   WRITE(2,*)'G12=',G12
C   WRITE(2,*)'G13=',G13
C   WRITE(2,*)'G23=',G23
C   WRITE(2,*)'v12=',v12
C   WRITE(2,*)'v21=',v21
C   WRITE(2,*)'v13=',v13
C   WRITE(2,*)'v31=',v31
C   WRITE(2,*)'v23=',v23
C   WRITE(2,*)'v32=',v32
C
C
C   Create new Jacobian matrix - Consistent tangent moduli
TERM15 = (1.0+Dland)*VC1*(1.0-EXP(-(aT*DTIME)**Vb))/PROPS(16)
TERM15 = 1.0+TERM15
DO 106 i1=1,NTENS
    DO 107 j1=1,NTENS
        TERM14=DSTRANe(j1)
        IF (TERM14.EQ.0.0) THEN
            TERM10=TERM15
        ELSE
            TERM10=1.0+(DSTRANve(j1)+DSTRANp(j1))/TERM14
        END IF
        DDSdde(i1,j1) = CX(i1,j1)/TERM10
    107 CONTINUE
106 CONTINUE
C
C   UPDATING MEMORY FUNCTIONS
C
PsHist = STATEV(19) + Pst*DTIME
GsHist = STATEV(20) + Ost*Qst*DTIME
PcHist = STATEV(21) + Pct*DTIME
GcHist = STATEV(22) + Oct*Qct*DTIME
PtHist = STATEV(23) + Ptt*DTIME
GtHist = STATEV(24) + Ott*Qtt*DTIME
C
CALL ViscoElasticity(STRANve,DSTRANve,STRANe,DSTRANe,
1   SNveOld,DTIME,PROPS,NPROPS,NTENS,Dland,VC1,Vb,aT)
C
C   Updating stress and strain components
C
DO 104 i1=1,NTENS
    STRANe(i1) = STRANe(i1)+DSTRANe(i1)
    STRANve(i1) = STRANve(i1)+DSTRANve(i1)
    STRANp(i1) = STRANp(i1)+DSTRANp(i1)
    STRESS(i1) = STRESS(i1)+DSTRES(i1)
104 CONTINUE
C

```

```

C   TOTAL CHANGE IN SPECIFIC ENERGY OF INCREMENT
C   -----
C
      TDE =0.0
      DO 101 k1=1,NTENS
          TDE = TDE + (STRESS(k1)-0.5*DSTRES(k1))*DSTRAN(k1)
101  CONTINUE
C
C   CHANGE IN SPECIFIC ELASTIC STRAIN ENERGY OF INCREMENT
      DEE =0.0
      DO 102 k1=1,NTENS
          DEE = DEE + (STRESS(k1)-0.5*DSTRES(k1))*DSTRANe(k1)
102  CONTINUE
C
C   CHANGE IN SPECIFIC PLASTIC STRAIN ENERGY OF INCREMENT
      DEP = 0.0
      DO 103 k1=1,NTENS
          DEP = DEP + (STRESS(k1)-0.5*DSTRES(k1))*DSTRANp(k1)
103  CONTINUE
C
C   TOTAL STRAIN ENERGY CHANGES IN INCREMENT
      SSE = SSE + DEE
      SPD = SPD + DEP
      SCD = SCD + TDE - DEE - DEP
C
C   TRANSFERING THE PARAMETERS TO PROPS ARRAY
C
      CALL Parameters2(STATEV,NSTATV,NTENS,SNveOld,
1         PsHist,GsHist,PcHist,GcHist,PtHist,GtHist,Dland,
2         STRANe,STRANve,STRANp)
C
      RETURN
      END

```

```

C *****
C ***** SUBROUTINES OF UMAT *****
C *****
C
C
C
C ***** SUBROUTINE PARAMETERS1 *****
C ***** RETRIEVE THE MODEL PARAMETERS FROM STATEV ARRAY *****
C
  SUBROUTINE Parameters1(STATEV,NSTATV,NTENS,
1     SNveOld,PsHist,GsHist,PcHist,GcHist,PtHist,GtHist,Dland,
2     STRANe,STRANve,STRANp)
C
  IMPLICIT REAL*8 (A-H,O-Z)
  DIMENSION STATEV(NSTATV),
1     SNveOld(NTENS),STRANe(NTENS),STRANve(NTENS),STRANp(NTENS)
C
  DO 900 k1=1,NTENS
    SNveOld(k1) = STATEV(k1)
900 CONTINUE
    k1=k1+1
    PsHist = STATEV(k1)
    k1=k1+1
    GsHist= STATEV(k1)
    k1=k1+1
    PcHist = STATEV(k1)
    k1=k1+1
    GcHist= STATEV(k1)
    k1=k1+1
    PtHist = STATEV(k1)
    k1=k1+1
    GtHist = STATEV(k1)
    k1=k1+1
    Dland = STATEV(k1)
C
  DO 901 i1=1,NTENS
    k1=13+i1
    STRANe(i1) = STATEV(k1)
    k1=k1+NTENS
    STRANve(i1) = STATEV(k1)
    k1=k1+NTENS
    STRANp(i1) = STATEV(k1)
901 CONTINUE
C
  RETURN
  END

```

```

C
C
C ***** SUBROUTINE PARAMETERS2 *****
C ***** TRANSFER THE MODEL PARAMETERS TO STATEV ARRAY *****
C
  SUBROUTINE Parameters2(STATEV,NSTATV,NTENS,
1     SNveOld,PsHist,GsHist,PcHist,GcHist,PtHist,GtHist,Dland,
2     STRANe,STRANve,STRANp)
C
  IMPLICIT REAL*8 (A-H,O-Z)
  DIMENSION STATEV(NSTATV),
1     SNveOld(NTENS),STRANe(NTENS),STRANve(NTENS),STRANp(NTENS)
C
  DO 950 k1=1,NTENS
    STATEV(k1) = SNveOld(k1)
950 CONTINUE
    k1=k1+1
    STATEV(k1) = PsHist
    k1=k1+1
    STATEV(k1) = GsHist
    k1=k1+1
    STATEV(k1) = PcHist
    k1=k1+1
    STATEV(k1) = GcHist
    k1=k1+1
    STATEV(k1) = PtHist
    k1=k1+1
    STATEV(k1) = GtHist
    k1=k1+1
    STATEV(k1) = Dland
C
  DO 951 i1=1,NTENS
    k1=13+i1
    STATEV(k1) = STRANe(i1)
    k1=k1+NTENS
    STATEV(k1) = STRANve(i1)
    k1=k1+NTENS
    STATEV(k1) = STRANp(i1)
951 CONTINUE
C
  RETURN
  END

```

```

C ***** SUBROUTINE INFILTERV *****
C ***** FILTERS VERY SMALL VALUES OF A VECTOR *****
C

```

```

SUBROUTINE InFilterV(TERMV,NN)
IMPLICIT REAL*8 (A-H,O-Z)
DIMENSION TERMV(NN)
DO 1001 k1=1,NN
  TERM1=TERMV(k1)
  IF (ABS(TERM1).LT.(1.0E-10)) THEN
    TERMV(k1)=0.0
  ENDIF
1001 CONTINUE
C
RETURN
END

```

```

C ***** SUBROUTINE INFILTERM *****
C ***** FILTERS VERY SMALL VALUES OF A MATRIX *****
C

```

```

SUBROUTINE InFilterM(TAM,MM,NN)
IMPLICIT REAL*8 (A-H,O-Z)
DIMENSION TAM(MM,NN)
DO 1002 i1=1,MM
  DO 1003 j1=1,NN
    TERM1=TAM(i1,j1)
    IF (ABS(TERM1).LT.(1.0E-10)) THEN
      TAM(i1,j1)=0.0
    ENDIF
1003 CONTINUE
1002 CONTINUE
C
RETURN
END

```

```

C ***** SUBROUTINE ELASTICITY *****
C *** CALCULATES ELASTIC COMPLIANCE (SM) AND STIFFNESS (CM) MATRICES ***
C

```

```

SUBROUTINE Elasticity(PROPS,NPROPS,NTENS,CM,SM,TEMP)
C
IMPLICIT REAL*8 (A-H,O-Z)
DIMENSION PROPS(NPROPS),CM(NTENS,NTENS),SM(NTENS,NTENS)
TERM1 = 1.0-PROPS(13)*(TEMP-PROPS(27))
Y11 = PROPS(1)*TERM1
Y22 = PROPS(2)*TERM1
Y33 = PROPS(3)*TERM1
G12 = PROPS(4)*TERM1

```

```

G13      = PROPS(5)*TERM1
G23      = PROPS(6)*TERM1
SM(1,1) = 1.0/Y11
SM(2,2) = 1.0/Y22
SM(3,3) = 1.0/Y33
SM(1,2) = -0.5*(PROPS(8)/Y22+PROPS(7)/Y11)
SM(2,1) = SM(1,2)
SM(1,3) = -0.5*(PROPS(10)/Y33+PROPS(9)/Y11)
SM(3,1) = SM(1,3)
SM(2,3) = -0.5*(PROPS(12)/Y33+PROPS(11)/Y22)
SM(3,2) = SM(2,3)
SM(4,4) = 1.0/G12
SM(5,5) = 1.0/G13
SM(6,6) = 1.0/G23
C
CALL MatInverse(SM,CM,NTENS)
RETURN
END

C
C
C ***** SUBROUTINE TENSION *****
C ***** PLASTIC STRAIN AND MULTIPLIER RELATED TO TENSION YIELD *****
C
SUBROUTINE Tension(DpDSS,DqDSS,NTENS,Cve,DSTRAN,Ptt,Qtt,Ott,
1      DfDSSt,dlandT)
C
IMPLICIT REAL*8 (A-H,O-Z)
DIMENSION DpDSS(NTENS),DqDSS(NTENS),DfDSSt(NTENS),
1      TERMp(NTENS),Cve(NTENS,NTENS),DSTRAN(NTENS)
C
DfDp = -1.0
DfDq = 0.0
DfDpt = -1.0
C
DO 1101 k1=1,NTENS
DfDSSt(k1)=DfDp*DpDSS(k1)+DfDq*DqDSS(k1)
1101 CONTINUE
C
DO 1102 i1=1,NTENS
TERMp(i1)=0.0
DO 1103 j1=1,NTENS
TERMp(i1)=TERMp(i1)+Cve(i1,j1)*DfDSSt(j1)
1103 CONTINUE
1102 CONTINUE
C
TERM10=0.0

DO 1104 k1=1,NTENS
TERM10=TERM10+DfDSSt(k1)*TERMp(k1)
1104 CONTINUE

```

```

C
  DO 1105 i1=1,NTENS
    TERMp(i1)=0.0
    DO 1106 j1=1,NTENS
      TERMp(i1)=TERMp(i1)+Cve(i1,j1)*DSTRAN(j1)
1106    CONTINUE
1105 CONTINUE
C
  TERM14=0.0
  DO 1107 k1=1,NTENS
    TERM14=TERM14+DfDSSs(k1)*TERMp(k1)
1107 CONTINUE
C
  Ptt = 0.0
  Qtt  = 0.0
  Ott  = 0.0
  dlandT = TERM14/TERM10
C
  RETURN
  END

C
C
C ***** SUBROUTINE SHEAR *****
C ***** PLASTIC STRAIN AND MULTIPLIER RELATED TO SHEAR YIELD *****
C
  SUBROUTINE Shear(SNrMis,PROPS,NPROPS,STATEV,NSTATV,DpDSS,DqDSS,
1    NTENS,HP,Cve,DSTRAN,dT,bT,b1T,Pamax,Pa1max,Pb,Pst,Qst,Ost,
2    DTIME,DfDSSs,dlandS)
C
  IMPLICIT REAL*8 (A-H,O-Z)
  DIMENSION PROPS(NPROPS),DpDSS(NTENS),DqDSS(NTENS),DfDSSs(NTENS),
1    TERMp(NTENS),Cve(NTENS,NTENS),DSTRAN(NTENS),STATEV(NSTATV)
C
  IF (Pamax .EQ. 0.0) THEN
    DfDp = 2.0*dT*HP/(Pb*Pb)
    DfDpamax = 0.0
    DfDb = 0.0
  ELSE
    DfDp = -bT*(1.0-HP/Pamax)
    DfDpamax = -0.5*bT*HP*HP/(Pamax*Pamax)
    DfDb = -HP*(1.0-0.5*HP/Pamax)
  END IF
C
  DfDq = 1.0
C
  DfDd = -1.0
  TERM10 = SNrMis/PROPS(33)
  TERM14 = (1.0-PROPS(32))/PROPS(32)
  DbDSNrVP = b1T*(TERM10**TERM14)/(3.0*PROPS(32)*PROPS(33))
  DbDSNrDP = DbDSNrVP*SQRT(1.5)

```

```

TERM14 = EXP(-TERM10)
TERM13 = PROPS(37)-1.0
TERM14 = TERM14*((1.0-TERM14)**TERM13)
DPamaxDSNrVP = PROPS(37)*Pa1max*TERM14/(3.0*PROPS(33))
DPamaxDSNrDP = DPamaxDSNrVP*SQRT(1.5)
C
DO 1201 k1=1,NTENS
    DfDSSs(k1)=DfDp*DpDSS(k1)+DfDq*DqDSS(k1)
1201 CONTINUE
C
DO 1202 i1=1,NTENS
    TERMp(i1)=0.0
    DO 1203 j1=1,NTENS
        TERMp(i1)=TERMp(i1)+Cve(i1,j1)*DfDSSs(j1)
1203 CONTINUE
1202 CONTINUE
C
TERM10=0.0
DO 1204 k1=1,NTENS
    TERM10=TERM10+DfDSSs(k1)*TERMp(k1)
1204 CONTINUE
C
DO 1205 i1=1,NTENS
    TERMp(i1)=0.0
    DO 1206 j1=1,NTENS
        TERMp(i1)=TERMp(i1)+Cve(i1,j1)*DSTRAN(j1)
1206 CONTINUE
1205 CONTINUE
C
TERM13=0.0
DO 1207 k1=1,NTENS
    TERM13=TERM13+DfDSSs(k1)*TERMp(k1)
1207 CONTINUE
C
TERM14 = (DfDb*DbDSNrVP+DfDpamax*DPamaxDSNrVP)*DfDp
TERM14 = TERM14-(DfDb*DbDSNrDP+DfDpamax*DPamaxDSNrDP)*DfDq
C
IF (TERM14 .EQ. 0.0) THEN
    Pst = 0.0
    Qst = 0.0
    Ost = 0.0
    dlandS = TERM13/TERM10
ELSE
    Pst = TERM10/TERM14
    Qst = TERM13/TERM14
    Ost = EXP(STATEV(19) + Pst*DTIME)
    dlandS = STATEV(20)/Ost + Qst*DTIME
END IF
C
RETURN
END

```

```

C
C
C ***** SUBROUTINE CAP *****
C ***** PLASTIC STRAIN AND MULTIPLIER RELATED TO CAP YIELD *****
C
SUBROUTINE Cap(SNrMis,PROPS,NPROPS,STATEV,NSTATV,DpDSS,DqDSS,
1   NTENS,HP,Cve,DSTRAN,Phi,Betaii,PoreP,BKcV,dT,bT,Pamax,
2   Pa1max,Pa,QaMis,Pb,fC,Pct,Qct,Oct,DTIME,DfDSSc,dlandC)
C
IMPLICIT REAL*8 (A-H,O-Z)
DIMENSION PROPS(NPROPS),DpDSS(NTENS),DqDSS(NTENS),DfDSSc(NTENS),
1   TERMp(NTENS),Cve(NTENS,NTENS),DSTRAN(NTENS),STATEV(NSTATV)
C
TERM10 = HP-Pa
TERM13 = Pb-Pa
TERM14 = SQRT(TERM13*TERM13-TERM10*TERM10)
DfDp = TERM10*QaMis/(TERM13*TERM14)
IF (Pamax .EQ. 0.0) THEN
    DqaDpa = -2.0*dT*Pa/(Pb*Pb)
ELSE
    DqaDpa = bT*(1.0-Pa/Pamax)
END IF
DfDq = 1.0
TERM15 = QaMis*TERM10/(TERM13*TERM13*TERM14)
DfDpa = TERM15*(HP-Pb)-DqaDpa*TERM14/TERM13
DfDpb = TERM15*TERM10
C
IF (PoreP .EQ. 0.0) THEN
    DpaDSNVP = 0.0
ELSE
    DpaDSNVP = -3.0*BKcV*Betaii*Betaii
END IF
C
TERM10 = SNrMis/PROPS(33)
TERM14 = EXP(-TERM10)
TERM13 = PROPS(37)-1.0
TERM14 = TERM14*((1.0-TERM14)**TERM13)
DPamaxDSNrVP = PROPS(37)*Pa1max*TERM14/(3.0*PROPS(33))
DPamaxDSNrDP = DPamaxDSNrVP*SQRT(1.5)
DPaDSNrVP = (1.0-Phi)*DPamaxDSNrVP
DPaDSNrDP = (1.0-Phi)*DPamaxDSNrDP
C
DO 1301 k1=1,NTENS
    DfDSSc(k1)=DfDp*DpDSS(k1)+DfDq*DqDSS(k1)
1301 CONTINUE
C
DO 1302 i1=1,NTENS
    TERMp(i1)=0.0
    DO 1303 j1=1,NTENS
        TERMp(i1)=TERMp(i1)+Cve(i1,j1)*DfDSSc(j1)
1303 CONTINUE
1302 CONTINUE
1302 CONTINUE

```

```

C
  TERM10=0.0
  DO 1304 k1=1,NTENS
    TERM10=TERM10+DfDSSc(k1)*TERMp(k1)
1304 CONTINUE
C
  DO 1305 i1=1,NTENS
    TERMp(i1)=0.0
    DO 1306 j1=1,NTENS
      TERMp(i1)=TERMp(i1)+Cve(i1,j1)*DSTRAN(j1)
1306 CONTINUE
1305 CONTINUE
C
  TERM13=0.0
  DO 1307 k1=1,NTENS
    TERM13=TERM13+DfDSSc(k1)*TERMp(k1)
1307 CONTINUE
C
  TERM15 = DfDpa*DpaDSNVP*DfDp
  TERM14 = DfDpa*DPaDSNrVP*DfDp-DfDpa*DPaDSNrDP*DfDq
C
  IF (TERM14 .EQ. 0.0) THEN
    Pct = 0.0
    Qct = 0.0
    Oct = 0.0
    dlandC = TERM13/(TERM10+TERM15)
  ELSE
    Pct = (TERM10+TERM15)/TERM14
    Qct = TERM13/TERM14
    Oct = EXP(STATEV(21) + Pct*DTIME)
    dlandC = STATEV(22)/Oct + Qct*DTIME
  END IF
C
  RETURN
  END

C
C
C ***** SUBROUTINE YIELD *****
C *** CALCULATE THE ENVELOPE FUNCTIONS AND DETERMINE THE YIELD MODE ***
C
  SUBROUTINE Yield(SNrMis,PROPS,NPROPS,HP,QMis,TEMP,Phi,Betaii,
1    PoreP,dT,bT,b1T,Pamax,Pa1max,Pa,QaMis,Pb,Pt,fT,fS,fc,ModYield)
C
  IMPLICIT REAL*8 (A-H,O-Z)
  DIMENSION PROPS(NPROPS)

```

```

C
C Shear-envelope parameters
C
  TERM11 = SNrMis/PROPS(33)
  TERM12 = 1.0-TEMP/PROPS(27)
C Ice cohesion (d)
  dT = PROPS(25)*EXP(PROPS(26)*TERM12)
C Ice friction parameter (b)
  TERM10 = PROPS(31)
  b1T = PROPS(28)*EXP(PROPS(30)*(TERM12**TERM10))
  TERM10 = 1.0/PROPS(32)
  bT = b1T*(TERM11**TERM10)
C Hydrostatic pressure at max. shear strength
  TERM10 = PROPS(36)
  Pa1max = PROPS(34)*EXP(PROPS(35)*(TERM12**TERM10))
  TERM10 = PROPS(37)
  TERM10 = (1-EXP(-TERM11))**TERM10
  Pamax = Pa1max*TERM10

C
C Cap-envelope parameters
C
C Pressure at max. shear strength (pa)
  Pa = (1.0-Phi)*Pamax + 3.0*Betaii*PoreP
C Melting Pressure (pb)
  Pb = (PROPS(27)-TEMP)/PROPS(38)
  IF (Pamax .EQ. 0.0) THEN
    QaMis = dT*(1.0-Pa*Pa/(Pb*Pb))
  ELSE
    QaMis = dT+bT*Pa-0.5*bT*Pa*Pa/Pamax
  END IF

C
C Tension-envelope parameter --- Pressure at tensile strength (pt)
  Pt = (1.0-Phi)*PROPS(39)

C
C CALCULATING THE YIELD ENVELOPE FUNCTIONS
C -----
C
C Tension-yield envelope
  fT = -Pt-HP
C
C Cap-yield envelope
  TERM10 = Pb-Pa
  TERM13 = TERM10*TERM10-(HP-Pa)*(HP-Pa)
  fC = QMis-QaMis*SQRT(TERM13)/TERM10

C
C Shear-yield envelope
  IF (Pamax .EQ. 0.0) THEN
    IF (HP .EQ. 0.0) THEN
      TERM10=0.0
    ELSE
      TERM10=1.0 + Pt/HP
    END IF

```

```

TERM13 = Pb*Pb
Fe1  = dT*(1.0-Pt*Pt/TERM13)
Fe2  = Fe1+0.5*TERM13*TERM10/dT
fS   = QMis-dT*(1.0-HP*HP/TERM13)
ELSE
  TERM10 = bT*(1.0-HP/Pamax)
  Fe1    = dT-bT*Pt-0.5*bT*Pt*Pt/Pamax
  Fe2    = Fe1-(HP+Pt)/TERM10
  Fe3    = QaMis-(HP-Pa)/TERM10
  TERM10 = 0.5*bT*HP*HP/Pamax
  fS     = QMis-dT-bT*HP+TERM10
END IF
C
C DETERMINING THE YIELD MODE
C -----
C
IF (fT .GE. 0.0) THEN
  IF (QMis .LE. Fe1) THEN
C     Tension mode (zone 1)
C     ModYield = 1
  ELSE IF (QMis .GE. Fe2) THEN
C     Shear mode (zone 3)
C     ModYield = 3
  ELSE
C     Tension-shear mode (zone 2)
C     ModYield = 2
  END IF
ELSE IF (HP .GE. Pa) THEN
  IF (fC .GE. 0.0) THEN
C     Cap mode (zone 5)
C     ModYield = 5
  ELSE
C     No plastic deformation (zone 6)
C     ModYield = 6
  END IF
ELSE
  IF (fS .LT. 0.0) THEN
C     No plastic deformation (zone 6)
C     ModYield = 6
  ELSE IF (QMis .LE. Fe3) THEN
C     Shear mode (zone 3)
C     ModYield = 3
  ELSE
C     Shear-Cap envelops (zone 4)
C     ModYield = 4
  END IF
END IF
C
RETURN
END

```

```

C
C
C ***** SUBROUTINE CUTTING *****
C ***** CALCULATE PLASTIC MULTIPLIER OF THE CUT *****
C
C      SUBROUTINE Cutting(dlandX,dlandX0,fX,fXold,Alpha)
C
C      IMPLICIT REAL*8 (A-H,O-Z)
C      DIMENSION PROPS(NPROPS)
C
C      TERM10=-fX/(fX-fXold)
C      IF (TERM10.GE.20.0) THEN
C          Alpha=Alpha*10.0
C      END IF
C      TERM10=2*fX-fXold
C      IF (TERM10.LE.0.0) THEN
C          Alpha=Alpha/10.0
C      END IF
C      dlandX=(1-Alpha)*dlandX0+Alpha*dlandX
C
C      RETURN
C      END

```

```

C
C
C ***** SUBROUTINE ViscoElasticity *****
C ***** Viscoelastic calculation *****
C
C
C      SUBROUTINE ViscoElasticity(STRANve,DSTRANve,STRANe,DSTRANe,
1          SNveOld,DTIME,PROPS,NPROPS,NTENS,Dland,VC1,Vb,aT)
C
C      IMPLICIT REAL*8 (A-H,O-Z)
C      DIMENSION STRANve(NTENS),DSTRANve(NTENS),SNveOld(NTENS),
1          PROPS(NPROPS),STRANe(NTENS),DSTRANe(NTENS)
C
C      DO 4001 k1=1,NTENS
C          TERM7=2*DTIME
C          TERM7=(1.0+Dland)*VC1*(1.0-EXP(-(aT*(TERM7**Vb))))
C          TERM8=STRANe(k1)+DSTRANe(k1)
C          SNveOld(k1)=STRANve(k1)+TERM7*TERM8/PROPS(16)
4001 CONTINUE
C
C      RETURN
C      END

```

```

C
C
C ***** SUBROUTINE STRUCTURAL *****
C ***** STRUCTURAL CHANGE FUNCTION IN VISCOELASTIC MODEL (Dland) *****
C
C     SUBROUTINE Struct(Vb,TIME,DTIME,Aland,Bland,DSNMisP,SNMisP,Dland)
C
C     IMPLICIT REAL*8 (A-H,O-Z)
C     DIMENSION TIME(2)
C
C     TERM13=2.0*Vb
C     TERM14=TIME(2)+DTIME
C     Dland=Aland*ABS(DSNMisP)/(TERM14**TERM13)
C
C     IF (SNMisP.NE.0) THEN
C         TERM10=1.0+DSNMisP/SNMisP
C         IF (TERM10.LE.0.0) THEN
C             WRITE(*,*) '*** Negative argument in ln function (Dland ve)'
C         ELSE
C             TERM10=LOG(TERM10)
C             Dland=Dland+Bland*ABS(DSNMisP)/(TERM10*(TERM14**TERM13))
C         END IF
C     END IF
C
C     RETURN
C     END

C
C
C ***** SUBROUTINE POROELASTICITY *****
C ***** POROELASTICITY *****
C
C     SUBROUTINE PoroElasticity(PorMod,Phi0,Phi,Pv,CM,SM,CX,SX,STRESS,
1     DSTRES,STRANe,DSTRANe,NTENS,NDI,NSHR,Alpha,Betakk,BKcV)
C
C     IMPLICIT REAL*8 (A-H,O-Z)
C     DIMENSION CM(NTENS,NTENS),SM(NTENS,NTENS),CX(NTENS,NTENS),
1     SX(NTENS,NTENS),TERM(NTENS),DSTRES(NTENS),DSTRANe(NTENS),
2     STRESS(NTENS),STRANe(NTENS),CTmp(NTENS,NTENS)
C
C     Initial Guess for effective stress
C
C     DO 2001 i1=1,NDI
C         DSTRES(i1)=0.0
C         DO 2002 j1=1,NDI
C             DSTRES(i1) = DSTRES(i1) + CM(i1,j1)*DSTRANe(j1)
2002     CONTINUE

```

```

                TERM(i1) = DSTRES(i1)
2001 CONTINUE
    k1=NDI
    DO 2003 i1=1,NSHR
        k1=k1+1
        DSTRES(k1) = CM(k1,k1)*DSTRANe(k1)
        TERM(k1) = DSTRES(k1)
2003 CONTINUE
C
    DO 1999 i1=1,NTENS
        DO 2000 j1=1,NTENS
            CTmp(i1,j1) = 0.0
2000 CONTINUE
1999 CONTINUE
C
C    Iteration for poroelastic calculations
C
    ks=0
    TERM4=1.0
    DO WHILE ((TERM4.GT.1E-10).AND.(ks.LE.100))
        ks=ks+1
        DO 2004 k1=1,NTENS
            DSTRES(k1) = (1.0-Alpha)*DSTRES(k1) + Alpha*TERM(k1)
2004 CONTINUE
C
C    Poroelastic calculation
C
    CALL PorElas(PorMod,Phi0,Phi,Pv,CM,SM,CX,SX,
1    STRESS,DSTRES,STRANe,DSTRANe,NTENS,NDI,NSHR,Alpha,Betakk,BKcV)
C
    TERM4=0.0
    DO 2005 i1=1,NDI
        TERM(i1)=0.0
        DO 2006 j1=1,NDI
            TERM(i1) = TERM(i1) + CX(i1,j1)*DSTRANe(j1)
            TERM5 = ABS(CTmp(i1,j1)-CX(i1,j1))
            IF (TERM5.GT.TERM4) THEN
                TERM4=TERM5
            END IF
            CTmp(i1,j1)=CX(i1,j1)
2006 CONTINUE
2005 CONTINUE
    k1=NDI
    DO 2007 i1=1,NSHR
        k1=k1+1
        TERM(k1) = CX(k1,k1)*DSTRANe(k1)
        TERM5 = ABS(CTmp(k1,k1)-CX(k1,k1))
        IF (TERM5.GT.TERM4) THEN
            TERM4=TERM5
        END IF
        CTmp(k1,k1)=CX(k1,k1)
2007 CONTINUE

```

```

C
      IF (ks.GT.100) THEN
        WRITE(*,*) '***** Too many iterations ',
1         'for updating strain/stress (ks in poroelastic model)'
      END IF
    END DO
  C
  RETURN
  END

C
C ***** SUBROUTINE PORELAS *****
C ***** POROELASTICITY *****
C
  SUBROUTINE PorElas(PorMod,Phi0,Phi,Pv,CM,SM,CX,SX,STRESS,DSTRES,
1    STRANe,DSTRANe,NTENS,NDI,NSHR,Alpha,Betakk,BKcV)
  C
    IMPLICIT REAL*8 (A-H,O-Z)
    DIMENSION CM(NTENS,NTENS),SM(NTENS,NTENS),CX(NTENS,NTENS),
1    SX(NTENS,NTENS),STRESS(NTENS),
2    DSTRES(NTENS),STRANe(NTENS),DSTRANe(NTENS),PLm(NDI),
3    BSkemR(NTENS),BSkemV(NTENS),BSkem(NTENS),
4    BetaR(NTENS),BetaV(NTENS),Beta(NTENS)
  C
  C Initialization
  C
    Pv=0.0
    PvR=0.0
    PvV=0.0
    Phi=0.0
    PhiR=0.0
    PhiV=0.0
    Phit=0.0
    Bc=0.0
    BcR=0.0
    BcV=0.0
    DO 3001 i1=1,NTENS
      BSkemR(i1)=0.0
      BSkemV(i1)=0.0
      BSkem(i1)=0.0
      BetaR(i1)=0.0
      BetaV(i1)=0.0
      Beta(i1)=0.0
    DO 3002 j1=1,NTENS
      CX(i1,j1)=0.0

```

```

          SX(i1,j1)=0.0
3002      CONTINUE
3001 CONTINUE
C
C ----- Reuss & Voigt Analogies
C   Water Bulk moduli
      WK=2.196E+09
C
C   Inverse of Reuss and Voigt effective Bulk moduli
      BmReff=0.0
      TERM1=0.0
      DO 3003 k1=1,NDI
          PLm(k1)=SM(k1,1)+SM(k1,2)+SM(k1,3)
          BmReff=BmReff+PLm(k1)
          TERM1=TERM1+CM(k1,1)+CM(k1,2)+CM(k1,3)
3003 CONTINUE
      BmVeff=9.0/TERM1
      Bmeff=0.5*(BmReff+BmVeff)
C
C Drained Poroelastic model
C
      ModInt=INT(PorMod)
      Frac=PorMod-ModInt
      IF (Frac.GE.0.5) THEN
          ModInt=ModInt+1
      END IF
C
C Selects the poroelastic mode 1:drained, 2:undrained, 3:transition
C
      IF ((ModInt.EQ.1).OR.(ModInt.EQ.3)) THEN
          Pv=0.0
          TERM1=0.0
          TERM3=0.0
          DO 3004 i1=1,NDI
              TERM1=TERM1+PLm(i1)*(STRESS(i1)+0.5*DSTRES(i1))
              TERM2=0.0
              DO 3005 j1=1,NDI
                  TERM2=TERM2+CM(i1,j1)*PLm(j1)
3005          CONTINUE
              TERM3=TERM3+TERM2*(STRANe(i1)+0.5*DSTRANe(i1))
3004          CONTINUE
          TERM1=1.0+Phi0-TERM1
C
C   Positive sign in below equation was not acceptable
      PhiR=0.5*(TERM1-SQRT(TERM1*TERM1-4.0*Phi0))
      PhiV=Phi0/(1.0-TERM3)
      Phi=0.5*(PhiR+PhiV)
      PhiT=Phi
      BcR=BmReff*PhiR/(1.0-PhiR)+PhiR*(1.0/WK-BmReff)
      BcV=BmVeff*PhiV/(1.0-PhiV)+PhiV*(1.0/WK-BmVeff)
      Bc=Bmeff*Phi/(1.0-Phi)+Phi*(1.0/WK-Bmeff)
      DO 3006 k1=1,NDI

```

```

      BSkemR(k1)=PhiR*PLm(k1)/(BcR*(1.0-PhiR))
      BSkemV(k1)=PhiV*PLm(k1)/(BcV*(1.0-PhiV))
      BSkem(k1)=0.5*(BSkemR(k1)+BSkemV(k1))
3006   CONTINUE
      DO 3007 i1=1,NDI
         BetaV(i1)=0.0
         BetaR(i1)=0.0
         Beta(i1)=0.0
         DO 3008 j1=1,NDI
            BetaR(i1)=BetaR(i1)+CM(i1,j1)*BSkemR(j1)
            BetaV(i1)=BetaV(i1)+CM(i1,j1)*BSkemV(j1)
            Beta(i1)=Beta(i1)+CM(i1,j1)*BSkem(j1)
3008   CONTINUE
         BetaR(i1)=(1.0-PhiR)*BcR*BetaR(i1)
         BetaV(i1)=(1.0-PhiV)*BcV*BetaV(i1)
         Beta(i1)=(1.0-Phi)*Bc*Beta(i1)
3007   CONTINUE
C
      k1=NDI
      DO 3009 i1=1,NSHR
         k1=k1+1
3009   CONTINUE
      DO 3010 i1=1,NTENS
         DO 3011 j1=1,NTENS
            SX(i1,j1)=SM(i1,j1)/(1.0-Phi)
            CX(i1,j1)=CM(i1,j1)*(1.0-Phi)
3011   CONTINUE
3010   CONTINUE
      ELSE IF (ModInt.NE.2) THEN
         WRITE(*,*) '***** Error: PorMod is not d, u, or t'
      END IF
C
C Undrained Poroelastic model
C
      IF ((ModInt.EQ.2).OR.(ModInt.EQ.3)) THEN
C ----- Reuss Analogy
         PhiR=Phi0
         TERM1=Phi0
         TERM2=Phi0
         kk=0
         DO WHILE ((TERM1.GT.1.0E-10).AND.(kk.LE.100))
            kk=kk+1
            PhiR=(1.0-Alpha)*PhiR+Alpha*TERM2
            BcR=BmReff*PhiR/(1.0-PhiR)+PhiR*(1.0/WK-BmReff)
            PvR=0.0
            DO 3012 k1=1,NDI
               BSkemR(k1)=PhiR*PLm(k1)/(BcR*(1.0-PhiR))
               PvR=PvR-BSkemR(k1)*(STRESS(k1)+0.5*DSTRES(k1))
3012   CONTINUE
            TERM2=(1.0+PvR/(0.13986*WK))**0.13986
            TERM2=Phi0/TERM2
            IF (kk.GT.100) THEN

```

```

          WRITE(*,*) '***** Too many iterations ',
1          'for updating porosity (Undrained Reuss model)'
          END IF
          TERM1=ABS(PhiR-TERM2)
        END DO
C ----- Voigt Analogy
        PhiV=Phi0
        TERM1=Phi0
        TERM2=Phi0
        kk=0
        DO WHILE ((TERM1.GT.1.0E-10).AND.(kk.LE.100))
          kk=kk+1
          PhiV=(1.0-Alpha)*PhiV+Alpha*TERM2
          BcV=BmVeff*PhiV/(1.0-PhiV)+PhiV*(1.0/WK-BmReff)
          DO 3014 k1=1,NDI
            BSkemV(k1)=PhiV*PLm(k1)/(BcV*(1.0-PhiV))
3014          CONTINUE
          DO 3015 i1=1,NDI
            BetaV(i1)=0.0
            DO 3016 j1=1,NDI
              BetaV(i1)=BetaV(i1)+CM(i1,j1)*BSkemV(j1)
3016            CONTINUE
            BetaV(i1)=(1.0-PhiV)*BcV*BetaV(i1)
3015          CONTINUE
          PvV=0.0
          DO 3017 k1=1,NDI
            PvV=PvV-BetaV(k1)*(STRANe(k1)+0.5*DSTRANe(k1))/BcV
3017          CONTINUE
          TERM2=(1.0+PvV/(0.13986*WK))*0.13986
          TERM2=Phi0/TERM2
          IF (kk.GT.100) THEN
            WRITE(*,*) '***** Too many iterations ',
1            'for updating porosity (Undrained Voigt model)'
            END IF
            TERM1=ABS(PhiV-TERM2)
          END DO
C ----- Reuss & Voigt Analogies
        Phi=0.5*(PhiR+PhiV)
        Phit=0.5*(Phit+Phi)
        Bc=Bmeff*Phi/(1.0-Phi)+Phi*(1.0/WK-Bmeff)
        Pv=0.0
        DO 3018 k1=1,NDI
          BSkem(k1)=Phi*PLm(k1)/(Bc*(1.0-Phi))
          Pv=Pv-BSkem(k1)*(STRESS(k1)+0.5*DSTRES(k1))
3018          CONTINUE
        DO 3019 i1=1,NDI
          BetaR(i1)=0.0
          Beta(i1)=0.0
          DO 3020 j1=1,NDI
            BetaR(i1)=BetaR(i1)+CM(i1,j1)*BSkemR(j1)
            Beta(i1)=Beta(i1)+CM(i1,j1)*BSkem(j1)
3020          CONTINUE

```

```

        BetaR(i1)=(1.0-PhiR)*BcR*BetaR(i1)
        Beta(i1)=(1.0-Phi)*Bc*Beta(i1)
3019    CONTINUE
        DO 3021 k1=1,NDI
            Pv=Pv-Beta(k1)*(STRANe(k1)+0.5*DSTRANe(k1))/Bc
3021    CONTINUE
        Pv=0.5*Pv
C
        k1=NDI
        DO 3022 i1=1,NSHR
            k1=k1+1
3022    CONTINUE
C
        DO 3023 i1=1,NTENS
            DO 3024 j1=1,NTENS
                SX(i1,j1)=SM(i1,j1)/(1.0-Phi)
                SX(i1,j1)=SX(i1,j1)-Bc*BSkem(i1)*BSkem(j1)
                CX(i1,j1)=CM(i1,j1)*(1.0-Phi)
                CX(i1,j1)=CX(i1,j1)+Beta(i1)*Beta(j1)/Bc
3024    CONTINUE
3023    CONTINUE
        END IF
C
C Transition Poroelastic model
C
        IF (ModInt.EQ.3) THEN
            Phi=Phit
            Bc=Bmeff*Phi/(1.0-Phi)+Phi*(1.0/WK-Bmeff)
            Pv=0.0
            DO 3025 k1=1,NDI
                BSkem(k1)=Phi*PLm(k1)/(Bc*(1.0-Phi))
                Pv=Pv-BSkem(k1)*(STRESS(k1)+0.5*DSTRES(k1))
3025    CONTINUE
            DO 3026 i1=1,NDI
                Beta(i1)=0.0
                DO 3027 j1=1,NDI
                    Beta(i1)=Beta(i1)+CM(i1,j1)*BSkem(j1)
3027    CONTINUE
                Beta(i1)=(1.0-Phi)*Bc*Beta(i1)
3026    CONTINUE
            DO 3028 k1=1,NDI
                Pv=Pv-Beta(k1)*(STRANe(k1)+0.5*DSTRANe(k1))/Bc
3028    CONTINUE
                Pv=0.5*Pv
                k1=NDI
                DO 3029 i1=1,NSHR
                    k1=k1+1
3029    CONTINUE
C
C
                write(*,*) 'Computed St and Ct ...'
                DO 3030 i1=1,NTENS
                    DO 3031 j1=1,NTENS

```

```

          SX(i1,j1)=SM(i1,j1)/(1.0-Phi)
          SX(i1,j1)=SX(i1,j1)-Bc*BSkem(i1)*BSkem(j1)
          CX(i1,j1)=CM(i1,j1)*(1.0-Phi)
          CX(i1,j1)=CX(i1,j1)+Beta(i1)*Beta(j1)/Bc
3031          CONTINUE
3030          CONTINUE
          END IF
C
          BKcV = 1.0/BcV
          Betakk = 0.0
          DO 3032 k1=1,NTENS
              Betakk = Betakk + Beta(k1)
3032          CONTINUE
          TERM1 = CX(1,1)*CX(2,3)*CX(2,3)
          TERM1 = TERM1-CX(1,1)*CX(2,2)*CX(3,3)
          TERM1 = TERM1-2*CX(2,3)*CX(1,2)*CX(1,3)
          TERM1 = TERM1+CX(2,2)*CX(1,3)*CX(1,3)
          TERM1 = TERM1+CX(1,2)*CX(1,2)*CX(3,3)
          SX(1,1) = 0.5*(SX(1,1)+(CX(2,3)*CX(2,3)-CX(2,2)*CX(3,3))/TERM1)
          SX(2,2) = 0.5*(SX(2,2)+(CX(1,3)*CX(1,3)-CX(1,1)*CX(3,3))/TERM1)
          SX(3,3) = 0.5*(SX(3,3)+(CX(1,2)*CX(1,2)-CX(1,1)*CX(2,2))/TERM1)
          SX(1,2) = 0.5*(SX(1,2)+(CX(3,3)*CX(1,2)-CX(2,3)*CX(1,3))/TERM1)
          SX(2,1) = SX(1,2)
          SX(1,3) = 0.5*(SX(1,3)+(CX(1,3)*CX(2,2)-CX(1,2)*CX(2,3))/TERM1)
          SX(3,1) = SX(1,3)
          SX(2,3) = 0.5*(SX(2,3)+(CX(1,1)*CX(2,3)-CX(1,2)*CX(1,3))/TERM1)
          SX(3,2) = SX(2,3)
          SX(4,4) = 0.5*(SX(4,4)+1.0/CX(4,4))
          SX(5,5) = 0.5*(SX(5,5)+1.0/CX(5,5))
          SX(6,6) = 0.5*(SX(6,6)+1.0/CX(6,6))
C
          CALL MatInverse(SX,CX,NTENS)
C
          DO 3033 i1=1,NTENS
              DO 3034 j1=1,NTENS
3034          CONTINUE
3033          CONTINUE
C
          RETURN
          END

```

```

C
C
C ***** SUBROUTINE STRANDev *****
C ***** DEVIATORIC STRAIN AND DSTRAIN *****
C
C
C      SUBROUTINE STRANDev(SN,DSN,SNvol,DSNvol,SNdev,DSNdev,NTENS,NDI,
1      NSHR)
C
C      IMPLICIT REAL*8 (A-H,O-Z)
C      DIMENSION SN(NTENS),DSN(NTENS),SNdev(NTENS),DSNdev(NTENS)
C
C      SNvol=0.0
C      DSNvol=0.0
C      DO 6001 k1=1,NDI
C          SNvol=SNvol+SN(k1)
C          DSNvol=DSNvol+DSN(k1)
6001 CONTINUE
C      DO 6002 k1=1,NDI
C          SNdev(k1)=SN(k1)-SNvol/3.0
C          DSNdev(k1)=DSN(k1)-DSNvol/3.0
6002 CONTINUE
C      k1=NDI
C      DO 6003 i1=1,NSHR
C          k1=k1+1
C          SNdev(k1)=SN(k1)
C          DSNdev(k1)=DSN(k1)
6003 CONTINUE
C
C      RETURN
C      END

C
C
C ***** SUBROUTINE STRESDev *****
C ***** HYROSTATIC PRESSURE, DEVIATORIC STRESS AND THEIR INCREMENTS *****
C
C
C      SUBROUTINE STRESDev(SS,DSS,HP,DHP,SSdev,DSSdev,NTENS,NDI,NSHR)
C
C      IMPLICIT REAL*8 (A-H,O-Z)
C      DIMENSION SS(NTENS),DSS(NTENS),SSdev(NTENS),DSSdev(NTENS)
C
C      HP=0.0
C      DHP=0.0
C      DO 6011 k1=1,NDI
C          HP=HP-SS(k1)/3.0

```

```

        DHP=DHP-DSS(k1)/3.0
6011 CONTINUE
        DO 6012 k1=1,NDI
            SSdev(k1)=SS(k1)+HP
            DSSdev(k1)=DSS(k1)+DHP
6012 CONTINUE
        k1=NDI
        DO 6013 i1=1,NSHR
            k1=k1+1
            SSdev(k1)=SS(k1)
            DSSdev(k1)=DSS(k1)
6013 CONTINUE
C
        RETURN
        END

C
C
C ***** SUBROUTINE STSMISES *****
C ***** MISES STRESS AND HYDROSTATIC PRESSURE *****
C
C
C     SUBROUTINE STSMises(SSdev,QMis,NDI,NSHR,NTENS)
C
C     IMPLICIT REAL*8 (A-H,O-Z)
C     DIMENSION SSdev(NTENS)
C
C     SJ2D=0.0
C     DO 7007 k1=1,NDI
C         SJ2D=SJ2D+SSdev(k1)*SSdev(k1)/2.0
7007 CONTINUE
        k1=NDI
        DO 7008 i1=1,NSHR
            k1=k1+1
            SJ2D=SJ2D+SSdev(k1)*SSdev(k1)
7008 CONTINUE
        QMis=SQRT(3.0*SJ2D)
C
        RETURN
        END

```

```

C
C
C ***** SUBROUTINE STNMISES *****
C ***** MISES STRAIN *****
C
C
C SUBROUTINE STNMises(SNdev,DSNdev,SNMis,DSNMis,NDI,NSHR,NTENS)
C
C IMPLICIT REAL*8 (A-H,O-Z)
C DIMENSION SNdev(NTENS),DSNdev(NTENS)
C
C Mises deviatoric equivalent strain
C
C SNMis=0.0
C DSNMis=0.0
C DO 7011 k1=1,NDI
C     SNMis=SNMis+SNdev(k1)*SNdev(k1)
C     DSNMis=DSNMis+DSNdev(k1)*DSNdev(k1)
7011 CONTINUE
C k1=NDI
C DO 7012 i1=1,NSHR
C     k1=k1+1
C     SNMis=SNMis+2.0*SNdev(k1)*SNdev(k1)
C     DSNMis=DSNMis+2.0*DSNdev(k1)*DSNdev(k1)
7012 CONTINUE
C SNMis = SQRT(2.0*SNMis/3.0)
C DSNMis = SQRT(2.0*DSNMis/3.0)
C
C RETURN
C END

C
C
C ***** SUBROUTINE INVARIENTS *****
C ***** STRESS AND STRAIN INVARIANTS *****
C
C
C SUBROUTINE Invariants(SS,DSS,SN,DSN,NDI,NSHR,NTENS,HP,DHP,SSdev,
1     DSSdev,SNdev,DSNdev,SNvol,DSNvol,SNMis,DSNMis,QMis,DQMis,
2     SJ1,SJ2D,SJ3D)
C
C IMPLICIT REAL*8 (A-H,O-Z)
C DIMENSION SS(NTENS),DSS(NTENS),SN(NTENS),DSN(NTENS),
1     SSdev(NTENS),DSSdev(NTENS),SNdev(NTENS),DSNdev(NTENS)
C
C HP:                Hydrostatic Pressure
C DHP:               Increment in hydrostatic Pressure

```

```

C   SJ1:           First invariant of stress tensor
C   SSdev(NTENS): Deviatoric stress
C   DSSdev(NTENS): Increment in deviatoric stress
C   SNdev(NTENS):  Deviatoric strain
C   DSNdev(NTENS): Increment in deviatoric strain
C   SNvol:         Volumetric strain
C   DSNvol:        Increment in volumetric strain
C   SNMis:         Mises Equivalent (deviatoric) strain
C   DSNMis:        Increment in Mises Equivalent (deviatoric) strain
C   QMis:          Mises Equivalent (deviatoric) stress
C   DQMis:         Increment in Mises Equivalent (deviatoric) stress
C   SJ2D:         Second invariant of deviatoric stress tensor
C   SJ3D:         Third invariant of deviatoric stress tensor

```

C

C Deviatoric stress

C

```

      HP=0.0
      DHP=0.0
      DO 7021 k1=1,NDI
          HP=HP-SS(k1)/3.0
          DHP=DHP-DSS(k1)/3.0
7021 CONTINUE
      SJ1=-3.0*HP
      DO 7022 k1=1,NDI
          SSdev(k1)=SS(k1)+HP
          DSSdev(k1)=DSS(k1)+DHP
7022 CONTINUE
      k1=NDI
      DO 7023 i1=1,NSHR
          k1=k1+1
          SSdev(k1)=SS(k1)
          DSSdev(k1)=DSS(k1)
7023 CONTINUE

```

C

C Deviatoric strain

C

```

      SNvol=0.0
      DSNvol=0.0
      DO 7024 k1=1,NDI
          SNvol=SNvol+SN(k1)
          DSNvol=DSNvol+DSN(k1)
7024 CONTINUE
      DO 7025 k1=1,NDI
          SNdev(k1)=SN(k1)-SNvol/3.0
          DSNdev(k1)=DSN(k1)-DSNvol/3.0
7025 CONTINUE
      k1=NDI
      DO 7026 i1=1,NSHR
          k1=k1+1
          SNdev(k1)=SN(k1)
          DSNdev(k1)=DSN(k1)
7026 CONTINUE

```

```

C
C Mises equivalent stress
C
  SJ2D=0.0
  DQMis=0.0
  DO 7027 k1=1,NDI
    SJ2D=SJ2D+SSdev(k1)*SSdev(k1)/2.0
    DQMis=DQMis+DSSdev(k1)*DSSdev(k1)/2.0
7027 CONTINUE
  k1=NDI
  DO 7028 i1=1,NSHR
    k1=k1+1
    SJ2D=SJ2D+SSdev(k1)*SSdev(k1)
    DQMis=DQMis+DSSdev(k1)*DSSdev(k1)
7028 CONTINUE
  QMis=SQRT(3.0*SJ2D)
  DQMis=SQRT(3.0*DQMis)
C
C Mises equivalent strain
C
  SNMis=0.0
  DSNMis=0.0
  DO 7029 k1=1,NDI
    SNMis=SNMis+SNdev(k1)*SNdev(k1)/3.0
    DSNMis=DSNMis+DSNdev(k1)*DSNdev(k1)/3.0
7029 CONTINUE
  k1=NDI
  DO 7030 i1=1,NSHR
    k1=k1+1
    SNMis=SNMis+2.0*SNdev(k1)*SNdev(k1)/3.0
    DSNMis=DSNMis+2.0*DSNdev(k1)*DSNdev(k1)/3.0
7030 CONTINUE
  SNMis=SQRT(2.0*SNMis)
  DSNMis=SQRT(2.0*DSNMis)
  RETURN
  END

```

```

C
C
C ***** SUBROUTINE MATINVERSE *****
C ***** INVERSE THE MATRIX OF NTENS DIMENSION *****
C
C      SUBROUTINE MatInverse(TAM,TAMINV,NN)
C
C      IMPLICIT REAL*8 (A-H,O-Z)
C      DIMENSION TAM(NN,NN),TAMINV(NN,NN)
C
C      TERM111 = TAM(1,1)*TAM(2,3)*TAM(2,3)
C      TERM111 = TERM111-TAM(1,1)*TAM(2,2)*TAM(3,3)
C      TERM111 = TERM111-2*TAM(2,3)*TAM(1,2)*TAM(1,3)
C      TERM111 = TERM111+TAM(2,2)*TAM(1,3)*TAM(1,3)
C      TERM111 = TERM111+TAM(1,2)*TAM(1,2)*TAM(3,3)
C      TAMINV(1,1) = (TAM(2,3)*TAM(2,3)-TAM(2,2)*TAM(3,3))/TERM111
C      TAMINV(2,2) = (TAM(1,3)*TAM(1,3)-TAM(1,1)*TAM(3,3))/TERM111
C      TAMINV(3,3) = (TAM(1,2)*TAM(1,2)-TAM(1,1)*TAM(2,2))/TERM111
C      TAMINV(1,2) = (TAM(3,3)*TAM(1,2)-TAM(2,3)*TAM(1,3))/TERM111
C      TAMINV(2,1) = TAMINV(1,2)
C      TAMINV(1,3) = (TAM(1,3)*TAM(2,2)-TAM(1,2)*TAM(2,3))/TERM111
C      TAMINV(3,1) = TAMINV(1,3)
C      TAMINV(2,3) = (TAM(1,1)*TAM(2,3)-TAM(1,2)*TAM(1,3))/TERM111
C      TAMINV(3,2) = TAMINV(2,3)
C      TAMINV(4,4) = 1.0/TAM(4,4)
C      TAMINV(5,5) = 1.0/TAM(5,5)
C      TAMINV(6,6) = 1.0/TAM(6,6)
C
C      RETURN
C      END

```

